## *Field and flow effects on tethered polymer chains*

Gavin John Bown

# Field and Flow Effects on Tethered Polymer Chains

1999

Gavin John Bown

Van Mildert College

University of Durham

Supervisor:

Professor Randal W Richards



A thesis submitted to the University of Durham in partial fulfilment of the regulations for the degree of Doctor of Philosophy.

# Abstract

## Field and Flow Effects on Tethered Polymer Chains

**Gavin John Bown**

**PhD Thesis 1999**

Solvated brush layers formed by linear polystyrenes have been investigated under quiescent and solvent shear-flow conditions using neutron reflectometry. Cyclohexane and toluene were used as solvents, and the polystyrene chains were tethered by one end to macroscopically flat silicon substrates via short poly-4-vinylpyridine end-groups. The brush systems were studied using a purpose built flow reflectometry cell.

The brush height was found to increase with improving thermodynamic quality of the solvent due to increasingly strong repulsive excluded volume interactions between chain segments. Model fitting of the reflectivity data revealed that the polymer volume fraction profile was well described by parabola-like functions in agreement with the predictions of self-consistent field theory.

No changes in the reflectivity profiles were observed upon exposure of the brush layers to solvent flow-induced area average shear rates of up to 147 000 $s^{-1}$. This observation has been rationalised through a number of considerations, including comparison with recent theoretical predictions.

Aqueous micellar dispersions of diblock copolymers of styrene and ethylene oxide have been studied using small angle neutron scattering in the concentration range 0.05 to 6.5 weight % copolymer. The micelles formed were found to be spherically symmetric, consisting of a polystyrene core surrounded by a corona of highly stretched solvated polyethylene oxide chains. At higher concentrations, the intermicellar interaction has been interpreted using an analytic structure factor originally developed to describe macroion solutions.

On subjecting the dispersions to Couette shear, no evidence for long-range ordering of the micelles was observed in the diffraction patterns.

# Acknowledgements

First and foremost I would like to thank my supervisor, Professor Randal Richards, whose tireless enthusiasm and support over the last three years have been hugely appreciated. It's been a pleasure working for you "boss".

This work would not have been possible without the help and guidance of several people, and I would therefore like to express my gratitude to: Tom Kiff and Lian Hutchings for making/helping me to make the polymers, Gordon Forrest and Andy Bosanko for GPC analysis, Terry Harrison for computer support, Neil and Jim for building the cell, Helene and Jean for help with organising/fixing things generally and John Webster, Steve King, Richard Heenan, Jeff Penfold and Sean Langridge at RAL for helping me with the neutron experiments and data fitting.

My six years in Durham would not have been such a hugely enjoyable experience had it not been for the great friends that I've made along the way. The IRC has provided a great working environment, and thanks go especially to Pecky, Runner, Rich Ainsworth, Andy B, Foggy, Rachel, Angela, Andreas, the Helens T & V, Bos, Lian and Richard T.
My life outside the IRC (and indeed before I joined the IRC) has benefited greatly from the influence of the following people: Ian Wallis, The Oxon, Dan and Ralph (and all the lads past and present from Gradsoc AFC), "Owens" and Sam Law. Huge thanks also to the many musicians that I have had the pleasure of working with in my various jazz pursuits: Jez Light, Mark Brown, Steve Summers, Ray Dales, Stui Ellerton (the worlds greatest drummer), Ian Halford (the worlds second greatest drummer, ha ha - sorry mate!!) and Neil Harland. I think it's fair to say that we've done some cracking gigs (not to mention a few dodgy ones!!) over the last few years.

Finally and most importantly, I would like to thank Mum, Dad and Ali. Without your unwavering love and support through good times and bad, none of this would have been possible.

## Declaration

The work reported in this thesis has been carried out at the Durham site of the Interdisciplinary Research Centre in Polymer Science and Technology and the Rutherford Appleton Laboratory, Chilton, Oxfordshire between October 1996 and September 1999. This work has not been submitted for any other degree either in Durham or elsewhere and is the original work of the author except where otherwise stated.

## Statement of Copyright



## Financial Support

I gratefully acknowledge the provision of a maintenance grant by the EPSRC.

## CONTENTS

# CHAPTER 1

# INTRODUCTION

# CHAPTER 1

# INTRODUCTION

## 1.1 General Introduction

Polymer brushes [1,2] are formed when one end of the polymer molecules are constrained to lie in a plane such that the distance between the tethered ends is less than the Flory radius of gyration of the chains. In this case, forced lateral overlap of neighbouring chains occurs, and if the brush layer is immersed in a thermodynamically good solvent then the chains stretch strongly in the direction normal to the grafting surface due to repulsive excluded volume interactions between chain segments. In so doing, the polymer molecules maximise their enthalpically favourable interaction with the solvent molecules, and the height of the resulting solvated brush layer is commonly found to be several times the unperturbed radius of gyration of the free chains in solution. Brush layers can be formed by grafting end-functionalised polymers to macroscopically flat solid substrates (such as silicon or quartz) and immersing them in a suitable solvent [3-6] (or homopolymer matrix [7]). They can also be formed at the air-liquid [8] and liquid-liquid interfaces.

Interest in tethered polymer layers extends back to the middle of this century when it was discovered that the end-grafting of polymer molecules to colloidal particles was an extremely effective way of preventing flocculation [9-13]. This phenomenon highlights one of the most useful applications of tethered polymer layers; namely that they can be used to modify the properties of surfaces and interfaces. In the case of colloidal stabilisation, the presence of a grafted polymer layer can modify the interaction between the colloidal particles. The many applications of tethered polymer layers include the compatibility of bioimplants [14], the development of new adhesive materials [15,16], chromatographic devices [17], lubricants [18], the prevention of protein adsorption at biosurfaces [19] and drug delivery systems [20].

Theoretical calculations [21,22] predict that the monomer density for solvated polymer brushes shows a parabolic decay with increasing distance from the grafting surface, and this has been confirmed by numerous experimental studies [3-6, 8]. Indeed, the determination of the monomer density profile for polymer brushes is of some importance in understanding their properties and potential applications, and one of the best techniques for probing the structure of polymer brushes is neutron reflectometry [23-26].

The specular reflection of neutrons from a surface (or interface) allows the composition profile to be determined in the direction normal to the surface. In the study of hydrocarbon systems, the technique exploits the fact that the nuclear scattering lengths for hydrogen and deuterium are markedly different, meaning that deuterium labelling can be used to "highlight" regions of interest in the system. With solid-liquid interfacial systems, neutron reflectometry is one of the only techniques that can be used to probe the structural features of the system due to the "buried" nature of the interface. Several groups have carried out neutron reflectometry studies on polystyrene brush systems [3-6, 8], and all of them found that the monomer density profiles within the brush layers showed a parabola-like decay with increasing distance from the grafting surface, while brush heights in thermodynamically good solvents were found to be several times the unperturbed radius of gyration of the brush chains.

The equilibrium properties of brushes and adsorbed layers are now reasonably well understood, and more recently much attention has been focussed on the dynamic properties of these systems. The shear-induced deformation of tethered polymer layers is important in applications such as adsorption and separation processes (e.g. chromatography), oil recovery, waste water treatment and high performance coatings and lubricants. Much theoretical and experimental work has therefore been undertaken in recent years to try and establish the effect of solvent flow-induced shear on the structure of polymer brush layers.

The best experimental evidence to date for shear effects on brush layers was obtained by Klein and coworkers [27]. They used a surface forces apparatus to measure the normal force between two polymer brush layers grafted onto mica sheets when they were sheared past each other in a good solvent. They found that the normal forces between the two layers became increasingly repulsive as the oscillatory shear velocity was increased, and this implied that the brush layers were stretching as a result of

shear. It was found that above a critical shear rate, the brushes stretched by approximately 20%.

These experimental findings lead to the development of a series of theoretical models all attempting to predict the effect of solvent shear flow on the structure of tethered polymer layers [28-35]. The majority of these theories predict a shear induced swelling of the brush layer in response to solvent flow, and this has lead to the proposal of a somewhat novel application for polymer brushes as pressure-sensitive automated microvalves [36] (i.e. the expansion of two closely spaced brush layers in response to increasing fluid velocity reduces the cross-sectional area for flow).

Nguyen et al [37] used neutron reflectometry to study the effect of shear on polystyrene brush layers in thermodynamically good and poor solvents. A flow reflectometry cell was used to facilitate solvent flow past the brush layers; however, no effect of shear was seen in the reflectivity profiles obtained from the experiments.

Block copolymers form micelles [38] when dispersed in a selective solvent for one of the blocks at concentrations above a critical micelle concentration. Depending on the concentration, temperature and relative length of the blocks, these micelles may be spherical, elliptical or cylindrical in shape. The structure of spherical micelles consists of a spherical core of the insoluble block surrounded by a shell (or corona) of the swollen soluble block chains, and in this case the shell chains can effectively be considered to form a tethered layer grafted over the spherical core surface. The decay in shell monomer density with increasing distance from the core has been shown (via self-consistent field calculations [39]) to go from the parabolic form associated with planar polymer brushes to the power-law decay associated with star polymers, as the curvature of the grafting surface (i.e. the core) is increased.

Numerous experimental investigations have been carried out in recent years to elucidate the association characteristics of diblock copolymers in solution and to establish the morphology of the micelles formed. A whole array of different copolymer/solvent systems have been investigated using techniques such as light scattering [40-42], small angle neutron [43-45] and X-ray [46,47] scattering and fluorescence studies [48]. Small angle neutron scattering (SANS) [49] provides an ideal tool for studying polymeric micellar systems, since it allows the composition, size and shape characteristics of the micelles to be investigated (along with any inter-micellar long-range ordering phenomena) over a length scale range of approximately 5-10 000Å. As

with neutron reflectometry, deuterium labelling can be used in SANS experiments to selectively highlight specific regions of interest in the systems under investigation.
As the micelle number density is increased (by increasing the concentration of the copolymer dispersion), the micelle shell regions begin to overlap, and this leads to the formation of gel phases. The micelles have quasi-crystalline order within these phases (usually body- or face-centred cubic for spherical micelles and hexagonal packing for rod-like micelles), and much work has been carried out in investigating shear-induced long-range ordering of these phases [50-52] using small angle neutron and X-ray scattering.
Applications of block copolymers in solution include heterophase stabilisation, solubilisation of otherwise insoluble substances, colloidal stabilisation and drug delivery.

## 1.2 Aims and Objectives of this Work

The aims of the work presented in this thesis can be summarised as follows:

- The design and construction of a flow reflectometry cell for the study of polymer brushes under quiescent and shear-flow conditions.

- Investigation of the volume fraction profiles for solvated polymer brushes (formed by end-grafted polystyrenes) using neutron reflectometry, and comparison of these profiles with theoretical predictions.

- Investigation of the effect of solvent shear flow on the structure and dimensions of end-grafted polystyrene brush layers using neutron reflectometry, and comparison of the results obtained with theoretical predictions.

- Investigation of a) the morphology of micelles formed by dispersions of poly(styrene-*b*-ethylene oxide) copolymers in water using small angle neutron scattering and b) the effect of Couette shear on the long-range organisation of the micelles within the dispersions.

## 1.3 References


1 Prigogine, I; Rice, S A (Eds.). '*Advances in Chemical Physics – Volume XCIV.*' John Wiley and Sons, Inc. (1996).

2 Milner, S T. *Science*, 1991, **251**, 905.

3 Karim, A; Satija, S K; Douglas, J F; Ankner, J F; Fetters, L J. *Physical Review Letters*, 1994, **73**, 3407.

4 Liu, Y; Quinn, J; Rafailovich, M H; Sokolov, J. *Macromolecules*, 1995, **28**, 6347.

5 Field, J B; Toprakcioglu, C; Ball, R C; Stanley, H B; Dai, L; Barford, W; Penfold, J; Smith, G; Hamilton, W. *Macromolecules*, 1992, **25**, 434.

6 Perahia, D; Wiesler, D G; Satija, S K; Fetters, L J; Sinha, S K; Milner, S T. *Physical Review Letters*, 1994, **72**, 100.

7 Thompson, H L. '*Molecular Architecture and Functional Group Effects on Segregation in Polymers.*' PhD Thesis, University of Durham, 1998.

8 Kent, M S; Lee, L T; Factor, B J; Rondelez, F; Smith, G S. *J. Chem. Phys.* 1995, **103**, 2320.

9 van der Waarden, M. *J. Colloid Sci.* 1950, **5**, 317.

10 Mackor, E L. *J. Colloid Sci.* 1951, **6**, 492.

11 Clayfield, E J; Lumb, E C. *J. Colloid Interface Sci.* 1966, **22**, 269.

12 Meier, D J. *J. Phys. Chem.* 1967, **71**, 1861.

13 Hesselink, F T. *J. Phys. Chem.* 1969, **73**, 3488.

14 Ward, R S. *IEEE Eng. Med. Biol. Mag.* 1989, **6**, 22.

15 Raphael, E; de Gennes, P G. *J. Phys. Chem.* 1992, **96**, 4002.

16 Ji, H; de Gennes, P G. *Macromolecules*, 1993, **26**, 520.

17 van Zanten, J H. *Macromolecules*, 1994, **27**, 6797.

18 Joanny, J F. *Langmuir*, 1992, **8**, 989.

19 Amiji, M; Park, K. *J. Biomater. Sci. Polymer Ed.* 1993, **4**, 217.

20 Lee, R J; Low, P S. *J. Biol. Chem.* 1994, **269**, 3198.

21 Milner, S T; Witten, T A; Cates, M E. *Macromolecules*, 1988, **21**, 2610.

22 Milner, S T; Witten, T A; Cates, M E. *Europhysics Letters*, 1988, **5**, 413.

23 Bucknall, D G in '*Modern Techniques for Polymer Characterisation.*' Pethrick, R A; Dawkins, J V (Eds). John Wiley and Sons Ltd (1999).

24 Richards, R W (Ed). *'Scattering Methods in Polymer Science'*. Ellis Horwood (1995).

25 Russell, T P. *Materials Science Reports*, 1990, **5**, 171.

26 Penfold, J. *'The Adaptation of Methods in Multilayer Optics for the Calculation of Specular Neutron Reflection'*. Rutherford Appleton Laboratory Report, RAL-88-088 (1988).

27 Klein, J; Perahia, D; Warburg, S. *Nature*, 1991, **352**, 143.

28 Rabin, Y; Alexander, S. *Europhysics Letters*, 1990, **13**, 49.

29 Barrat, J L. *Macromolecules*, 1992, **25**, 832.

30 Kumaran, V. *Macromolecules*, 1993, **26**, 2464.

31 Harden, J L; Cates, M E. *Physical Review E*, 1996, **53**, 3782.

32 Aubouy, M; Harden, J L; Cates, M E. *J. Phys. II France*. 1996, **6**, 969.

33 Saphiannikova, M G; Pryamitsyn, V A; Cosgrove, T. *Macromolecules*, 1998, **31**, 6662.

34 Lai, P Y; Binder, K. *J. Chem. Phys.* 1993, **98**, 2366.

35 Miao, H; Guo, H; Zuckermann, M J. *Macromolecules*, 1996, **29**, 2289.

36 Sevick, E M; Williams, D R M. *Macromolecules*, 1994, **27**, 5285.

37 Nguyen, D; Clarke, C J; Eisenberg, A; Rafailovich, M H; Sokolov, J; Smith, G S. *J. Appl. Cryst.* 1997, **30**, 680.

38 Hamley, I W. *'The Physics of Block Copolymers.'* Oxford University Press (1998).

39 Dan, N; Tirrell, M. *Macromolecules*, 1992, **25**, 2891.

40 Xu, R; Winnik, M A; Hallett, F R; Riess, G; Croucher, M D. *Macromolecules*, 1991, **24**, 87.

41 Bronstein, L M; Chernyshov, D M; Timofeeva, G I; Dubrovina, L V; Valetsky, P M. *Langmuir*, 1999, **15**, 6195.

42 Dewhurst, P F; Lovell, M R; Jones, J L; Richards, R W; Webster, J R P. *Macromolecules*, 1998, **31**, 7851.

43 Nakano, M; Matsuoka, H; Yamaoka, H; Poppe, A; Richter, D. *Macromolecules*, 1999, **32**, 697.

44 Higgins, J S; Blake, S; Tomlins, P E; Ross-Murphy, S B; Staples, E; Penfold, J; Dawkins, J V. *Polymer*, 1988, **29**, 1968.

45 Mortensen, K; Brown, W; Almdal, K; Alami, E; Jada, A. *Langmuir*, 1997, **13**, 3635.

46 Hickl, P; Ballauff, M; Jada, A. *Macromolecules*, 1996, **29**, 4006.

47 Cogan, K A; Gast, A P; Capel, M. *Macromolecules*, 1991, **24**, 6512.

48 Wilhelm, M; Zhao, C L; Wang, Y; Xu, R; Winnik, M A; Mura, J L; Riess, G; Croucher, M D. *Macromolecules*, 1991, **24**, 1033.

49 King, S M in *'Modern Techniques for Polymer Characterisation.'* Pethrick, R A; Dawkins, J V (Eds). John Wiley and Sons Ltd (1999).

50 Pople, J A; Hamley, I W; Fairclough, J P A; Ryan, A J; Booth, C. *Macromolecules*, 1998, **31**, 2952.

51 Leyh, B; Creutz, S; Gaspard, J P; Bourgaux, C; Jerome, R. *Macromolecules*, 1998, **31**, 9258.

52 McConnell, G A; Lin, M Y; Gast, A P. *Macromolecules*, 1995, **28**, 6754.

# CHAPTER 2

# THEORY

# CHAPTER 2

# THEORY

## 2.1 Polymer Brushes

The size of an isolated polymer coil (of a given degree of polymerisation) in solution is determined by the thermodynamic quality of the solvent. For the case of a low molecular weight thermodynamically good solvent (i.e. the solvent molecules are of a similar size to the chain segments and the interaction between the two components is attractive), the coil will expand slightly due to repulsive excluded volume interactions between the chain segments (positive excluded volume) as they seek to maximise their contact with the solvent molecules. In the case of a thermodynamically poor solvent (i.e. the interaction between the polymer segments and the solvent molecules is repulsive) the interaction between the polymer segments becomes attractive (negative excluded volume), and the coil collapses in on itself in order to minimise segment-solvent interactions. For any given polymer-solvent system, the thermodynamic quality of the solvent improves with increasing temperature, and the transition between the poor and good solvent regimes occurs at the theta temperature ($T_\theta$). At this temperature the excluded volume is zero, and the polymer coil has its unperturbed dimensions.

The behaviour of polymer molecules when one of their ends is tethered to a surface or an interface is qualitatively different to that of free chain molecules in solution.[1] This is due to the fact that the presence of the grafting surface limits the configurational

space of the chains, and the 2-dimensional anchoring changes the way in which neighbouring chains interact with each other.

Consider the case of polymer molecules tethered by one end to a planar substrate and immersed in a thermodynamically good solvent. If the distance between points of attachment at the substrate is greater than the radius of gyration of the chains then no interaction between different chains will occur. Here the grafted chains are swollen within the constraints imposed by the presence of the grafting surface, and form a series of 'mushrooms' (figure 2.1). If the distance between points of attachment at the substrate surface is less than the radius of gyration then the chains are forced to interact with one another. In this case, repulsive intermolecular excluded volume interactions cause the chains to stretch strongly in the direction normal to the grafting surface. In so doing, the chains minimise their contact with each other and maximise their enthalpically favourable interaction with the solvent molecules. The chain stretching is counterbalanced by an elastic restoring force of entropic origin (since the chains are being stretched away from their random walk configurations), and the resulting structure is referred to as a polymer brush. The brush height, $h$ (defined as the distance from the grafting surface at which the polymer volume fraction falls to zero) for polymer brushes in good solvents is several times the unperturbed radius of gyration of the polymer chains. However, as the thermodynamic quality of the solvent is reduced, the brush layer collapses as the polymer segments seek to minimise their enthalpically unfavourable interactions with the solvent molecules.

The shape of the polymer volume fraction profile (i.e. the distribution of polymer as a function of distance from the grafting surface) has been the subject of numerous theoretical models.[2]

Alexander [3] used a scaling argument to describe the characteristics of semi-dilute polymer brushes. The dimensionless grafting density, $\sigma$, is defined as the number of chains grafted in an area the square of the segment size and can be expressed in terms of the average distance between grafting sites, $d$, and the statistical segment length, $a$ (approximately equal to the cube root of the monomer volume).

$$\sigma = \frac{a^2}{d^2} \qquad \textbf{Equation 2.1}$$

a)

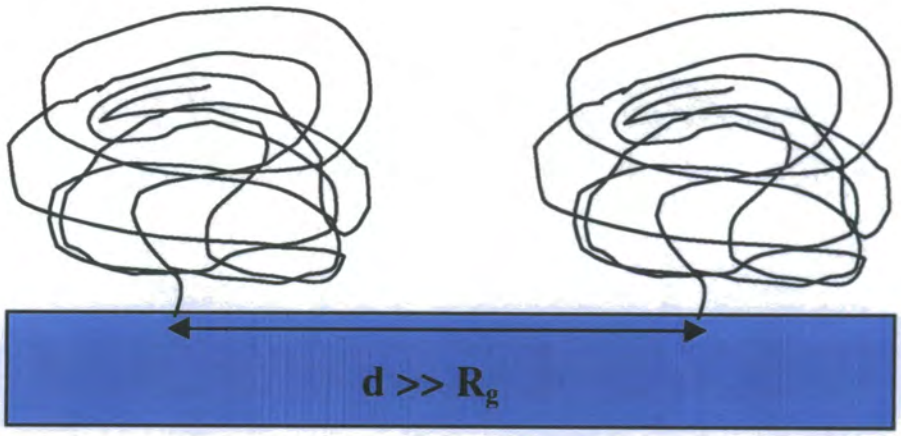


b)

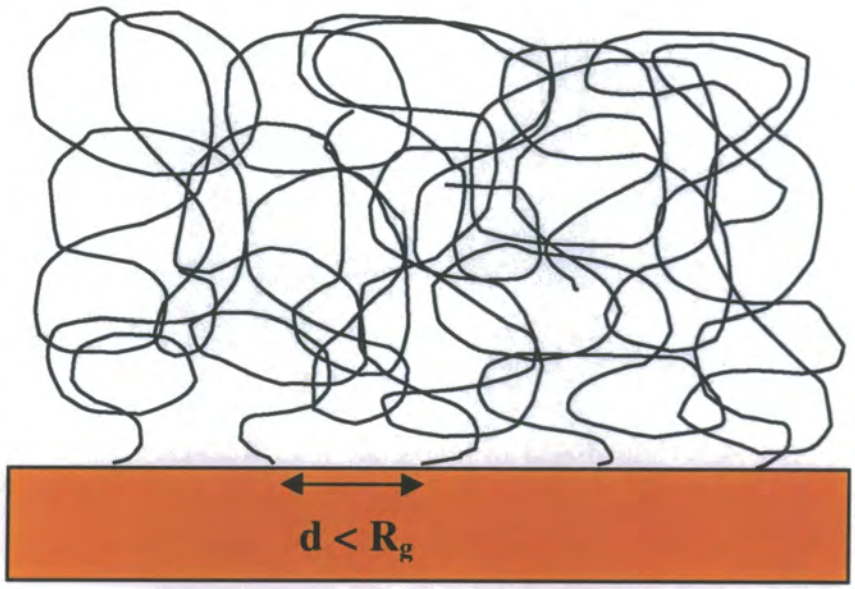


**Figure 2.1** Schematic illustration of: a) Mushrooms b) Polymer brush.

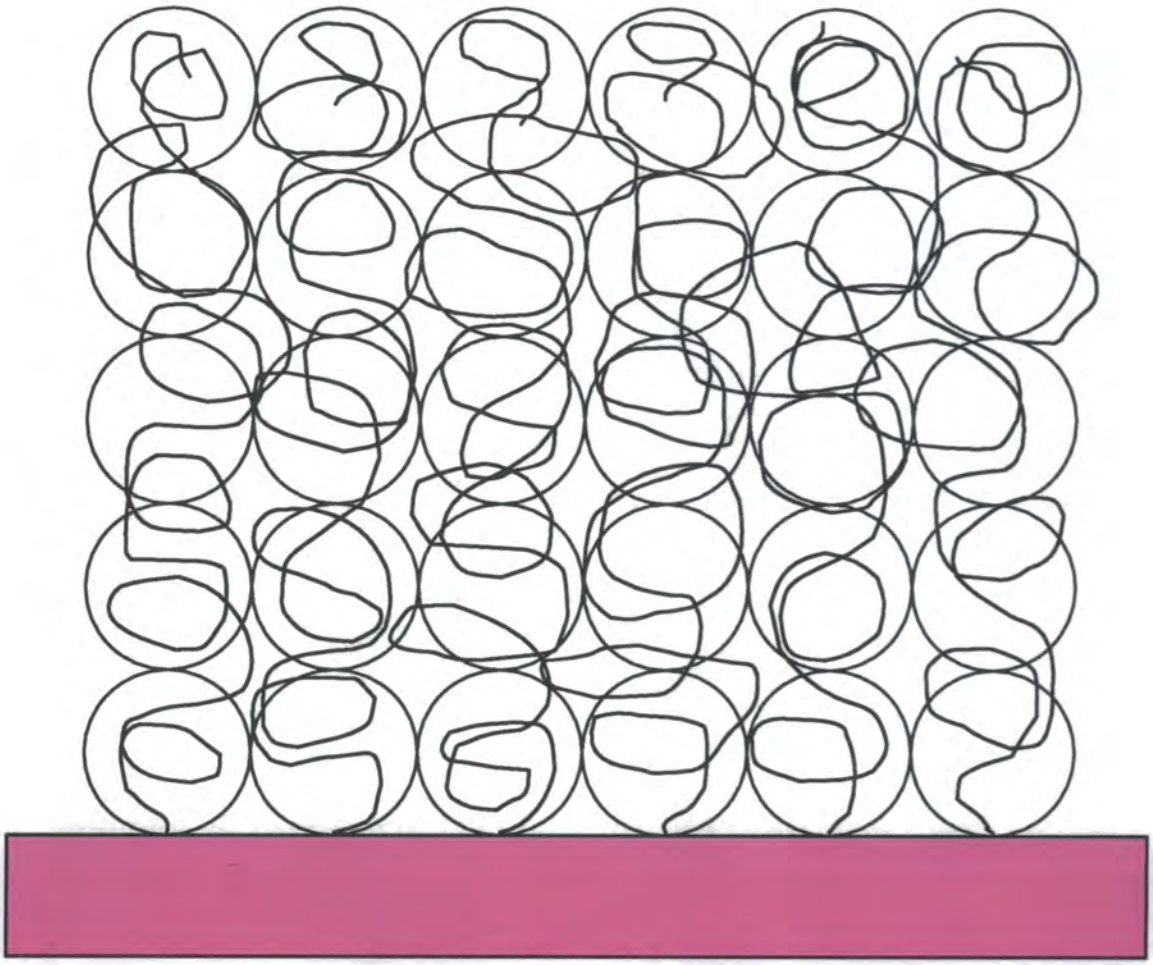

**Figure 2.2** The blob model for a semi-dilute polymer brush.

Conditions inside the brush are semi-dilute for relatively low grafting densities, and the average distance between grafting sites can be expressed as:

$$d = a\sigma^{-1/2} \qquad \textbf{Equation 2.2}$$

The brush chains can be divided into a series of 'blobs' with the blob size being equal to $d$ (figure 2.2). Each blob contains $N_b$ subunits, and $d$ can also be defined as:

$$d = aN_b^{3/5} \qquad \textbf{Equation 2.3}$$

The blobs fill the space within the brush, and the polymer volume fraction inside the brush ($\phi_p$) can be expressed as:

$$\phi_p \sim \frac{a^3 N_b}{d^3} \qquad \textbf{Equation 2.4}$$

The polymer volume fraction is thus related to the grafting density as:

$$\phi_p \sim \sigma^{2/3} \qquad \textbf{Equation 2.5}$$

The volume of one chain consisting of $N$ monomer units is $hd^2$, where $h$ is the height of the grafted chain (or brush height). This leads to an expression for the brush height:

$$h \sim Na\sigma^{1/3} \qquad \textbf{Equation 2.6}$$

When conditions within the brush are concentrated (i.e. at higher grafting densities), the brush characteristics can be described using an energy balance argument proposed by de Gennes.[4] The free energy cost associated with stretching a brush chain from its Gaussian statistics to the brush height, $h$, is given by:

$$\frac{F_{stretch}}{k_B T} = \frac{h^2}{a^2 N} \qquad \textbf{Equation 2.7}$$

where $N$ is the degree of polymerisation of the brush chains.

The excluded volume interaction free energy per unit volume can be expressed as:

$$\frac{F_{EV}}{k_B T} = \frac{v\phi_p^2 k_B T}{2a^6} \qquad \textbf{Equation 2.8}$$

where the excluded volume parameter, $v$, is defined in terms of the segment size and the Flory-Huggins parameter as $a^3(1-2\chi)$. Since the volume associated with a single chain can be defined as $\frac{ha^2}{\sigma}$, the total free energy per chain can be expressed in terms of the brush height, $h$ as:

$$\frac{F_{chain}}{k_BT} \sim \frac{h^2}{2a^2N} + \frac{vN^2\sigma}{2ha^2} \qquad \textbf{Equation 2.9}$$

Finally, minimising equation 2.9 with respect to $h$ enables the brush height to be expressed as:

$$h \sim N(v\sigma)^{1/3} \qquad \textbf{Equation 2.10}$$

Thus it can be seen from equations 2.6 and 2.10 that both the Alexander and the de Gennes theories predict that the brush height scales linearly with the degree of polymerisation and the cube root of the grafting density. However, the de Gennes argument highlights the role of the thermodynamic quality of the solvent in determining the brush height (i.e. the brush height increases with improving solvent quality).

The models proposed by Alexander and de Gennes both assume that all chains within the brush behave alike and that all of the free chain ends are located at the tip of the brush. The polymer volume fraction profiles corresponding to the models presented above thus take the form of a step-function (i.e. the polymer volume fraction is constant throughout the brush – see figure 2.3).

Milner et al [5-7] used a self consistent field (SCF) method to determine the concentration profiles for polymer brushes. The solution of the SCF equations indicated that the polymer volume fraction within the brush showed a parabolic decay with increasing distance from the grafting surface in contrast to the step-function profiles predicted by Alexander and de Gennes.

The SCF calculations involved determining the partition function for a single chain in the field due to all of the other chains in a self-consistent fashion (since it is initially unknown) i.e. no assumptions were made about the monomer density profile.

The chain trajectory can be expressed as the function $r(t)$ where $r$ represents the position in space of monomer unit number $t$. The free energy can be expressed as two parts: the stretching energy and the effective mean field potential $U(r)$. The single-chain partition function, $Z_{SC}$ is expressed as:

$$Z_{SC} = \sum_{\{r(t)\}} \exp(-S_k) \qquad \textbf{Equation 2.11}$$

The sum in equation 2.11 is over all possible chain configurations ($r(t)$), and $S_k$ is expressed for each possible chain configuration as:

$$S_i = \int dt \left[ \frac{1}{2} \left( \frac{dr_i}{dt} \right)^2 - U(r(t)) \right] \qquad \textbf{Equation 2.12}$$

Under conditions of strong stretching, the sum of equation 2.11 is dominated by the configuration that minimises equation 2.12. Equations 2.11 and 2.12 are analogous to the path integral formulation of quantum mechanics with the stretching energy corresponding to the particle kinetic energy and $S_i$ corresponding to the action. A strongly stretched configuration corresponds to the trajectory of a particle with a large momentum, and this can be described by the classical limit of quantum mechanics i.e. a particle takes a path which minimises the action. Equation 2.13 is the analogue of Newton's second law of motion and represents the equation of motion for the trajectories of the polymer chains.

$$\frac{d^2 r}{dt^2} = -\nabla U \qquad \textbf{Equation 2.13}$$

Boundary conditions must also be defined for the brush system. One end of every chain is known to be located at the wall (i.e. the grafting surface); however, the

location of the free end is unknown, although the local stretching must be zero there in the absence of an applied force.

Returning to the quantum mechanical analogy, each polymer chain corresponds to a particle dropped from rest at some distance from the wall, moving through the potential such that it arrives at the wall after a time corresponding to the degree of polymerisation of the chains. For chains grafted to a planar surface, the form of the self-consistent potential is a function only of the distance from the wall, $z$. For monodisperse chains (i.e. assuming that all of the chains have the same length), a quadratic form for the potential is required since this is an "equal time" potential in which particles dropped from any position arrive at the origin at the same time.

The self-consistent potential thus takes the form of a simple harmonic oscillator as defined in equation 2.14.

$$U(z) = Bz^2 - A \qquad \textbf{Equation 2.14}$$

The time taken for the particle to fall to the origin is equal to one quarter of the period of the simple harmonic oscillator, and this time corresponds to the chain length, $N$. This enables the constant $B$ to be defined as:

$$B = \frac{\pi^2}{8N^2} \qquad \textbf{Equation 2.15}$$

The constant $A$ is defined by the relationship between the potential and the volume fraction. A suitable choice for this relationship is $U(\phi) = -v\phi$, where $v$ is the excluded volume parameter. The value of $A$ is fixed by the requirement that $\int_0^h \phi(z)dz$ defines the coverage (where $h$ is the brush height), and the potential of equation 2.14 can now be converted to an expression for the volume fraction profile, $\phi(z)$:

$$\phi(z) = \frac{B}{v}(h^2 - z^2) \qquad \textbf{Equation 2.16}$$

The brush height is expressed as:

$$h = \left(\frac{12}{\pi^2}\right)^{1/3} N(\sigma v)^{1/3} \qquad \textbf{Equation 2.17}$$

It can be seen from equation 2.17 that the brush height predicted by SCF theory shows the same dependence on $N$ and $\sigma$ as the simple scaling models of Alexander and de Gennes. However, whilst the scaling theory assumes that all chains behave alike and that all of the free chain ends are located at the tip of the brush (corresponding to a step-function volume fraction profile), the SCF calculations reveal that the free chain ends are distributed throughout the entire brush height and that the volume fraction profile is parabolic. Figure 2.3 illustrates schematically the step-function and parabolic polymer volume fraction profiles.

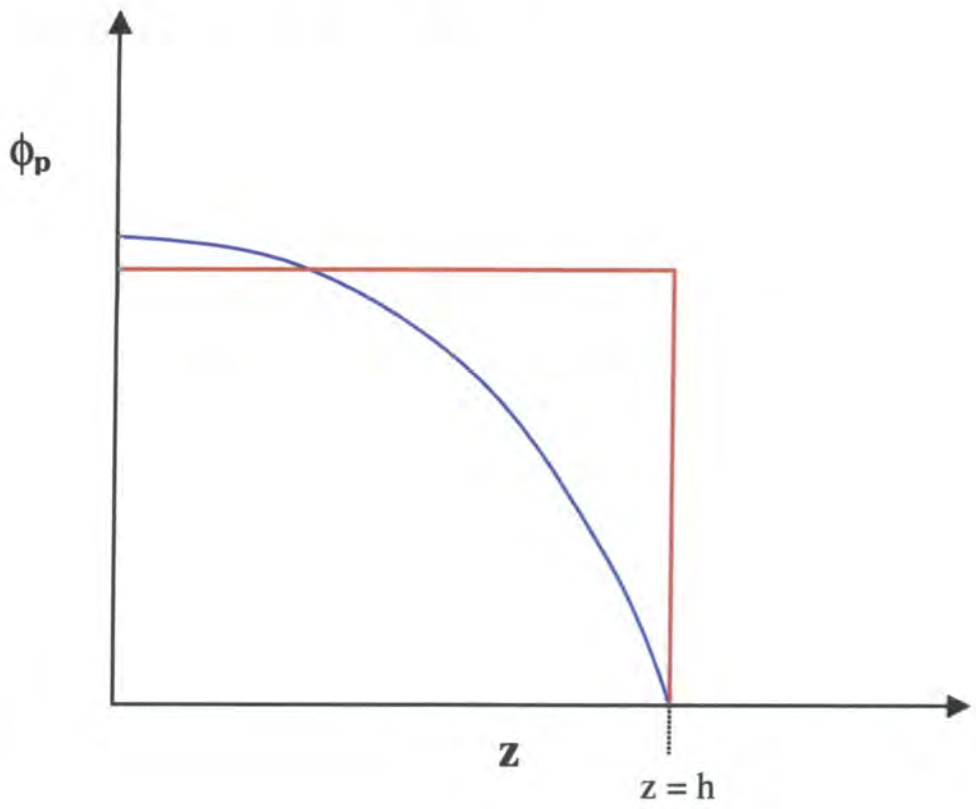


**Figure 2.3** Schematic illustration of the step-function (red) and parabolic polymer volume fraction profiles (polymer volume fraction, $\phi_P$, versus distance from the grafting surface, $z$).

## 2.2 Polymer Brushes Under Shear

Several theoretical models have been developed to describe the effect of shear on the structure of polymer brush layers.

Rabin and Alexander [8] treated the brush as a series of closely packed "blobs" with the blob diameter being equal to the distance between grafting sites. The effect of shear was approximated as a force acting on the free surface of the brush causing the chains to elongate and tilt in the flow direction. The theory predicts that the height of the brush layer is not affected by shearing the brush against a thermodynamically good solvent. Barrat, [9] however, revisited the model of Rabin and Alexander and considered the response of the brush layer to a fixed shear force, $F_{//}$, applied to the free end of each grafted chain. The resulting model predicts that the shear force leads to an increase in the brush height of up to 25%. However, quantitative comparison of this model with experiment is difficult since it is the shear rate, $\dot{\gamma}$, that is the experimentally relevant parameter whereas the effective boundary shear force, $F_{//}$, is unknown.

Kumaran [10] considered the effect of hydrodynamic interactions in a grafted polymer brush exposed to solvent shear flow. It was found that the interactions caused a net upward force on the brush chains, which could in turn lead to an increase in the brush height. The shear-induced expansion of the brush was calculated using a perturbation analysis, and the increase in brush height was found to be proportional to the square of the fluid velocity at the surface for small deviations from the equilibrium state. However, as deviations from the equilibrium configuration became larger, the increase in brush height was found to vary as a linear function of the fluid velocity, and in the limit of large fluid velocities the maximum brush expansion was predicted to be 33%.

The three theories presented above all effectively ignore the details of solvent flow within the brush, and simply model the frictional force between brush chains and solvent molecules as a force applied to the free surface of the brush. Harden and Cates, [11] however, presented a theoretical approach for studying the deformation of grafted polymer layers exposed to strong shear flows in which the deformation of the brush chains and the solvent flow profile within the layer were calculated in a mutually consistent fashion. The depth of penetration of the shear flow into the brush

is equal to the distance between grafting sites, $d$, and the drag force exerted on each chain, $F_{//}$, is given by equation 2.18.

$$F_{//} \cong 6\pi\eta\dot{\gamma}d^2 \cong \frac{\dot{\gamma}\tau k_B T}{d} \qquad \textbf{Equation 2.18}$$

where $\eta$ is the solvent viscosity and $\tau$ is the Zimm relaxation time of the brush chains. The model predicts that a non-linear increase in the brush height occurs as a function of the applied force, with appreciable swelling of the brush layer occurring for shear rates exceeding the reciprocal Zimm relaxation time ($\tau^{-1}$) of the brush chains (equation 2.19).

$$\dot{\gamma} > \tau^{-1} \qquad \text{(i.e. } \dot{\gamma}\tau > 1\text{)} \qquad \textbf{Equation 2.19}$$

where: $\tau^{-1} = \frac{k_B T}{\eta d^3}$

An asymptotic swelling of ~25% is predicted for high shear rates ($\dot{\gamma}\tau >> 1$).

It is important to note that all four of the theories discussed so far assume an Alexander-de Gennes step-function profile for the variation in monomer density throughout the brush in the quiescent state. This step-function model assumes that all of the brush chains behave alike and that the free chain ends are all located at the outer extremity of the brush. In reality however, the quiescent brush monomer density profile is known to be parabolic (with the free chain ends distributed throughout the brush), and it thus seems reasonable that models based on Alexander-de Gennes-type brushes are likely to be quantitatively inaccurate in their predictions for the effect of shear on the brush structure.

The inherent limitation of using the Alexander-deGennes brush model was partially overcome in another theoretical treatment developed by Harden et al.[12] In this model, a dual chain brush configuration is proposed (as illustrated schematically in figure 2.3) in which only a fraction of the brush chains ($f$) are exposed to the flow. These

chains are thus tilted and stretched by the shear flow, while the remaining fraction of the chains $(1-f)$ lie deeper within the brush where the flow is screened.

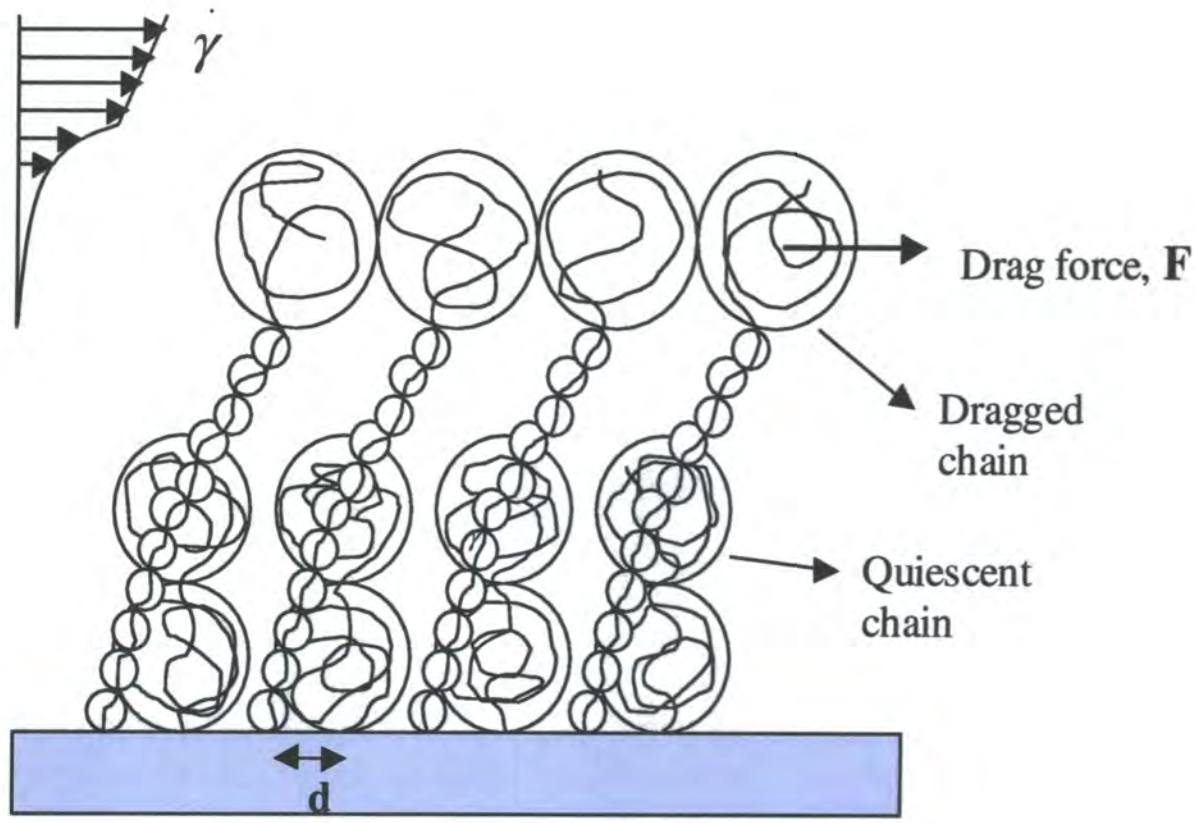


**Figure 2.3** Schematic illustration of the dual-chain brush model. A fraction, $f$, of the chains are tilted and stretched by the shear flow ("dragged" chains) while the remaining fraction, $1-f$, lie deeper within the brush where the flow is screened ("quiescent" chains). The shear rate ($\dot{\gamma}$) profile at the outer region of the brush is also illustrated.

With this model, the effective normalised grafting density ($\sigma = \frac{a^2}{d^2}$) in the outer region of the brush is lower than the value at the grafting surface (this applies also to the true parabolic brush profile, whereas for the step-function profile the effective value of $\sigma$ is constant throughout the brush).

Each of the dragged chains experiences a force, $F_{//}$, which is expressed as:

$$F_{//} \cong \frac{\eta \dot{\gamma}}{f\sigma} \qquad \textbf{Equation 2.20}$$

The dragged fraction of chains does not remain fixed, but responds to the applied shear. The deformation of the dragged chains in response to the applied force competes with excluded volume and chain elasticity effects to determine both the dependence of $f$ on the applied shear-flow and the structure of the brush layer as a whole. For low shear rates, the majority of the chains stretch while a minority lie retracted in the quiescent region (i.e. $f > 1-f$). However, as the shear rate is increased, the brush layer acts in such a way as to expose less of the chains to the solvent flow (i.e. more chains retract into the quiescent region). At sufficiently high shear rates, a minority of the chains are exposed to the flow while the majority lie retracted in the quiescent region (i.e. $f < 1-f$).

In quantitative terms, this model predicts that the brush layer is more susceptible to shear fields when compared to models based on Alexander-de Gennes-type brushes. More specifically, the dual-chain model predicts that the onset of strong swelling occurs at a lower threshold shear-rate ($\gamma\tau > 0.23$ as opposed to $\gamma\tau > 1$ as predicted for an Alexander-de Gennes-type brush – see equation 2.19) and that the asymptotic value of the relative swelling is somewhat larger.

### 2.2.1 Other Theories

Saphiannikova et al.[13] used a Brownian dynamics method to simulate the behaviour of polymer brushes under shear. The results of these simulations show that the height of the brush and the monomer distribution within the brush (averaged in the lateral dimensions) are unaffected by shear providing that the stretching force per chain ($f_c$) does not exceed the "Gaussian" threshold $\frac{f_c a}{k_B T} << 1$ (where $a$ is the segment size).

When the chains are stretched beyond this threshold, however, the brush collapses in a way similar to the contraction observed in thermodynamically poor solvents.

Lai and Binder [14] carried out Monte Carlo (MC) simulations of brushes exposed to shear flow in which the jump rate of monomers to neighbouring lattice sites was greater in the flow direction than in the direction against the flow. A parabolic brush profile was used, and the brush height and fluid velocity profile within the brush were determined self-consistently. It was found that the height of the brush decreased slightly as a result of solvent flow.

Miao et al [15] also carried out MC simulations in which they determined the fluid velocity profile within the brush self-consistently. However, a parabolic profile was not assumed. The results of the simulations indicated that the chains tilted and stretched in the flow direction, although the height of the brush was essentially unaffected by the flow.

## 2.3 Block Copolymer Micelles

Block copolymers form micelles when dispersed in a selective solvent for one of the blocks at concentrations above a critical micelle concentration (cmc). These micelles consist of a core region (formed by the insoluble blocks) surrounded by a shell (or corona) of the soluble blocks.

Two possible models exist for the association of molecules into micelles:[16] open and closed association. With open association, a continuous distribution of micelles exists containing 1, 2, 3, 4, . . ., $n$ molecules. A continuous series of equilibrium constants is associated with this distribution of micelles; however, the open association model does not lead to the concept of a cmc. The cmc is not a thermodynamic property of the system, and can be described simply as the concentration at which a sufficient number of micelles are formed as detected by any given analytical technique (e.g. light scattering or small angle neutron scattering). The closed association process can be described as a thermodynamic equilibrium between unimers ($A$) and micelles ($A_p$) consisting of $p$ unimers as defined in equation 2.1.

$$A \rightleftharpoons \left(\frac{1}{p}\right) A_p \qquad \textbf{Equation 2.21}$$

The equilibrium constant, $K$ can then be defined as:

$$K = \frac{[A_p]^{1/p}}{[A]} \qquad \textbf{Equation 2.22}$$

The scenario for block copolymer micelles dispersed in a solvent medium is qualitatively similar to that for polymer brushes at planar interfaces, since the solvated coronal chains are effectively grafted over the surface of the core (formed by the insoluble blocks).

### 2.3.1 Scaling Theories

The Alexander-de Gennes [3,4] model for polymer brushes at planar interfaces predicts that the density profile normal to the interface is a step-function. This model was developed further by de Gennes [17] to provide a simple scaling model for block copolymer micelles consisting of a core of $B$ blocks and a corona (or shell) of $A$ blocks. In the limit of short coronal chains, and assuming uniformly stretched chains for the core radius, $R_B$, de Gennes predicted that the core radius scaled as:

$$R_B \sim a N_B^{2/3} \left(\frac{\gamma a^2}{T}\right)^{1/3} \qquad \textbf{Equation 2.23}$$

where $a$ is the segment length, $N_B$ is the degree of polymerisation of the core chains and $\gamma$ is the $A-B$ interfacial tension. The number of chains per micelle (or aggregation number), $p$ was predicted to scale as:

$$p \sim \frac{N_B \gamma a^2}{T} \qquad \textbf{Equation 2.24}$$

Daoud and Cotton [18] developed a model to describe star-like polymers dispersed in a good solvent in which the arms of the star were confined at one end on a spherical surface. This model has been applied to describe block copolymer micellar dispersions with the number of arms, $f$, being replaced by the aggregation number, $p$. Halperin [19] used the Daoud-Cotton model as the basis for a scaling description of the structure of micelles formed by $AB$ diblock copolymers in a highly selective solvent. Micelles consisting of a small insoluble $B$ core surrounded by an extended swollen $A$ corona were considered for the condition $N_A >> N_B$ (where $N_A$ and $N_B$ are the degrees of polymerisation of the $A$ and $B$ blocks respectively). Rather than assuming a constant monomer density profile for the corona, the density profile was allowed to fall off with increasing distance from the core as is the case for star-polymers, and the scaling behaviours of the core and total micelle radii ($R_B$ and $R$ respectively) were obtained as follows:

$$R_B \propto N_B^{3/5} \qquad \textbf{Equation 2.25}$$

$$R \propto N_B^{4/15} N_A^{3/5} \qquad \textbf{Equation 2.26}$$

Zhulina and Birshtein [20] applied scaling theory to the specific case of micelles formed by an $AB$ diblock copolymer in a solvent selective for the $A$ block and identified four different regions depending on the copolymer composition. The scaling behaviour of $R_A$, $R_B$ and $p$ in these four regions can be summarised as follows:

- Region I $\quad N_A < N_B^{\nu/6}$

$$R_B \propto N_B^{2/3} \qquad R_A \propto N_A^{\nu} \qquad p \propto N_B \qquad \textbf{Equation 2.27}$$

- Region II $\quad N_B^{\nu/6} < N_A < N_B^{(1+2\nu)/6\nu}$

$$R_A \propto N_A N_B^{(\nu-1)/6\nu} \qquad \textbf{Equation 2.28}$$

- Region III $N_B^{(1+2\nu)/6\nu} < N_A < N_B^{(1+2\nu)/5\nu}$

$R_B \propto N_B N_A^{-2\nu/(1+2\nu)}$ $R_A \propto N_A^{3\nu/(3\nu+1)}$ $p \propto N_B^2 N_A^{-6\nu/(1+2\nu)}$ **Equation 2.29**

- Region IV $N_A > N_B^{(1+2\nu)/5\nu}$

$R_B \propto N_B^{3/5}$ $R_A \propto N_A^{\nu} N_B^{2(1-\nu)/5}$ $p \propto N_B^{4/5}$ **Equation 2.30**

The parameter $\nu$ is the Flory scaling exponent for the radius of gyration of linear polymers ($R_g \sim M^{\nu}$, where $\nu = 0.5$ for a theta solvent and 0.588 for a good solvent).

It is interesting to note that all of the scaling theories discussed above predict that the aggregation number and core radius are independent of the coronal chain length for micelles with a small core and a large corona.

### 2.3.2 SCF Theories

Noolandi and Hong [21] considered the system of $AB$ diblock copolymer micelles in solution, with the insoluble $B$ blocks forming the spherical micelle core surrounded by a uniform corona of $A$ blocks. The results obtained from the mean field theory were in excellent agreement with the small angle X-ray scattering results acquired by Plestil et al [22] for poly(styrene-*b*-butadiene) micelles in heptane. The core radius was found to scale as $R_B \sim N_B^{0.64}$ while the aggregation number was found to scale as $p \sim N_B^{0.9}$. Whitmore and Noolandi [23] developed this approach and obtained scaling relations for the core radius and shell thickness (equation 2.31).

$R_B \sim N_B^{\beta} N_A^{\mu}$ $R_A \sim N_A^{\omega}$ **Equation 2.31**

where: $0.67 \leq \beta \leq 0.76$, $-0.1 \leq \mu \leq 0$ and $0.5 \leq \omega \leq 0.86$.

The predictions of Whitmore and Noolandi show reasonable agreement with experimental findings.

Nagarajan and Ganesh [24] developed a theory for the micellisation of $AB$ diblock copolymer molecules in a selective solvent. The micelles were assumed to have a completely segregated core region consisting solely of the insoluble $B$ blocks and a shell consisting of the soluble $A$ blocks and the solvent. They found that the solvent-compatible $A$ blocks could influence the micellar properties, particularly when the solvent was a very good one. By combining the experimental results obtained for various micellar systems with results obtained for model systems, Nagarajan and Ganesh obtained universal scaling relations, and these are given in equations 2.32 to 2.34.

$$R_B = \frac{3N_B^2\left(\frac{\gamma_{BS}a^2}{k_BT}\right) + N_B^{3/2} + N_B N_A^{1/2}\left(\frac{R_B}{R_A}\right)^{1/3}}{\left[1 + N_B^{-1/3} + \left(\frac{N_B}{N_A}\right)\left(\frac{R_A}{R_B}\right)^2\right]^{1/3}} a \qquad \textbf{Equation 2.32}$$

$$p = \frac{4\pi N_B\left(\frac{\gamma_{BS}a^2}{k_BT}\right) + \left(\frac{4\pi}{3}\right)N_B^{1/2} + \left(\frac{4\pi}{3}\right)N_A^{1/2}\left(\frac{R_B}{R_A}\right)}{1 + N_B^{-1/3} + \left(\frac{N_B}{N_A}\right)\left(\frac{R_A}{R_B}\right)^2} \qquad \textbf{Equation 2.33}$$

$$\frac{R_A}{R_B} = 0.867\left[\frac{1}{2} + \frac{N_A N_B^2}{(N_A + N_B)^3} - \chi_{AS}\right]^{1/5} N_A^{6/7} N_B^{-8/11} \qquad \textbf{Equation 2.34}$$

The parameters $\gamma_{BS}$ and $\chi_{AS}$ in equations 2.32 to 2.34 are the core-solvent interfacial tension and the coronal block-solvent interaction parameter respectively.

## 2.3 Neutron Reflectometry

The specular reflection of neutrons from surfaces and interfaces [25-28] provides information about the depth-composition profile of thin planar samples. The technique probes the neutron refractive index profile normal to the surface from which the neutrons are reflected, and is thus able to provide detailed structural information about layer thicknesses, surface and interfacial widths and profiles.

The wave-like properties of neutrons allows them to be reflected and refracted in an exactly analogous way to other forms of electromagnetic radiation such as light and X-rays. The reflectivity of neutrons is thus dependent on both their wavelength and incident angle as well as the chemical composition (i.e. nuclear structure) perpendicular to the interface.

Nuclear scattering lengths vary randomly across the periodic table, and an important factor with regard to the study of hydrocarbon systems is the large difference between the nuclear scattering lengths of hydrogen and deuterium. This feature means that isotopic substitution can be used to manipulate the neutron refractive index profile within the sample.

The neutron scattering length density (SLD) of a polymer molecule, $\rho_N$, can be expressed in terms of the monomer mass and physical density ($m$ and $\rho$ respectively) and the sum of the nuclear scattering lengths for all atoms present in the monomer ($\Sigma b_i$).

$$\rho_N = \frac{\rho N_A}{m} \Sigma b_i \qquad \textbf{Equation 2.35}$$

For the case of a polymer brush immersed in solvent, the SLD of any given volume element within the brush ($\rho_B$) can be expressed in terms of the volume fractions of polymer and solvent present ($\phi_P$ and $\phi_S$ respectively, where $\phi_P = 1 - \phi_S$) along with their SLD's ($\rho_P$ and $\rho_S$ respectively).

$$\rho_B = \rho_P \phi_P + \rho_S \phi_S \qquad \textbf{Equation 2.36}$$

The essence of the neutron reflectivity experiment is to measure the specular reflection as a function of the wave vector or momentum transfer, $Q$ (= |**Q**|). This is illustrated schematically in figure 2.4.

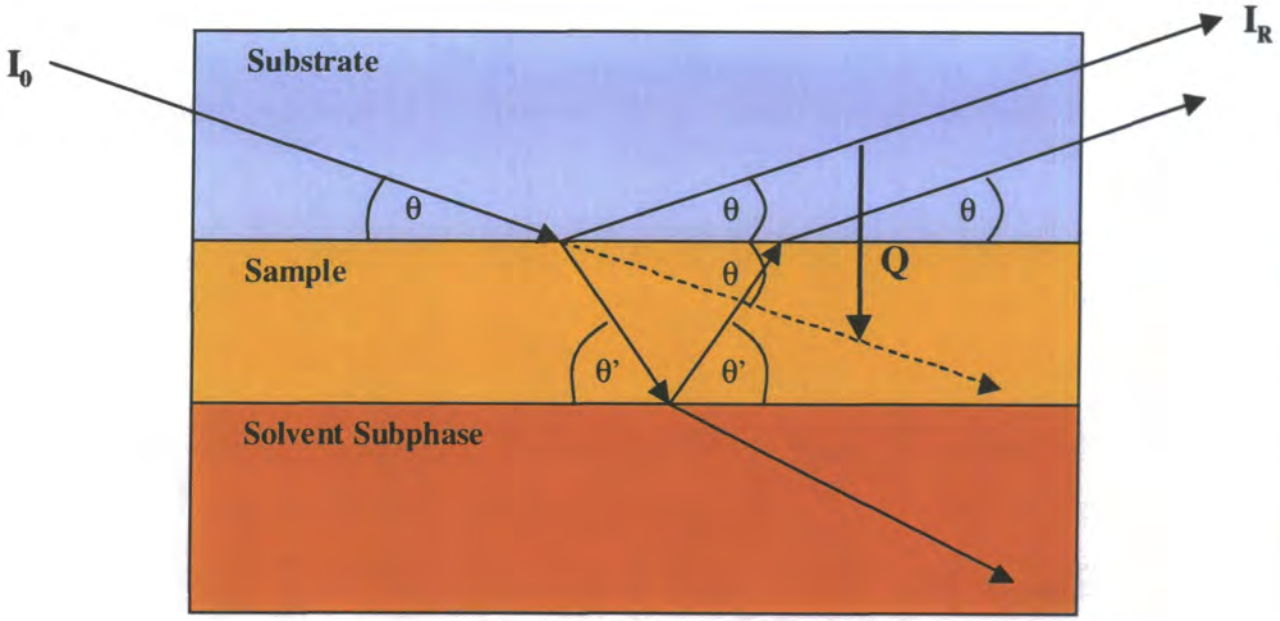


**Figure 2.4** Schematic illustration of the neutron reflectivity experiment.

The reflectivity, $R(Q)$, is defined as the ratio of the reflected and incident beam intensities ($I_R$ and $I_0$ respectively).

$$R(Q) = \frac{I_R(Q)}{I_0(Q)} \qquad \textbf{Equation 2.37}$$

The refraction and reflection of neutrons involves the interference between the incident neutron wave and waves scattered in the forward direction. When a neutron wave impinges on a boundary between two media, the refractive index, $n$, at the boundary is defined by $n = \overline{k_2} / \overline{k_1}$ where $\overline{k_1}$ and $\overline{k_2}$ are the neutron wavevectors inside and outside the lower medium respectively. The momentum (or wavevector)

transfer, $Q$, is defined as:

$$Q = \overline{k_1} - \overline{k_2} = \frac{4\pi}{\lambda}\sin\theta \qquad \textbf{Equation 2.38}$$

where $\lambda$ and $\theta$ are the neutron wavelength and the incident angle respectively.

The neutron refractive index can also be expressed in terms of the scattering length density (SLD), $\rho_N$, as:

$$n = 1 - \frac{\lambda^2 \rho_N}{2\pi} - i\lambda A \qquad \textbf{Equation 2.39}$$

The imaginary term, $i\lambda A$, in equation 2.39 takes into account incoherence and absorption effects, and is only significant for strong neutron absorbers (e.g. cadmium or boron). For polymers this term is small and can be neglected.

The neutron refractive index for most materials is less than unity, and at small incident angles total external reflection is observed ($R(Q) = 1$). From Snell's law, the critical angle below which total external reflection occurs can be expressed as $\cos\theta_C = n$. For very small values of $\theta$, the value of $\cos\theta$ approximates to $1 - \frac{\theta_C^2}{2}$, and the critical angle can thus be expressed as:

$$\theta_C = \lambda\left(\frac{\rho_N}{\pi}\right)^{1/2} \qquad \textbf{Equation 2.40}$$

The problem of data interpretation in neutron reflectivity experiments remains a constant one, since the conversion of the $R(Q)$ profile into a depth composition profile ($\phi(z)$) is in most cases a nontrivial exercise. Phase information from the neutron wave is lost (through a square term) on reflection from surfaces or interfaces meaning that Fourier transform inversion from $R(Q)$ to $\phi(z)$ is generally not possible (except in one case, the Kinematic Approximation, which is discussed later). Data

analysis is thus usually carried out via a process of proposing layer models for the depth composition profile from which the exact reflectivity profiles are calculated. The precise form of the model profiles can be altered by varying a given set of parameters, and the calculated reflectivity profiles can be compared with the experimental ones in an iterative fashion with the differences between the two being minimised through the use of a least squares algorithm. However, due to the loss of phase information, any given reflectivity is not unique to a single composition profile. It is therefore expedient to try and gain some prior knowledge of the experimental system using complementary analytical techniques in order to partially overcome this inherent ambiguity.

Fresnels Law gives the reflectivity from a single interface:

$$R(Q) = \frac{16\pi^2}{Q^4}\Delta\rho_N^2 \qquad \textbf{Equation 2.41}$$

For a single thin film, the reflectivity can be expressed as:

$$R(Q) = \left|\frac{r_{01} + r_{12}\exp(-2i\beta)}{1 + r_{01}r_{12}\exp(-2i\beta)}\right|^2 \qquad \textbf{Equation 2.42}$$

The term, $r_{ij}$, in equation 2.42 is the Fresnel coefficient at the $ij$ interface, and can be expressed as:

$$r_{ij} = \frac{p_i - p_j}{p_i + p_j} \qquad \textbf{Equation 2.43}$$

where $p_i = n_i \sin\theta_i = (n_i^2 - n_{i-1}^2 \cos^2\theta_{i-1})^{1/2}$, and $n_i$ and $d_i$ are the neutron refractive index and thickness of the $i^{th}$ layer respectively.

The term $\beta_i$ describes the change in phase of the neutron wave on traversing through

the film, and is expressed as:

$$\beta_i = \frac{2\pi}{\lambda} n_i d_i \sin\theta_i \qquad \textbf{Equation 2.44}$$

In order to allow for interfacial roughness, the reflected intensity is modified by a Debye-Waller-like factor (equation 2.45) where $R$ and $R_0$ are the reflectivities with and without roughness respectively, and $\sigma$ is the root mean square Gaussian roughness.

$$R = R_0 \exp(-q_0 q_1 < \sigma^2 >) \qquad \textbf{Equation 2.45}$$

where $q_i = \frac{4\pi}{\lambda} \sin\theta_i$.

Allowing for this roughness, the Fresnel coefficient becomes:

$$r_{ij} = \frac{p_i - p_j}{p_i + p_j} \exp -0.5(q_i q_j < \sigma^2 > \qquad \textbf{Equation 2.46}$$

This method of calculation can be extended to more than one discrete layer, but rapidly becomes mathematically cumbersome. To calculate the reflectivity for multiple layers (either discrete multilayers or a concentration gradient divided into a series of discrete layers), the matrix method of Abeles can be used. The division of the SLD profile into a series of discrete layers is illustrated schematically in figure 2.5.
The characteristic matrix per layer is defined as:

$$M_j = \begin{bmatrix} \exp(i\beta_{j-1}) & r_j \exp(i\beta_{j-1}) \\ r_j \exp(-i\beta_{j-1}) & \exp(-i\beta_{j-1}) \end{bmatrix} \qquad \textbf{Equation 2.47}$$

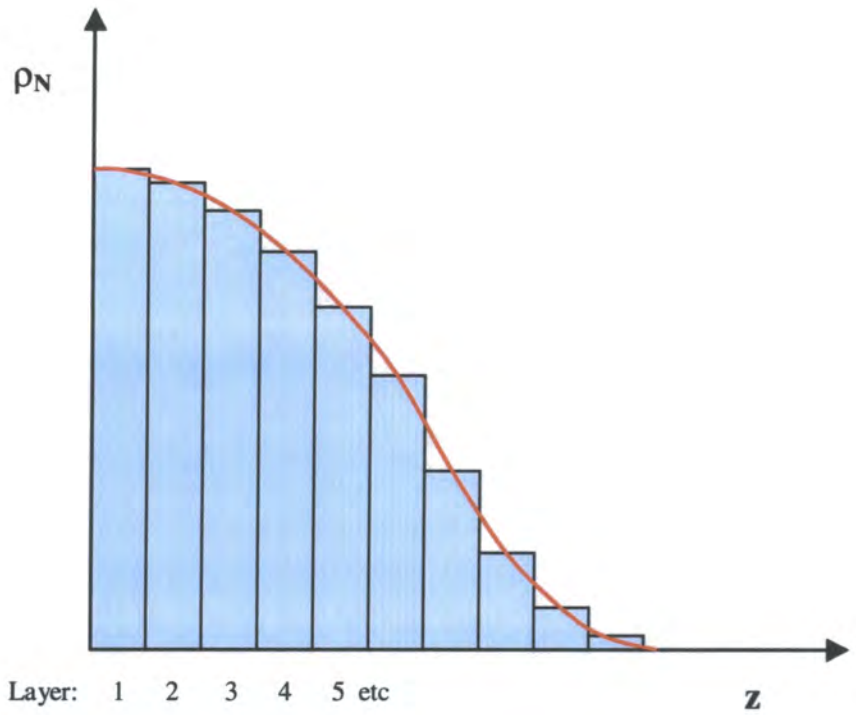


**Figure 2.5** Schematic illustration of the division of a scattering length density profile into a series of discrete layers of uniform thickness.

For $n$ layers, the matrix elements $M_{11}$ and $M_{21}$ of the resultant matrix, $M_R$, give the reflectivity:

$$R = \frac{M_{21}M_{21}^*}{M_{11}M_{11}^*} \qquad \textbf{Equation 2.48}$$

This method provides a useful way of extracting composition profiles from the reflectivity data using least-squares model fitting procedures.

Direct Fourier transform inversion of the $R(Q)$ data into SLD ($\rho(z)$) and hence volume fraction ($\phi(z)$) profiles is impossible except for one specific case. An approximate analytic expression relating the reflectivity profile to the Fourier

transform of the derivative of the SLD profile $\left(\frac{d\rho}{dz}\right)$ is:

$$R(Q) = \frac{(4\pi)^2}{Q^4}\left|\int \frac{d\rho}{dz}\exp(iQz)dz\right|^2 \qquad \textbf{Equation 2.49}$$

This is known as the "Kinematic Approximation", and is strictly only valid for thin layers and at large $Q$ values. It can be used in the interpretation of reflectivity data obtained for monolayers at the air-liquid interface.

Technical details about the CRISP and SURF reflectometers at the Rutherford Appleton Laboratory are available from the ISIS homepage.[29,30]

## 2.4 Small Angle Neutron Scattering (SANS)

Small angle neutron scattering [31-33] is a simple diffraction technique that provides information about the size, shape and association behaviour of molecules. The SANS experiment is illustrated schematically in figure 2.5.

The principles of scattering length density and contrast (i.e. the use of deuterium labelling to manipulate the SLD characteristics of the experimental system) in the SANS experiment are exactly the same as for neutron reflectometry. Essentially, the SANS experiment involves measuring the differential scattering cross-section, $\frac{d\Omega}{d\Sigma}(Q)$, as a function of the momentum transfer, $Q$. The momentum transfer can be defined as:

$$Q = \left|\overline{k_s} - \overline{k_i}\right| = \frac{4\pi n}{\lambda}\sin(\theta) \approx \frac{4\pi}{\lambda}\frac{r_{\text{det}}}{L_{sd}} \quad \text{(for small } \theta\text{)} \qquad \textbf{Equation 2.50}$$

In equation 2.30, $\overline{k_s}$ and $\overline{k_i}$ $\left(=\frac{2\pi}{\lambda}\right)$ are the wavevectors of the scattered and incident neutrons respectively, $\lambda$ is the neutron wavelength, $n$ is the neutron

refractive index (taken as unity), $\theta$ is the scattering angle, $L_{sd}$ is the sample-detector distance and $r_{det}$ is the radial distance at the detector.

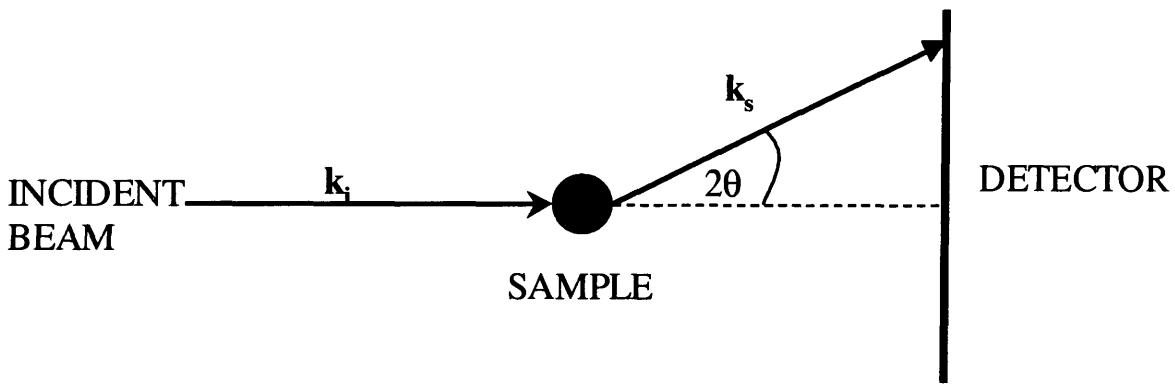


**Figure 2.5** Schematic illustration of the SANS experiment.

As with neutron reflectometry, $Q$ quantifies length scales in reciprocal space, and is the independent variable in SANS experiments. The diffraction pattern produced by the neutrons is recorded on a large 2-dimensional area detector.

The differential scattering cross-section, $\frac{d\Sigma}{d\Omega}(Q)$, is the dependent variable in SANS experiments, and is often incorrectly referred to as the scattering intensity, $I(Q)$. The detector actually measures the scattered neutron flux (i.e. the number of neutrons of a given wavelength scattered through a specific angle arriving on a small area of the detector per unit time). The neutron flux is expressed as:

$$I(Q) = I_0(\lambda)\Delta\Omega\eta(\lambda)T(\lambda)V_s\frac{\partial\Sigma}{\partial\Omega}(Q) \qquad \textbf{Equation 2.51}$$

where $I_0$ is the incident flux, $\Delta\Omega$ is the solid angle element (defined by the detector pixel size), $\eta$ is the detector efficiency, $T$ is the neutron transmission of the sample and $V_s$ is the volume of the sample illuminated by the neutron beam.

In order to place the differential scattering cross-section data on an absolute scale, a stable isotropic "standard" sample (of known scattering cross-section) has to be measured. On the LOQ diffractometer at the Rutherford Appleton Laboratory, a standard consisting of a blend of 49% perdeuterated polystyrene in a hydrogenous polystyrene matrix is used (in conjunction with an appropriate copolymer background sample). The acquisition of scattering and transmission data for these standards enables a calibration constant to be determined. The experimental data can then be placed on an absolute scale by dividing out the $\Delta\Omega\eta(\lambda)$ terms in equation 2.31.

The differential scattering cross-section contains all of the information regarding the size, shape and interactions between the scattering centres in the sample, and can be expressed in a general form as:

$$\frac{d\Sigma}{d\Omega}(Q) = NV^2(\Delta\rho)^2 P(Q)S(Q) + B \qquad \textbf{Equation 2.52}$$

where $N$ is the number concentration of scattering centres, $V$ is the volume of one scattering centre, $\Delta\rho$ is the contrast (representing SLD changes within the system) and $B$ is the background signal. The terms $P(Q)$ and $S(Q)$ are the form factor and structure factor respectively. $P(Q)$ describes the effect of interference between neutrons scattered from different regions of the same particle while $S(Q)$ describes the effect of interference between neutrons scattered from different particles. Various analytical expressions exist for $P(Q)$ and $S(Q)$ (depending on the exact nature of the scattering centres), and these terms are discussed in more detail in chapter 6.

The SANS experiments were carried out using the LOQ diffractometer at the Rutherford Appleton Laboratory, and details for this instrument can be found on the LOQ homepage [34] and instrument manual [35].

$$\rho_e = \frac{R_p}{R_s} = \tan(\psi \exp i\Delta)$$ **Equation 2.55**

When measuring the thickness of films, a "slab" model is often used to analyse the ellipsometry data, and this model assumes that the upper medium/film and film/substrate interfaces are parallel. The film on the substrate is assumed to have thickness, $d$, and refractive index, $n$. The Fresnel coefficients for this optical system are then modified with an exponential term containing the parameter, $\beta$.

$$\beta = 2\pi n \frac{d}{\lambda} \cos\phi_0$$ **Equation 2.56**

where $\phi_0$ is the incident angle.

The technique is capable of measuring film thicknesses with sub-nanometre accuracy.

## 2.6 Glossary of Symbols

### 2.6.1 General

| | |
|---|---|
| $a$ | Statistical segment length (monomer size) |
| $k_B$ | Boltzmann constant |
| $N_A$ | Avogadro constant |
| $T$ | Absolute temperature |

### 2.6.2 Polymer Brushes

| | |
|---|---|
| $d$ | Distance between grafting sites |
| $F_{chain}$ | Total free energy per chain |
| $F_{EV}$ | Excluded volume interaction free energy |
| $F_{stretch}$ | Free energy cost of stretching a brush chain |

| | |
|---|---|
| $h$ | Brush height |
| $N$ | Degree of polymerisation |
| $N_b$ | Number of subunits in a blob |
| $r(t)$ | Monomer position function |
| $R_g$ | Radius of gyration |
| $t$ | Monomer index |
| $T_\theta$ | Theta temperature |
| $U(r)$ | Effective mean-field potential |
| $U(z)$ | Self-consistent potential |
| $v$ | Excluded volume parameter |
| $z$ | Distance normal to grafting surface |
| $Z_{SC}$ | Single chain partition function |
| $\chi$ | Interaction parameter |
| $\phi_p$ | Polymer volume fraction |
| $\phi(z)$ | Polymer volume fraction as a function of distance normal to the grafting surface |
| $\sigma$ | Normalised grafting density |

### 2.6.3 Polymer Brushes Under Shear

| | |
|---|---|
| $d$ | Distance between grafting sites |
| $f$ | Fraction of dragged chains |
| $f_c$ | Stretching force per chain |
| $F_{//}$ | Effective boundary shear force |
| $\dot{\gamma}$ | Shear rate |
| $\eta$ | Solvent viscosity |
| $\tau$ | Zimm relaxation time |

### 2.6.4 Block Copolymer Micelles

| | |
|---|---|
| $f_a$ | Number of arms in a star polymer |
| $N_A$ | Coronal chain degree of polymerisation |
| $N_B$ | Core chain degree of polymerisation |
| $p$ | Aggregation number |
| $R$ | Total micelle radius |
| $R_A$ | Coronal (shell) thickness |
| $R_B$ | Core radius |
| $\nu$ | Flory scaling exponent |
| $\chi$ | Interaction parameter |
| $\gamma$ | Interfacial tension |

### 2.6.5 Neutron Reflectometry

| | |
|---|---|
| $b$ | Nuclear scattering length |
| $d$ | Layer thickness |
| $I_0$ | Incident intensity |
| $I_R$ | Reflected intensity |
| $\bar{k}$ | Neutron wavevector |
| $m$ | Monomer mass |
| $M$ | Matrix element |
| $n$ | Neutron refractive index |
| $Q$ | Momentum transfer |
| $r$ | Fresnel coefficient |
| $R(Q)$ | Reflectivity |
| $z$ | Distance normal to the surface/interface |
| $\beta$ | Phase change |
| $\phi_P$ | Polymer volume fraction |
| $\phi_S$ | Solvent volume fraction |

| | |
|---|---|
| $\phi(z)$ | Polymer volume fraction as a function of distance normal to the surface/interface |
| $\lambda$ | Neutron wavelength |
| $\theta$ | Incident angle |
| $\theta_c$ | Critical angle for total external reflection |
| $\rho$ | Physical density |
| $\rho_B$ | Scattering length density of a polymer brush volume element |
| $\rho_N$ | Neutron scattering length density |
| $\rho_P$ | Polymer scattering length density |
| $\rho_S$ | Solvent scattering length density |
| $\sigma$ | Root mean square Gaussian roughness |

### 2.6.6 Small Angle Neutron Scattering

| | |
|---|---|
| $B$ | Background signal |
| $\frac{d\Sigma}{d\Omega}(Q)$ | Differential scattering cross-section |
| $I(Q)$ | Neutron flux |
| $I_0(\lambda)$ | Incident flux |
| $\overline{k_i}$ | Incident neutron wavevector |
| $\overline{k_s}$ | Scattered neutron wavevector |
| $L_{sd}$ | Sample-to-detector distance |
| $n$ | Neutron refractive index |
| $N$ | Number concentration of scattering centres |
| $P(Q)$ | Form factor |
| $Q$ | Momentum transfer |
| $r_{\text{det}}$ | Radial distance at detector |
| $S(Q)$ | Inter-particle structure factor |
| $T(\lambda)$ | Neutron transmission of sample |
| $V$ | Volume of scattering centre |

| | |
|---|---|
| $V_s$ | Illuminated sample volume |
| $\eta(\lambda)$ | Detector efficiency |
| $\lambda$ | Neutron wavelength |
| $\theta$ | Scattering angle |
| $\Delta\Omega$ | Solid angle element defined by detector pixel size |

### 2.6.7 Ellipsometry

| | |
|---|---|
| $\frac{A_p^i}{A_s^i}$ | Incident amplitude ratio |
| $\frac{A_p^r}{A_s^r}$ | Reflected amplitude ratio |
| $d$ | Layer thickness |
| $d_p^i - d_s^i$ | Incident phase difference |
| $d_p^r - d_s^r$ | Reflected phase difference |
| $n$ | Refractive index |
| $p, s$ | Ellipsometric planes |
| $R_p, R_s$ | Fresnel coefficients |
| $\phi_0$ | Incident angle |
| $\lambda$ | Wavelength |
| $\rho$ | Ellipticity |
| $\psi, \Delta$ | Ellipsometric angles |

## 2.7 References


1 Prigogine, I; Rice, S A (Eds.). '*Advances in Chemical Physics – Volume XCIV.*' John Wiley and Sons, Inc. (1996).

2 Jones, R A L; Richards, R W. '*Polymers at Surfaces and Interfaces.*' Cambridge University Press (1999).

3 Alexander, S. *Le Journal de Physique*, 1977, **38**, 983.

4 de Gennes, P G. *Macromolecules*, 1980, **13**, 1069.

5 Milner, S T; Witten, T A; Cates, M E. *Macromolecules*, 1988, **21**, 2610.

6 Milner, S T; Witten, T A; Cates, M E. *Europhysics Letters*, 1988, **5**, 413.

7 Milner, S T. *Science*, 1991, **251**, 905.

8 Rabin, Y; Alexander, S. *Europhysics Letters*, 1990, **13**, 49.

9 Barrat, J L. *Macromolecules*, 1992, **25**, 832.

10 Kumaran, V. *Macromolecules*, 1993, **26**, 2464.

11 Harden, J L; Cates, M E. *Physical Review E*, 1996, **53**, 3782.

12 Aubouy, M; Harden, J L; Cates, M E. *J. Phys. II France*. 1996, **6**, 969.

13 Saphiannikova, M G; Pryamitsyn, V A; Cosgrove, T. *Macromolecules*, 1998, **31**, 6662.

14 Lai, P Y; Binder, K. *J. Chem. Phys.* 1993, **98**, 2366.

15 Miao, H; Guo, H; Zuckermann, M J. *Macromolecules*, 1996, **29**, 2289.

16 Hamley, I W. "*The Physics of Block Copolymers.*" Oxford University Press (1998).

17 Liebert, L (Ed). '*Solid State Physics.*' Volume **14**. Academic, New York (1978).

18 Daoud, M; Cotton, J P. *Journal de Physique*, 1982, **43**, 531.

19 Halperin, A. *Macromolecules*, 1987, **20**, 2943.

20 Zhulina, E B; Birshtein, T M. *Polymer Science USSR*, 1986, **27**, 570.

21 Noolandi, J; Hong, K M. *Macromolecules*, 1983, **16**, 1443.

22 Plestil, J; Baldrian, J. *Makromoleculaire Chemie*, 1975, **176**, 1009.

23 Whitmore, M D; Noolandi, J. *Macromolecules*, 1985, **18**, 657.

24 Nagarajan, R; Ganesh, K. *Journal of Chemical Physics*, 1989, **90**, 5843.

25 Bucknall, D G in '*Modern Techniques for Polymer Characterisation.*' Pethrick, R A; Dawkins, J V (Eds). John Wiley and Sons Ltd (1999).

26 Richards, R W (Ed). '*Scattering Methods in Polymer Science'*. Ellis Horwood (1995).

27 Russell, T P. *Materials Science Reports*, 1990, **5**, 171.

28 Penfold, J. '*The Adaptation of Methods in Multilayer Optics for the Calculation of Specular Neutron Reflection'*. Rutherford Appleton Laboratory Report, RAL-88-088 (1988).

29 http://www.isis.rl.ac.uk/largescale/crisp/CRISP.htm

30 http://www.isis.rl.ac.uk/largescale/surf/surf.htm

31 King, S M in '*Modern Techniques for Polymer Characterisation.*' Pethrick, R A; Dawkins, J V (Eds). John Wiley and Sons Ltd (1999).

32 Higgins, J S; Benoit, H C. '*Polymers and Neutron Scattering.*' Clarendon Press, Oxford (1994).

33 Goodwin, J W (Ed). '*Colloidal Dispersions.*' Royal Society of Chemistry (1982).

34 http://www.isis.rl.ac.uk/largescale/loq/loq.htm

35 King, S M; Heenan, R K. *The LoQ Handbook*, 1996, Rutherford Appleton Laboratory Report, RAL-TR-96-036.

36 Richards, R W; Peace, S K (Eds). '*Polymer Surfaces and Interfaces III.*' John Wiley and Sons (1999).

37 Azzam, R M A; Bashara, N M. '*Ellipsometry and Polarised Light.*' North Holland, Amsterdam (1977).

# CHAPTER 3

# SOLID-LIQUID INTERFACIAL STUDIES – EXPERIMENTAL ASPECTS

# CHAPTER 3

# SOLID-LIQUID INTERFACIAL STUDIES - EXPERIMENTAL ASPECTS

In order to study properly the structure and dynamics of polymer brush layers at the solid-liquid interface, there were several areas of preparatory work that had to be undertaken prior to the neutron reflectivity measurements. In this chapter the three key areas of preparatory work will be discussed, namely: design and construction of a flow reflectometry cell, polymer synthesis and brush layer preparation/characterisation.

## 3.1 Design and Construction of a Flow Reflectometry Cell

An apparatus had to be constructed that would allow solid-liquid interfacial studies of polymer brush layers to be carried out under both quiescent and shear flow conditions using neutron reflectometry. Important design considerations included easy access of the neutron beam to the interface, the development of Poiseuille geometry laminar flow in the region to be studied, access to a wide range of shear rates, precise temperature control and measurement (since the quiescent brush dimensions are temperature dependent in theta solvents) and ease of disassembly and cleaning.

### 3.1.1 Flow Characteristics

Poiseuille flow is the laminar flow of a fluid in a pipe under a constant pressure gradient [1-2]. A more convenient geometry for experimental investigations is that of flow of a fluid between 2 parallel plates, and the flow characteristics for this situation are geometrically similar to those of flow through a pipe.

If we define x as the position of a flow element with respect to the 2 plates (x=0 represents the position midway between the plates) and v as the flow velocity of that fluid element, then the velocity profile between the plates is parabolic with a

maximum at x=0 (the flow velocity at the plate-liquid interface is zero). The shear rate (or velocity gradient) profile is linear, and decreases from a maximum at x=0 to zero at the plates themselves.

The area average shear rate, $\dot{\gamma}_{AV}$, is equal to half the maximum shear rate between the plates and can be defined in terms of the volumetric flow rate (Q), the width and separation of the plates (w and h respectively) as:

$$\dot{\gamma}_{AV} = \frac{2Q(m+2)}{wh^2(m+1)} \qquad \textbf{Equation 3.1}$$

(m = a dimensionless shear rate exponent = 1 for Newtonian fluids).

The entry length, $L_e$, is defined as the distance after which laminar flow is fully developed and is given by:

$$L_e = \frac{c\rho Qh}{2w\mu} \qquad \textbf{Equation 3.2}$$

where ρ and μ are the fluid density and viscosity respectively and c is a dimensionless experimental constant.

### 3.1.2 Cell Construction

The design used was loosely based on that of Baker et al [3]. Single crystal <111> silicon blocks (low boron content) were purchased from Kristalhandel Kelpin for use as substrates for the brush layers since they allowed high transmission of neutrons and could be easily surface treated to facilitate adsorption of the polymer molecules. The blocks had dimensions 140×50×20mm and were polished to 5-10Å flatness by Gooch and Hausego Ltd on one or both of the large faces. The key features of the cell are illustrated in figure 3.1(a-d). The base block was made from 316 stainless steel due to the excellent chemical resistance and shape retension properties of this material

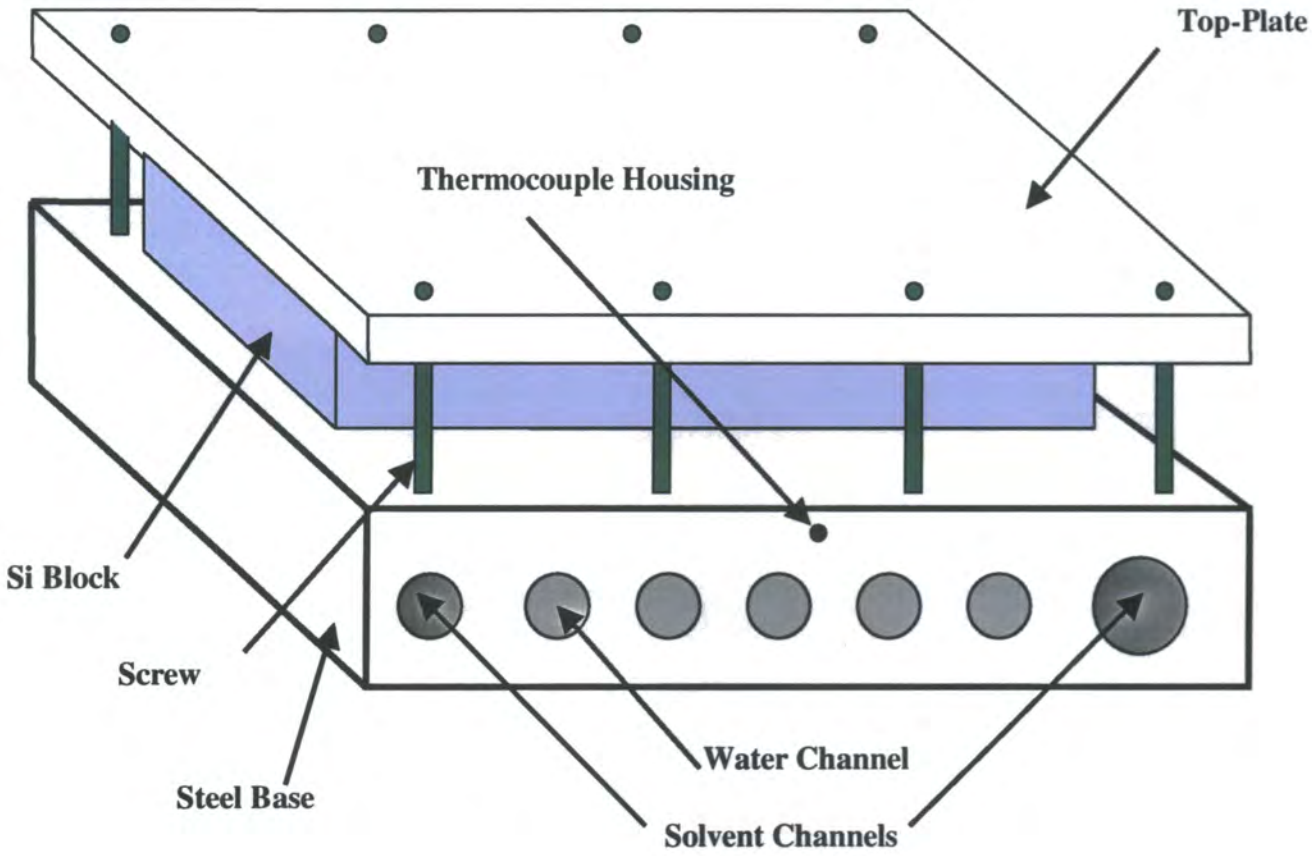


**Figure 3.1a** Schematic illustration of the Durham flow reflectometry cell.

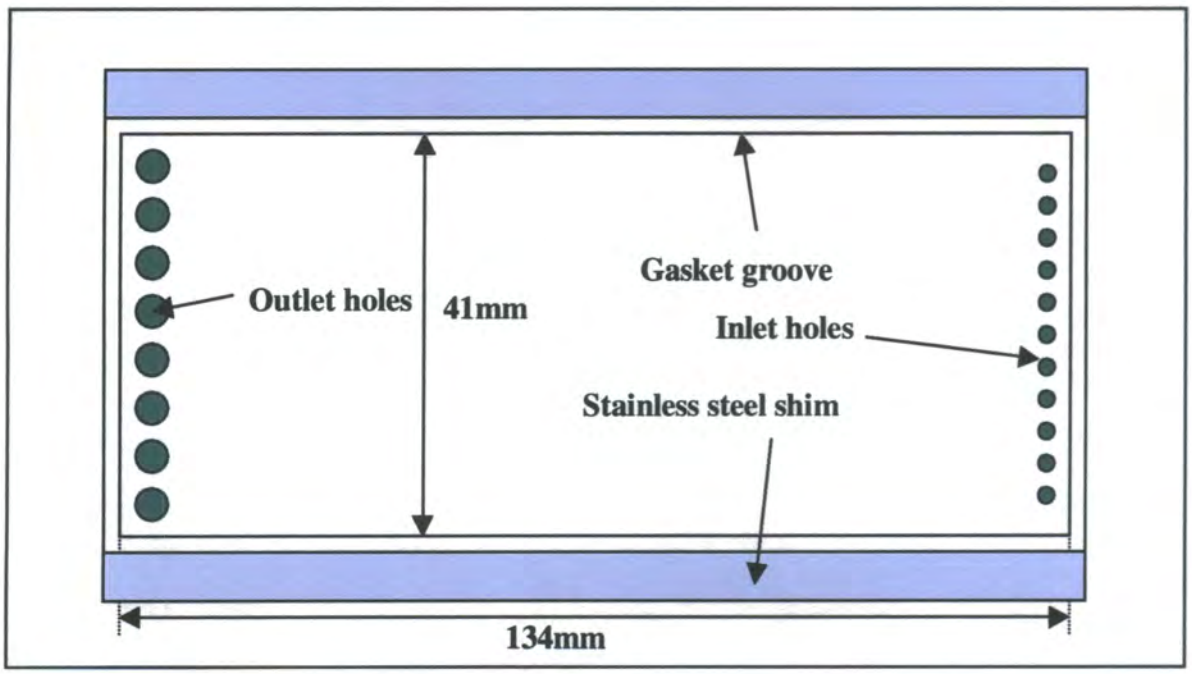


**Figure 3.1b** Schematic illustration of the upper surface of the steel base block showing the "test region".

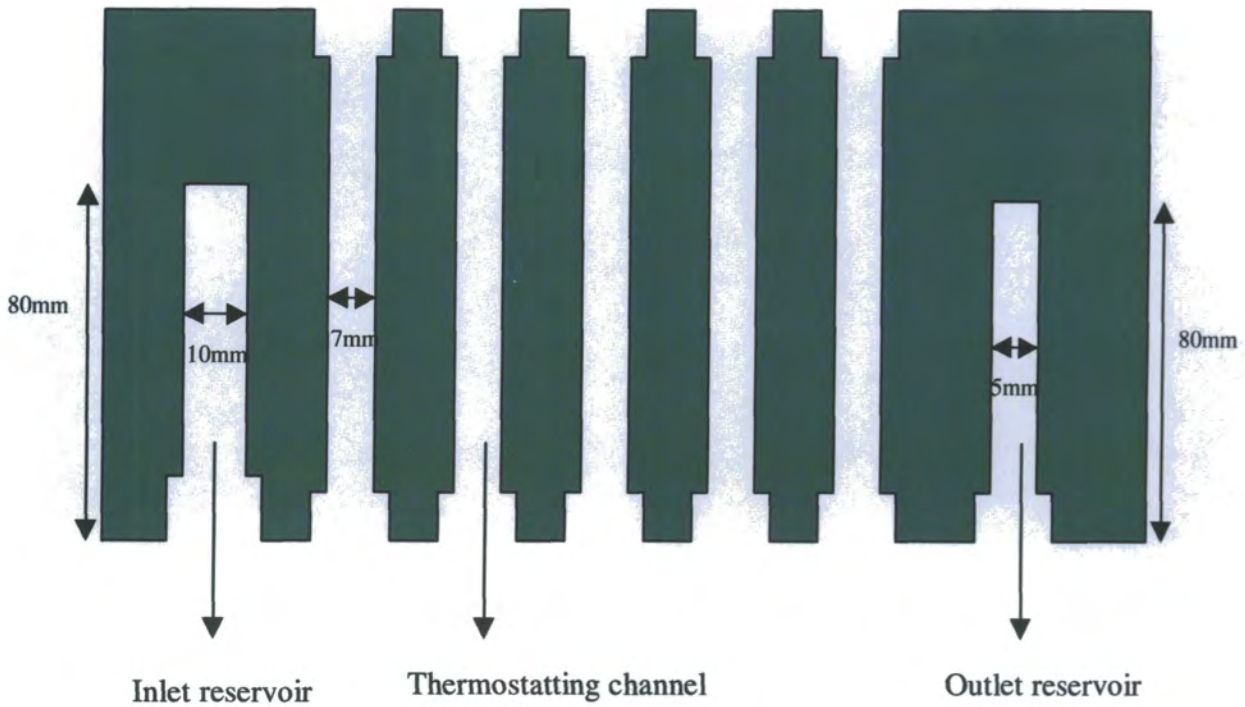


**Figure 3.1c** Cross sectional view through the steel base block illustrating the inlet and outlet reservoirs along with the thermostatting channels.

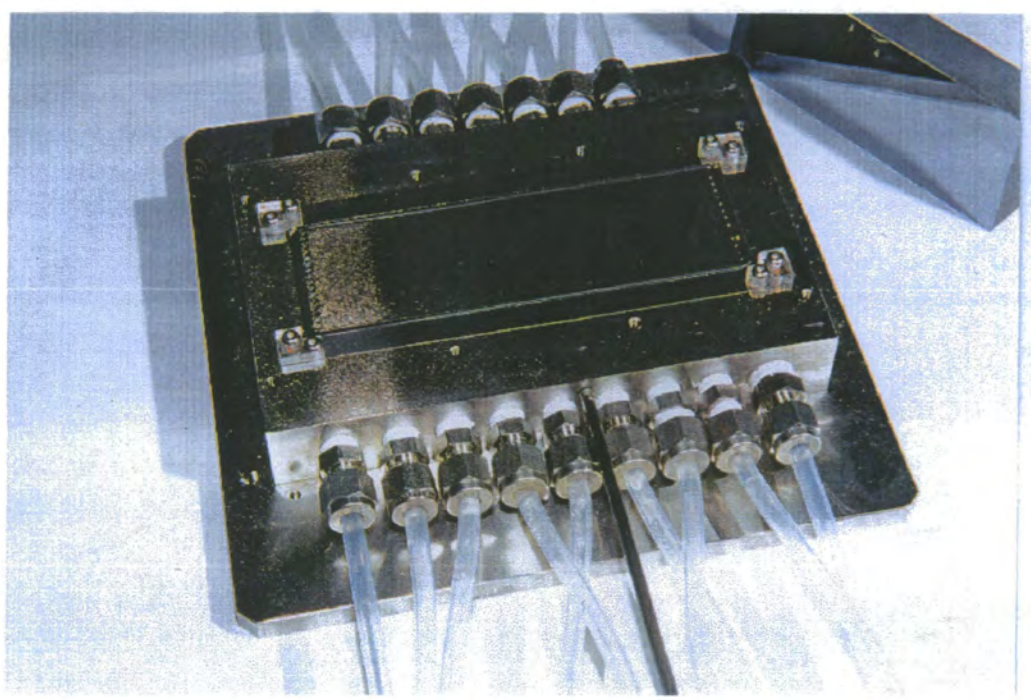

**Figure 3.1d** Photograph of the flow reflectometry cell with the silicon block and top-plate removed (one of the silicon blocks is shown in the background).

(teflon is a common choice of material for these applications. However, whilst it is easy to machine and has excellent chemical resistance, it is also susceptible to creep which could lead to obvious problems where very precise geometrical definition is required). The base block had dimensions 170×110×25mm, and a groove was milled into one of the large faces enclosing a rectangular area of dimensions 134×41mm in the centre of the face. This rectangular area was to form the lower surface of the "test region" i.e. the channel through which solvent would be pumped (with the silicon substrate forming the upper surface) in order to subject the brush layers to shear. The steel surface was lapped and polished to a flatness of 10-15μm to further aid the development of laminar flow through the test region.

As can be seen from equation 3.1, the shear rate is inversely proportional to the product of the width of the channel and the square of the separation between the upper and lower surfaces. The width of the silicon blocks and thus the width of the test region were selected so as to allow adequate space for the standard 30mm beam width used on the neutron reflectometer. Consequently, in order to be able to reach high shear rates the separation between silicon and steel in the test region had to be as small as possible whilst retaining precise geometrical definition. A separation of 100μm was thus selected, and was defined by attaching 2 stainless steel shims of thickness 100μm to the base block flush with the outer edges of the gasket groove parallel to the long axis of the base block. This configuration meant that when the silicon block was clamped on to the gasket until it came to rest on the shims, a 100μm flow channel would be defined.

Uniform clamping was facilitated by means of a stainless steel top-plate (170×84mm) through which 4 screws (equally separated from each other) passed on both sides parallel to the long axis. These screws inserted into a corresponding series of holes drilled into the base block, and a sheet of teflon was placed underneath the top-plate to protect the silicon block.

A torque driver was used to ensure that all of the screws were uniformly tightened.

Cylindrical inlet and outlet reservoirs (diameter=10mm, length=80mm and diameter=5mm, length=80mm respectively) were drilled into opposite ends of one side of the base block to allow fluid to flow evenly into and out of the test region without creating excessive turbulence or non-uniform flow. The reservoirs were tapped with NPT compression fittings to allow tubing to be connected to pump fluid

in and out. Entry of fluid to the test region was facilitated by drilling 14 evenly spaced 1mm diameter holes across the width of the test region down to the inlet reservoir. A corresponding series of 16 evenly spaced 2mm diameter exit holes were drilled down to the outlet reservoir at the other end. The diameters of the inlet reservoir and inlet holes used were based on velocity head calculations, although the inlet hole diameter chosen was ultimately governed by the fact that it would have been impractical to attempt to drill holes less than 1mm in diameter through stainless steel.

For fluid to emerge from the inlet holes evenly across the test region, the velocity head in the inlet reservoir had to be much smaller than that in the inlet holes. For a steady, incompressible flow, the equation of conservation of mass is:

$$v_1 A_1 = v_2 A_2 \qquad \textbf{Equation 3.3}$$

In equation 3.3, $A_1$ and $A_2$ are the total cross sectional areas of the inlet reservoir and inlet holes respectively while $v_1$ and $v_2$ are the respective fluid velocities through these regions. For the dimensions used in the Durham cell the values of $A_1$ and $A_2$ are 78.54 and 11.00mm$^2$ respectively, and thus the ratio $v_2 : v_1$ is 7.14:1. The velocity head is defined as $\frac{\rho v^2}{2}$, and thus the velocity head in the inlet reservoir is ~2% of that in the inlet holes thereby satisfying the criterion for even emergence of fluid across the test region. To test this, water was pumped into the inlet reservoir at various flow rates with the top-plate and silicon block removed; the heights of the jets emerging from the inlet holes were found to be equal.

Temperature control was facilitated by drilling a further 7 evenly spaced holes (diameter=7mm) through the base block. These thermostatting channels were tapped at both ends with NPT compression fittings and linked together in series with tubing to allow water to be pumped through the base block. Due to the excellent thermal conductivity of steel, the temperature of the experimental system could be precisely regulated by controlling the temperature of the water circulating through the base block, and a Lauda low temperature thermocirculator with an operating temperature range of -35 to 200$^0$C was purchased for this purpose. Temperature measurement was

facilitated by drilling a hole through the base block to house a platinum resistance thermometer, such that the tip of the thermometer resided directly under the centre of the test region.

Entry length values (equation 3.2) calculated for cyclohexane and toluene at $25^0$C based on the dimensions of the Durham cell are shown in table 3.1. A value of Q=1200ml/min was used in the calculations since this was the largest flow rate used in the neutron reflectivity experiments.

| **Solvent** | **μ (mPas)** [4] | **$L_e$ (mm)** |
|---|---|---|
| Cyclohexane | 0.894 | 2.1 |
| Toluene | 0.560 | 3.7 |

**Table 3.1** Entry lengths for cyclohexane and toluene at $25^0$C calculated using the dimensions of the Durham flow reflectometry cell. (c=0.1, Q=1200$cm^3min^{-1}$)

## 3.2 Brush Polymer Synthesis

The aim with the polymer synthesis was to produce a monodisperse perdeuterated polystyrene of molecular weight 400,000-500,000 $gmol^{-1}$. To facilitate end-adsorption of the molecules to the silicon substrate it was decided to attach short chains of poly-4-vinylpyridine (30-40 monomer units) by copolymerisation or other means to one end of each polystyrene chain. The synthesis proved to be more difficult than first anticipated and was attempted by Mr F T Kiff, myself and Dr L R Hutchings before a successful route was developed. What follows is an account of the 4 synthetic strategies (all using anionic polymerisation [5-6] and standard high vacuum techniques) that were adopted in an attempt to produce a satisfactory polymer.

### 3.2.1 Solvent and Monomer Purification

Benzene was washed with concentrated sulphuric acid, water, sodium bicarbonate (aq) and then water again before being distilled. It was then dried over calcium

hydride and degassed by a series of freeze-thaw cycles. Tetrahydrofuran (THF) was refluxed over sodium, vacuum distilled and stored over sodium wire. It was placed on the vacuum line over sodium benzophenone and degassed. Dimethylformamide (DMF) was dried over type 4A molecular sieve and degassed. It was then titrated with diphenylmethylpotassium (DPMK) to remove any impurities that might otherwise interfere with the anionic polymerisation process. 4-vinyl-pyridine was vacuum distilled before being dried over calcium hydride and degassed. Deutero-styrene was dried over calcium hydride and degassed before being further purified via sacrificial polymerisation. This process involves distilling the deutero-styrene monomer off calcium hydride and then titrating it using 10-15μL aliquots of secondary butyllithium solution. As soon as an orange colour persists (due to the generation of living deutero polystyryl lithium) the monomer is flash distilled from the polymerising mixture. 1,1-diphenylethylene (DPE) was dried over type 3A molecular sieve, degassed and then titrated with DPMK until a slight red/orange colour persisted.

### 3.2.2 Size Exclusion Chromatography (SEC)

SEC was used to ascertain molecular weights and polydispersities of the polymers synthesised and was carried out using either chloroform or THF as eluent. The THF solvent system used Polymer Laboratories columns containing Plgel packing (polystyrene divinylbenzene copolymer) with a 10μm particle size and mixed-bed pore sizes. A triple detector system was employed utilising Viscotek right angle laser light scattering (RALLS), differential refractometry and viscometry detectors.
The chloroform solvent SEC apparatus used similar columns but with a 5μm particle size and pore sizes of 100, 1000 and $1\times10^5$Å. A single Polymer Laboratories refractive index detector was used.

### 3.2.3 Synthetic Route 1

This route was based on the work of Gauthier and Eisenberg [7] and involved the polymerisation of deutero-styrene in benzene using n-butyl lithium as the initiator. The living polystyrene chain ends were capped with one unit of 1,1-DPE (an excess of 1,1-DPE was added since it does not homopolymerise) to modify the reactivity of the

chain ends in order to prevent side reactions occuring when the 4-vinylpyridine monomer was added. The 4-vinylpyridine was then injected into the capped living polystyryl lithium solution in order to copolymerise the poly-4-vinylpyridine tails onto the polystyrene molecules. Upon completion, the reaction was terminated using nitrogen sparged methanol.

Chloroform GPC data for the polymer synthesised in this way (code=TK327) are given in table 3.2. Whilst the polystyrene block had the desired molecular weight and was fairly monodisperse, the GPC trace of the copolymer showed that it had a very high polydispersity. It is interesting to note that the molecular weight of the copolymer is less than that of the polystyrene block, a feature possibly arising from the fact that poly-4-vinylpyridine experiences a weak interaction with the column packing thus giving a false (long) high elution time. The very high polydispersity of the copolymer indicated that coupling side-reactions had occurred upon addition of the 4-vinylpyridine monomer. The most probable nature of the coupling reaction is illustrated in figure 3.2, and involves the donation of the pyridine ring nitrogen lone

| **Sample** | **$M_n$ ($gmol^{-1}$)** | **$M_w/M_n$** |
|---|---|---|
| Polystyrene block | 430,000 | 1.15 |
| Copolymer | 347,000 | 2.4 |

**Table 3.2** Molecular weight and polydispersity data for the polymer TK327

pairs to the Lewis acidic lithium cations, thus exposing the sites ortho- to the nitrogen atoms to attack by the living polystyrene chain ends [8]. The coupling reactions would occur alongside the normal copolymerisation reaction thus leading to a mixture of different species in the final polymer produced.

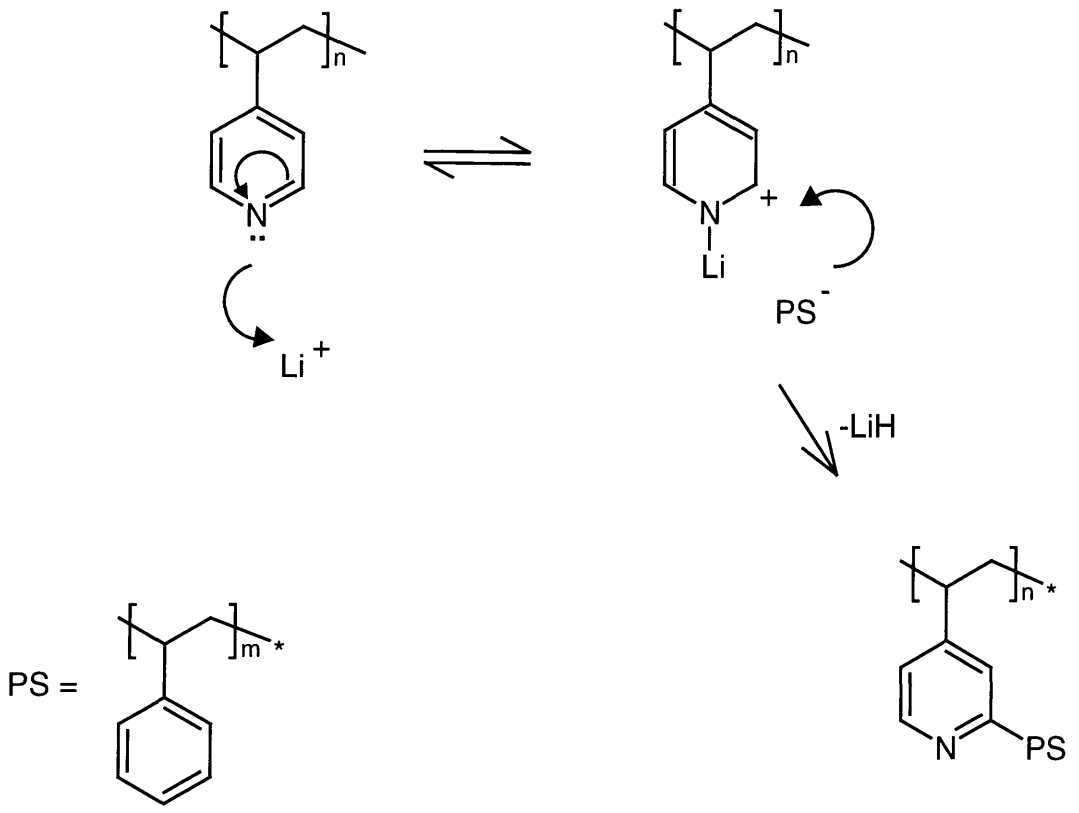


**Figure 3.2** Probable mechanism for the coupling reaction occurring during the diblock copolymerisation of styrene and 4-vinylpyridine

### 3.2.4 Synthetic Route 2

Due to the problems with coupling that occurred when using synthetic route 1, an alternative route was designed by Dr L R Hutchings. Essentially, this route involved separately synthesizing the polystyrene and poly-4-vinylpyridine blocks via anionic polymerisation and then linking the 2 blocks together using dichlorodimethylsilane as illustrated in figure 3.3.

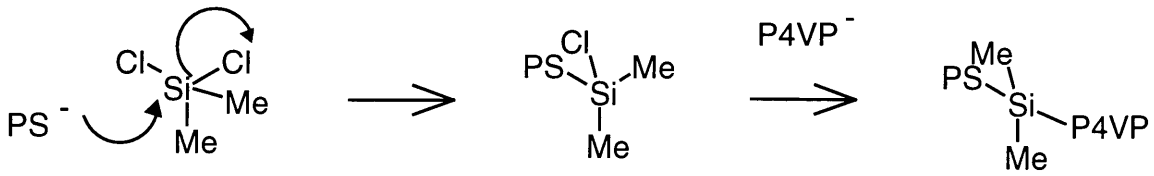


**Figure 3.3** Reaction pathway for synthetic route 2

The deutero-polystyrene was synthesised in benzene using n-butyl lithium as initiator, and the living chain ends were capped with dichlorodimethylsilane (a 25 fold excess of this reagent was added so as to ensure that disubstitution reactions did not occur). The excess silane was then co-distilled out with benzene several times and the dry polymer redissolved in an 85:15 mixture of THF and DMF.

The poly-4-vinylpyridine was synthesised in an 85:15 mixture of THF and DMF using diphenylmethyl potassium (DPMK) as initiator. This polymerisation reaction was carried out at 195K so as to prevent the occurrence of poly-4-vinylpyridine self-coupling reactions [9] (figure 3.4), and whilst maintaining the living poly-4-vinylpyridine at this temperature, the silane capped polystyrene solution was cannulated in to complete the reaction.

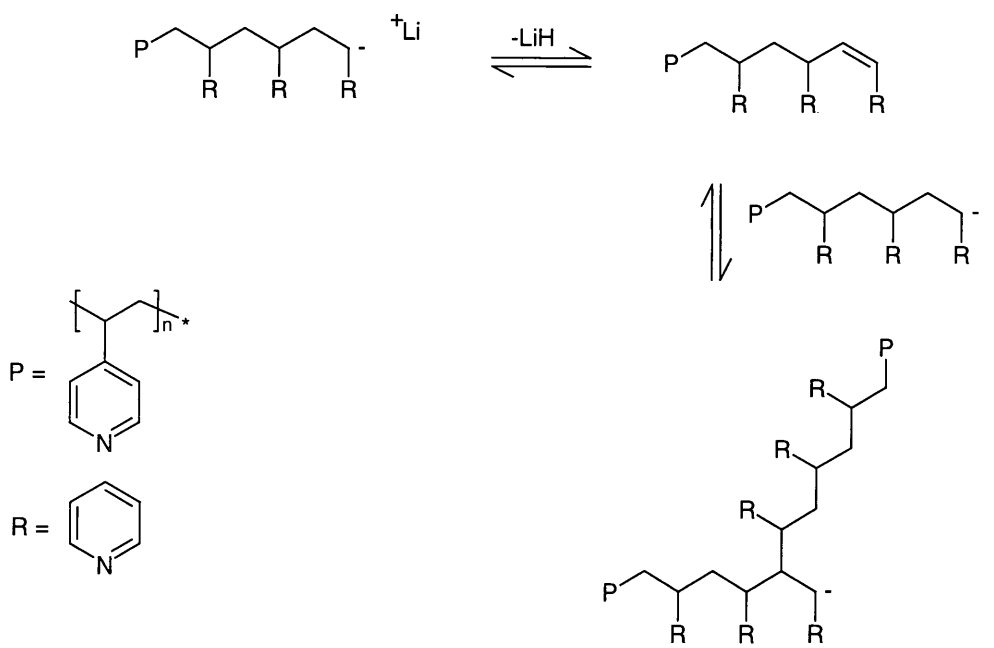


**Figure 3.4** The poly-4-vinylpyridine self coupling reaction

Unfortunately, the low temperature also prevented the final stage of the reaction (i.e. the displacement of the chlorine atom from the silane capped polystyrene by the living poly-4-vinylpyridine thus fusing the 2 blocks together) from occurring and thus this route was unsuccessful.

### 3.2.5 Synthetic Route 3

As mentioned previously, the problems with coupling that occurred when using route 1 appeared to be due to the presence of lithium ions from the n-butyl lithium initiator. It was thought that a possible solution to this problem was to use a potassium based initiator on the grounds that potassium is less Lewis acidic than lithium and would thus be less likely to initiate the coupling reactions.

Consequently, a new synthetic route was developed based on route 1 but using diphenylmethyl potassium as initiator. Since DPMK is not soluble in benzene, the deutero-styrene polymerisation had to be carried out in THF. This situation was not ideal since in THF the propagation step of the polymerisation is very fast, leading to a broadening in the molecular weight distribution of the polystyrene so formed. In order to circumnavigate this problem partially, the reaction was carried out at 195K and then warmed to room temperature upon completion before adding excess 1,1-DPE to cap and deactivate the living chain ends. The required amount of 4-vinylpyridine was then injected as a solution in THF, and upon completion the reaction was killed using nitrogen sparged methanol.

$^1$H NMR data indicated that the stoichiometries of the polymers produced by this route were correct while chloroform SEC data showed that the high polydispersities associated with the coupling reactions of route 1 were no longer evident (the polydispersities of the polymers produced by this route were low). However, whilst the problem of coupling seemed to have been overcome, the molecular weights of the polymers produced using this route consistently disagreed with the desired molecular weight, a problem attributed to inaccurate determination of the initiator concentration. However, further development of this synthetic route became unnecessary when an alternative and successful route (synthetic route 4) was found.

### 3.2.6 Synthetic Route 4

It was discovered that the key to the problems with synthetic route 1 lay in the fact that not enough time was being allowed for the 1,1-DPE capping reaction to take place before the addition of the 4-vinylpyridine monomer. As mentioned previously, the purpose of this capping reaction was to deactivate (partially) the living polystyrene chain ends in order to reduce the occurrence of coupling reactions. However, only 30 minutes had been allowed for the capping reaction to take place in synthetic route 1, and whilst visually this appeared to be long enough (as judged by an orange to red colour change upon capping) in reality not all of the chain ends would have been capped when the 4-vinylpyridine was introduced.

Deutero-styrene in benzene was initiated using n-butyl lithium and then excess 1,1-DPE was added and left to react overnight. The benzene was then pumped out and replaced with THF before injecting the 4-vinylpyridine as a solution in THF. After completion, the reaction was terminated using nitrogen sparged methanol.

The target polystyrene molecular weight was 450,000gmol$^{-1}$, and the quantity of 4-vinylpyridine used was calculated so as to add 30-40 units per polystyrene chain (~1% w/w) . SEC data acquired in THF showed that the copolymer produced by this route (code=LRH3.52) was monodisperse and had the required molecular weight. The molecular weight and polydispersity details for this polymer are given in table 2.

| **Sample** | **$M_n$ (gmol$^{-1}$)** | **$M_w/M_n$** |
|---|---|---|
| Polystyrene block | 423,000 | 1.05 |
| Copolymer | 418,000 | 1.05 |

**Table 3.3** Molecular weight and polydispersity data for the polymer LRH3.52

The polymers TK327 and LRH3.52 were both used in the neutron reflectivity studies of polymer brush layers discussed in chapters 4 and 5.

## 3.3 Brush Layer Preparation

It was important to be able to produce end-tethered polymer layers with grafting densities high enough to lie well within the brush regime (i.e. the distance between grafting sites is significantly less than the unperturbed radius of gyration of the polymer chains). Furthermore, it was desirable to have reproducibility in terms of the dimensions of the layers formed for individual samples and vital that the polymer molecules were strongly enough attached to the silicon surface so as not to undergo significant desorption under solvent shear flow.

### 3.3.1 Silicon Surface Preparation

As discussed in the previous section, the polymers used were deutero-polystyrenes with short poly-4-vinylpyridine chains attached to one end. The key to the grafting process was to ensure hydrogen bonding between the nitrogen atoms of the pyridine rings and the hydrogen atoms of the silanol groups present on the surfaces of the silicon blocks. As such, the silicon blocks were subjected to a surface treatment process [10-11] prior to adsorption of the polymer to produce hydrophilic oxide layers with high densities of surface silanol groups.

The blocks were initially treated by immersion in "piranha" solution (a 7:1 mixture of concentrated sulphuric acid and 27.5% hydrogen peroxide (aq)) at 70-80$^0$C for 10-15 minutes in order to remove any traces of organic material that would otherwise interfere with the subsequent etching process. The etching process was carried out by immersing the blocks in a 9:1 mixture of UHQ water and 40% hydrofluoric acid (aq) for 5 minutes so as to strip off completely the native oxide layer. (The success of this procedure could be crudely assessed by noting the hydrophobicity of the block surface when washing off any residual HF following etching). The blocks were then immediately re-immersed in piranha solution for a further 10-15 minutes so as to regrow a hydrophilic oxide layer with a high density of surface silanol groups (water contact angles lay within the range 10-16° for newly treated blocks as compared to 25-30° for untreated blocks as received from the supplier).

The blocks were characterised by optical ellipsometry prior to adsorption of the polymer, and it was found that the above procedure produced oxide layers with a thickness of 18±4Å.

### 3.3.2 Polymer adsorption

The ideal method for producing polymer films on solid substrates is spin coating from a solution of the polymer in a suitable solvent [12]. Unfortunately, due to the size of the silicon substrates required for use in the reflectometry cell this method was not feasible. The actual adsorption process used involved preparing a 0.75 w/w solution of the polymer in analar cyclohexane (a theta solvent for polystyrene) and then immersing the treated surfaces of the silicon blocks in this solution at room temperature for a period of 3-4 days. The theta temperature for deutero-polystyrene in cyclohexane is 303K, and thus carrying out the adsorption process at just below the theta temperature means that: a) there is a thermodynamic driving force for adsorption to occur (i.e. the formation of hydrogen bonds between the poly-4-vinylpyridine chains and the silicon surface) and b) the coils are slightly collapsed, thus allowing more coils access to the substrate surface.

The blocks were then removed from the solution and placed in an oven to anneal at 413K under vacuum for a period of 24-36 hours. The purpose of annealing was to increase the molecular motion within the sample so as to allow as many poly-4-vinylpyridine end groups as possible to attach to the silicon surface. Subsequent to the adsorption and annealing processes a thick, uneven polymer layer was visible to the naked eye. Consequently, the coated blocks were washed in toluene (an extremely good solvent for polystyrene) to remove excess ungrafted polymer. Following this toluene wash the polymer layer was invisible to the naked eye, and the dry layer thicknesses were measured using ellipsometry. The layers were repeatedly washed and the thicknesses re-measured until no further change in layer thickness was observed.

Ellipsometry measurements indicated that the above process consistently produced even polymer layers with dry layer thicknesses in the range 100±10Å. It should be noted that the use of longer adsorption times did not increase the final layer thicknesses achieved, and thus 100Å would appear to be the maximum attainable

layer thickness for this system. The precise layer thicknesses of the samples used in the neutron reflectivity experiments are given in chapter 4.

Other groups have reported work involving the reactive grafting of polymers onto silicon substrates [13-14] (e.g. by using trialkoxysilane end groups which reactively bond with the hydrolysed silicon surface). However, the diblock copolymer adsorption method used in this work produces comparable grafting densities [12] without the need for special storage and handling procedures for the polymers.

## 3.4 Glossary of Symbols

| | |
|---|---|
| $A_1$ | Cross-sectional area of inlet reservoir |
| $A_2$ | Total cross sectional area of inlet holes |
| $c$ | Dimensionless experimental constant in the range 0.03 to 0.1 |
| $h$ | Separation between plates (for flow between 2 parallel plates) |
| $L_e$ | Entry length |
| $m$ | Dimensionless shear rate exponent |
| $Q$ | Volumetric flow rate |
| $v$ | Fluid velocity |
| $v_1$ | Fluid velocity through inlet reservoir |
| $v_2$ | Fluid velocity through inlet holes |
| $w$ | Width of plates (for flow between 2 parallel plates) |
| $\dot{\gamma}_{AV}$ | Area average shear rate |
| $\mu$ | Fluid viscosity |
| $\rho$ | Fluid density |

## 3.5 References


1 von Mises, R; Friedrichs, K O. '*Fluid Dynamics*' (1971). Springer-Verlay New York Inc.

2 Cloke, V M; Higgins, J S; Lin Phoon, C; Richardson, S M; King, S M; Done, R; Cooper, T E. *LoQ Factfile*, 1996, 3-56

3 Baker, S M; Smith, G; Pynn, R; Butler, P; Hayter, J; Hamilton, W; Magid, L. *Rev. Sci. Instrum.* 1994, **65**(2) 412

4 Lide, RD (Ed). *CRC Handbook of Chemistry and Physics*. 77th Edition (1996). CRC Press.

5 Hsieh, H L; Quirk, R P. *'Anionic Polymerisation – Principles and Practical Applications'* (1996). Dekker (New York).

6 Morton, M. *'Anionic Polymerisation – Principles and Practice'* (1983). New York Academic Press.

7 Gauthier, S; Eisenberg, A. *Macromolecules*, 1987, **20**, 760

8 Wakefield, B J. *'The Chemistry of Organolithium Compounds'* (1974). Pergamon Press.

9 Toreki, W; Hogen-Esch, T E. *ACS Polymer Preprints*, 1988, **29**, 416

10 Frantz, P; Granick, S. *Langmuir,* 1992, **8**, 1176

11 Kern, W; Puotinen, D A. *RCA Review,* June 1970, 187

12 Liu, Y; Quinn, J; Rafailovich, M H, Sokolov, J; Zhong, X; Eisenberg, A. *Macromolecules,* 1995, **28**, 6347

13 Karim, A; Tsukruk V V; Douglas, J F; Satija, S K; Fetters, L J; Reneker, D H; Foster, M D. *J Phys II,* 1995, **5**, 1441

14 Jones, R A L; Lehnert, R J; Schonherr, H; Vancso, J. *Polymer,* 1999, **40**, 525

# CHAPTER 4

# POLYMER BRUSHES – QUIESCENT STUDIES

# CHAPTER 4

# POLYMER BRUSHES – QUIESCENT STUDIES

Before any shear studies were undertaken, it was essential to characterise the quiescent brush dimensions fully to develop a frame of reference for the subsequent shear investigations. Several other groups have reported work involving the study of polymer brush characteristics at the solid-liquid [1-6] and air-liquid [7-8] interfaces, and their findings will be compared with results obtained in this work. It is worth noting that neutron reflectometry is one of the few techniques that can be used to investigate solid-liquid interfacial systems due to the "buried" nature of the interface. X-rays are unable to penetrate the substrate with sufficient intensity, and whilst it is conceivable that optical ellipsometry could be used, this technique would not provide anywhere near the length scale resolution achievable with neutrons.

## 4.1 Experimental

The neutron reflectometry experiments were carried out on the SURF reflectometer at the Rutherford Appleton Laboratory [9-10]. A chopper frequency of 50Hz was used to select an incident neutron wavelength ( $\lambda$ ) range of 0.55 to 6.8Å, and in order to cover a sufficiently large Q-range (equation 4.1) 2 or 3 incident angles ( $\theta$ ) were used (depending on the nature of the particular experiment) and the data for the different angles combined to produce the reflectivity profile. The incident angles were defined by adjusting the angle of a goniometer on which the sample stage was mounted. For all experiments the pre-sample collimating slits were set such that the illuminated length of the sample was 80mm. The sample preparation procedure has already been discussed in chapter 3; prior to the neutron reflectometry measurements the dry polymer layer thicknesses were measured using ellipsometry. A check on the ellipsometry measurements was made using neutrons by placing the silicon block on

the sample stage and collecting reflectivity data for incident angles of 0.28 and 0.9° (covering a Q-range of 0.009-0.36Å$^{-1}$).

$$Q = \frac{4\pi}{\lambda}\sin\theta \qquad \textbf{Equation 4.1}$$

For solid-liquid interfacial measurements the sample block was placed in the flow reflectometry cell and fixed in place by screwing down the top plate. The whole cell was mounted on the reflectometer sample stage, the thermo-circulator was connected, the platinum resistance thermometer inserted in the base block and tubing connected to the NPT fittings at the inlet and outlet reservoirs. The solvents used for the brush layer investigations were cyclohexane and toluene; for the quiescent studies these solvents were introduced to the cell using glass syringes connected to the inlet/outlet reservoir tubing and clamped in a vertical position. Reflectivity profiles for the solid/liquid interfacial experiments were collected over 3 incident angles: 0.35, 0.8 and 1.8° (covering a Q-range of 0.011-0.72Å$^{-1}$).

It is vital for neutron reflectometry measurements that the sample is aligned properly to ensure that the incident neutrons reach the desired interface and all reflected neutrons reach the detector. With air-liquid or air-solid studies this alignment procedure is relatively straightforward, and involves aligning the sample using a laser beam that follows the path of the neutrons. However, due to the buried nature of the interface in solid-liquid interfacial studies, this alignment has to be carried out neutronically. The neutronic alignment procedure[10] initially involves stepping the sample vertically upwards (with the detector set at zero angle) so that the neutron beam passes first through the neutron transparent silicon block and then eventually through the neutron opaque steel base block. The sample height value half-way between these 2 extremes on a neutron counts versus sample height plot represents the position of the interface. The sample stage goniometer is then aligned by scanning an angular range about the lowest angle to be used in the experiments (with the detector also set at this angle) and noting the position of the maximum in the resulting neutron counts versus angle plot.

Table 4.1 gives neutron scattering length density values [11-12] for the various components of the polymer brush system. The brush polymers themselves were perdeuterated to make them highly visible to neutrons, and the cyclohexane and toluene solvents used in the experiments were "contrast matched" to the silicon substrate.

| Component | Scattering Length Density ($Å^{-2}$) |
|---|---|
| Poly(styrene-$d_8$) | $6.47\times10^{-6}$ |
| Silicon | $2.095\times10^{-6}$ |
| Toluene-$d_8$ | $5.67\times10^{-6}$ |
| Toluene-$h_8$ | $0.94\times10^{-6}$ |
| Cyclohexane-$d_{12}$ | $6.70\times10^{-6}$ |
| Cyclohexane-$h_{12}$ | $-0.28\times10^{-6}$ |

**Table 4.1** Neutron scattering length density values for the various components of the brush system

Contrast matching exploits the fact that the scattering length density values for the deuterated solvents are higher than that of silicon while the values for the hydrogenous solvents are lower. Thus if hydrogenous and deuterated components are mixed in the correct volumetric ratio according to equation 4.2 then the scattering length density of the mixture will equal that of silicon.

$$\rho_N = \rho_H \phi_H + \rho_D \phi_D \qquad \textbf{Equation 4.2}$$

In equation 4.2, $\rho_N$ is the total scattering length density ($=2.07\times10^{-6}Å^{-2}$ if contrast matching to silicon) while $\rho$ and $\phi$ represent respectively the scattering length density and volume fraction values of the deuterated and hydrogenous (subscript D and H respectively) solvent components. Table 4.2 gives the volumes of hydrogenous

and deuterated solvent required to make silicon contrast matched cyclohexane or toluene.

| Solvent | Target scattering length density ($Å^{-2}$) | Volume required per 100mls | |
|---|---|---|---|
| | | Deuterated (mls) | Hydrogenous (mls) |
| Cyclohexane | $2.07\times10^{-6}$ | 33.67 | 66.33 |
| Toluene | $2.07\times10^{-6}$ | 23.89 | 76.11 |

**Table 4.2** Details of the preparation of cyclohexane and toluene contrast matched to silicon

When the solvents are contrast matched to silicon, the boundary between the silicon substrate and the solvent subphase is invisible to neutrons and thus any reflectivity observed is due only to the presence of the deuterated brush polymer.

## 4.2 Data Fitting

Volume fraction profiles for solvated polymer brushes are predicted to be parabolic [13-14], and studies by other groups have shown this to be true. Consequently the data obtained in this work were fitted using parabola-like profiles, with the reflectivity calculated using the optical matrix method of Abeles [15]. The Abeles method has already been discussed in chapter 2, but the key elements of this method with particular regard to functional form fitting of neutron reflectivity data will now be discussed in more detail.

The shape of the polymer volume fraction profile can be described in terms of a functional form (e.g. parabola, error function, exponential...etc...), and the precise features of the profile (e.g. the volume fraction of polymer at the substrate surface or the distance from the substrate at which the volume fraction of polymer falls to zero) can therefore be controlled using a set of parameters that comprise the given functional form. The volume fraction profile is divided into a series of strips (or

layers) of uniform thickness (figure 4.1) and since the scattering length densities of the brush polymer and the solvent subphase are known, the scattering length density of each layer can be calculated from equation 4.3.

$$\rho_L = \rho_P \phi_P + \rho_{sol} \phi_{sol} \qquad \textbf{Equation 4.3}$$

where: $\rho_L$ = total scattering length density of a given layer

$\rho_p$ = polymer scattering length density

$\phi_P$ = polymer volume fraction within the layer

$\rho_{sol}$ = solvent scattering length density

$\phi_{sol}$ = solvent volume fraction within the layer = $1 - \phi_P$

Thus the polymer volume fraction profile leads to the scattering length density profile which in turn is used to calculate the reflectivity profile.

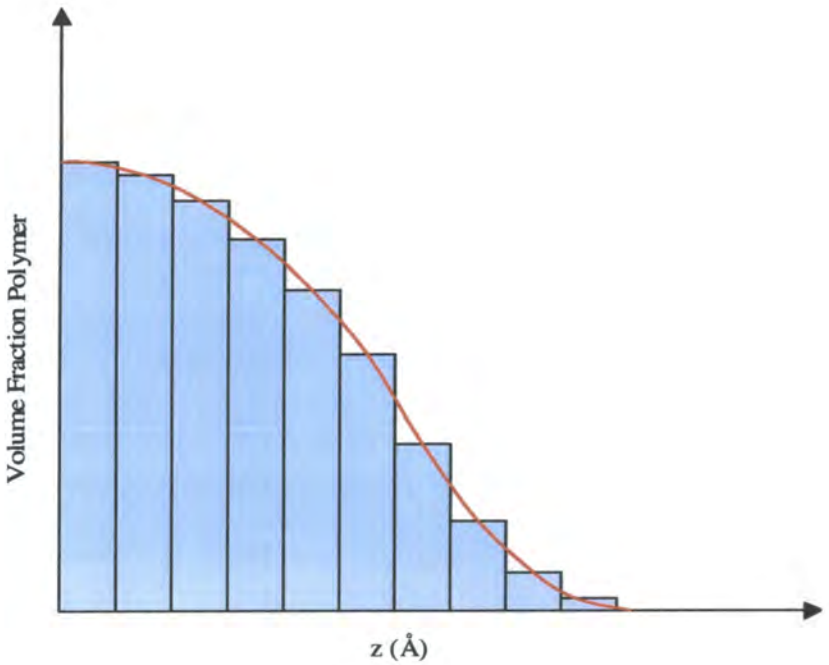


**Figure 4.1** Schematic illustration of the division of a polymer volume fraction profile (red line) into a series of layers of uniform thickness.

Fitting programs were written that vary the parameters describing the volume fraction profile and compare the resulting calculated reflectivity to the experimentally obtained reflectivity. By using a least squares minimising algorithm such as a SIMPLEX form, the experimental data can be iteratively fitted using the chosen functional form (the goodness of the fit being $\chi^2$).

In addition to the parameters describing the volume fraction profile functional forms, another independent parameter was used in the data fitting procedure. This parameter, $\sigma_r$, was used to describe a Gaussian roughness at the substrate surface [16] (i.e. about $z = 0$) where $\sigma_r$ represents the root mean square standard deviation of the Gaussian. An illustration of this Gaussian roughness is given in figure 4.2.

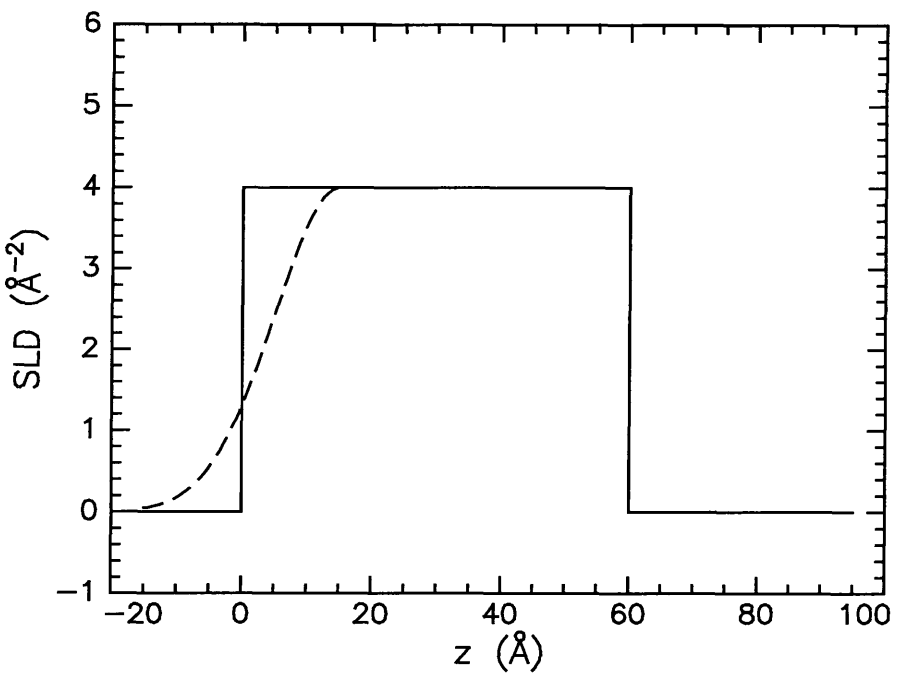


**Figure 4.2** Scattering length density (SLD) profile for a uniform 60Å layer of scattering length density $4\times10^{-6}$Å$^{-2}$ surrounded by media of scattering length density zero (solid line). The dashed line shows how the profile would be modified if a 10Å Gaussian roughness ($\sigma_r$) were applied across the vertical step upwards in scattering length density at $z = 0$.

Two qualitatively similar functional forms were used to fit the reflectivity data: a modified parabolic function and a parabola with an exponential tail.

For the modified parabolic function (equation 4.4), the polymer volume fraction ($\phi_P$) is expressed as a function of the distance from the substrate surface ($z$) in terms of the surface volume fraction ($\phi_S$, i.e. the value of $\phi_P$ at $z = 0$), the brush height ($h$, i.e. the value of $z$ at which $\phi_P$ falls to zero) and a profile exponent ($\alpha$).

$$\phi_P = \phi_S \left[ 1 - \left( \frac{z^2}{h^2} \right) \right]^{\alpha} \qquad \textbf{Equation 4.4}$$

Increasing the value of the exponent ($\alpha$) has the effect of making $\phi_P$ fall off more rapidly with increasing $z$ in the main body of the profile whilst adding an exponential-like tail region at higher $z$ ($\alpha = 1$ describes a pure parabola). The effect of varying $\alpha$ on the shape of the volume fraction profile is illustrated in figure 4.3.

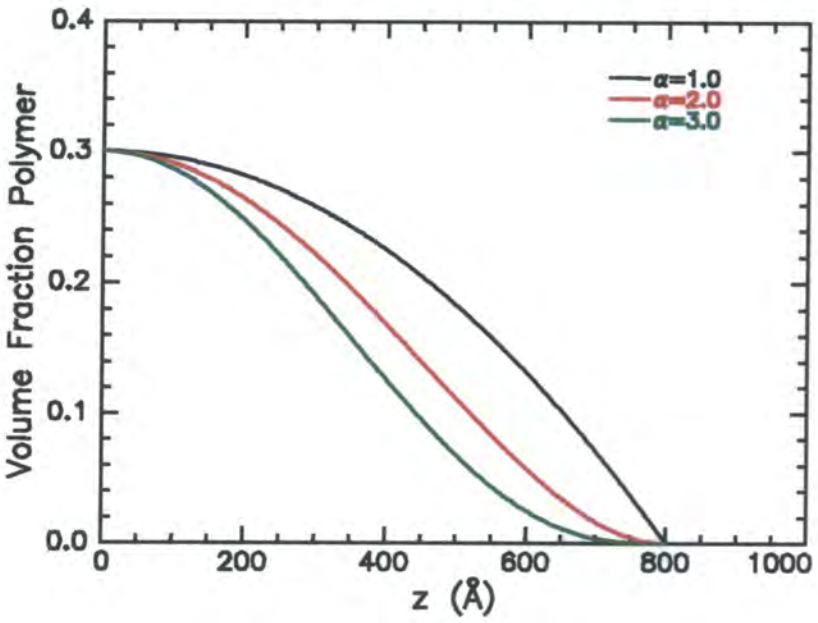


**Figure 4.3** Effect of varying $\alpha$ on the shape of the modified parabolic profile. All 3 profiles shown have $\phi_S = 0.3$ and $h = 800$ Å.

Although the modified parabolic function allows the expression of an exponential-like tail region near the outer extremity of the brush, the data were also fitted, where appropriate, using a parabola with an exponential tail. This profile switched from the modified parabolic function of equation 4.4 to an exponential function at a given value of $z$ ($z = z_e$). Thus the profile was expressed as follows:

$$\phi_P = \phi_S\left[1-\left(\frac{z^2}{h^2}\right)\right]^{\alpha} \qquad \text{for } z < z_e \qquad \textbf{Equation 4.5}$$

$$\phi_P = Ae^{-Bz} \qquad \text{for } z \geq z_e \qquad \textbf{Equation 4.6}$$

At $z = z_e$, the gradients $\left(\frac{d\phi_P}{dz}\right)$ and $\phi_P$ values of the 2 functions must be equal so as not to have any discontinuity in the overall profile. Incorporating these conditions, the exponential function parameters $A$ and $B$ can be defined (equations 4.7 and 4.8).

$$A = \frac{2\phi_S \alpha z_e\left[1-\left(\frac{z_e^2}{h^2}\right)^{\alpha-1}\right]}{h^2 Be^{-bz_e}} \qquad \textbf{Equation 4.7}$$

$$B = \frac{2\alpha z_e\left[1-\left(\frac{z_e^2}{h^2}\right)^{\alpha-1}\right]}{h^2\left[1-\left(\frac{z_e^2}{h^2}\right)^{\alpha}\right]} \qquad \textbf{Equation 4.8}$$

In reality there were several other qualitatively similar functional forms that could also have been used to fit the reflectivity data (e.g. error function, tanh or stretched

exponential functions). However, it is somewhat pointless to attempt to fit a given set of data using a whole series of functional forms all describing very similar shapes for the volume fraction profile. It is the shape of the volume fraction profile that is the important feature, not the way in which that shape is parameterised.

All of the data were fitted using the MULF suite of programs written by Dr J R P Webster at the Rutherford Appleton Laboratory. The Fortran code for the model routines containing the functional forms described above was written by myself and then incorporated into the MULF programs by Dr Webster.

## 4.3 Results

All of the solvated brush experiments were carried out using either cyclohexane or toluene as the solvent, and the solvent was always contrast matched to silicon. Since the reflectivity for these systems was very weak, no critical edge was observed in the reflectivity profiles and consequently a separate experiment was performed each time the reflectometer was used to ascertain the value of a scale factor calculated using the critical reflection region. When total external reflection occurs, a critical edge is seen at low Q values, but due to instrumental factors this critical edge is not located at exactly $R(Q)=1$ in the raw reflectivity data. Consequently, the data must be divided through by a scale factor such that the critical edge reflectivity equals unity. This scale factor was obtained from the reflectivity of cyclohexane-$d_{12}$ in contact with an uncoated silicon block.

The neutron beam passes through several centimetres of silicon and it was necessary to account for transmission effects (using transmission data) in the subsequent data reduction process. The transmission data were obtained by collecting 2 data sets (with both detector angle and incident angle set to zero) of the form $R$ versus $\lambda$: one with the beam passing through the silicon block and the other with the beam passing through air only. Dividing the silicon transmission data by the air transmission data yielded the transmission factors which were subsequently used to normalise the observed reflectivity data to an absolute scale and to correct for any wavelength dependence (since a white beam of neutrons was being used).

Results obtained for the 2 polymers used in these experiments (codes TK327 and LRH3.52, see chapter 3 for details) will be discussed separately.

### 4.3.1 LRH 3.52 Polymer

One brush layer sample was used for all the quiescent neutron reflectometry studies of the polymer LRH 3.52, and this sample is assigned the code "block 1". The sample was prepared and characterised as outlined in chapter 3, and dry layer ellipsometry measurements taken at 16 points across the sample surface indicated that the average layer thickness was 102Å. This value was confirmed by obtaining the dry layer neutron reflectivity spectrum, subsequently fitted using a single uniform layer with a scattering length density equal to that of deutero-polystyrene. The layer thickness value was allowed to vary during fitting, and a value of 106Å was returned by the program ( $\chi^2 = 78.4$ ). The experimental data and fit are shown in figure 4.4.

Assuming that the dry layers are solid polystyrene (i.e. assuming ideal packing of the chains within the layer), the volume of film covering a defined surface area of the substrate can be calculated. Since the density of deutero-polystyrene is known ($1.12 gcm^{-3}$), number of molecules per unit area of substrate surface and thus the area per molecule and average distance between grafting sites ( $d$ ) can be calculated. The unperturbed radius of gyration ($R_g$) of the polystyrene chains can be calculated as a function of molecular weight ($M_w$) from [17]:

$$R_g = 0.28 M_w^{1/2} \qquad \textbf{Equation 4.9}$$

Calculations based on the dry film thickness (from ellipsometry) for block 1 show that $d = 80$ Å, and thus since $R_g = 186$ Å for the polystyrene chains in LRH 3.52 it is clear that the brush condition $d << R_g$ has been satisfied for this sample.

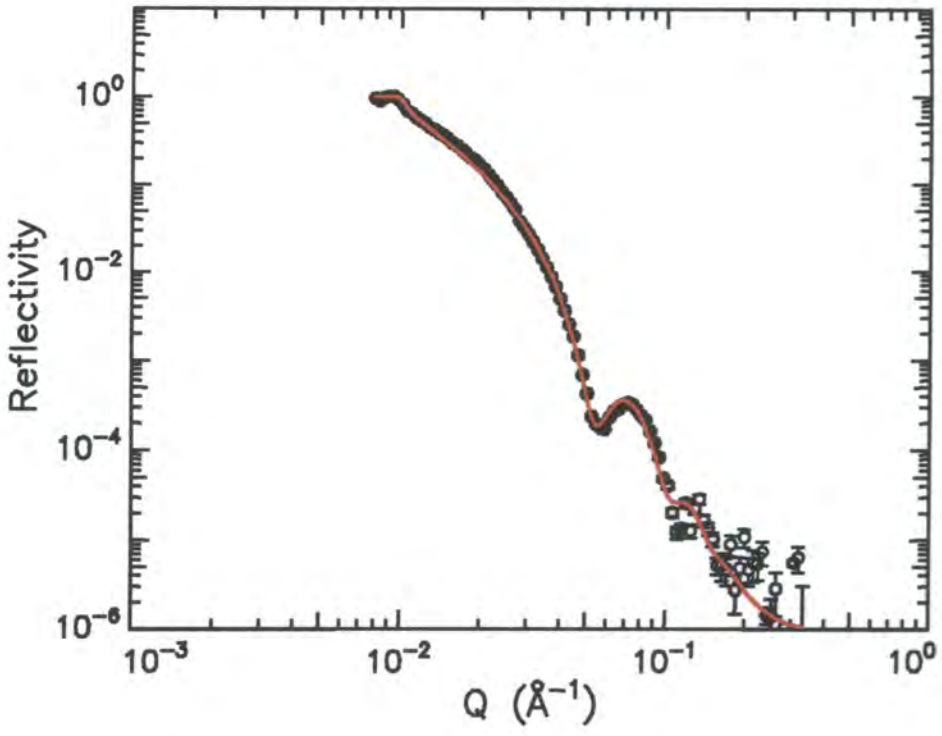


**Figure 4.4** Dry layer neutron reflectivity profile for the sample "block 1" (polymer LRH 3.52). The red line is a fit to the data for a single uniform deutero-polystyrene layer of thickness 106Å.

Initially, experiments were performed using cyclohexane as solvent at various different temperatures. Cyclohexane is a theta solvent for polystyrene; however, since the theta temperature varies slightly depending on the deuteration characteristics of the polymer/solvent system, the fact that a mixture of deuterated and hydrogenous cyclohexane was being used meant that the theta temperature would have been somewhere between 303 and 309K [18] (the theta temperatures for deuteropolystyrene in $C_6H_{12}$ and $C_6D_{12}$ respectively).

Reflectivity data were collected in cyclohexane at temperatures of 303, 313, 318 and 328K (figure 4.5). Following the run at 328K the temperature was then reduced stepwise, with reflectivity data being collected at 313 and 303K in order to check the occurrence of desorption (figure 4.6). The solvent was then changed to toluene (a thermodynamically good solvent for polystyrene) and data were collected for this system at 298K (figure 4.5).

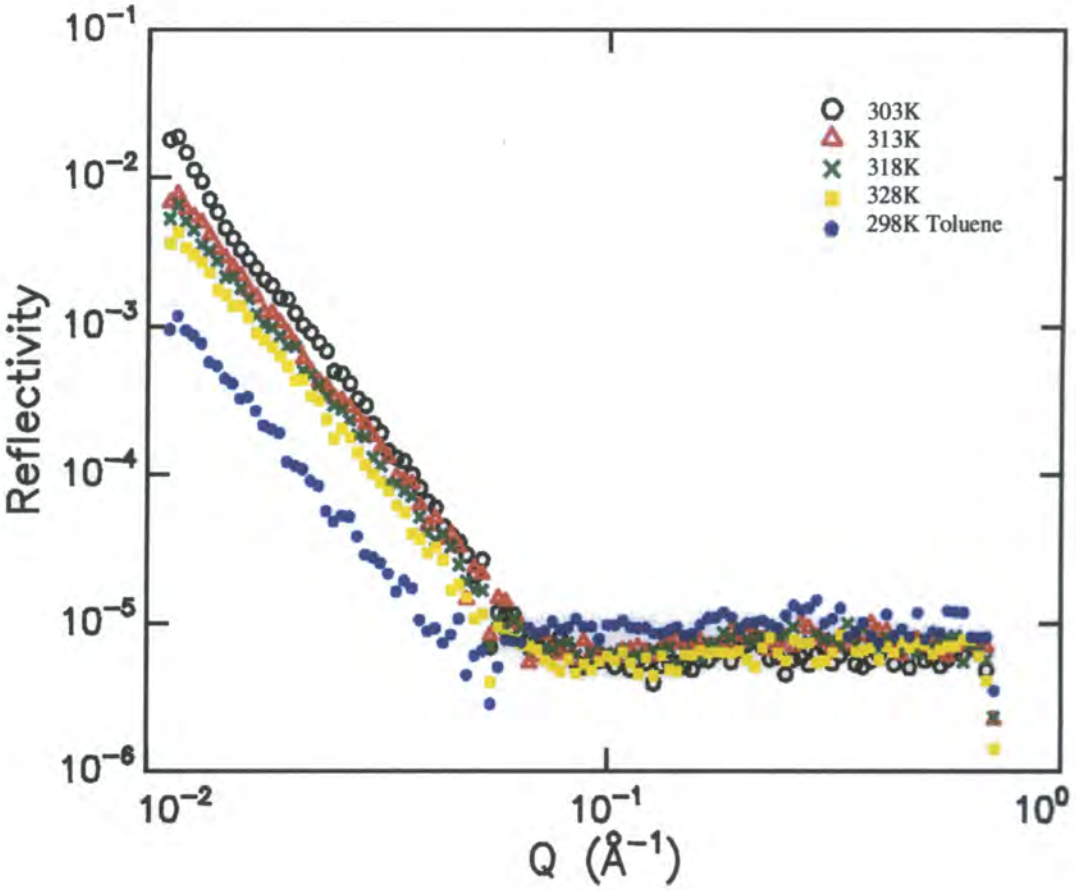


**Figure 4.5** Reflectivity profiles obtained for block 1 with cyclohexane as solvent at 303, 313, 318 and 328K. The reflectivity profile acquired with toluene as solvent at 298K is also shown.

Clearly the reflected intensity falls off as the temperature is increased to 328K in cyclohexane, and in toluene the intensity drops even further.

These observations can be attributed to the brush molecules stretching from the grafting surface due to the increasingly strong excluded volume interactions within the brush as the solvent quality is improved. As the brush becomes more stretched, the monomer density is distributed throughout a larger volume (i.e. the average monomer concentration within any given volume element decreases) leading to a reduction is the reflected intensity.

Figure 4.6 compares the reflectivity profiles acquired at 303 and 313K in cyclohexane on increasing and reducing the temperature. The 2 profiles at each temperature are virtually superimposable indicating that little or no desorption of the brush chains occurred as a result of warming the system to 328K.

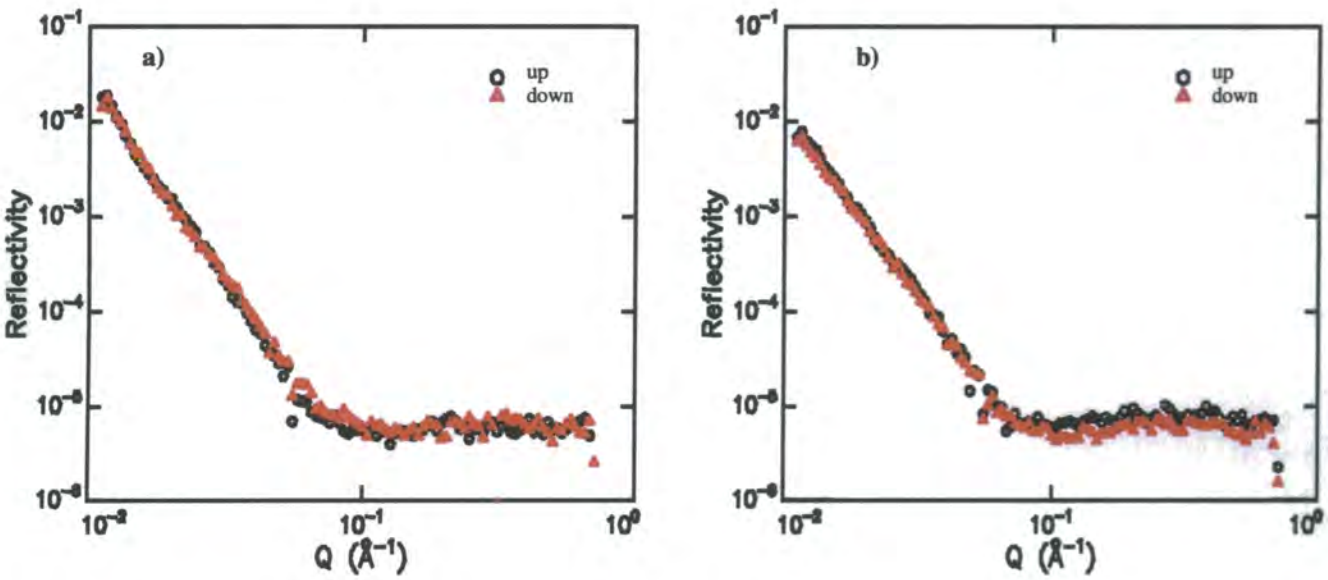


**Figure 4.6** Reflectivity profiles for block 1 in cyclohexane at a) 303K and b) 313K. The black circles represent data collected whilst stepping up in temperature. The red triangles represent data collected whilst stepping back down in temperature.

The volume fraction profiles obtained from fits to the data shown in figure 4.5 using a modified parabolic function (equation 4.4) are displayed in figure 4.7, and the brush

parameters for these fits are listed in table 4.3 along with the interfacial roughness ($\sigma_r$) and $\chi^2$ values.

| T (K) | $\phi_s$ | h (Å) | $\alpha$ | $\sigma_r$ (Å) | $\chi^2$ |
|---|---|---|---|---|---|
| 303 | 0.255 | 670 | 1.57 | 5.0 | 72.0 |
| 313 | 0.20 | 850 | 1.95 | 8.5 | 90.2 |
| 318 | 0.175 | 990 | 1.4 | 15.0 | 91.0 |
| 328 | 0.152 | 1240 | 1.66 | 12.1 | 47.6 |
| 298 (toluene) | 0.08 | 1700 | 3.19 | 12.0 | 12.0 |

**Table 4.3** Values obtained from fits to the data shown in figure 4.5 using a modified parabolic function (equation 4.4).

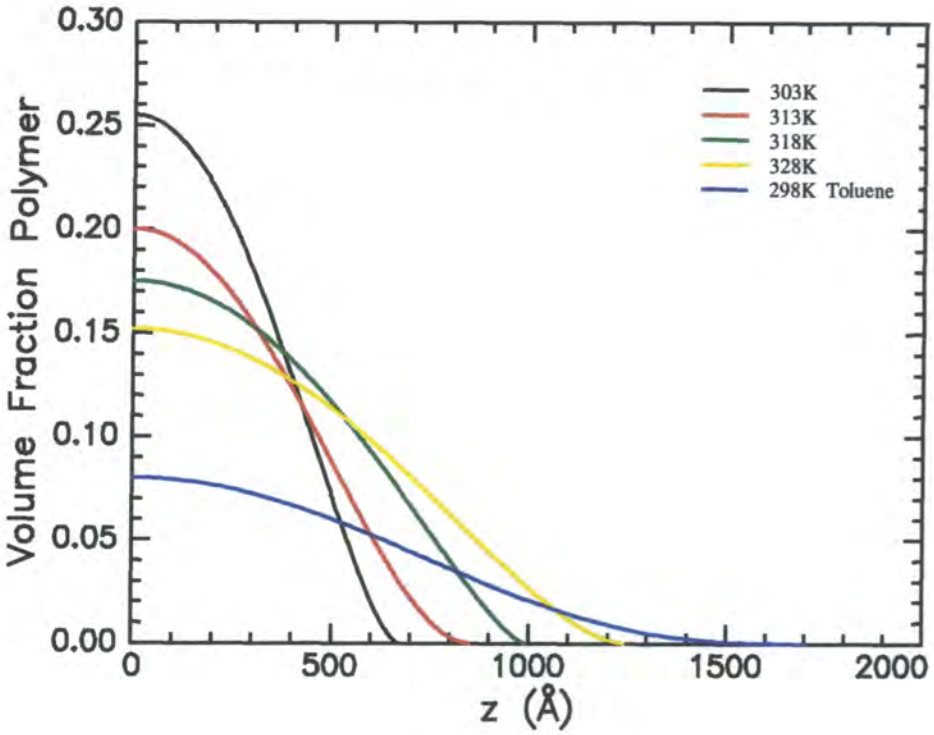


**Figure 4.7** Volume fraction profiles obtained from fits to the reflectivity data shown in figure 4.5 using a modified parabolic function. (Solvent was cyclohexane unless otherwise indicated).

The modified parabolic fits clearly show that the brush chains are stretching away from the grafting surface as the solvent quality is improved, with the brush height increasing and the surface volume fraction decreasing as the temperature in cyclohexane is increased. Comparing the observed brush heights with the unperturbed radius of gyration of the polystyrene chains (186Å) it can be seen that even at a near-theta temperature in cyclohexane (303K) the brush height is equal to $3.6R_g$. This shows just how strong the intermolecular excluded volume interactions are in the brush even when the thermodynamic quality of the solvent is not particularly good. At the maximum temperature studied in cyclohexane (328K) the brush height is $6.7R_g$, whilst in toluene the brush height increases still further to $9.1R_g$ indicating that the chains are strongly stretched when the solvent quality is good. The actual modified parabolic fits to some of these reflectivity data are displayed in figure 4.8.

The areas under the volume fraction profiles enable the adsorbed amount of polymer per unit area of the substrate surface to be calculated. Since a value for the adsorbed amount could also be calculated independently from the dry layer ellipsometry measurements, this provided a useful means of checking the veracity of the volume fraction profiles obtained from fits to the reflectivity data. Since at any given point in the volume fraction profile the sum of the volume fractions of polymer and solvent must equal unity, the total volume fraction of polymer present across the entire height of the profile must be equal to $\frac{\int_0^h \phi_P dz}{h}$. Since the density of the polymer is known it is therefore trivial to convert this total volume fraction to the mass of polymer per unit area. Adsorbed amounts calculated for the profiles shown in figure 4.7 are listed in table 4.4, and it can be seen that there is good agreement between the values calculated from the cyclohexane profiles and the value obtained from the ellipsometry measurements taken prior to the neutron experiments ($11.40 mgm^{-2}$). However, the value calculated from the toluene profile is considerably less than those for the

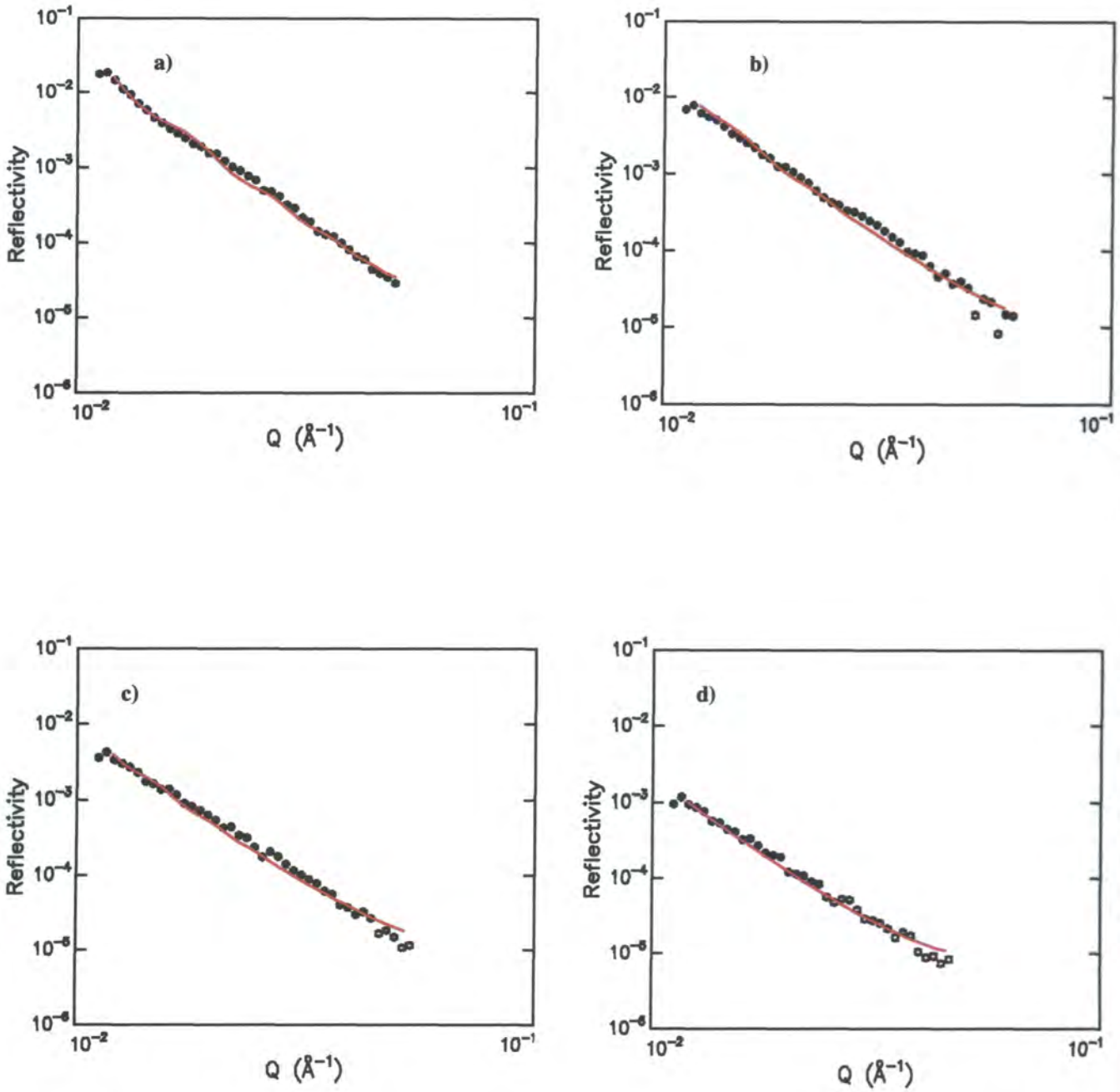


**Figure 4.8** Fits to the neutron reflectivity data using a modified parabolic function. The experimental data are displayed over the fitted Q-range and the red lines show the fits. a) 303K in cyclohexane, b) 313K in cyclohexane, c) 328K in cyclohexane and d) 298K in toluene.

cyclohexane profiles implying that some desorption had occurred as a result of toluene exposure. When the dry layer thickness for block 1 was remeasured on the ellipsometer following the neutron reflectometry experiments, it was found that the thickness had indeed decreased from the pre-experimental value of 102Å to 56Å. This new value corresponded to a distance between grafting sites of 108Å meaning that the sample was still within the brush regime even after desorption had occurred, and the

| T (K) | Adsorbed amount of polymer ($mgm^{-2}$) |
|---|---|
| 303 (cyclohexane) | 11.10 |
| 313 (cyclohexane) | 10.24 |
| 318 (cyclohexane) | 11.71 |
| 328 (cyclohexane) | 12.02 |
| 298 (toluene) | 6.78 |

**Table 4.4** Adsorbed amounts of polymer calculated from the volume fraction profiles shown in figure 4.7. The values calculated (for comparison) from the drylayer ellipsometry measurements were 11.40$mgm^{-2}$ (cyclohexane) and 6.27$mgm^{-2}$ (toluene).

calculated value for the adsorbed amount obtained from this reduced dry layer thickness (6.27$mgm^{-2}$) agrees well with the value calculated from the volume fraction profile resulting from a modified parabolic fit to the reflectivity data (table 4.4). It seems clear that the desorption occurred as a result of the toluene experiment since cyclohexane reflectivity profiles run at 303K and 313K while the temperature was coming down from 328K were virtually identical with those obtained while the temperature was increasing. However, since block 1 had been washed several times in toluene to remove any ungrafted polymer at the sample preparation stage, this *in situ* desorption during the reflectivity experiments in toluene was initially hard to explain. The most probable explanation for this phenomenon lay in the fact that when filling the cell with solvent prior to the reflectivity experiments, the syringes were pumped several times synergistically in order to purge any air from the cell (which might otherwise have interfered with the neutron data). Thus, the highly stretched

conformations of the brush chains in toluene coupled with the shear resulting from solvent flow during the air purging procedure would have led to some desorption occurring. Confirmation of this theory was obtained during the shear experiments (chapter 5) when it was found that cyclohexane shear flow produced negligible desorption of the brush chains whereas toluene shear flow led to an approximately 50% decrease in the dry film thickness as measured by ellipsometry.

As a means of further checking the veracity of the modified parabolic fits to the reflectivity data, additional fits were also carried out for some of the data using the modified parabola/exponential tail model (equations 4.5 to 4.8). The results of these fits to the cyclohexane data at 313K and 328K and the toluene data at 298K are displayed in table 4.5. Figure 4.9 shows the volume fraction profiles described by the data in table 4.5, and compares the modified parabola and modified parabola/exponential tail volume fraction profiles obtained from fits to the cyclohexane data at 313K and 328K. It is worth pointing out that when the exponential tail function is used (i.e. an exponential tail cutting in at $z \geq z_e$) the parameter $h$ is no longer the actual brush height, but rather a parameter describing the shape of the modified parabolic region of the profile ( $z < z_e$ ).

| T (K) | $\phi_S$ | h (Å) | $\alpha$ | $z_e$ (Å) | $\sigma_r$ (Å) | $\chi^2$ |
|---|---|---|---|---|---|---|
| 313K | 0.193 | 865 | 1.88 | 750 | 11.9 | 71.4 |
| 328K | 0.153 | 1220 | 1.55 | 1090 | 11.8 | 47.6 |
| 298K (toluene) | 0.083 | 1650 | 3.02 | 1300 | 5.3 | 10.0 |

**Table 4.5** Values of the parameters obtained from modified parabola/exponential tail fits to cyclohexane (313K and 328K) and toluene (298K) data.

The 2 models used to fit the data give very similar results for the volume fraction profiles.

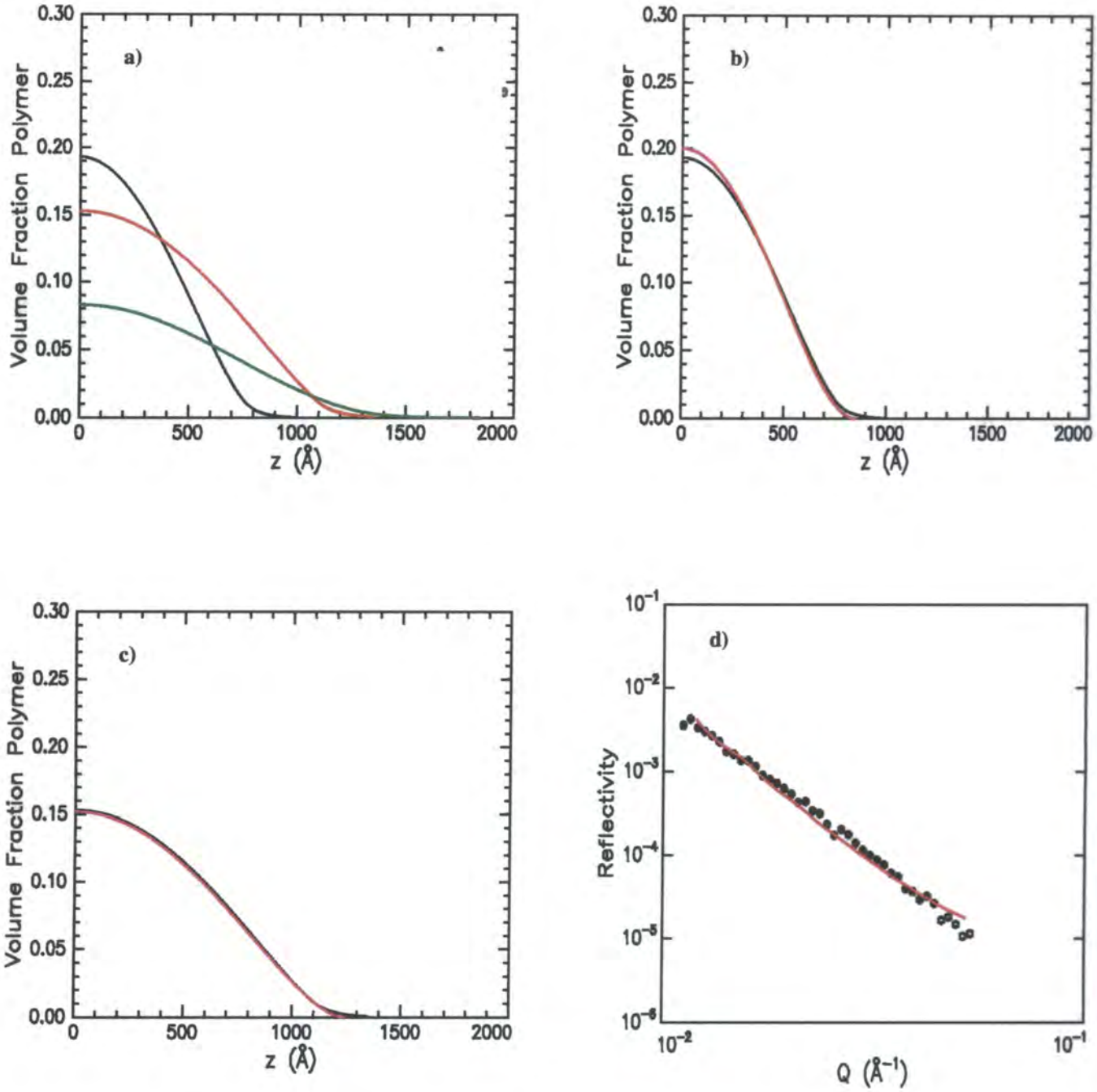


**Figure 4.9** a) Volume fraction profiles obtained from fits to the reflectivity data using a modified parabola/exponential tail function (black curve=313K in cyclohexane, red curve=328K in cyclohexane, green curve=298K in toluene). b) and c) comparison of modified parabolic (red curves) and modified parabola/exponential tail (black curves) profiles for cyclohexane at 313K and 328K respectively. d) reflectivity data for cyclohexane at 328K displayed over the fitted Q-range. The red line is the modified parabola/exponential tail fit.

### 4.3.2 TK327 Polymer

Quiescent studies using TK327 as the brush polymer were actually the first experiments to be carried out. The high polydispersity of this copolymer (chapter 3) meant that it was not ideal for the brush experiments. However, the scheduling of the first session on the neutron reflectometer meant that it was the only polymer available at the time (since a satisfactory synthetic route to a more monodisperse copolymer had not yet been found).

In spite of the high degree of coupling present in TK327, it was felt that this polymer could still be used for the brush experiments due to the fact that the actual polystyrene chains were fairly monodisperse. It was highly probable that TK327 would have contained a variety of species ranging from relatively uncoupled through to highly coupled copolymer, and it therefore seemed likely that the presence of coupled polymer on the substrate surface would simply lead to localised regions of artificially high grafting density. However, the neutron beam only sampled the average dimensions of the brush over the total illuminated area (80×30mm), and thus any such macroscopic inhomogeneities would have been unlikely to have had any significant adverse effect on the system as a whole.

The dry layer thickness of the sample used in these experiments (sample code="block 2") was measured using ellipsometry, and the average value obtained from 16 measurements across the substrate surface was 94Å. This corresponded to an average distance between grafting sites on the substrate surface ($d$) of 88Å which was considerably less than the unperturbed radius of gyration of the polystyrene chains ($R_g = 197$ Å) thus satisfying brush conditions.

All of the experiments were carried out using cyclohexane (contrast matched to silicon) as the solvent, and reflectivity profiles were collected at temperatures of 298, 308 and 318K. Figure 4.10 shows these reflectivity profiles, and as with the data collected for the polymer LRH3.52 the reflectivity is seen to decrease with increasing temperature due to stretching of the brush chains normal to the grafting surface with improving solvent quality.

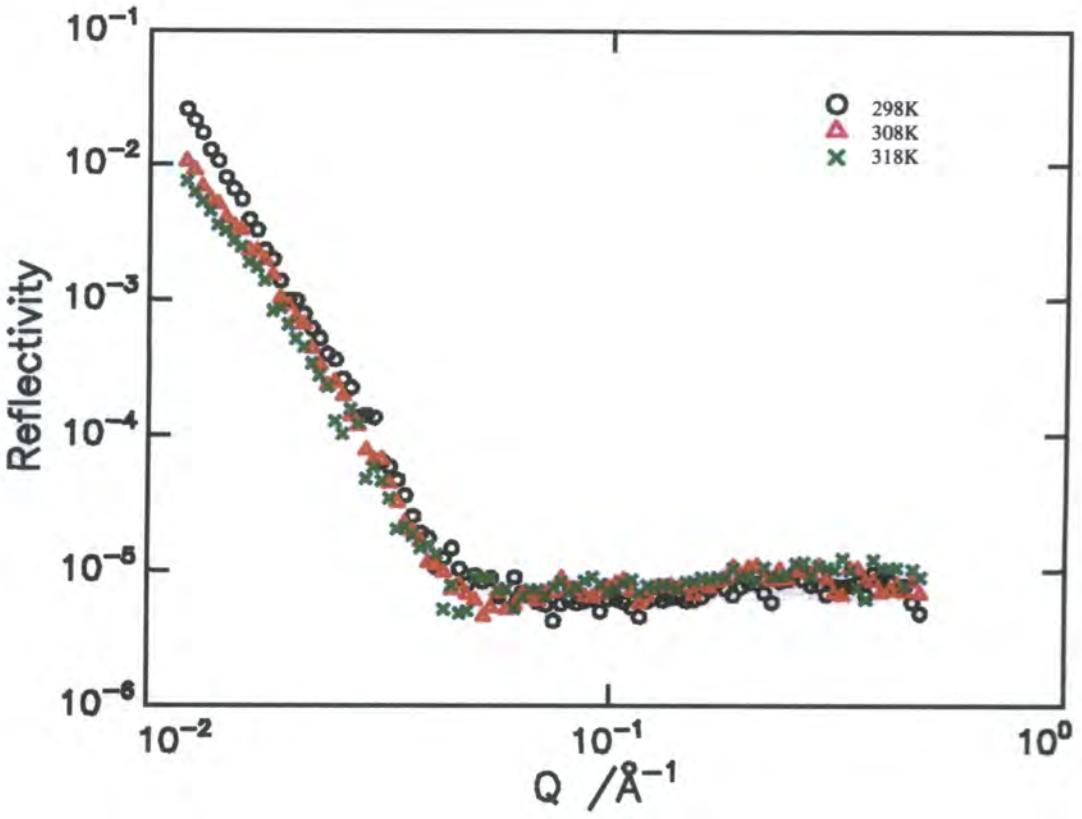


**Figure 4.10** Reflectivity profiles obtained for block 2 with cyclohexane as solvent at temperatures of 298, 308 and 318K.

To check whether desorption had occurred, additional reflectivity profiles were collected at 308 and 298K following the experiment at 318K. These profiles are shown in figure 4.11, and it can be seen that the 2 reflectivity profiles obtained at each temperature are virtually superimposable indicating that negligible desorption had occurred during the course of the experiments.

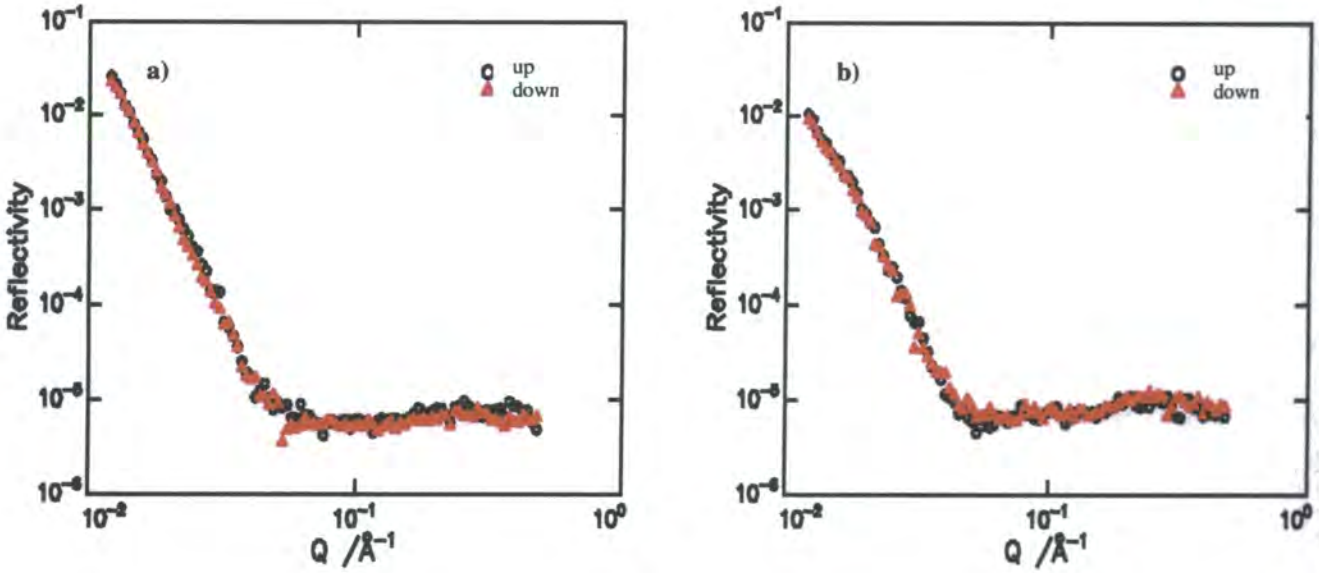


**Figure 4.11** Reflectivity profiles collected during the temperature increase (up) and decrease (down) cycles at a)298K and b)308K.

Volume fraction profiles obtained from fits to the reflectivity data using a modified parabolic function are shown in figure 4.12, and values for the parameters defining these fits are given in table 4.6. As with the results for the polymer LRH3.52 (block 1), the brush heights increase and the surface volume fractions decrease with increasing temperature due to stretching of the brush molecules normal to the grafting surface as the thermodynamic quality of the solvent improves. The adsorbed amounts of polymer obtained from integration of the volume fraction profiles are given in table 4.7, and it can be seen that there is good agreement between the values for the 3 different temperatures. Good agreement was also obtained between these values for the adsorbed amount and the value obtained from the dry layer thickness as measured by ellipsometry (10.5mgm$^{-2}$).

| T (K) | $\phi_s$ | h (Å) | $\alpha$ | $\sigma_r$ (Å) | $\chi^2$ |
|---|---|---|---|---|---|
| 298 | 0.29 | 620 | 2.2 | 32.9 | 5.5 |
| 308 | 0.23 | 715 | 1.6 | 29.3 | 4.2 |
| 318 | 0.21 | 1060 | 3.4 | 31.3 | 2.9 |

**Table 4.6** Parameters obtained from modified parabolic fits to the reflectivity data for block 2.

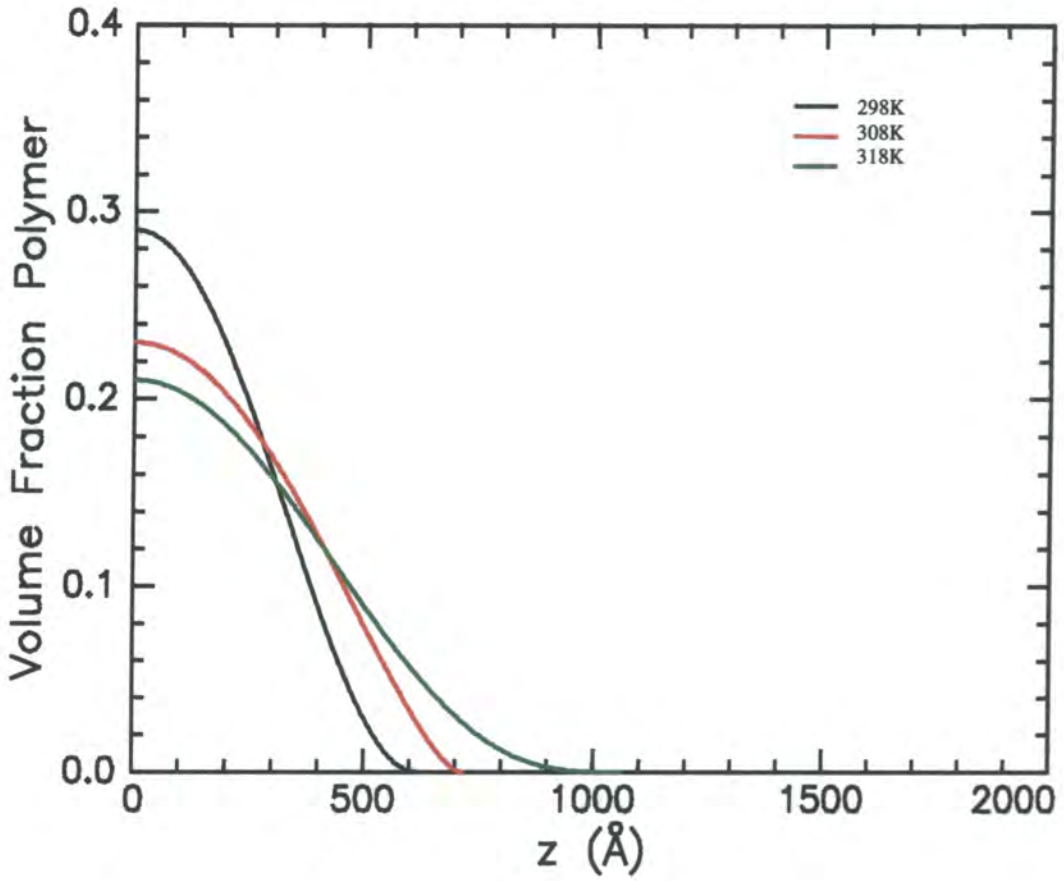


**Figure 4.12** Volume fraction profiles obtained from fits to the reflectivity data for block 2 using a modified parabolic function.

| T (K) | Adsorbed amount of polymer ($mgm^{-2}$) |
|---|---|
| 298K | 10.36 |
| 308K | 10.62 |
| 318K | 10.84 |

**Table 4.7** Adsorbed amounts of polymer calculated from the volume fraction profiles shown in figure 4.12. The value for the adsorbed amount obtained from the dry layer thickness measured by ellipsometry was $10.5mgm^{-2}$.

The actual fits to the reflectivity data (from which the volume fraction profiles shown in figure 4.12 were obtained) are shown in figure 4.13.

From comparison of the brush heights with the unperturbed radius of gyration (197Å), the brush is quite strongly stretched even at 298K (which is slightly below the theta temperature). Indeed, the brush height increases from $3.1R_g$ at 298K to $5.4R_g$ at 318K.

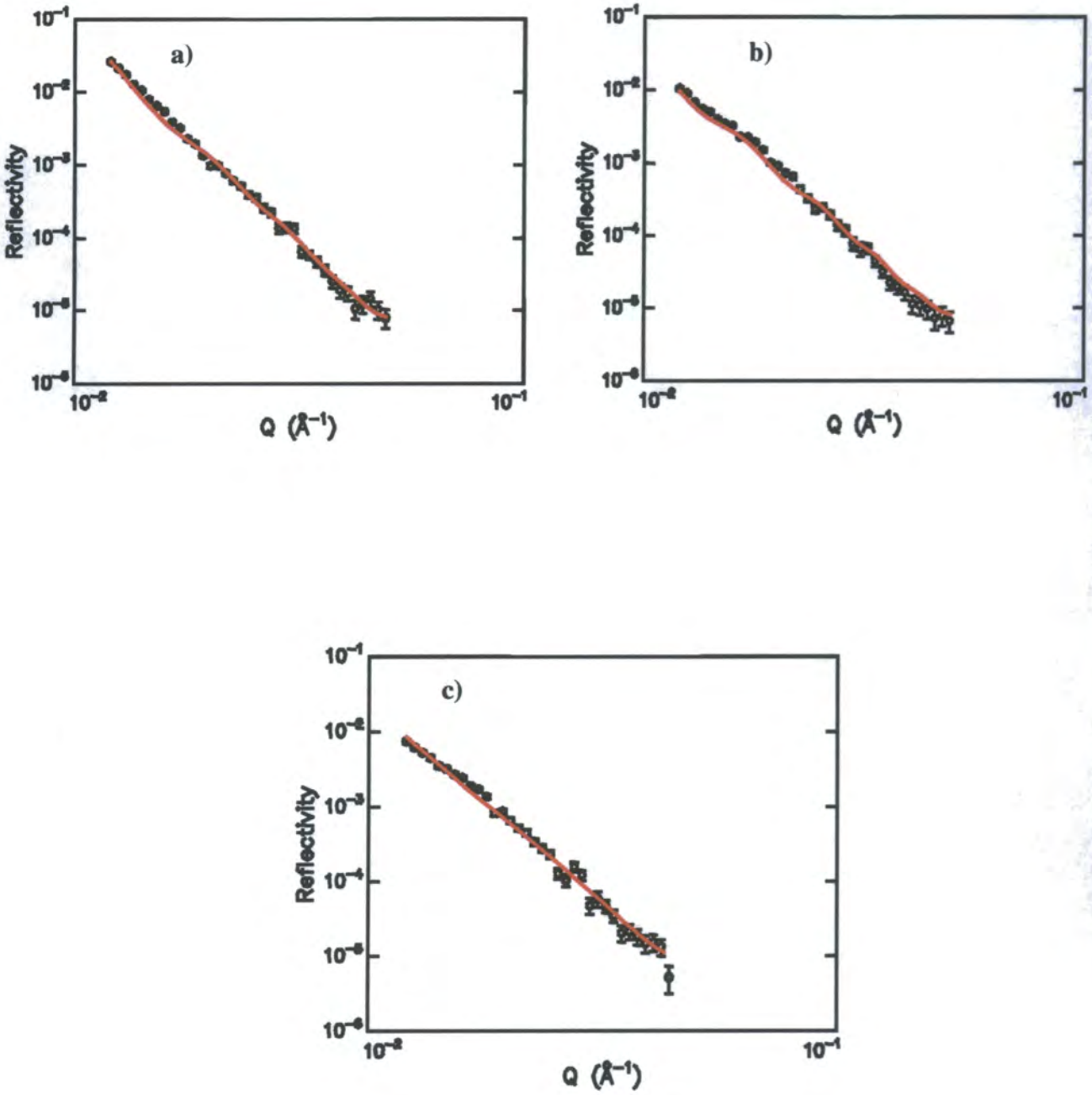


**Figure 4.13** Neutron reflectivity data for block 2 with cyclohexane as solvent at a) 298K, b) 308K and c) 318K. The data are displayed over the fitted Q-range and the red lines represent the fits.

## 4.4 Discussion

The quiescent results obtained clearly show that the volume fraction profiles for solvated polymer brushes are well described by parabola-like functions in agreement with the self consistent field calculations of Milner et al [13-14]. The reflectivity decreases with improving solvent quality for both of the samples studied, and fits to the reflectivity data (using functions based on parabolas) revealed that this trend was due to the brush height increasing and the surface volume fraction of polymer decreasing with improving solvent quality. This trend is consistent with brush theory; as the thermodynamic quality of the solvent improves, the chains stretch in the direction normal to the grafting surface due to repulsive excluded volume interactions between chain segments. By stretching, the chain segments maximise their enthalpically favourable interaction with the solvent molecules, and thus for a given polymer/solvent system and temperature the brush reaches an equilibrium height at which the tendency for the chains to stretch is exactly balanced by an elastic restoring force of entropic origin. This restoring force arises from the fact that there is an entropic penalty associated with stretching the polymer chains out of their favoured random walk conformations. The results showed that the brush height was considerably greater than the unperturbed radius of gyration of the chains even at temperatures below the theta temperature. However, whilst collapse of the brush layer to a block-like structure (with a volume fraction profile approximating to a step-function) is expected in the presence of a thermodynamically extremely poor solvent, the lowest temperatures explored in this work were only marginally sub-theta meaning that the poor solvent regime was barely sampled.

Furthermore, the fits showed that rather than having a rapid decrease to zero in polymer volume fraction at the brush height (as would be the case for a pure parabola), the profiles had a more gradual exponential decay near $z = h$. This was clearly observed with the modified parabolic fits to the reflectivity data (equation 4.4) where values of the profile exponent ($\alpha$) greater than unity were consistently found. This phenomenon has been observed in simulations of polymer brushes [19-20], and arises due to the fact that the SCF calculations are likely to fail close to the tip of the brush; the chain ends in this region are no longer strongly stretched and thus fluctuations occur around the most probable chain conformation [21].

The grafting interaction was strong enough to support stretching of the chains in cyclohexane, although some desorption was observed in toluene. However, this desorption most probably occurred as a result of shearing of the brush chains when the solvent was briefly flowed back and forth through the cell during filling in order to purge any air from the system.

Another interesting point of discussion concerns the presence or absence of a depletion layer [22]. If a repulsive interaction exists between the substrate surface and the segments of the polymer molecules then it is predicted that the polymer volume fraction profile will contain a depletion layer in the region near to the grafting surface[23-24]. A schematic example of such a depletion layer is shown in figure 4.14.

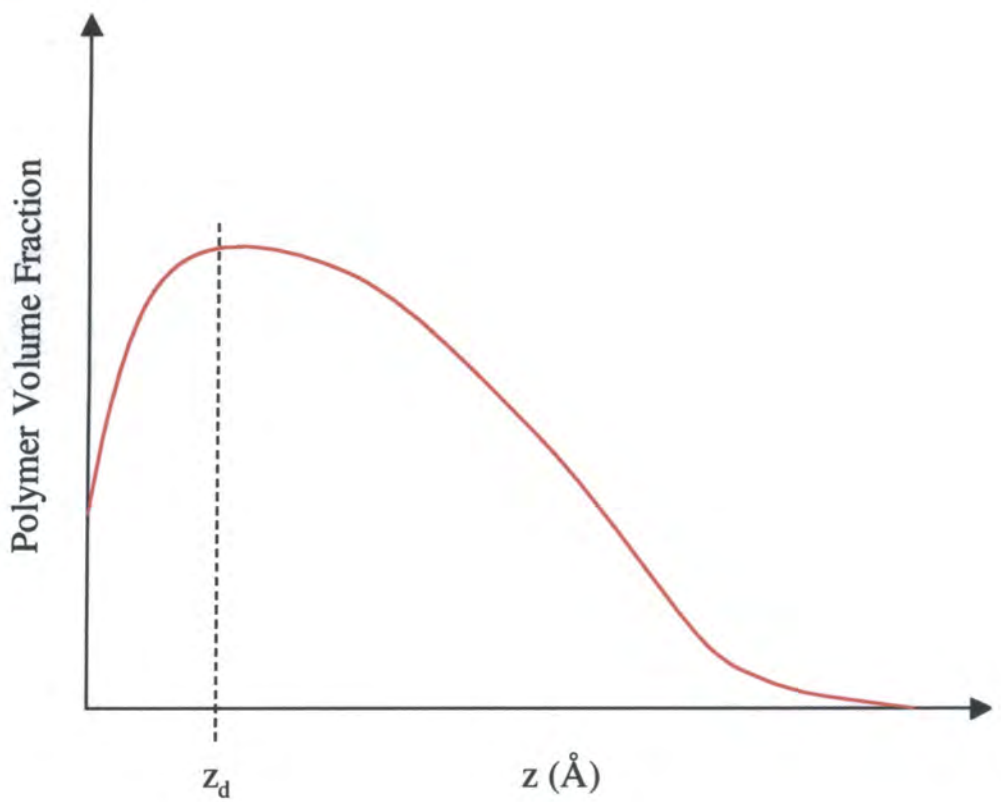


**Figure 4.14** Schematic illustration of a polymer volume fraction profile containing a depletion layer from $z = 0$ to $z_d$.

Referring to the illustration of Gaussian interfacial roughness at the substrate surface shown in figure 4.2, it can be seen that this roughness [25] approximates quite well to a depletion layer at the grafting surface [7]. Consequently, one would expect the presence of a depletion layer to yield roughness ($\sigma_r$) values greater than the 5-10Å expected for the intrinsic roughness of the substrate surface. Referring to table 4.3, it can be seen that the fitted roughness values obtained for block 1 are at most only slightly greater than the value expected for genuine interfacial roughness, and thus it seems safe to conclude that little or no depletion exists for this system. Whilst the interaction between the hydrophilic surface of the silicon block and the hydrophobic polystyrene segments is expected to be repulsive, the presence of chains of poly-4-vinylpyridine adsorbed at the surface may well reduce or eliminate any such repulsion.

The fitted roughness values obtained for block 2 however (see table 4.6) are ~30Å at all 3 temperatures, suggesting that depletion may exist for this brush sample. However, atomic force microscopy (AFM) studies of films of the polymers LRH3.52 and TK327 adsorbed onto silicon wafers (figure 4.15) revealed that while the LRH3.52 film was fairly homogeneous in terms of its surface coverage, the TK327 film had a distinct structure in the grafting plane. This in-plane structure consisted of islands of high and low surface coverage, a feature that may well have been associated with the coupling present in this polymer (chapter 3), and it is the presence of this in-plane structure that would have given rise to the artificially high interfacial roughness values obtained for block 2. Thus whilst it is hard to categorically confirm or deny the presence of depletion in the 2 samples studied here based on the experimental evidence, it would certainly appear that no significant depletion existed.

a)

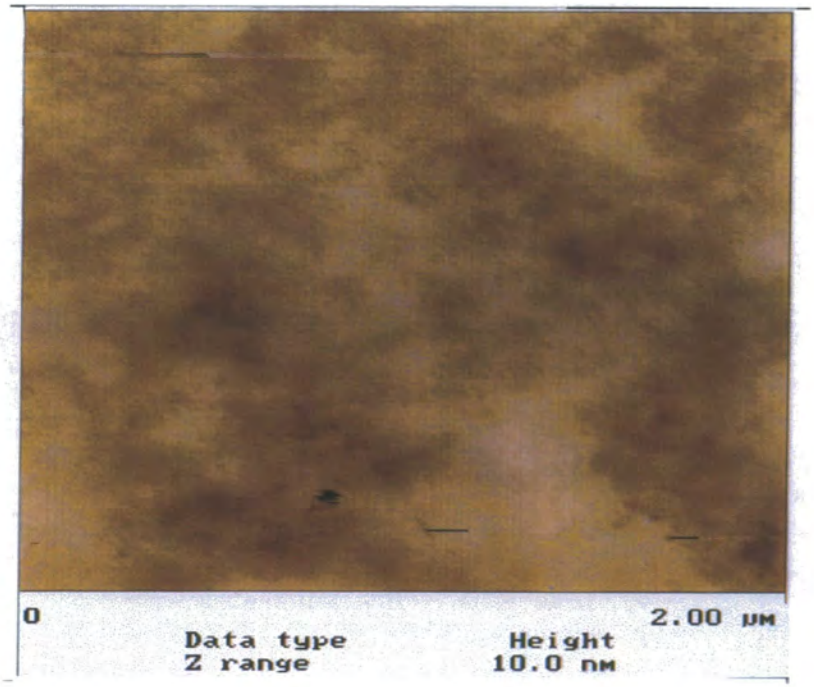


b)

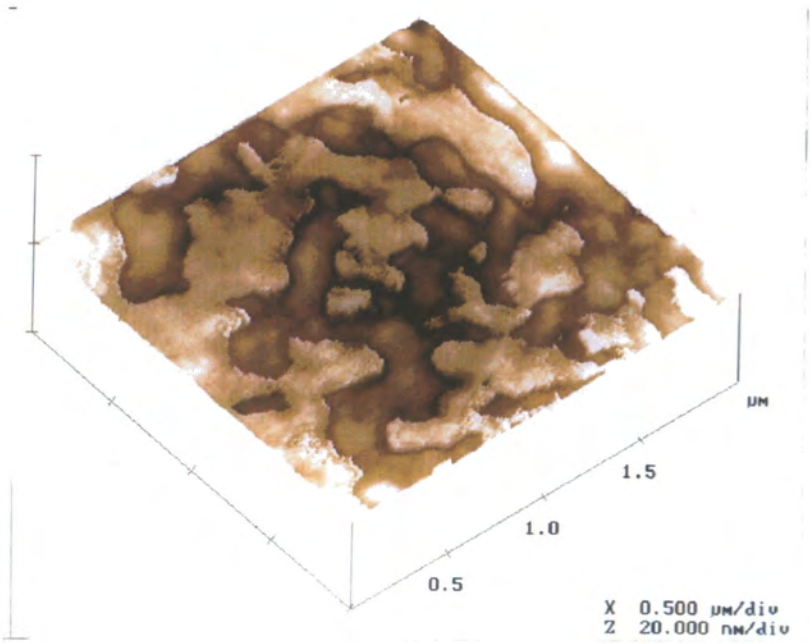


**Figure 4.15** Atomic force microscopy (AFM) images of dry polymer films adsorbed to silicon a)LRH3.52 b)TK327. Lighter areas represent thicker regions of the film.

Table 4.8 compares the experimentally determined brush heights ($h_{exp}$) in cyclohexane for blocks 1 and 2 (from the modified parabolic fits) with the theoretical brush heights ($h_{calc}$) calculated using the predictions of Milner et al [13]. The theoretical brush height can be calculated from the degree of polymerisation ($N$), the normalised grafting density ($\sigma = \frac{a^2}{d^2}$), the monomer size ($a = 6.7$ Å for styrene) and the excluded volume parameter ($v$) according to equation 4.10.

$$h = \left(\frac{12}{\pi^2}\right)^{1/3} N(\sigma v)^{1/3} \qquad \textbf{Equation 4.10}$$

In equation 4.10, $v = a^3 w$ where the reduced temperature, $w$, is expressed in terms of the absolute temperature and the theta temperature ($T_\theta$) as $\frac{T - T_\theta}{T}$.

As discussed previously, the exact location of the theta temperature was not known since a mixture of hydrogenous and deuterated cyclohexane was used. However, the theta temperature was known to lie between 303K and 309K and thus a value of 306K has been assumed in the brush height calculations.

| **Sample** | **T (K)** | **$h_{exp}$ (Å)** | **$h_{calc}$ (Å)** | **$h_{calc}$/ $h_{exp}$** |
|---|---|---|---|---|
| Block 1 | 313 | 850 | 1465 | 1.72 |
| Block 1 | 318 | 990 | 1745 | 1.76 |
| Block 1 | 328 | 1240 | 2115 | 1.71 |
| Block 2 | 308 | 715 | 918 | 1.28 |
| Block 2 | 318 | 1060 | 1652 | 1.56 |

**Table 4.8** Comparison of experimental and theoretical (calculated) brush heights in cyclohexane. The experimental brush heights were determined from modified parabolic fits to the neutron reflectivity data.

Equation 4.10 can only be used while the solvent is good, since at the theta temperature the excluded volume parameter becomes zero and the expression becomes invalid. It is clear from table 4.8 that the experimentally obtained brush heights are consistently well below the calculated ones. The most likely reason for this discrepancy is the fact that the grafting densities achieved in the samples block 1 and block 2 were very low ($\sigma = 0.0072$ and 0.0058 respectively). The SCF calculations of Milner et al (from which equation 4.10 was derived) are valid for moderately high grafting densities, and thus it is logical to expect experimentally determined brush heights for samples with very low grafting densities to be somewhat less than those predicted by theory. It is interesting to note the very similar values obtained for $\frac{h_{calc}}{h_{\exp}}$ (table 4.8) for block 1 at the 3 different temperatures in cyclohexane. Plotting $\log_{10}(h_{\exp})$ versus $\log_{10}(w)$ for these 3 values of $h_{\exp}$ thus gave a straight line which was fitted by floating the value of the exponent of $\sigma$ using a least squares algorithm. The result of this fit showed that the experimental brush heights for block 1 in cyclohexane scaled as $\sigma^{0.445}$ and not as $\sigma^{1/3}$ as dictated by equation 4.10. However, whilst it may be true that equation 4.10 overestimates the brush heights when applied to the experimental systems presented in this work, a much fuller investigation would need to be carried out before any firm statements could be made about the scaling behaviour of the brush height. Whilst it would have been advantageous to have been able to explore brushes with a higher surface coverage, the high molecular weights of the polymers used in these studies and the method employed to graft the chains to the substrate meant that it was not possible to achieve grafting densities higher than those obtained for blocks 1 and 2. It is possible that spin casting the films or using chemically reactive end-groups [26] to bond the chains to the substrate surface might have produced higher grafting densities. However, solid/liquid interfacial systems do not readily allow precise control of the grafting density, and the best experimental system for achieving this remains that of spread films at the air/liquid interface [7-8] where the grafting density can be precisely controlled and varied by compression of the film. The primary focus of this area of the work was to provide the basis for subsequent investigations into the effect of solvent shear flow on the structure of the brush layers (chapter 5), and as such the main priority was to

characterise fully the quiescent brush structures for a known grafting density under a variety of solvent conditions.

The volume fraction profiles obtained for both blocks 1 and 2 agree well with the findings of other groups [1-2]. In particular, the results show a very close agreement with the findings of Karim et al [1] who studied polystyrene brushes ($M_w$=105000gmol$^{-1}$) chemically end-grafted to silicon with cyclohexane and toluene as the solvents. They achieved a normalised grafting density of 0.027 and observed almost identical trends in the shapes of the volume fraction profiles with improving solvent quality. It is interesting to note that their observed brush height in cyclohexane at 326.4K (h~550Å) was also considerably less than the ~845Å predicted by SCF theory (equation 4.10).

## 4.5 Glossary of Symbols

| | |
|---|---|
| $a$ | monomer size |
| $A$ | exponential tail parameter for polymer volume fraction profiles |
| $B$ | exponential tail parameter for polymer volume fraction profiles |
| $d$ | average distance between grafting sites |
| $h$ | brush height |
| $h_{calc}$ | calculated brush height |
| $h_{exp}$ | experimentally obtained brush height |
| $M_w$ | weight average molecular weight |
| $N$ | degree of polymerisation |
| $Q$ | momentum transfer |
| $R_g$ | unperturbed radius of gyration |
| $R(Q)$ | reflectivity (reflected intensity as a function of momentum transfer) |
| $T$ | absolute temperature |
| $T_\theta$ | theta temperature |
| $v$ | excluded volume parameter |
| $w$ | reduced temperature |
| $z$ | distance normal to the grafting surface |

$z_d$ depletion layer thickness

$z_e$ z-value at which the polymer volume fraction profile switches to an exponential function

$\alpha$ modified parabolic profile exponent

$\chi^2$ least squares minimisation parameter

$\phi_D$ deuterated solvent volume fraction

$\phi_H$ hydrogenous solvent volume fraction

$\phi_P$ polymer volume fraction

$\phi_S$ surface volume fraction

$\phi_{sol}$ solvent volume fraction

$\lambda$ neutron wavelength

$\theta$ neutron beam incident angle

$\rho_D$ neutron scattering length density of deuterated solvent

$\rho_H$ neutron scattering length density of hydrogenous solvent

$\rho_L$ neuton scattering length density of a layer in the scattering length density profile

$\rho_N$ neutron scattering length density for a mixture of hydrogenous and deuterated solvents

$\rho_P$ neutron scattering length density of the polymer

$\rho_{sol}$ neutron scattering length density of the solvent

$\sigma$ normalised grafting density

$\sigma_r$ interfacial roughness

## 4.6 References

1 Karim, A; Satija, S K; Douglas, J F; Ankner, J F; Fetters, L J. *Physical Review Letters*, 1994, **73**, 3407

2 Liu, Y; Quinn, J; Rafailovich, M H; Sokolov, J. *Macromolecules*, 1995, **28**, 6347

3 Field, J B; Toprakcioglu, C; Ball, R C; Stanley, H B; Dai, L; Barford, W; Penfold, J; Smith, G; Hamilton, W. *Macromolecules*, 1992, **25**, 434

4 Perahia, D; Wiesler, D G; Satija, S K; Fetters, L J; Sinha, S K; Milner, S T. *Physical Review Letters*, 1994, **72**, 100

5 Mansfield, T L; Iyengar, D R; Beaucage, G; McCarthy, T J; Stein, R S. *Macromolecules*, 1995, **28**, 492

6 Levicky, R; Koneripalli, N; Tirrell, M. *Macromolecules*, 1998, **31**, 3731

7 Kent, M S; Lee, L T; Factor, B J; Rondelez, F; Smith, G S. *J. Chem. Phys.* 1995, **103**, 2320

8 Baranowski, R; Whitmore, M D; *J. Chem. Phys.* 1995, **103**, 2343

9 http://www.rl.ac.uk/largescale/surf/surf.htm

10 Bucknall, D G; Langridge, S. '*Crisp Instrument Manual*' (1997). Rutherford Appleton Laboratory.

11 Lovesey, S W. 'Theory of Neutron Scattering from Condensed Matter – Volume 1', 1984, Oxford University Press.

12 Richards, R W (Ed). '*Scattering Methods in Polymer Science*' (1995). Ellis Horwood.

13 Milner, S T; Witten, T A; Cates, M E. *Macromolecules*, 1988, **21**, 2610

14 Milner, S T; Witten, T A; Cates, M E. *Europhysics Letters*, 1988, **5**, 413

15 Penfold, J; Thomas R K. *Journal of Physics-Condensed Matter*, 1990, **2**, 1369

16 Pethrick, R A; Dawkins, J V (Eds). '*Modern Techniques for Polymer Characterisation*' (1999). John Wiley and Sons Ltd.

17 Brandrup, J; Immergut, E H; Grulke, E A (Eds). '*Polymer Handbook - 4th Edition*' (1999). John Wiley and Sons Ltd.

18 Cotton, J P; Decker, D; Benoit, H; Farnoux, B; Higgins, J; Jannink, G; Ober, R; Picot, C; des Cloizeaux, J. *Macromolecules,* 1974, **7**, 863

19 Lai, P Y; Binder, K. *J. Chem. Phys.* 1992, **97**, 586

20 Grest, G S; Murat, M. *Macromolecules*, 1993, **26**, 3108

21 Jones, R A L; Richards, R W. '*Polymers at Surfaces and Interfaces*' (1999). Cambridge University Press.

22 Fleer, G J; Cohen Stuart, M A; Scheutjens, J M H M; Cosgrove, T; Vincent, B. '*Polymers at Interfaces*' (1993). Chapman and Hall.

23 Chakrabarti, A; Toral, R. *Macromolecules*, 1991, **23**, 2016

24 Wijmans, C J; Scheutjens, J M H M; Zhulina, E B. *Macromolecules*, 1992, **25**, 2657

25 Russell, T P. *Materials Science Reports*, 1990, **5**, 171

26 Jones, R A L; Lehnert, R J; Schonherr, H; Vansco, J. *Polymer*, 1999, **40**, 525

# CHAPTER 5

# POLYMER BRUSHES – SHEAR STUDIES

# CHAPTER 5

# POLYMER BRUSHES – SHEAR STUDIES

Having fully characterised the quiescent brush characteristics (chapter 4) for the experimental systems being used, the next step was to investigate the effect of shear on the structure of the brush layers. The brush layers were subjected to shear by flowing the solvent past them in the direction parallel to the grafting surface, and thus the magnitude of the shear rate could be controlled by adjusting the volumetric flow rate. The aim was to collect neutron reflectivity data for brush layers over a range of shear rates and for varying thermodynamic quality of the solvent. Any observed change in the shape of the reflectivity profiles as a result of shear (in comparison with the quiescent profiles) was to be interpreted in terms of a change in the polymer volume fraction profile by model fitting of the data.

## 5.1 Experimental

The SURF reflectometer setup and the experimental procedure for collecting reflectivity data were described in chapter 4, and the procedures used in the acquisition of data when the brush was subject to solvent shear flow were identical. However, because solvent flows through the cell to subject the brush layers to shear, a flow circuit had to be designed and is illustrated schematically in figure 5.1.

A digital gear-pump drive was purchased from Cole-Parmer along with 2 magnetically driven pressure-loaded pump heads allowing precise control of the volumetric flow rate in the ranges 6.3-210 and 163.5-5450ml $min^{-1}$ respectively. The pump system was connected to the inlet and outlet reservoirs of the flow cell using NPT compression fittings and tubing, and special care was taken to ensure that all

parts of the system (e.g. tubing, gaskets, etc) that were exposed to the flowing cyclohexane and toluene solvents had sufficient chemical resistance.

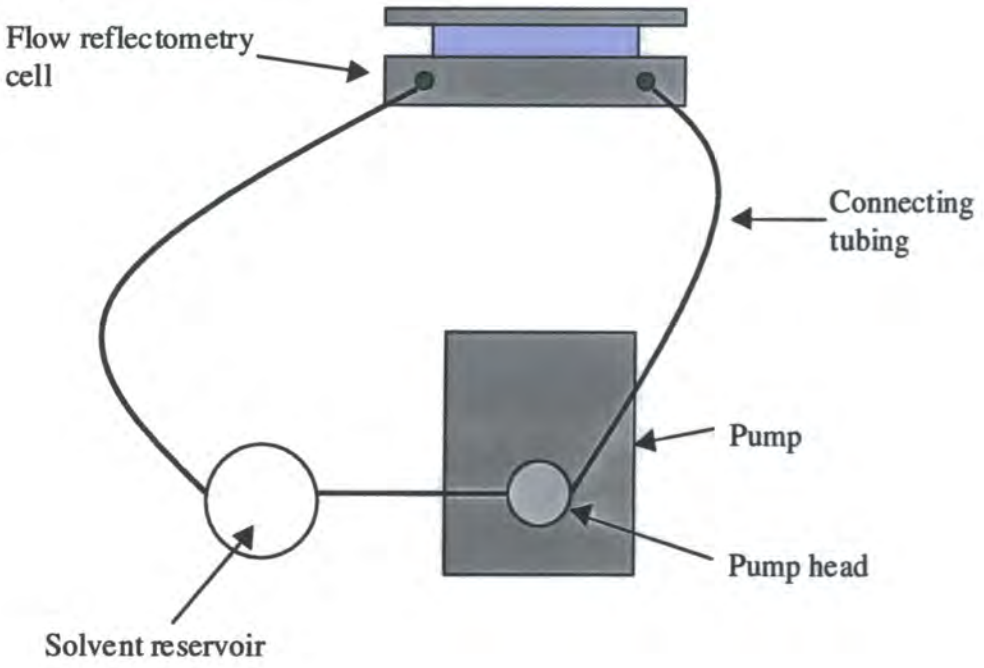


**Figure 5.1** Schematic illustration of the flow circuit used in the shear experiments

It was crucial that air bubbles did not accumulate in the flow cell since these could lead to artefacts in the reflectivity data. The presence of flowing solvent was beneficial in helping to prevent the build-up of air pockets; however, it was also important to provide a means of venting any air from the system, and this was facilitated by incorporating a solvent reservoir into the flow loop. The solvent reservoir consisted of a 100ml glass 3-necked round-bottom flask with ground glass joints. Ground glass screw-thread fittings were connected to 2 of the necks to allow the free ends of the solvent transport tubing to be inserted into the reservoir. The other ends of these tubing sections were connected to the pump uptake and flow cell outlet NPT fittings respectively. Thus when the pump was operational, fluid was drawn out of the solvent reservoir and pumped through the flow cell before draining back into the reservoir. The remaining neck of the reservoir housed a tap fitting which was used to release any pressure build-up within the reservoir vessel due to the increased

vapour pressures of the solvents when working at elevated temperatures. Prior to the start of neutron reflectometry experiments utilising this set-up the reservoir was filled with the required solvent, and the pump was primed with solvent using a syringe to prevent dry running damage to the gears. Enough solvent was introduced to the reservoir at the outset to ensure that it remained approximately half full following redistribution of fluid to the pump, tubing and cell upon commencement of flow.

## 5.2 Data Fitting

The reflectivity data obtained for solvent shear flow were fitted using the modified parabolic function described in chapter 4 (equation 4.4).

## 5.3 Results

Brush samples prepared using the polymers LRH3.52 and TK327 were studied under shear using cyclohexane and toluene as solvents. As with the quiescent experiments, the solvents were contrast matched to the silicon substrate (by mixing the hydrogenous and deuterated forms in the appropriate ratio - see chapter 4 for details) to 'highlight' the deuterated brush chains when a neutron beam was reflected from the system. The actual shear rates used in this work were 'area average shear rates' [1] ($\dot{\gamma}_{AV}$ - see equation 3.1), and the precise magnitude of the shear rate was controlled through the volumetric flow rate using the digital pump-drive.

For each set of experiments, reflectivity data for the quiescent state were collected before and after the application of shear in order that any permanent changes in the reflectivity profiles due to solvent shear flow could be detected.

### 5.3.1 TK327 Polymer

Shear experiments for this brush polymer were carried out alongside the quiescent experiments presented in chapter 4. The same brush sample was used in the shear experiments (block 2), and the quiescent reflectivity profiles shown in figure 4.10 constitute the pre-shear profiles. The system was studied at temperatures of 298, 308

and 318K, with the brush layers being subjected to solvent shear rates of 8000 and 16000$s^{-1}$ at each temperature. Following the acquisition of data at the highest shear rate, post-shear quiescent data were collected before moving on to the next temperature.

Figures 5.2 to 5.4 show the quiescent (pre-shear) reflectivity profiles along with the data collected for solvent shear rates of 8000 and 16000$s^{-1}$ at each temperature. It can be seen clearly that at each temperature the quiescent and shear profiles are virtually superimposable, and this implies strongly that solvent shear had no effect on the structure of the brush layer at any of the temperatures studied for this system.

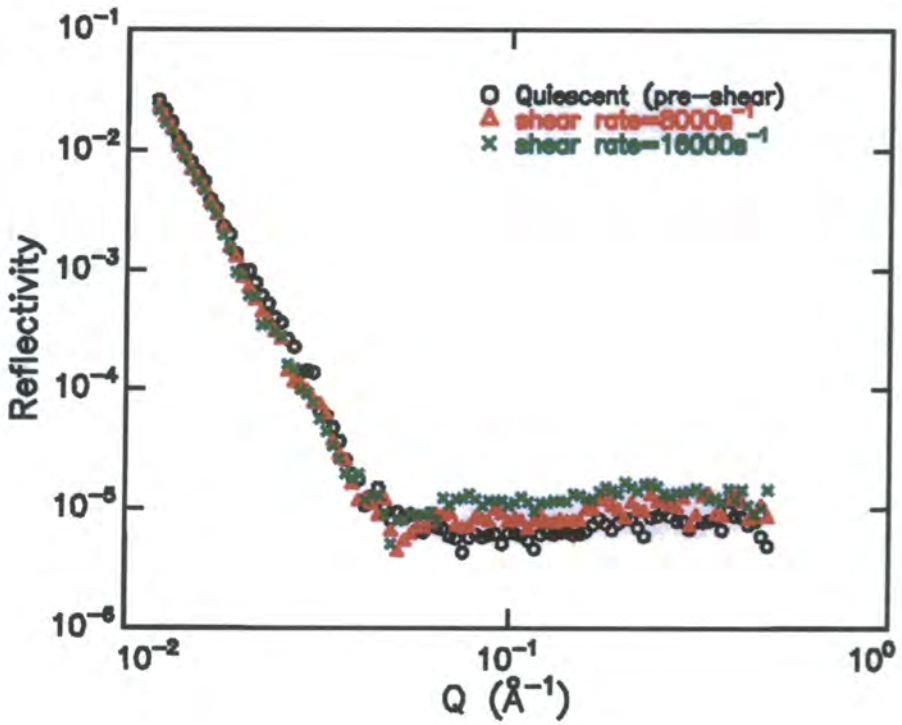


**Figure 5.2** Reflectivity profiles collected for block 2 in cyclohexane at 298K.

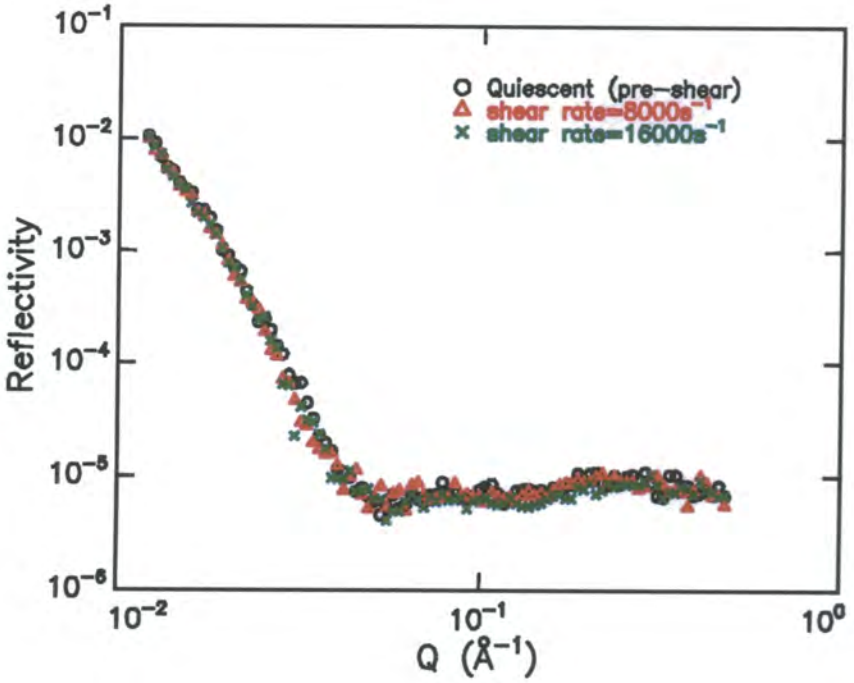


**Figure 5.3** Reflectivity profiles collected for block 2 in cyclohexane at 308K.

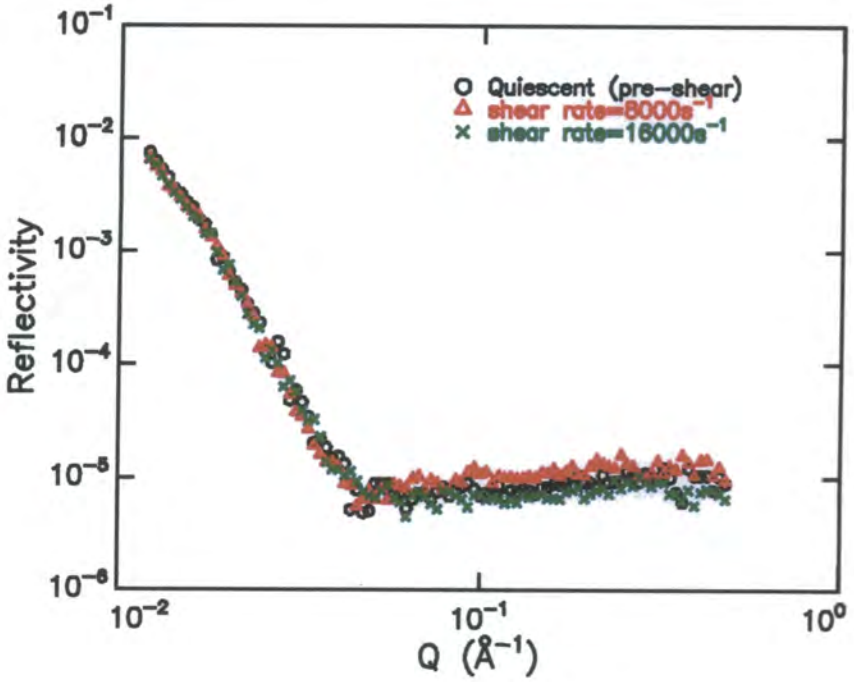


**Figure 5.4** Reflectivity profiles collected for block 2 in cyclohexane at 318K.

Figures 5.5 and 5.6 show reflectivity profiles for the quiescent state collected before and after the application of shear at 298K and 308K. The two profiles at each temperature are superimposable, indicating that little or no desorption had occurred on exposing the brush layer to solvent shear flow. When the dry layer thickness for block 2 was remeasured using ellipsometry subsequent to the neutron experiments, the value was virtually identical to that at the sample preparation stage, thus confirming that no significant desorption had occurred.

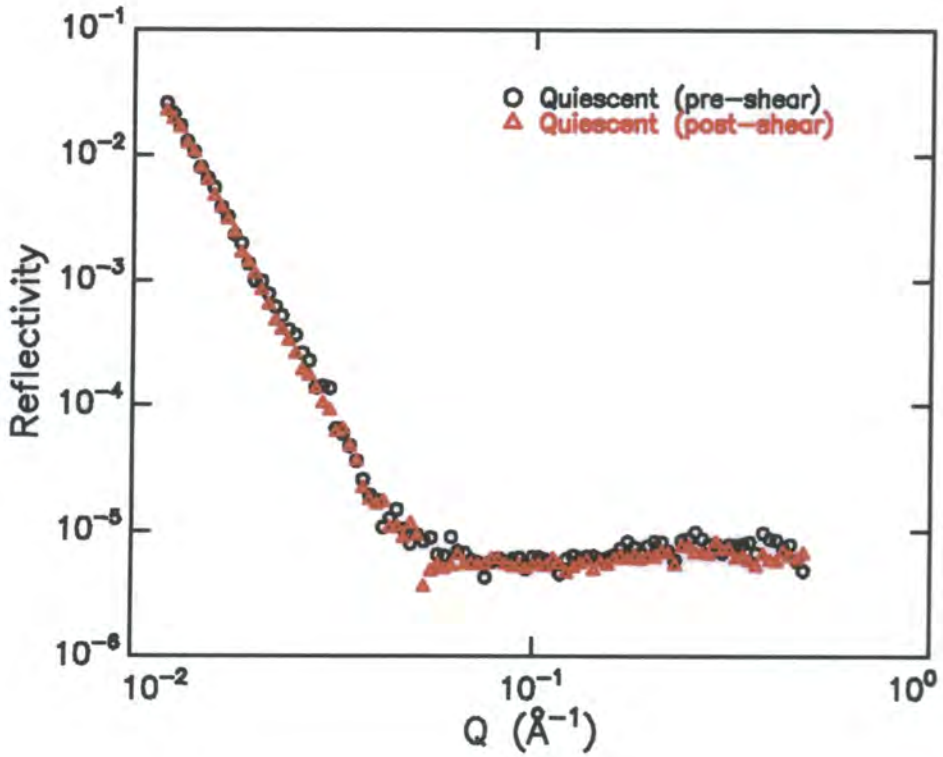


**Figure 5.5** Pre- and post-shear reflectivity profiles for block 2 in cyclohexane at 298K.

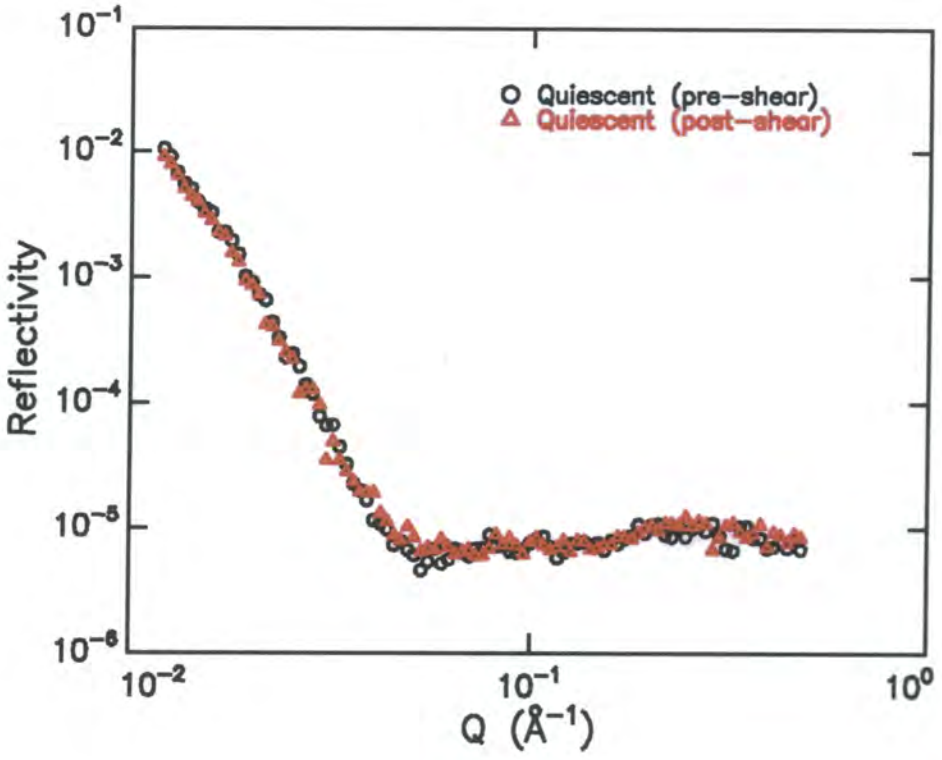


**Figure 5.6** Pre- and post-shear reflectivity profiles for block 2 in cyclohexane at 308K.

The volume fraction profiles obtained from modified parabolic fits to the pre-shear quiescent data at each of the 3 temperatures have already been displayed in figure 4.12 (when the quiescent brush characteristics were discussed in chapter 4). Since no significant changes in the shapes of the reflectivity profiles were observed as a result of shear, it has to be assumed that these volume fraction profiles describe the shape of the brush in the presence of shear also.

### 5.3.2 LRH3.52 Polymer

The quiescent (chapter 4) and shear experiments for this polymer were carried out over a total of three visits to the neutron reflectometer, and thus three separate brush samples were used.

#### 5.3.2.1 Cyclohexane

The brush layer used in these experiments is assigned the code "block 3", and the average dry layer thickness of this sample as measured by ellipsometry was 105Å. This corresponds to an average distance between grafting sites ($d$) of 77Å, thus putting the sample well within the brush regime ($R_g = 186$Å).

Reflectivity data were collected at temperatures of 308 and 328K, with shear rates of 65 000, 120 000 and 145 000$s^{-1}$ being explored at each temperature. The highest shear rate corresponded to a volumetric flow rate of 1200ml $min^{-1}$, and this was actually the highest flow rate achievable with the experimental set-up used. If the flow rate was increased further, the back-pressure within the flow loop became too high and the pump-head and pump-drive became magnetically decoupled.

Figures 5.7 and 5.8 show the reflectivity data obtained under quiescent (pre-shear) conditions along with the data obtained at the 3 different shear rates for temperatures of 308 and 328K respectively. As with the results obtained for TK327, it can be seen that the quiescent and shear profiles at each temperature are virtually superimposable i.e. no significant change is observed in the shapes of the reflectivity profiles as a result of shear.

If the shapes of the reflectivity profiles are not seen to change in response to shear, it can only be assumed (in the absence of other forms of experimental evidence) that the structures of the brush layers remain unchanged as a result of shear over the range of conditions studied.

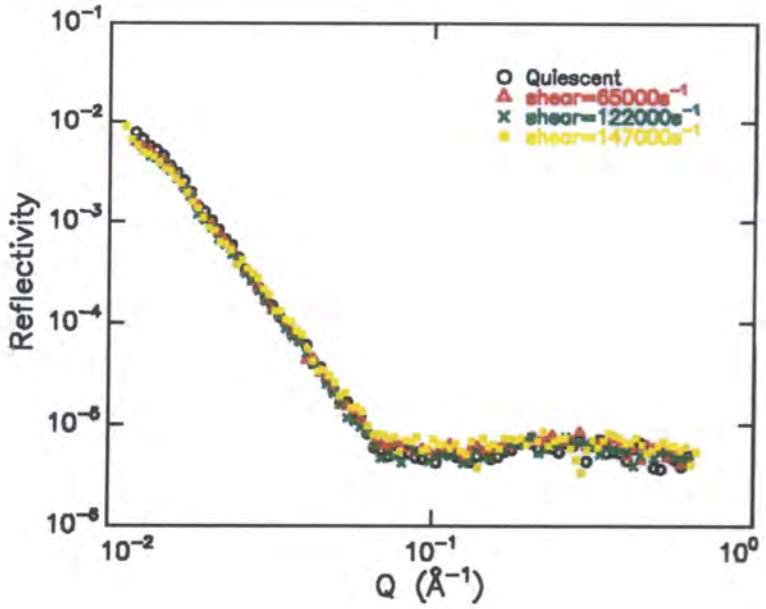


**Figure 5.7** Quiescent (pre-shear) and shear neutron reflectivity data for block 3 in cyclohexane at 308K.

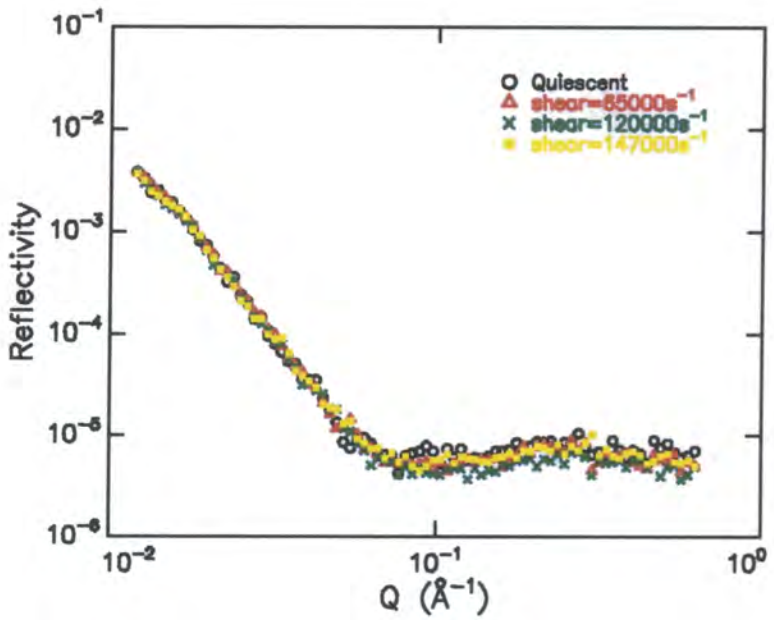


**Figure 5.8** Quiescent (pre-shear) and shear neutron reflectivity data for block 3 in cyclohexane at 328K.

Figure 5.9 compares the reflectivity data obtained in the quiescent state for block 1 (chapter 4) and block 3 at 328K, and it is interesting to note the similarity between the reflectivity profiles for the different samples. Whilst this similarity might be expected, it does help to confirm that the method used to form the brush layers is acceptably reproducible.

The reflectivity data for the quiescent state were fitted using a modified parabolic function (equation 4.4), and the polymer volume fraction profiles obtained from the fits are shown in figure 5.10. Table 5.1 summarises the brush parameters obtained from the fits, and the fits themselves are shown in figure 5.11.

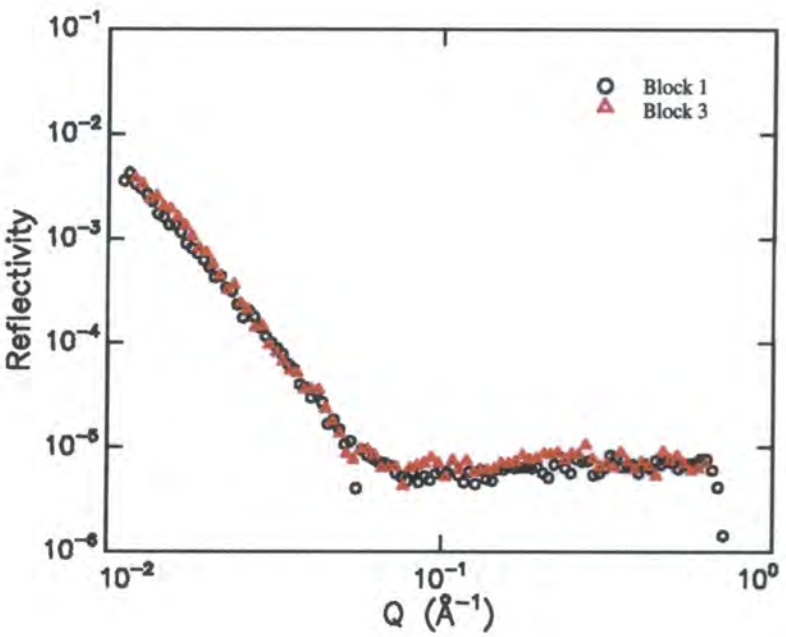


**Figure 5.9** Comparison of quiescent reflectivity profiles obtained for blocks 1 and 3 at 328K in cyclohexane.

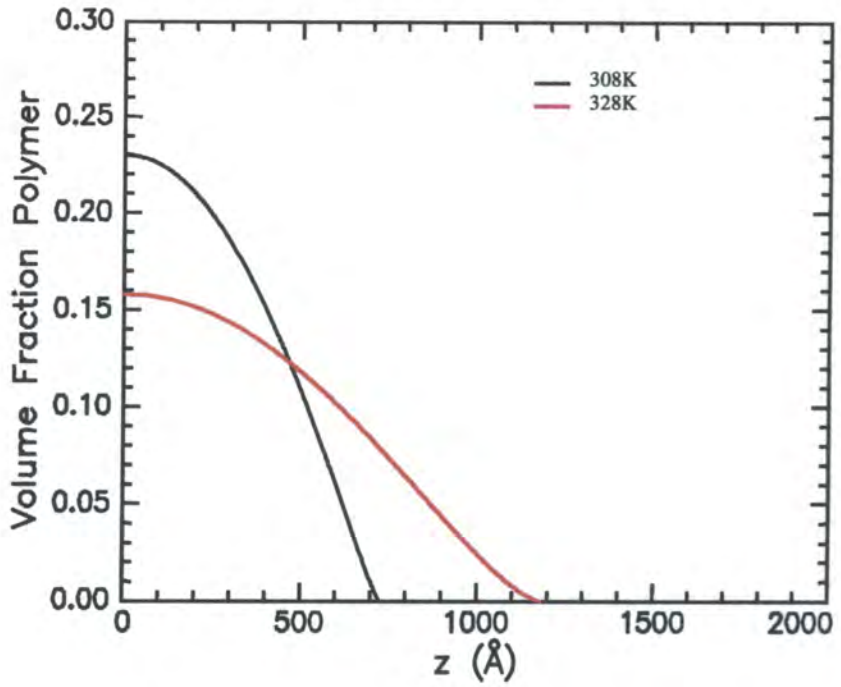


**Figure 5.10** Volume fraction profiles obtained from fits to reflectivity data acquired in the quiescent state for block 3 in cyclohexane at 308K and 328K.

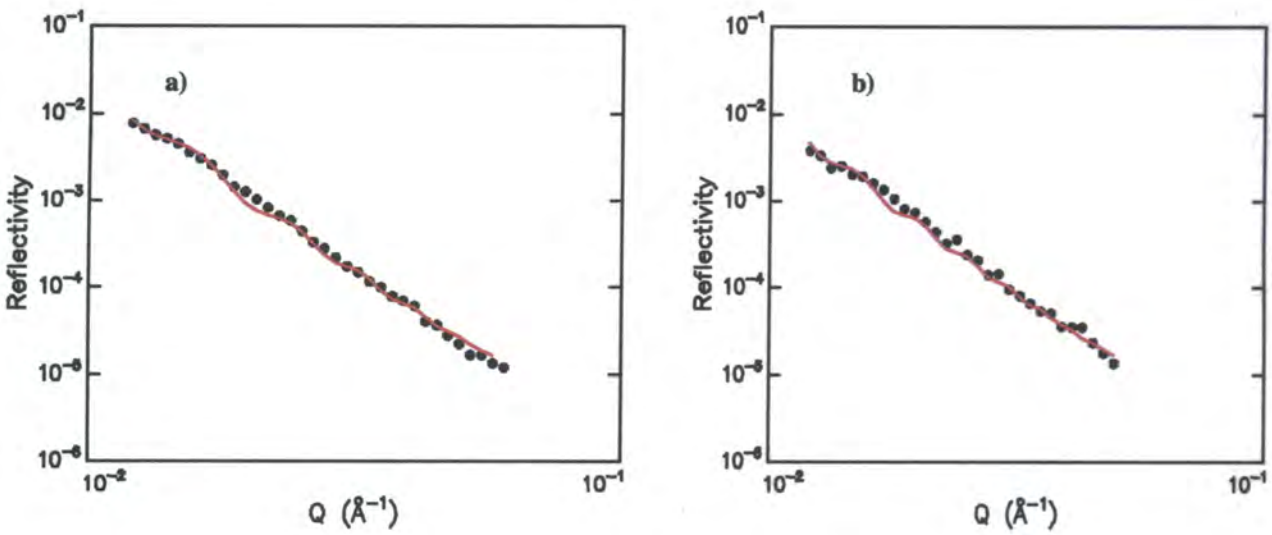


**Figure 5.11** Reflectivity data (acquired in the quiescent state) for block 3 in cyclohexane displayed over the fitted Q-range. Red lines are modified parabolic fits to the data. a) 308K b) 328K.

| T (K) | $\phi_s$ | h (Å) | $\alpha$ | $\sigma_r$ (Å) | $\chi^2$ |
|---|---|---|---|---|---|
| 308 | 0.23 | 725 | 1.17 | 9.7 | 55.4 |
| 328 | 0.158 | 1180 | 1.48 | 5.8 | 60.4 |

**Table 5.1** Parameters obtained from modified parabolic fits to the reflectivity data for block 3 in cyclohexane.

The volume fraction profiles in the quiescent state displayed in figure 5.10 show the same trends observed in the earlier quiescent state studies presented in chapter 4. As the solvent quality improves on increasing the temperature from 308K to 328K in cyclohexane, the brush height increases and the surface volume fraction decreases as the chains stretch away from the grafting surface. The good agreement observed between the reflectivity profiles obtained for blocks 1 and 3 in cyclohexane at 328K (figure 5.9) is reflected in the similarity of the volume fraction profiles obtained from fits to the data. Integrating under the volume fraction curves of figure 5.10 yields values for the polymer adsorbed amount of 11.90 and 12.36mgm$^{-2}$ at 308K and 328K respectively. As well as agreeing well with each other, these values also show good agreement with the adsorbed amount calculated from the dry layer thickness (11.8mgm$^{-2}$).

Since no significant changes were observed in the reflectivity profiles in the presence of solvent shear flow, it has to be assumed that the quiescent volume fraction profiles shown in figure 5.10 describe equally well the sheared brush structures.

Figure 5.12 shows reflectivity data for the quiescent state collected before and after the application of shear at 328K. The fact that the 2 profiles are virtually identical indicates that no significant desorption occurred during the course of the experiments, and this was confirmed when the dry layer thickness measured using ellipsometry subsequent to the neutron experiments was found to be virtually unchanged.

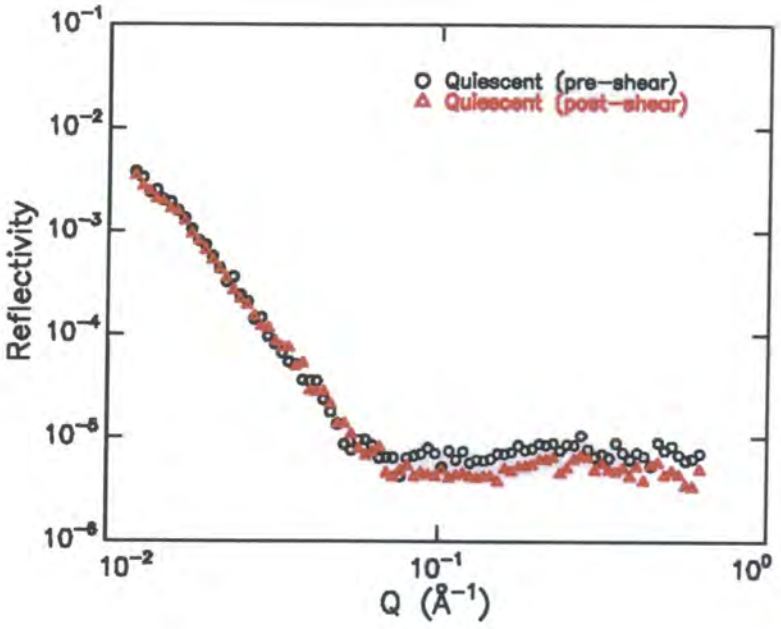


**Figure 5.12** Pre- and post-shear reflectivity profiles obtained in the quiescent state for block 3 in cyclohexane at 328K.

5.3.2.2 Toluene

The brush layer used in the toluene shear experiments is assigned the code "block 4". The average dry layer thickness for this sample measured using ellipsometry was 98Å corresponding to a distance between grafting sites ($d$) of 80Å. Due to problems with the neutron beam it was only possible to collect data for one shear rate ($\dot{\gamma}_{AV}$=122 000s$^{-1}$) along with the pre- and post-shear quiescent state data sets. Figure 5.13 shows the three reflectivity profiles obtained. Whilst the shear and post-shear quiescent state profiles are virtually identical, the reflectivity for the pre-shear quiescent experiment is slightly higher. It is tempting to state that this phenomenon represents a change in the brush structure as a result of shear, but it is far more likely that it actually arises due to chain desorption.

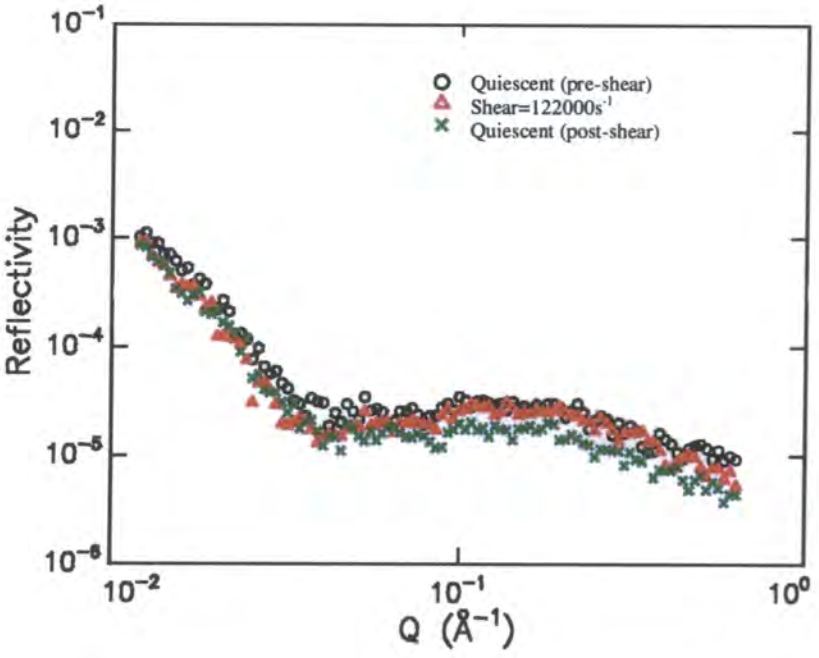


**Figure 5.13** Quiescent (pre- and post-shear) and shear state ($\dot{\gamma}_{AV}$=122000s$^{-1}$) neutron reflectivity profiles for block 4 in toluene at 298K.

The decrease in reflectivity between the pre-shear quiescent and shear state reflectivity profiles is indeed consistent with an increase in the brush height arising from the shear-induced stretching of the brush chains. However, the fact that the shape of the reflectivity profile remains virtually identical when the shear is switched off then implies that the brush layer retains its shear induced structure upon reverting back to quiescent conditions, and this seems unrealistic.

Evidence that the observed trends in the reflectivity profiles arose from chain desorption was obtained from modified parabolic fits to the data. Figure 5.14 shows the polymer volume fraction profiles obtained from fits to the pre-and post-shear reflectivity data (the fit to the post-shear data applies equally well to the shear data since the 2 data sets are virtually identical over the fitted Q-range), and values for the parameters describing these fits are given in table 5.2.

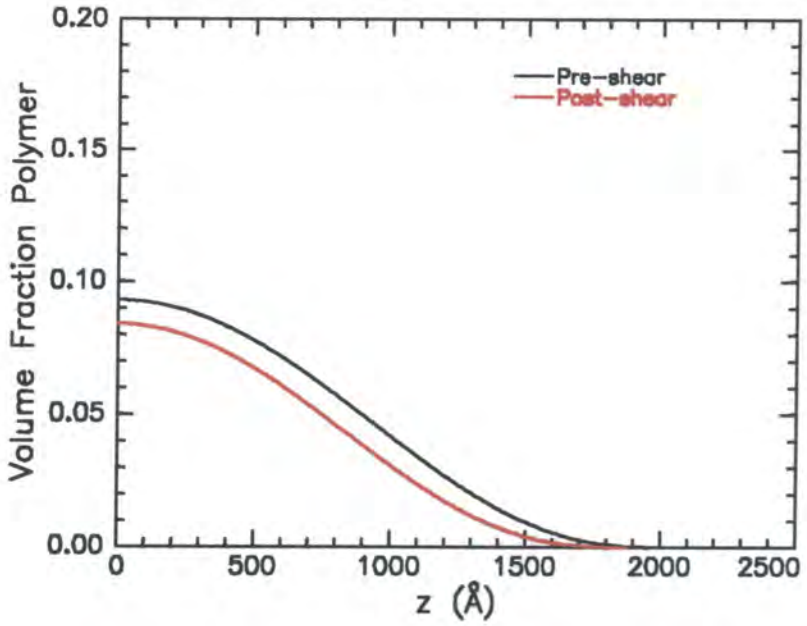


**Figure 5.14** Polymer volume fraction profiles obtained from modified parabolic fits to the pre- and post-shear quiescent state neutron reflectivity data acquired for block 4 in toluene at 298K.

| Data Set | $\phi_s$ | h (Å) | $\alpha$ | $\sigma_r$ (Å) | $\chi^2$ |
|---|---|---|---|---|---|
| Pre-shear | 0.093 | 2000 | 2.77 | 9.2 | 2.6 |
| Post-shear | 0.084 | 1650 | 2.98 | 5.3 | 3.0 |

**Table 5.2** Parameters obtained from modified parabolic fits to the pre- and post-shear quiescent state reflectivity data for block 4 in toluene at 298K.

Integrating under the volume fraction curves shown in figure 5.14 gave values of 9.82 and 7.13mgm$^{-2}$ for the adsorbed amount of polymer (pre- and post-shear respectively). The value obtained from the dry layer thickness as measured by ellipsometry was 11.0mgm$^{-2}$. This indicates that desorption occurred upon exposure of the brush layer to toluene during the pre-shear quiescent experiment. More significant desorption occurred during the subsequent shear experiment. Following the neutron experiments, the dry layer thickness of block 4 was remeasured using ellipsometry. The thickness was found to have decreased to 61Å ($d = 101$ Å), corresponding to a polymer

adsorbed amount of 6.83mgm$^{-2}$. Such desorption was also observed during the quiescent experiments on block 1 (chapter 4) when the adsorbed amount of polymer (determined from dry layer ellipsometry measurements) decreased from 11.40 to 6.27mgm$^{-2}$ as a result of exposing the brush layer to shear when purging air bubbles from the cell. It is also interesting to note in figure 5.15 the very similar shapes of the reflectivity profiles obtained for blocks 1 (quiescent – see chapter 4) and 4 (post-shear quiescent).

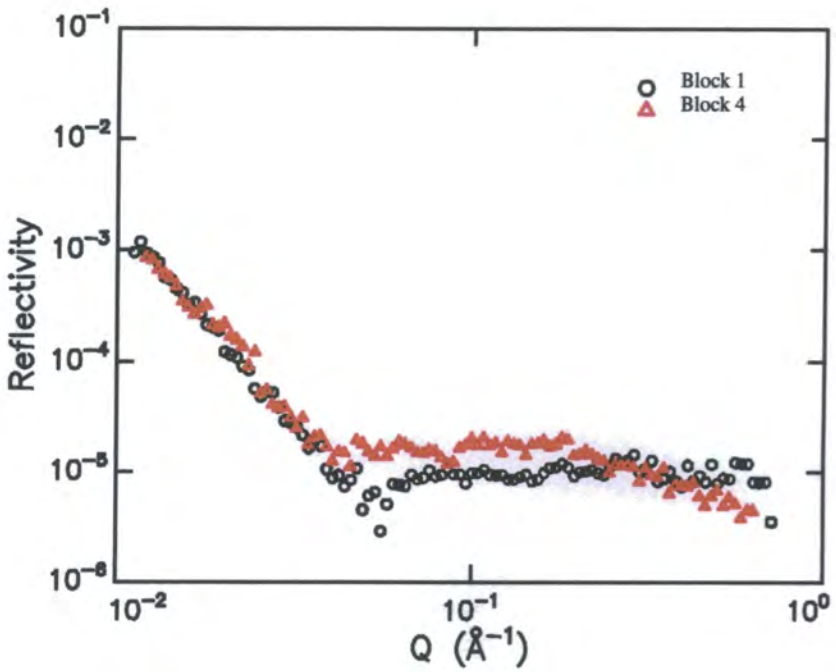


**Figure 5.15** Comparison of quiescent neutron reflectivity profiles obtained for block 1 (see chapter 4) and block 4 (post-shear quiescent) in toluene at 298K.

The actual modified parabolic fits to the pre- and post-shear quiescent data obtained for block 4 are shown in figure 5.16.

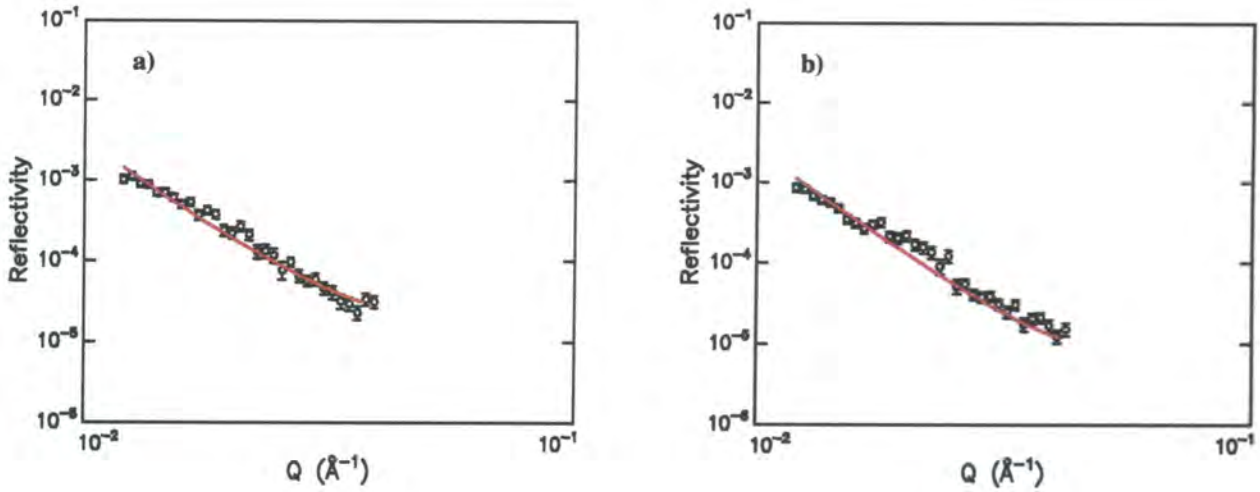


**Figure 5.16** Quiescent state neutron reflectivity data for block 4 in toluene at 298K displayed over the fitted Q-range. Red lines are modified parabolic fits to the data. a) Pre-shear b) Post-shear.

## 5.4 Discussion

The results presented above show clearly that solvent shear flow has no effect on the shapes of the neutron reflectivity profiles obtained for polymer brush layers under various conditions of solvent quality. However, it would be unwise at this juncture merely to conclude that the structures of the brush layers are unaffected by shear without first considering some of the pertinent experimental and theoretical factors.

### 5.4.1 Shear Rate Threshold

The work presented here was primarily designed to test the theoretical predictions of Harden and Cates and co-workers [2-3]. They initially considered an Alexander-de Gennes-type brush [4-5] and predicted that solvent shear flow would lead to a swelling of the brush (characterised by an increase in the brush height, $h$) for shear rates exceeding the reciprocal of the Zimm relaxation time [2] of the brush chains (equation 5.1a).

$$\dot{\gamma} > \frac{k_B T}{\eta d^3}$$ **Equation 5.1a**

In equation 5.1, $\eta$ is the solvent viscosity while all other symbols have their usual meanings. However, in a later paper [3] they took the first steps towards modelling the effects of shear flow for Milner, Witten and Cates [6] type parabolic brushes by partially relaxing the Alexander-de Gennes ansatz that all chains behave alike. In this paper they predict that the onset of shear induced brush swelling occurs at quantitatively lower shear rates than for step-function brushes (equation 5.1b).

$$\dot{\gamma} > 0.23\frac{k_B T}{\eta d^3}$$ **Equation 5.1b**

One of the problems associated with these studies concerns the definition of the shear rate. In this work, the area average shear rate ($\dot{\gamma}_{AV}$, equal to half the maximum shear rate between the upper and lower surfaces of the flow channel) has been used as a measure of the strength of the shear flow. However, the important factor with regard to equation 5.1 is the shear rate within the brush itself, and this is much more difficult to estimate [7].

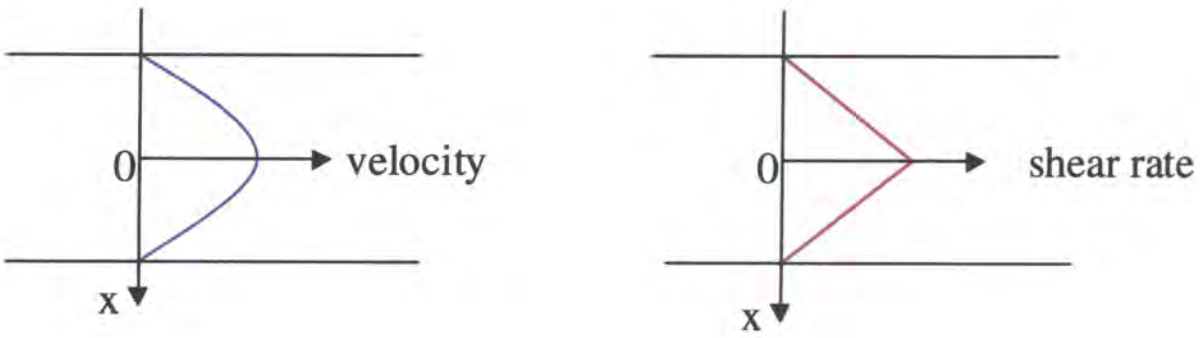


**Figure 5.17** Velocity and shear rate profiles for flow between 2 parallel plates as a function of position between the plates (x).

The velocity and shear rate profiles in the absence of a brush layer are illustrated schematically in figure 5.17, and it would obviously be a simple task to calculate the shear rate at any point in the flow channel for this case. However, the presence of an adsorbed brush layer would lead to quantitative differences in the flow velocity and shear rate profiles in the region near the grafting surface. Other groups have analysed the penetration of steady shear flows into parabolic brushes [8-9] and determined the theoretical fluid velocity profiles within the brush layers. They found that the penetration of the shear flow into the brush was quite small compared to the overall brush height. However, direct comparison of these theories with the experimental work presented here is difficult for various reasons, one being that the experimentally determined quiescent brush profiles are not purely parabolic.

With these problems in mind, and regardless of how the shear rate is defined, the best policy for studying shear induced brush swelling by neutron reflectometry in accordance with equation 5.1 is to subject the brush layers to the highest shear rates possible in the hope of seeing some change in the neutron reflectivity profiles. If and when a change is observed, quantitative comparisons with theory can start to be made. Table 5.3 compares values of the reciprocal Zimm relaxation time (calculated using $d$ values for the samples used in the shear studies) with the maximum area average shear rates used in the experiments reported above.

| **Sample** | **Solvent** | **T (K)** | **η (mPa s)** | **d (Å)** | $\dot{\gamma}_{AV}$ **(s$^{-1}$)** | $\frac{k_B T}{\eta d^3}$ |
|---|---|---|---|---|---|---|
| Block2 | Cyclohexane | 298 | 0.894 | 88 | 16 000 | $6.75\times10^{6}$ |
| Block2 | Cyclohexane | 323 | 0.615 | 88 | 16 000 | $1.06\times10^{7}$ |
| Block3 | Cyclohexane | 298 | 0.894 | 77 | 147 000 | $1.01\times10^{7}$ |
| Block3 | Cyclohexane | 323 | 0.615 | 77 | 147 000 | $1.59\times10^{7}$ |
| Block4 | Toluene | 298 | 0.560 | 101 | 122 000 | $7.13\times10^{6}$ |

**Table 5.3** Comparison of the highest area average shear rates used in the neutron reflectometry experiments with the reciprocal Zimm relaxation times calculated using the brush sample $d$ values. The latter values are calculated using literature values for the solvent viscosities [10] (cyclohexane at 298K and 323K, toluene at 298K).

Although viscosity data for cyclohexane at the experimental temperatures of 308K and 328K could not be found, it is very clear from the data in table 5.3 that the area average shear rates achieved in the experiments were at least 1 order of magnitude below the threshold shear rates predicted by equations 5.1a and 5.1b. Since the actual shear rates within the brush layers themselves would have been quantitatively lower than the area average shear rates, it is clear that the experiments carried out fell well short of the swelling threshold shear rates predicted by Harden and Cates. This in itself provides an explanation for the fact that no change was observed in the reflectivity profiles as a result of shear. However, it was not possible to explore shear rates higher than $147000s^{-1}$ with the experimental set-up used in this work since doing so led to magnetic decoupling of the pump. One way of getting closer to the threshold shear rate would be to reduce the value of the reciprocal Zimm relaxation time, and this could be achieved by using higher molecular weight polymers (since this would lead to an increase in the distance between grafting sites, $d$ ).

It is interesting to note that shear induced desorption of the brush chains occurred during the toluene experiments reported here, since Harden et al predict that a strong increase in desorption occurs at the swelling transition [3] given by equation 5.1b. The fact that the chains desorbed in the presence of shear (no desorption occurred when the brush layers were simply immersed in toluene for relatively long periods of time) indicated that the drag force exerted on the brush chains by the flowing solvent was strong enough to disrupt the hydrogen bonding that attached the chains to the substrate surface. However, the desorption observed in the experimental work presented here occurred over a time scale of a few minutes, and since the time required to collect statistically adequate neutron reflectivity data for these systems was approximately 3-4 hours it is clear that even if the desorption was preceded by chain stretching, the process could not be observed using neutron reflection.

### 5.4.2 Sensitivity of Neutron Reflectometry

Another possible explanation for the fact that no effect of shear was observed in the neutron reflectometry experiments concerns the sensitivity of the neutron reflection technique.

The susceptibility of the polymer brush to shear induced stretching is greater for brushes that are more strongly stretched in the quiescent state. This is due to the fact that the solvent flow is less screened for more strongly stretched brushes and is thus able to penetrate further into the brush. However, it can be seen from the quiescent polymer volume fraction profiles obtained in cyclohexane at 328K and toluene at 298K (figures 4.7, 4.9, 5.10 and 5.14) that polymer volume fractions near the tips of these brushes (where the shear flow will have most effect) are less than 0.02. Furthermore, the high $z$ regions of these profiles show an exponential-like decay in polymer volume fraction (i.e. the polymer volume fraction varies more slowly with respect to increasing distance from the grafting surface at the tips of the brushes than it does in the body of the profiles). The sensitivity of neutron reflectometry to changes in the volume fraction profile is poor when these changes occur in regions of very low polymer volume fraction. Additionally, neutron reflectometry is not very sensitive in detecting slowly varying composition profiles.

Thus it would appear that neutron reflectometry may well not be sufficiently sensitive to shear induced changes in the volume fraction profiles in the regions where these changes are likely to be most pronounced. Figure 5.18 illustrates this problem by showing the simulated neutron reflectivity for two subtly different polymer volume fraction profiles. The areas under the two volume fraction profiles are approximately equal, but one has a slightly higher brush height than the other. However, the reflectivity curves calculated for the two profiles are virtually identical thus highlighting the lack of sensitivity to subtle changes in the volume fraction profiles. Figure 5.18b shows similar pairs of volume fraction profiles along with the simulated reflectivities. However, in this case the difference between the two volume fraction profiles within each pair is more pronounced than for figure 5.18a, and a slight difference can be observed in the resulting reflectivity profiles. However, even for these more significant changes in the volume fraction profiles, the corresponding changes in the reflectivity profiles are very small. Figure 5.18b thus gives some indication of the magnitude of change required in the volume fraction profile for this change to be detectable by neutron reflectometry.

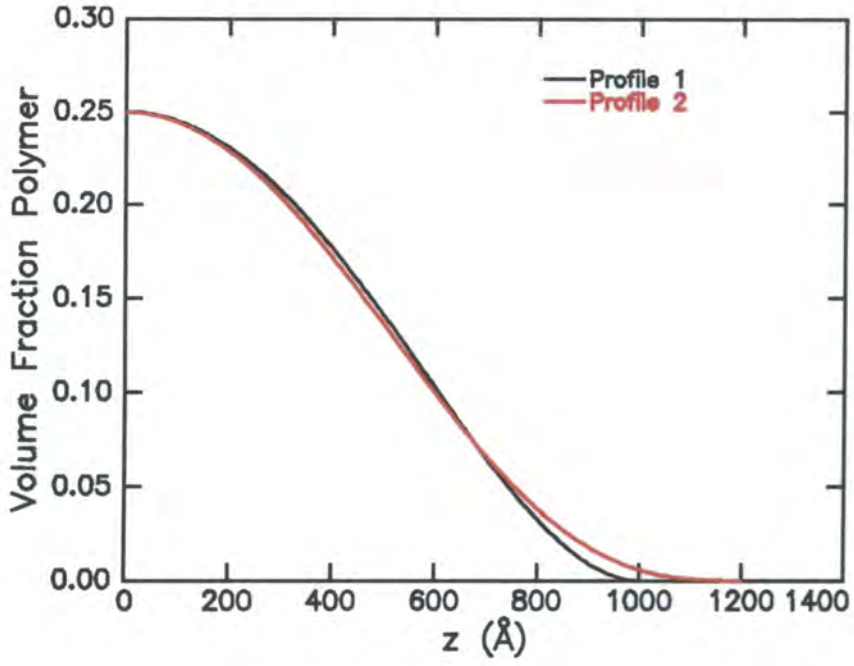


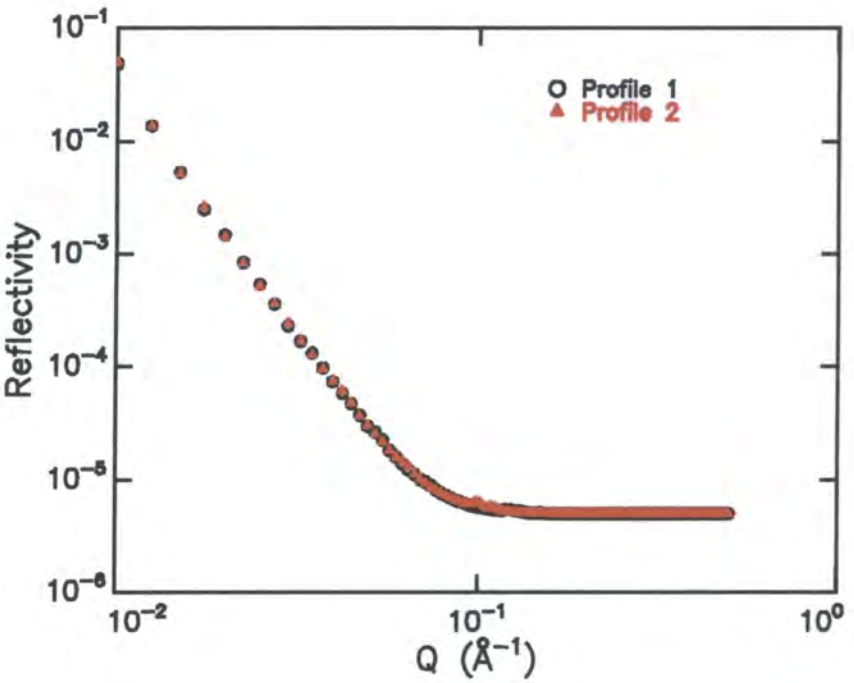


**Figure 5.18a** Simulated neutron reflectivity profiles (b) for 2 subtly different polymer volume fraction profiles (a) illustrating the lack of sensitivity of neutron reflectometry towards minor changes in the shape of the volume fraction profile.

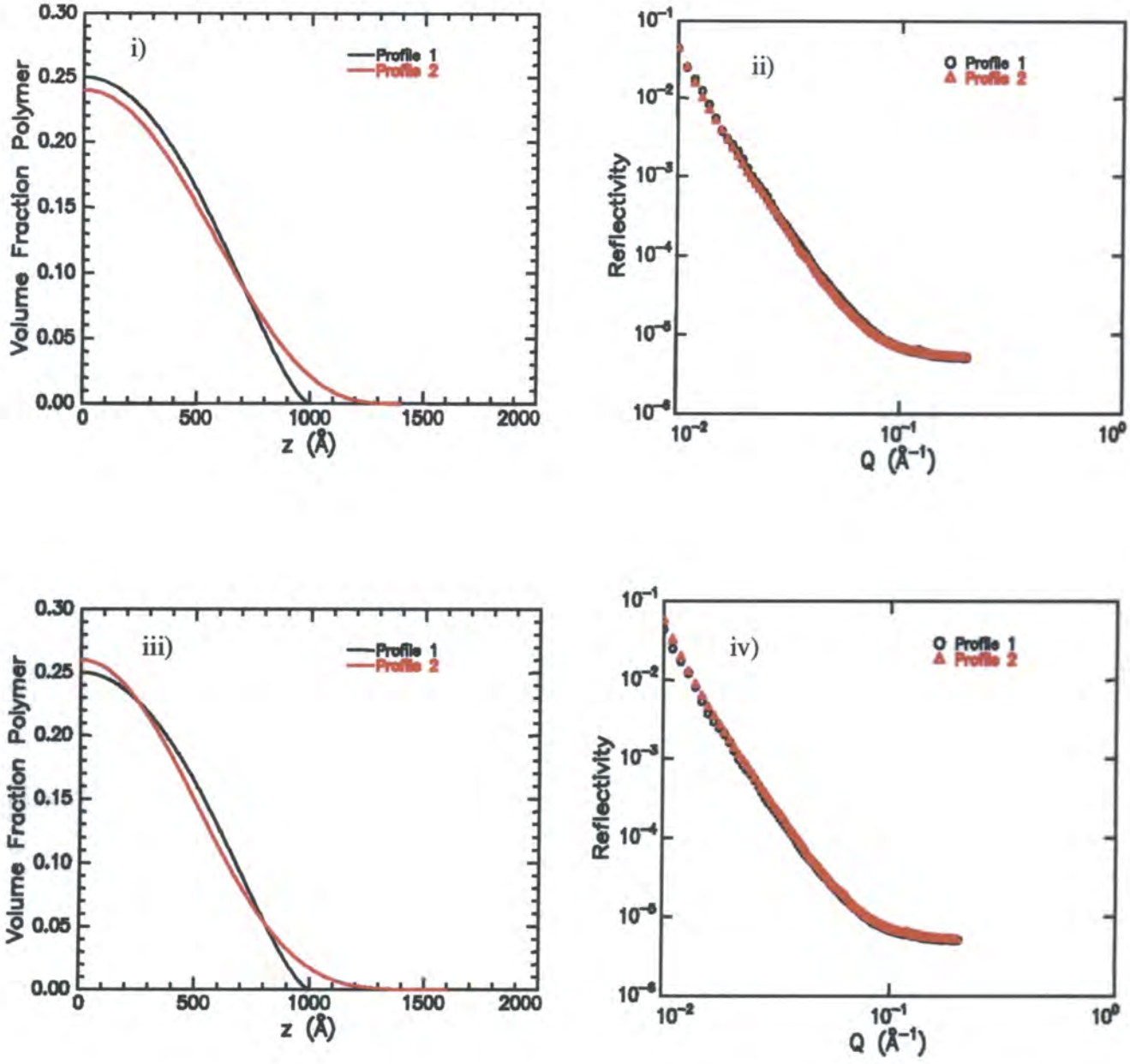


**Figure 5.18b** Simulated reflectivity profiles for two pairs of subtly different polymer volume fraction profiles. The reflectivity profiles shown in ii) and iv) correspond to the volume fraction profiles in i) and iii) respectively. (The colours in the volume fraction profiles correspond to those in the reflectivity profiles.)

### 5.4.3 Chain Tilting Versus Stretching

Miao et al [11] performed simulations of polymer brushes exposed to solvent shear flow using a Monte-Carlo algorithm and found that the shear flow caused the chains to tilt and stretch along the flow direction. However, they also predicted that shear had no significant effect on the local monomer densities or the brush height.
It seems logical the hydrodynamic drag force exerted on the brush chains by the flowing solvent would lead to chain tilting and stretching. It is also conceivable that the stretching and tilting processes might partially or fully negate each other in terms of the overall effect on local monomer densities within the brush.

What follows in this section is a simple argument based on thermodynamic and geometrical principles that leads to an expression for the condition under which chain tilting and stretching exactly balance one another in terms of the overall effect on localised monomer density.

The chain stretching and tilting processes are considered separately and are illustrated schematically in figures 5.19 and 5.20.

#### 5.4.3.1 Chain Stretching

A 3 layer system lying within the region of the brush affected most strongly by the solvent shear flow (i.e. in the tip of the brush) is considered. The layers have equal width ($2R$) with layer 1 being furthest from the grafting surface. The number of monomer units contained within spheres of radius $R$ (volume, $V = \frac{4}{3}\pi R^3$) before stretching are labelled $n_1, n_2$ and $n_3$ for the spheres in layers 1, 2 and 3 respectively. Similarly, the numbers of monomers contained within the spheres after stretching are labelled $n_1', n_2'$ and $n_3'$. Since the polymer volume fraction decreases with increasing distance from the grafting surface, $n_3 > n_2 > n_1$ and $n_3' > n_2' > n_1'$

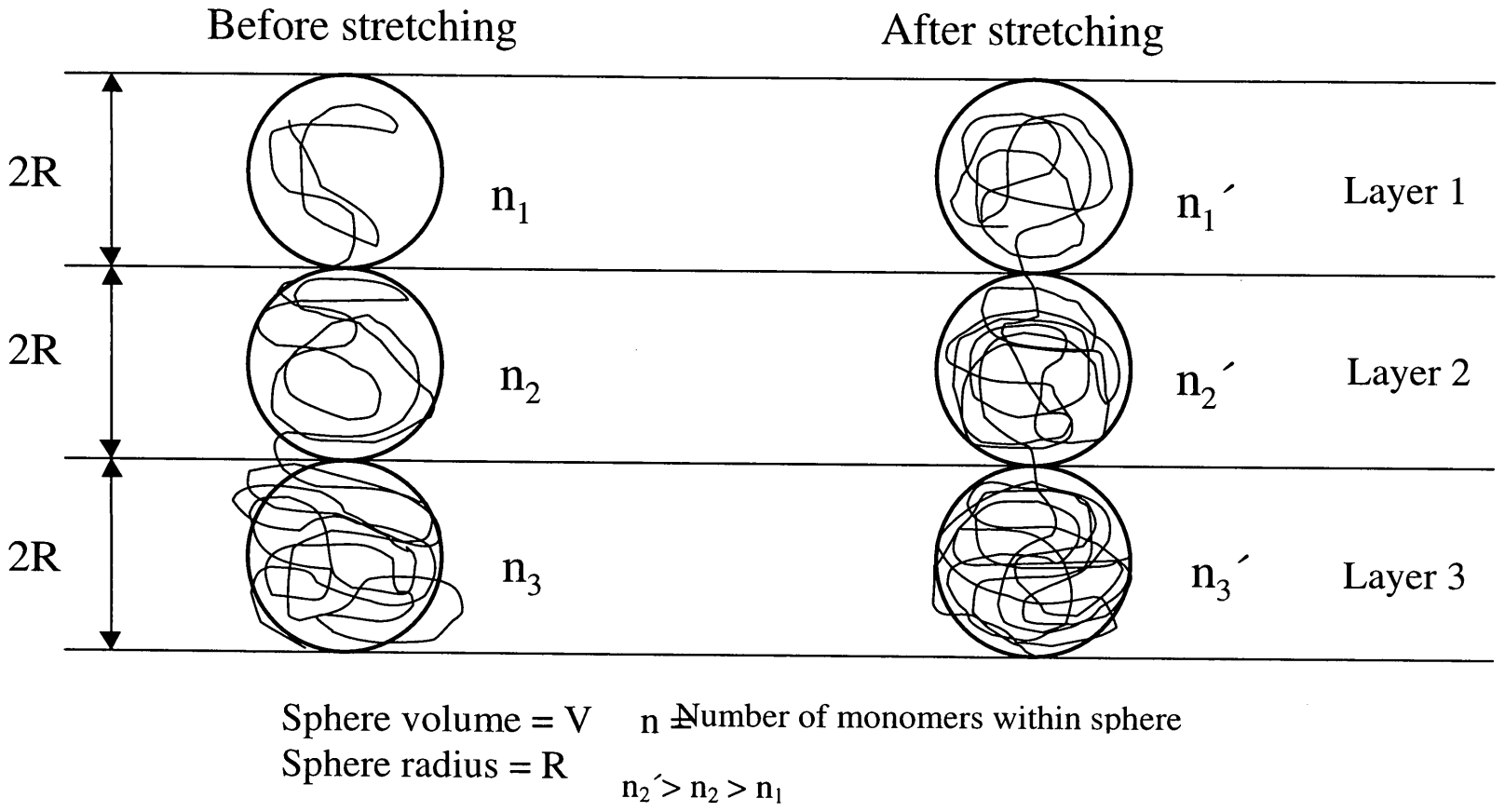


**Figure 5.19** Schematic illustration of chain stretching.

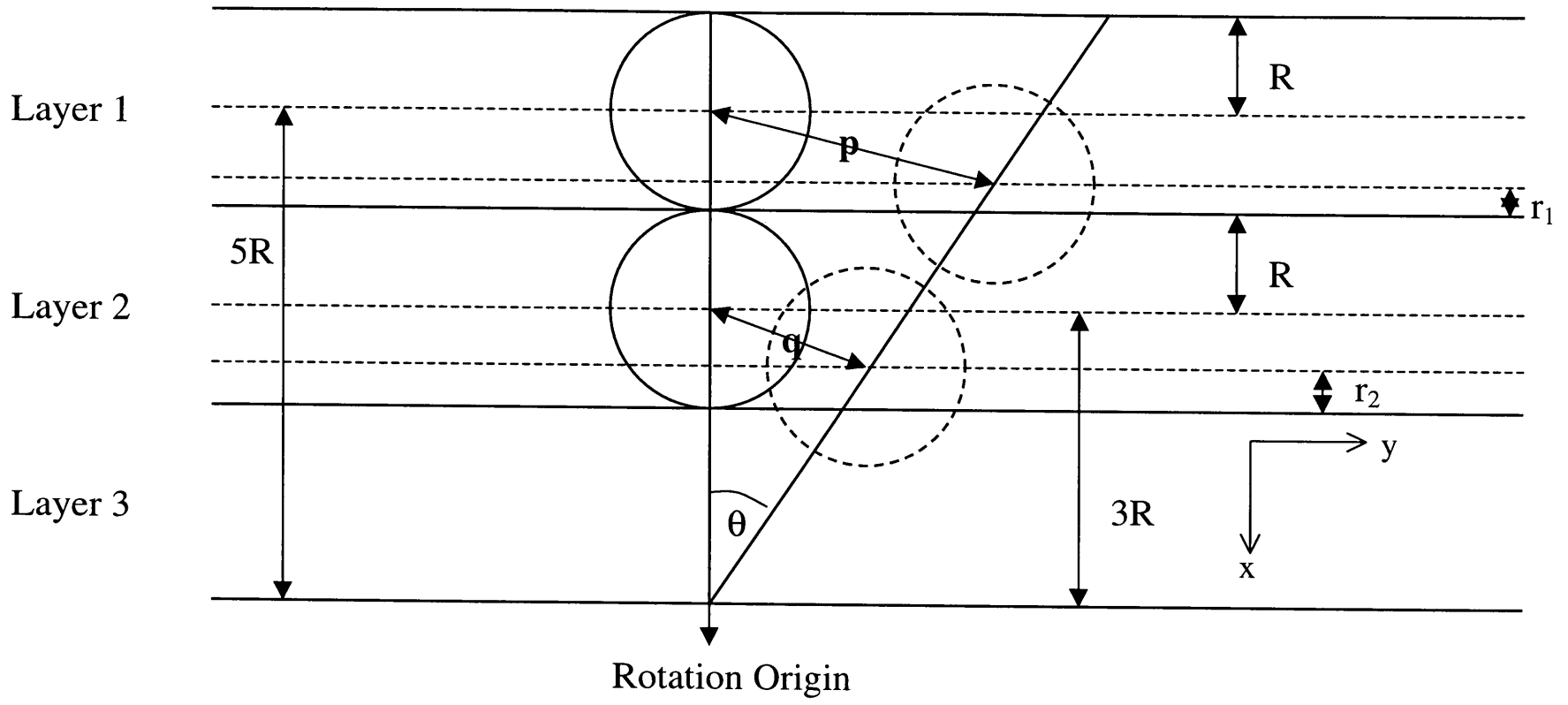


Horizontal dashed lines pass through centres of 4 spheres (dashed spheres represent tilting).

Sphere radii = R. Interlayer spacings = 2R. $r_2 > r_1$

**Figure 5.20** Schematic illustration of chain tilting

Now let us consider the change that occurs in the monomer number density within the layer 2 sphere upon shear induced chain stretching. Chain stretching will lead to the gain of monomer units from the layer 3 sphere and the loss of monomer units to the layer 1 sphere. However, since the chain segments within the layer 3 sphere are on average less stretched than those within the layer 2 sphere (since $n_3 > n_2$), it is assumed that sphere 2 will gain more monomer units from sphere 3 than it loses to sphere 2 (the entropic barrier to further stretching of the sphere 3 segments is lower since they are less stretched initially), and thus there is a net gain in monomer number density within the layer 2 sphere as a result of chain stretching. The polymer volume fractions within sphere 2 before and after stretching ($\phi_{p2}$ and $\phi_{p2}^{'}$ respectively) can thus be defined in terms of the monomer number densities ($n_2$ and $n_2^{'}$), the sphere volume ($V$) and the monomer unit mass ($m$) and density ($\rho$) as:

$$\phi_{p2} = \frac{n_2 m}{\rho V} \qquad \textbf{Equation 5.2}$$

$$\phi_{p2}^{'} = \frac{n_2^{'} m}{\rho V} \qquad \textbf{Equation 5.3}$$

where $n_2^{'} > n_2$ and $V = \frac{4}{3}\pi R^3$.

Thus, the volume fraction gain in sphere 2 due to chain stretching is given by:

$$\Delta\phi_{p2}(stretch) = \frac{3m(n_2^{'} - n_2)}{4\rho\pi R^3} \qquad \textbf{Equation 5.4}$$

5.4.3.2 Chain Tilting

Now let us consider the effect of chain tilting on the polymer volume fraction within layer 2. It can be seen from figure 5.20 that tilting the chains by an angle $\theta$ causes a

section of the layer 2 sphere to enter layer 3 ($V_{2\to3}$, polymer loss) and a section of the layer 1 sphere to enter layer 2 ($V_{1\to2}$, polymer gain).

It is important to be clear on the interpretation of the theory at this juncture. The chain stretching process was previously defined as leading to an increase in the polymer volume fraction within layer 2. Therefore, if the stretching and tilting processes are to have a mutually negating effect (i.e. no net change in the layer 2 polymer volume fraction occurs) then the tilting process must lead to a polymer volume fraction loss within layer 2. (Note that the theory would still hold if stretching led to a loss and tilting to a gain in polymer volume fraction within layer 2.) $V_{1\to2}$ and $V_{2\to3}$ are defined in equations 5.5 and 5.6.

$$V_{1\to2} = \int_{r_1}^{R} \pi(R^2 - x^2)dx = \pi\left[\frac{2R^3}{3} - R^2 r_1 + \frac{r_1^3}{3}\right] \qquad \textbf{Equation 5.5}$$

$$V_{2\to3} = \int_{r_2}^{R} \pi(R^2 - x^2)dx = \pi\left[\frac{2R^3}{3} - R^2 r_2 + \frac{r_2^3}{3}\right] \qquad \textbf{Equation 5.6}$$

Referring to figure 5.20, and using trigonometry:

$$p = 10R\sin\left(\frac{\theta}{2}\right) \qquad \textbf{Equation 5.7}$$

$$q = 6R\sin\left(\frac{\theta}{2}\right) \qquad \textbf{Equation 5.8}$$

Also:

$$\frac{R - r_1}{p} = \sin\left(\frac{\theta}{2}\right) \qquad \textbf{Equation 5.9}$$

$$\frac{R - r_2}{q} = \sin\left(\frac{\theta}{2}\right) \qquad \textbf{Equation 5.10}$$

Thus, substituting equations 5.7 and 5.8 into equations 5.9 and 5.10 gives:

$$r_1 = R - 10R\sin^2\left(\frac{\theta}{2}\right) \qquad \textbf{Equation 5.11}$$

$$r_2 = R - 6R\sin^2\left(\frac{\theta}{2}\right) \qquad \textbf{Equation 5.12}$$

Substituting equations 5.11 and 5.12 into equations 5.5 and 5.6 gives:

$$V_{1\to 2} = \pi\left[\frac{2R^3}{3} - R^2\left(R - 10R\sin^2\left(\frac{\theta}{2}\right)\right) + \frac{\left(R - 10R\sin^2\left(\frac{\theta}{2}\right)\right)^3}{3}\right] \qquad \textbf{Equation 5.13}$$

$$V_{2\to 3} = \pi\left[\frac{2R^3}{3} - R^2\left(R - 6R\sin^2\left(\frac{\theta}{2}\right)\right) + \frac{\left(R - 6R\sin^2\left(\frac{\theta}{2}\right)\right)^3}{3}\right] \qquad \textbf{Equation 5.14}$$

The number of monomers contained within the sphere sections $V_{1\to 2}$ and $V_{2\to 3}$ can thus be defined as:

$$n'_{1(1\to 2)} = \frac{V_{1\to 2}n'_1}{V} \qquad \textbf{Equation 5.15}$$

$$n'_{2(2\to 3)} = \frac{V_{2\to 3}n'_2}{V} \qquad \textbf{Equation 5.16}$$

where $V = \frac{4}{3}\pi R^3$.

Thus the overall volume fraction loss from layer 2 due to chain tilting can be defined as:

$$\Delta\phi_p(tilt) = \frac{(n'_{2(2\to3)} - n'_{1(1\to2)})m}{\rho V} = \frac{3m(n'_{2(2\to3)} - n'_{1(1\to2)})}{4\pi R^3 \rho} \qquad \textbf{Equation 5.17}$$

For no net change in the layer 2 polymer volume fraction to occur (i.e. tilting and stretching exactly cancel one another):

$$\Delta\phi_p(tilt) = \Delta\phi_p(stretch) \qquad \textbf{Equation 5.18}$$

Expressing equation 5.18 fully (using equations 5.4, 5.15, 5.16 and 5.17) gives:

$$\frac{\pi R^3 (n'_2 - n_2)}{V_{2\to3} n'_2 - V_{1\to2} n'_1} = 0.75 \qquad \textbf{Equation 5.19}$$

where $V_{1\to2}$ and $V_{2\to3}$ are given by equations 5.13 and 5.14 respectively.

Equation 5.19 represents a condition under which the effects of chain stretching and tilting cancel one another in terms of the overall effect on the volume fraction of a region of the brush (layer 2 in the calculations presented above). The theory presented above contains approximations and assumptions and is merely intended to illustrate a principal in fairly simple terms. Even if chain stretching and tilting were not to cancel one another exactly, a partial balancing throughout the region of the brush affected by shear flow would still act to reduce the overall change in the volume fraction profile. Such effects, coupled with the potentially low sensitivity of neutron reflectometry to changes in the volume fraction profile provide another possible explanation for the fact that no shear effect was observed in the experiments carried out.

## 5.5 Further Discussion

While most theories predict that shear leads to a swelling of the brush layer, Saphiannikova et al [12] predicted that it would lead to a collapse of the layer similar to the contraction observed when a brush is immersed is a thermodynamically poor solvent. It was predicted that this collapse would occur when the stretching force per chain arising from shear ( $f$ ) exceeded the "Gaussian Threshold" $\frac{fa}{k_B T} << 1$ ($a$ is the length of the Kuhn segment). The shear force per chain ( $f$ ) was expressed in terms of the shear rate ( $\dot{\gamma}$), the solvent viscosity ( $\eta$), the dimensionless grafting density ( $\sigma$ ) and the fraction of chains affected by the shear ( $\delta$ ) as $\frac{\dot{\gamma}\eta a^3}{k_B T \delta \sigma}$.

A shear induced collapse of the brush layer as observed by neutron reflectometry would manifest itself as an increase in the reflectivity similar to that observed when lowering the thermodynamic quality of the solvent. Clearly no such phenomenon was observed in the results of shear experiments presented in this chapter. Direct comparison of these results with the theory of Saphiannikova et al is difficult since the fraction of chains affected by shear ( $\delta$ ) is not known.

Nguyen et al [13] investigated the structures of brush layers exposed to solvent shear flow using a set-up similar to that used in the work presented here. They studied 3 brush polymers: a block copolymer of 130 units of deuterated styrene and 15 units poly-4-vinylpyridine, a 1580 unit deuterated polystyrene terminated with a trihydroxysilane and a random copolymer of deuterated styrene (96.8%) and 4-vinylpyridine (3.2%). They studied the brush layers against toluene and carbon tetrachloride (good solvents) and water (poor solvent) at maximum area average shear rates of approximately 3500-4000$s^{-1}$. No significant changes in the shapes of the reflectivity profiles were observed as a result of shear.

## 5.6 Conclusions

Polystyrene brush layers have been studied in cyclohexane and toluene at area average shear rates of up to 147 000$s^{-1}$ using neutron reflectometry. The experiments were carried out using a purpose built flow reflectometry cell.

In all cases, no changes in the reflectivity profiles were observed as a result of shear (in comparison to the profiles obtained in the quiescent state), although some shear-induced desorption of the brush chains did occur in toluene. Comparison of the experimental results with recent theory [3] revealed that the shear rates explored were below the predicted threshold for the onset of shear induced swelling, and this may provide some explanation as to why no shear effect was observed. Apart from simply using higher shear rates (which can lead to technical problems with the flow cell), one possible means of getting closer to this shear induced swelling threshold would be to use higher molecular weight brush chains.

The potential lack of sensitivity of the neutron reflection technique to subtle changes in the brush structure (such as those that might occur as a result of shear) has also been highlighted.

## 5.7 Glossary of Symbols

### 5.7.1 General Symbols

| | |
|---|---|
| $a$ | Monomer size |
| $d$ | Average distance between grafting sites |
| $f$ | Shear force per chain |
| $h$ | Brush height |
| $k_B$ | Boltzmann constant |
| $R_g$ | Unperturbed radius of gyration |
| $T$ | Absolute temperature |
| $z$ | Distance normal to the grafting surface |

| | |
|---|---|
| $\alpha$ | Modified parabolic profile exponent |
| $\chi^2$ | Least squares minimisation parameter |
| $\delta$ | Fraction of chains affected by shear |
| $\phi_p$ | Polymer volume fraction |
| $\phi_S$ | Polymer volume fraction at grafting surface |
| $\dot{\gamma}$ | Shear rate |
| $\dot{\gamma}_{AV}$ | Area average shear rate |
| $\eta$ | Viscosity |
| $\sigma$ | Normalised grafting density |
| $\sigma_r$ | Interfacial roughness at substrate surface |

### 5.7.2 Chain Tilting Versus Stretching Model Parameters

| | |
|---|---|
| $m$ | Monomer mass |
| $n_1, n_2, n_3$ | Number of monomer units within spheres 1, 2 and 3 before chain stretching |
| $n_1', n_2', n_3'$ | Number of monomer units within spheres 1, 2 and 3 after chain stretching |
| $n'_{1(1\rightarrow2)}$ | Number of monomers transferred from layer 1 to layer 2 due to chain tilting |
| $n'_{2(2\rightarrow3)}$ | Number of monomers transferred from layer 2 to layer 3 due to chain tilting |
| $r_1$ | Vertical tilt increment |
| $r_2$ | Vertical tilt increment |
| $R$ | Sphere radius |
| $V$ | Sphere volume |
| $V_{1\rightarrow2}$ | Sphere volume element transferred from layer 1 to layer 2 due to chain tilting |

| | |
|---|---|
| $V_{2\to3}$ | Sphere volume element transferred from layer 2 to layer 3 due to chain tilting |
| $\phi_{p2}$ | Polymer volume fraction within layer 2 before chain stretching |
| $\phi'_{p2}$ | Polymer volume fraction within layer 2 after chain stretching |
| $\Delta\phi_{p2}(stretch)$ | Layer 2 polymer volume fraction change due to chain stretching |
| $\Delta\phi_{p2}(tilt)$ | Layer 2 polymer volume fraction change due to chain tilting |
| $\rho$ | Monomer density |
| $\theta$ | Tilt angle |

## 5.8 References


1 Cloke, V M; Higgins, J S; Lin Phoon, C; Richardson, S M; King, S M; Done, R; Cooper, T E. *LoQ Factfile*, 1996, 3-56

2 Harden, J L; Cates, M E. *Physical Review E*, 1996, **53**, 3782

3 Aubouy, M; Harden, J L; Cates, M E. *Journal de Physique II*, 1996, **6**, 969

4 de Gennes, P G. *Macromolecules*, 1980, **13**, 1069

5 Alexander, S. *Le Journal de Physique*, 1977, **38**, 983

6 Milner, S T; Witten, T A; Cates, M E. *Macromolecules*, 1988, **21**, 2610

7 Clarke, C J. *Cavendish Laboratory, Cambridge University, UK.* Personal communication.

8 Milner, S T. *Macromolecules,* 1991, **24**, 3704

9 Lai, P Y; Binder, K. *J. Chem. Phys.* 1993, **98**, 2366

10 Lide, RD (Ed). *CRC Handbook of Chemistry and Physics*. 77th Edition (1996). CRC Press.

11 Miao, H; Guo, H; Zuckermann, M J. *Macromolecules*, 1996, **29**, 2289

12 Saphiannikova, M G; Pryamitsyn, V A; Cosgrove, T. *Macromolecules*, 1998, **31**, 6662

13 Nguyen, D; Clarke, C J; Eisenberg, A; Rafailovich, M H; Sokolov, J; Smith, G S. *J. Appl. Cryst.* 1997, **30**, 680

# CHAPTER 6

# DIBLOCK COPOLYMER MICELLES

# CHAPTER 6

# DIBLOCK COPOLYMER MICELLES

When dispersed in a selective solvent for one of the blocks, linear diblock copolymers form micelles of well defined morphology at concentrations above the critical micelle concentration (CMC). This phenomenon occurs due to the inherent amphiphilic nature of the block copolymer molecules.

The morphology of micelles formed by poly(styrene-*b*-ethylene oxide) copolymers (PS-PEO) dispersed in water has been studied using small angle neutron scattering [1] (SANS). The effect of Couette shear flow on the structure and organisation of the micelles has also been investigated.

## 6.1 Polymers

Four diblock copolymers of styrene and ethylene oxide were synthesised by Mr F T Kiff using standard anionic polymerisation techniques. The four polymers were synthesised to be as near identical as possible in terms of the block sizes. However, each polymer had a different locus of deuteration to allow the full range of contrasts to be explored during the SANS experiments. The molecular weight and composition of each copolymer are given in tables 6.1 and 6.2. The PEO block molecular weights could not be accurately determined from SEC data (since the copolymer molecular weight was calculated using PEO standards) but were calculated using mole percent styrene composition values for the copolymers determined by $^{13}C$ NMR (the styrene block molecular weights were determined accurately using SEC). The polymers are labelled PS-PEO with the letters "h" or "d" indicating whether the blocks are hydrogenous or deuterated (e.g. hPS-dPEO denotes hydrogenous polystyrene–deuterated polyethylene oxide).

| Copolymer | PS block[a] | | Total copolymer[b] | |
|---|---|---|---|---|
| | $M_n$ (g $mol^{-1}$) | $M_w/M_n$ | $M_n$ (g $mol^{-1}$) | $M_w/M_n$ |
| dPS-dPEO | 1280 | 1.10 | 7580 | 1.05 |
| dPS-hPEO | 1280 | 1.10 | 6670 | 1.05 |
| hPS-dPEO | 1430 | 1.07 | 8180 | 1.04 |
| hPS-hPEO | 1430 | 1.07 | 8490 | 1.04 |

**Table 6.1** Molecular weight and polydispersity data for the poly(styrene-*b*-ethylene oxide) copolymers used in the SANS experiments. [a] PS block calculated using PS standards. [b] Copolymer calculated using PEO standards.

| Copolymer | Mole % styrene from $^{13}C$ NMR | PEO block size (g $mol^{-1}$) |
|---|---|---|
| dPS-dPEO | 7.2 | 7060 |
| dPS-hPEO | 7.4 | 6290 |
| hPS-dPEO | 7.0 | 8745 |
| hPS-hPEO | 7.7 | 7235 |

**Table 6.2** PEO block molecular weights calculated from copolymer $^{13}C$ NMR data.

## 6.2 Experimental

The SANS experiments were performed on the LOQ diffractometer at the Rutherford Appleton Laboratory [2]. The copolymers were dispersed in water, a poor solvent for PS and a good solvent for PEO. Consequently the copolymers were expected to form micelles consisting of a PS core surrounded by a shell (or corona) of solvated PEO chains. The four copolymers had different patterns of deuteration with respect to each other, and thus contrast matching of the dispersion medium (water) was used to highlight different regions of the experimental system with respect to their visibility to neutrons. For example, the dPS-hPEO copolymer was dispersed in water contrast

matched to hPEO. This made the PEO chains invisible to neutrons whilst highlighting the deuterated PS chains.

(Such precise tailoring of the dispersion medium scattering length density (SLD) exploits the fact that $H_2O$ and $D_2O$ have markedly different SLD values (table 6.3). The total SLD of the dispersion medium, $\rho_N$, is related to the SLD's ($\rho$) and volume fractions ($\phi$) of $H_2O$ and $D_2O$ as: $\rho_N = \rho_{H_2O}\phi_{H_2O} + \rho_{D_2O}\phi_{D_2O}$).

Table 6.3 gives neutron scattering length density values for the various components of the experimental system while table 6.4 shows the dispersion medium SLD's used and the volume fractions of $H_2O$ and $D_2O$ ($\phi_{H_2O}$ and $\phi_{D_2O}$) required to achieve those contrasts.

| **Component** | **SLD ($\times 10^6$ Å$^{-2}$)** | **Density (g ml$^{-1}$)** |
|---|---|---|
| dPS | 6.47 | 1.12 |
| hPS | 1.41 | 1.05 |
| dPEO | 7.06 | 1.23 |
| hPEO | 0.64 | 1.127 |
| $H_2O$ | -0.56 | 0.997 |
| $D_2O$ | 6.38 | 1.104 |

**Table 6.3** Neutron scattering length density and physical density values for the various components of the experimental system.

| **Polymer** | **Water SLD ($\times 10^6$ Å$^{-2}$)** | $\phi_{H_2O}$ | $\phi_{D_2O}$ |
|---|---|---|---|
| dPS-dPEO | 0 | 0.919 | 0.081 |
| dPS-hPEO | 0.64 (= hPEO) | 0.827 | 0.173 |
| hPS-dPEO | 1.41 (= hPS) | 0.716 | 0.284 |
| hPS-hPEO | 6.38 ($D_2O$) | 0 | 1 |

**Table 6.4** Details of the water SLD's used for each copolymer and the volume fractions of $H_2O$ and $D_2O$ required to achieve them.

For the SANS experiments, the copolymer dispersions were placed in rectangular quartz cells. Transmission and scattering runs were performed for each sample.
In order to place the differential scattering cross-section on an absolute scale during the data normalisation procedure, the following complementary data were obtained:

- Transmission and scattering runs for the solvent only (all four water contrasts run individually in quartz cells)
- Direct beam transmission
- LoQ standards (scattering runs for the copolymer and blend calibration standards)

The data were normalised and written to ASCII files using the program "COLETTE"[3].

## 6.3 Results and Data Fitting

Light scattering studies were carried out at the Interdisciplinary Research Centre in Polymer Science and Technology (Durham University) by Lovell and co-workers [4] using the fully hydrogenous and fully deuterated copolymers prior to the SANS experiments. These experiments indicated that the CMC was $(3.5\pm0.4)\times10^{-5}$ g $ml^{-1}$ and that the value of the CMC was not significantly affected by deuteration. Below the CMC, the particle diameter was small indicating that the copolymer was present as unimers in solution. However, at concentrations above the CMC the particle diameter increased dramatically to a much larger asymptotic value (~160-165Å, estimated from dynamic light scattering), indicating that micelle formation had occurred via a closed association process.

Copolymer concentrations in the range $5\times10^{-4}$ to $6.5\times10^{-2}$ g $ml^{-1}$ were studied using SANS. Concentrations below this range were not investigated since the times required to obtain statistically acceptable data would have been prohibitively high. At concentrations above approximately $7\times10^{-2}$ g $ml^{-1}$, the viscosity of the copolymer dispersions increased dramatically, and this complicates transferral of the solutions to the quartz cells. In such cases, heating of the dispersions would have been necessary

to reduce the viscosity when filling the cells, and this in turn may have affected the equilibrium micelle morphology and the intermicellar interactions. Thus, in order to make best use of the LOQ beamtime available it was decided to restrict the concentration range studied and to carry all experiments out at 298K. Due to time constraints it was not always possible to obtain data for all four contrasts at every concentration, although at least three contrasts were studied for all but three of the concentrations.

In the remainder of this chapter, the copolymer dispersion concentrations are expressed as approximate copolymer weight percentages (e.g. $1\times10^{-2}$ g $ml^{-1}$ ~ 1%, $1\times10^{-3}$ g $ml^{-1}$ ~ 0.1% etc).

The results obtained are discussed under the headings of low and high concentration, based on the observed characteristics of the SANS profiles. The generalised form of the differential scattering cross section, $\frac{d\Sigma}{d\Omega}(Q)$, is defined as [1]:

$$\frac{d\Sigma}{d\Omega}(Q) = NV^2(\Delta\rho)^2 P(Q)S(Q) \qquad \textbf{Equation 6.1}$$

where $N$ is the number density of scattering centres, $V$ is the volume of one scattering centre and $(\Delta\rho)^2$ is the contrast. The term $P(Q)$ is known as the form factor and describes how $\frac{d\Sigma}{d\Omega}(Q)$ is modulated by interference effects between neutrons scattered by different parts of the same scattering centre. The term $S(Q)$ is referred to as the structure factor and describes how $\frac{d\Sigma}{d\Omega}(Q)$ is modulated by interference effects between neutrons scattered by different scattering centres within the sample.

The low concentration regime is thus defined as that in which no inter-particle interference effects are seen in the data (i.e. $S(Q)=1$ for all $Q$ values). The high concentration regime is therefore defined as that in which $S(Q)\neq 1$ for all $Q$ values.

### 6.3.1 Low Concentration

Data were acquired for all four contrasts at concentrations of 0.05, 0.1 and 1%. These data were fitted using the program "FISH" written by Dr R K Heenan [5].

No $Q^{-1}$ dependence [6] of the scattering cross-section was seen in the SANS data at low $Q$ values, and this indicated that the micelles were not rod-like in their morphology. The data were therefore fitted using a spherical core-shell model (illustrated schematically in figure 6.1). The core was assumed to be water free, consisting solely of PS (the hydrophobic block) and surrounded by a shell of hydrated PEO chains (water is an extremely good solvent for PEO at 298K). The shell chains in this case can be considered as forming a polymer brush, since they are effectively grafted over the spherical surface of the core. In fitting the SANS data the core was assumed to be a homogeneous sphere of radius $r_C$, with the form factor for this case expressed as [1]:

$$P(Q) = \left[\frac{3(\sin(Qr_C) - Qr_C\cos(Qr_C))}{(Qr_C)^3}\right]^2 \qquad \textbf{Equation 6.2}$$

In accordance with brush theory [7], the shell was described in the fitting program as having a parabolic decrease in EO monomer density with increasing distance from the core.

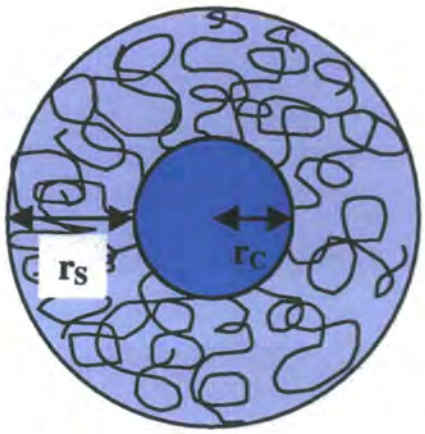


**Figure 6.1** Schematic illustration of a spherical core-shell micelle morphology. The micelle dimensions are described in terms of the core radius ($r_C$) and the shell thickness ($r_S$).

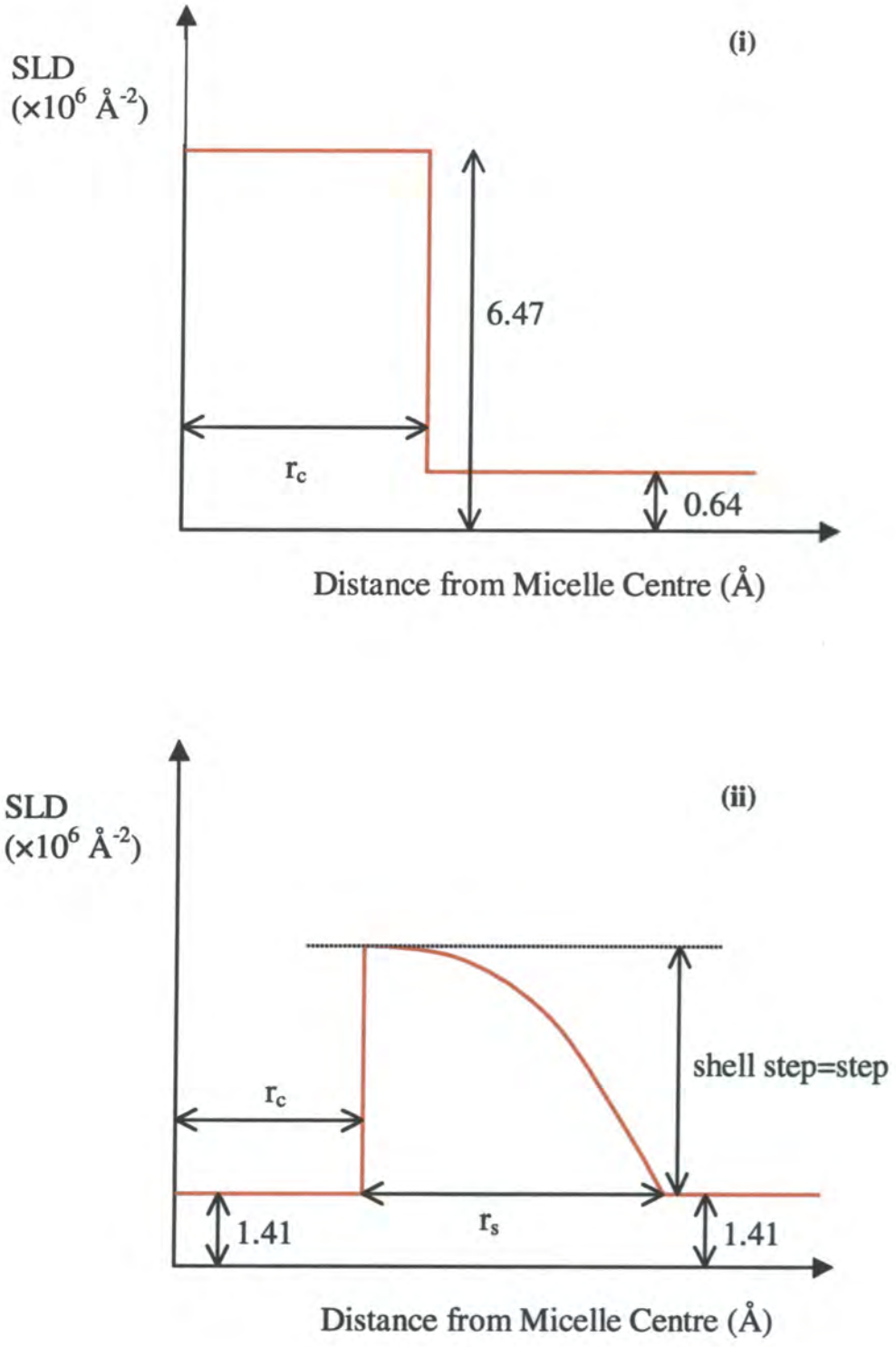


**Figure 6.2a** Schematic illustration of the SLD profiles used to describe the micelle morphology when fitting SANS data using the "FISH" program. (i) dPS-hPEO in water contrast matched to hPEO. (ii) hPS-dPEO in water contrast matched to hPS. (Homogeneous spherical core with a parabolic decrease in EO monomer density across the shell thickness, $r_s$.)

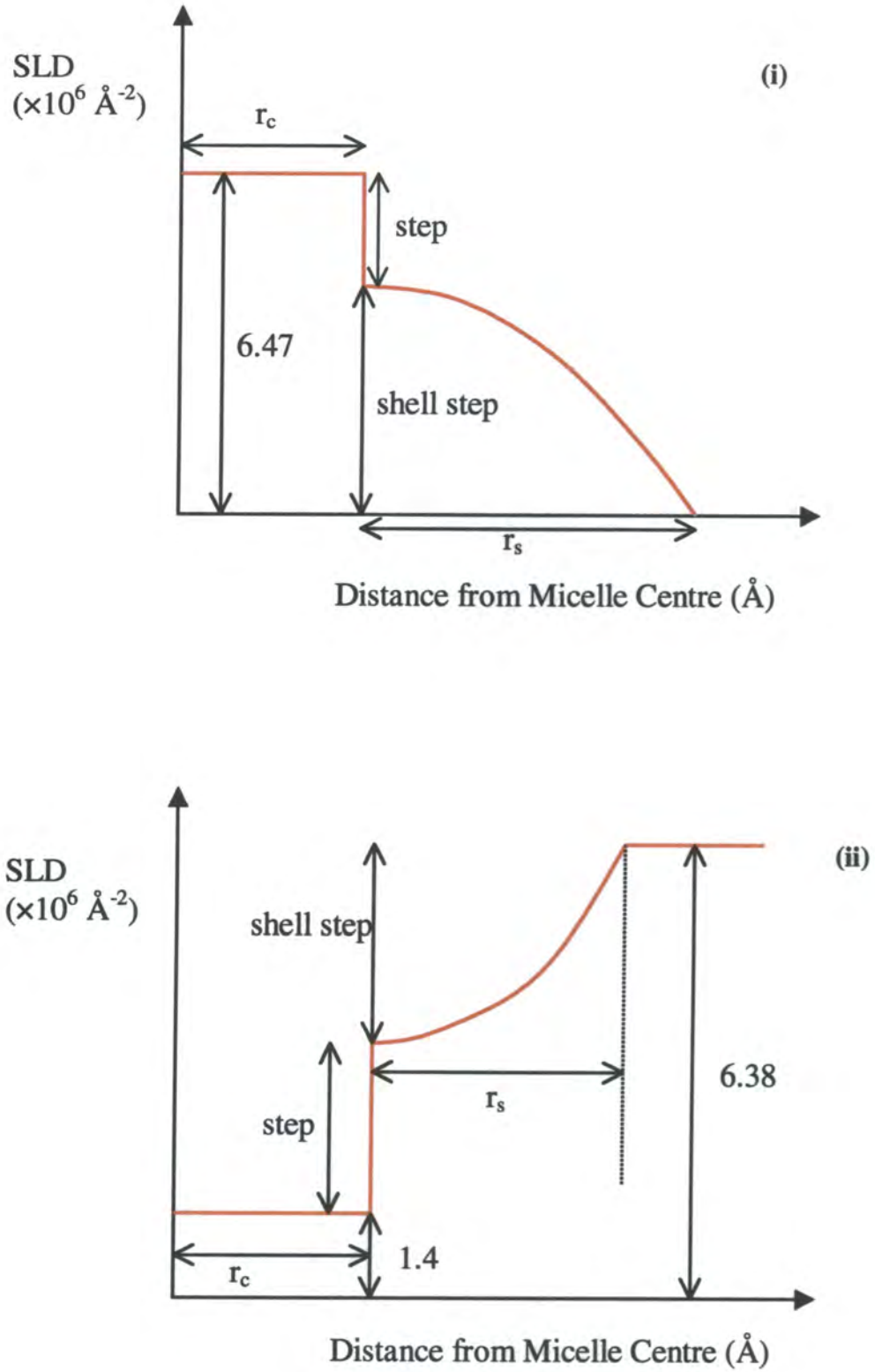


**Figure 6.2b** Schematic illustration of the SLD profiles used to describe the micelle morphology when fitting SANS data using the "FISH" program. (i) dPS-dPEO in $D_2O$ (ii) hPS-hPEO in $D_2O$. (Homogeneous spherical core with a parabolic decrease in EO monomer density across the shell thickness, $r_s$.)

The shapes of the neutron scattering length density profiles for each of the four contrasts based on this micelle morphology are illustrated schematically in figures 6.2a and 6.2b. The core radius ($r_C$) and shell thickness ($r_S$) are labelled in these figures along with the various scattering length density changes that characterise each system (known SLD values are indicated where appropriate).

Since an analytical expression for the form factor describing a parabolic shell profile has yet to be derived, the parabolic shape was approximated in the fitting program as six linear steps (the programming for this was carried out by Dr R K Heenan at the Rutherford Appleton Laboratory). The parameter "shell step" in figures 6.2a and 6.2b represents the total change in SLD across the shell, while the parameter "step" describes the vertical step in SLD at the PS-PEO interface.

When fitting the data, allowance was made for the fact that a distribution of micelle sizes would have existed in the dispersions (i.e. the micelle size was not monodisperse). This was done by putting a Schultz distribution [1,8] on the core radius. The width and skewness of the distribution is defined in terms of $\frac{\sigma}{\overline{r_C}}$ (where $\sigma$ is the standard deviation and $\overline{r_C}$ is the mean core radius).

Examples of the SANS data acquired for dispersion concentrations of 0.05, 0.1 and 1% are shown in figures 6.3 to 6.6 along with fits to data obtained using the "FISH" program. The parameters obtained from fits to the experimental data are given in table 6.5 (see figures 6.1, 6.2a and 6.2b for a schematic illustration of the meaning of the parameters with respect to the micelle morphology).

It can be seen from the values in table 6.5 that in this concentration range the micelle dimensions remain unchanged. Indeed, the values of $r_C$ and $r_S$ are very similar for all concentrations and contrasts (lying in the ranges 43-47Å and 124-141Å respectively). This near-constant value for the total micelle radius ($= r_C + r_S$) is in good agreement with the results of the light scattering studies discussed previously [4]. Values for the total micelle radius lie in the range 170-186Å, and this is slightly greater than the 160-165Å determined using light scattering.

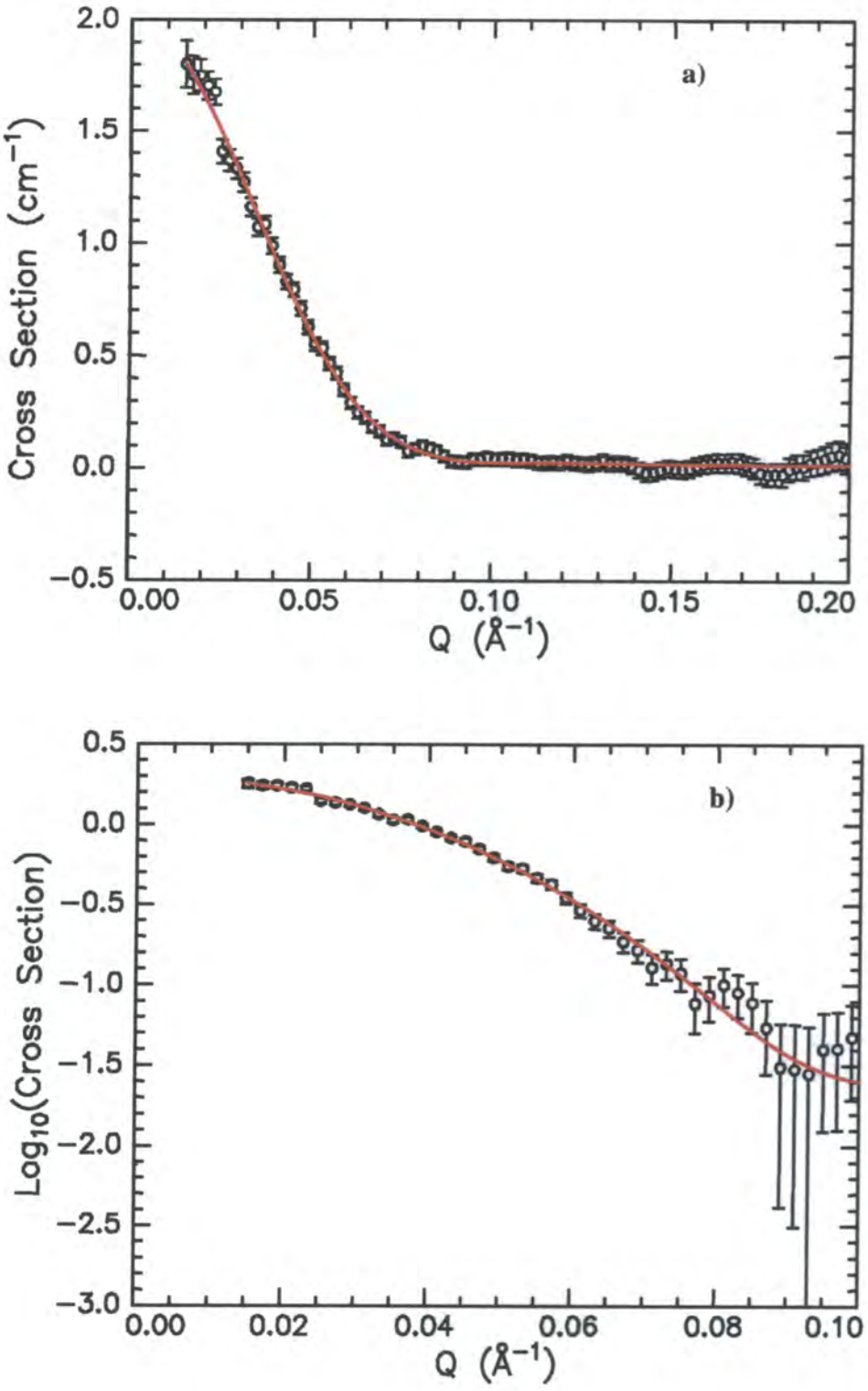


**Figure 6.3** SANS data for 1% dPS-hPEO in water contrast matched to hPEO. a) Scattering Cross Section (cm$^{-1}$) versus Q (Å$^{-1}$) b) Log$_{10}$ (Scattering Cross Section (cm$^{-1}$)) versus Q (Å$^{-1}$). Red lines are fits to the data.

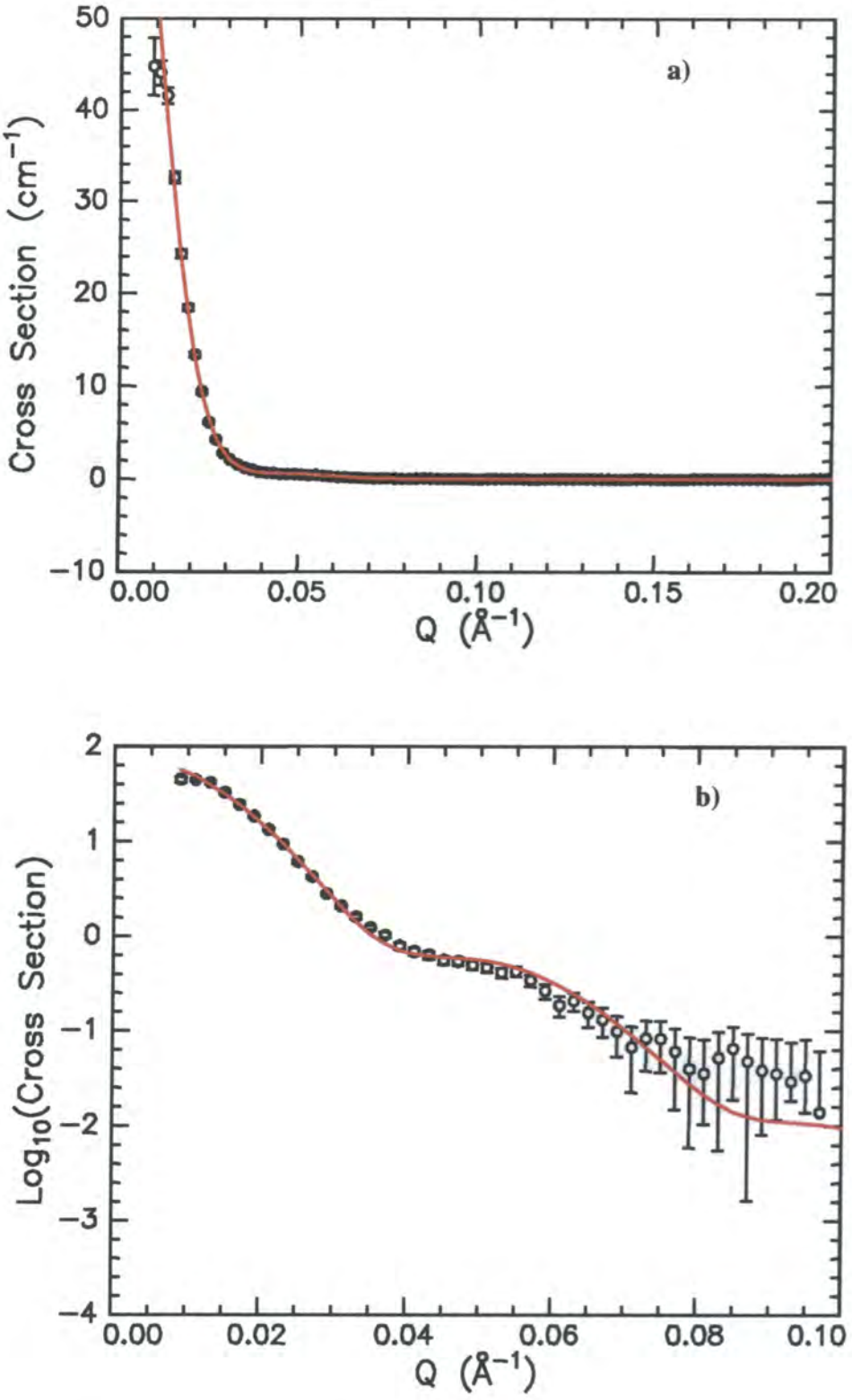


**Figure 6.4** SANS data for 1% dPS-dPEO in zero SLD water. a) Scattering Cross Section (cm$^{-1}$) versus Q (Å$^{-1}$) b) Log$_{10}$ (Scattering Cross Section (cm$^{-1}$)) versus Q (Å$^{-1}$). Red lines are fits to the data.

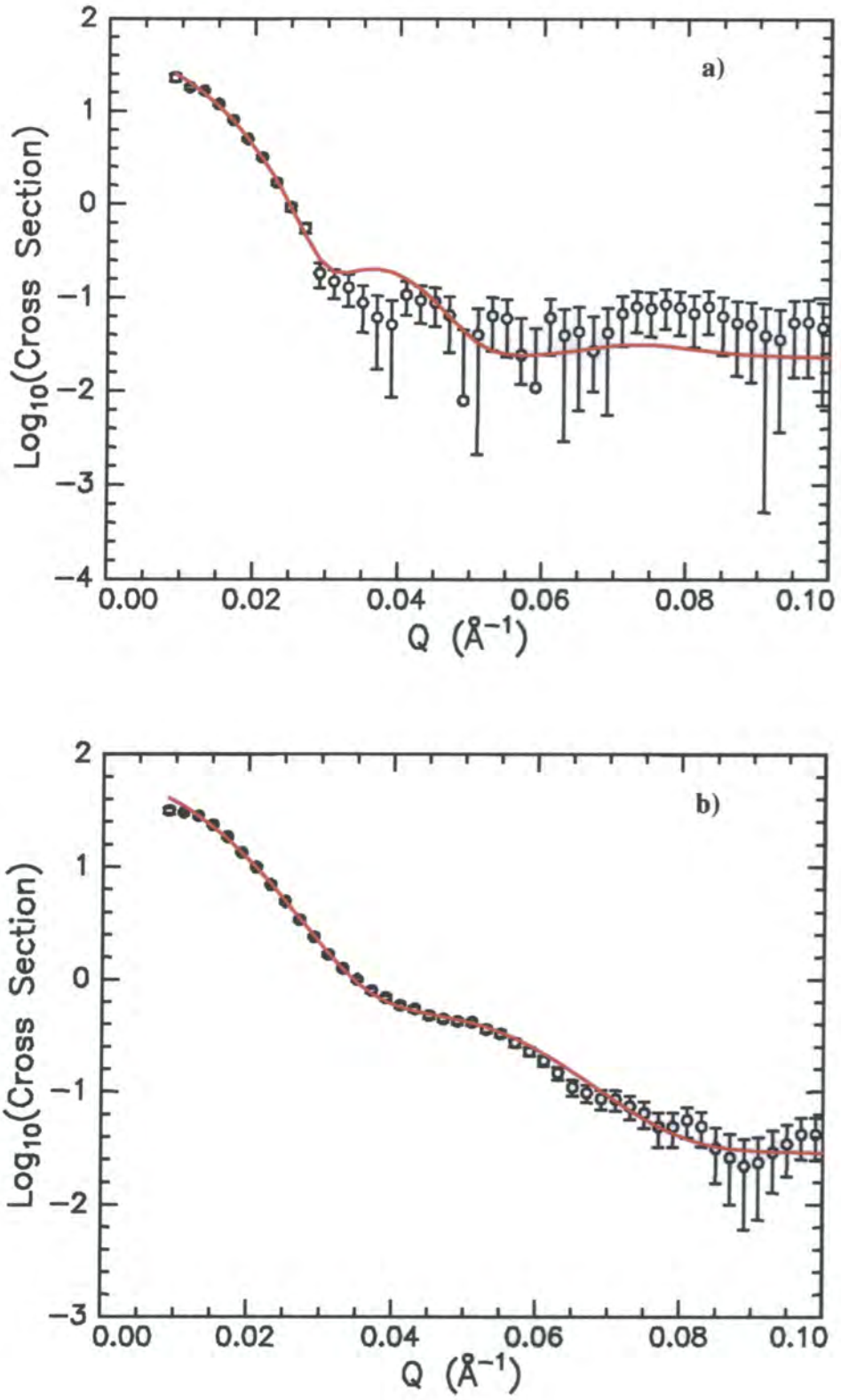


**Figure 6.5** SANS data for a) hPS-dPEO in water contrast matched to hPS b) hPS-hPEO in $D_2O$. Red lines are fits to the data.

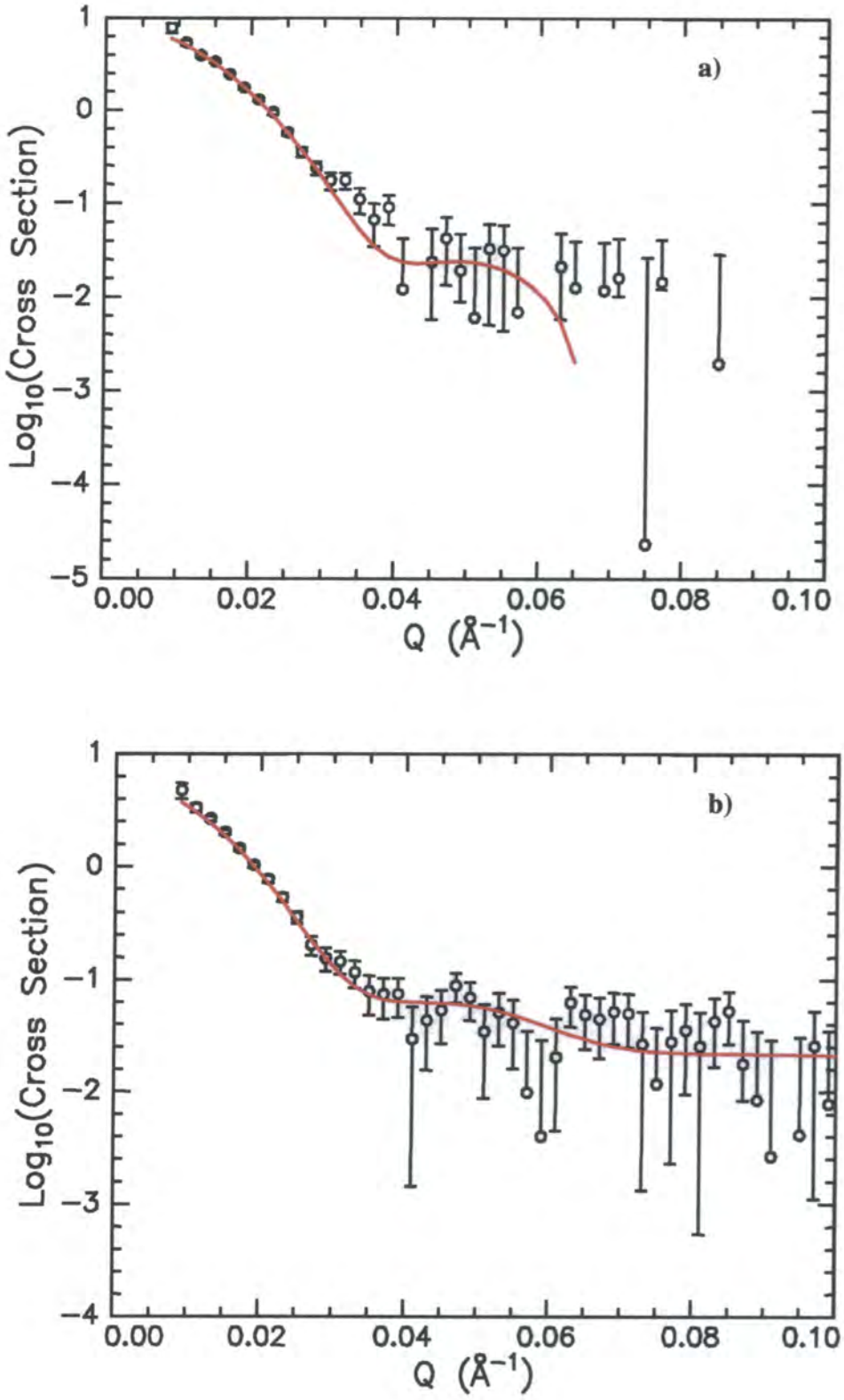


**Figure 6.6** SANS data for a) 0.1% dPS-dPEO in zero SLD water b) 0.05% dPS-dPEO in zero SLD water. Red lines are fits to the data.

| Polymer | Concentration (weight % polymer) | Dimensions (Å) | | SLD changes ($\times 10^6$ Å$^{-2}$) | | $\frac{\sigma}{=}$ / $r_c$ |
|---|---|---|---|---|---|---|
| | | $\overline{r_c}$ | $r_s$ | Step | Shell step | |
| dPS-hPEO | 1 | 43 | - | - | - | 0.14 |
| hPS-dPEO | 1 | 43 | 133 | 0.8 | 0.8 | 0.2 |
| dPS-dPEO | 1 | 43 | 127 | 5.5 | 0.968 | 0.3 |
| hPS-hPEO | 1 | 47 | 125 | 4.24 | 0.73 | 0.3 |
| dPS-hPEO | 0.1 | 47 | - | - | - | 0.22 |
| hPS-dPEO | 0.1 | 47 | 139 | 0.8 | 0.8 | 0.22 |
| dPS-dPEO | 0.1 | 46 | 124 | 5.14 | 1.32 | 0.29 |
| hPS-hPEO | 0.1 | 46 | 128 | 4.3 | 0.68 | 0.28 |
| dPS-hPEO | 0.05 | 43 | - | - | - | 0.29 |
| hPS-dPEO | 0.05 | 45 | 141 | 0.8 | 0.8 | 0.25 |
| dPS-dPEO | 0.05 | 43 | 139 | 5.55 | 0.916 | 0.3 |
| hPS-hPEO | 0.05 | 46 | 131 | 4.30 | 0.67 | 0.3 |

**Table 6.5** Parameters obtained from fits to SANS data using the "FISH" program

The accuracy of the fits obtained using FISH was checked by carrying out absolute intensity calculations. This involves calculating the percentages of PS and PEO by volume corresponding to the parameters obtained from any given fit to the experimental data. The calculated values can then be compared with the known percentages of PS and PEO by volume present in the dispersions (since the concentration of the dispersions and block molecular weights are known). Table 6.6 compares values for the percentages of PS and PEO by volume calculated by these two methods for the dPS-hPEO and dPS-dPEO dispersions; the agreement is acceptable for the two sets of values at each concentration.

| Polymer | Concentration | % Polymer by Volume [a] | | % Polymer by Volume [b] | |
|---|---|---|---|---|---|
| | (weight %) | PS | PEO | PS | PEO |
| dPShPEO | 1 | 0.142 | - | 0.15 | - |
| dPShPEO | 0.1 | 0.011 | - | 0.015 | - |
| dPShPEO | 0.05 | 0.0064 | - | 0.0075 | - |
| dPSdPEO | 1 | 0.18 | 0.61 | 0.14 | 0.68 |
| dPSdPEO | 0.1 | 0.013 | 0.051 | 0.013 | 0.068 |
| dPSdPEO | 0.05 | 0.0098 | 0.039 | 0.0068 | 0.034 |

**Table 6.6** Comparison of calculated values for the percentages of PS and PEO by volume present in the dispersions.
([a] Calculated from fits to the SANS data, [b] Calculated from the known solution compositions.)

Table 6.7 gives the unperturbed radii of gyration of the PEO blocks (in water at 298K) for each of the four copolymers, calculated using equation 6.3 [9].

$$R_g = (4.08\times10^{-18} M_W{}^{1.1})^{0.5}$$ **Equation 6.3**

| Polymer | PEO Block Molecular Weight (g mol$^{-1}$) | PEO $R_g$ (Å) |
|---|---|---|
| dPS-dPEO | 7060 | 26 |
| dPS-hPEO | 6290 | 25 |
| hPS-dPEO | 8745 | 30 |
| hPS-hPEO | 7235 | 27 |

**Table 6.7** Values for the unperturbed radius of gyration of PEO in water at 298K.

Table 6.8 gives aggregation numbers ($N_{agg} = \frac{\left(\frac{4}{3}\pi r_c^3\right)}{\left(\frac{m}{N_A \rho_{PS}}\right)}$, assuming that the core consists purely of PS, where $m$ is the PS block molecular weight and $\rho_{PS}$ is the physical density of PS) for each concentration/contrast along with the average distance between PEO chains at the core surface ($d_{PEO} = \left(\frac{4\pi r_c^2}{N_{agg}}\right)^{1/2}$) and the ratio of shell thickness ($r_S$) to unperturbed PEO radius of gyration ($R_g$).

| **Polymer** | **Concentration** (weight %) | $N_{agg}$ | $d_{PEO}$ (Å) | $\frac{r_S}{R_g}$ |
|---|---|---|---|---|
| dPS-hPEO | 1 | 185 | 11.2 | - |
| hPS-dPEO | 1 | 165 | 11.9 | 4.4 |
| dPS-dPEO | 1 | 225 | 10.2 | 4.8 |
| hPS-hPEO | 1 | 247 | 10.6 | 4.6 |
| dPS-hPEO | 0.1 | 258 | 10.3 | - |
| hPS-dPEO | 0.1 | 220 | 11.2 | 4.6 |
| dPS-dPEO | 0.1 | 270 | 9.9 | 4.8 |
| hPS-hPEO | 0.1 | 225 | 10.9 | 4.7 |
| dPS-hPEO | 0.05 | 225 | 10.2 | - |
| hPS-dPEO | 0.05 | 202 | 11.2 | 4.7 |
| dPS-dPEO | 0.05 | 225 | 10.2 | 5.3 |
| hPS-hPEO | 0.05 | 232 | 10.7 | 4.9 |

**Table 6.8** Aggregation numbers ($N_{agg}$), average distances between PEO chains at the micellar PS-PEO boundary ($d_{PEO}$) and degree of stretching of the PEO chains $\left(\frac{r_S}{R_g}\right)$ calculated from fits to the SANS data.

It can be seen from table 6.8 that aggregation numbers (i.e. the number of molecules per micelle) vary somewhat between the different concentrations/contrasts, although the values for eight of the twelve systems studied lie within the range 220-258. The aggregation number should not vary with changing concentration above the CMC for these dilute systems. The sizes of the blocks are very similar for the four different polymers, and thus their aggregation behaviour is expected to be similar also. The variation in aggregation number for the different concentrations/contrasts is random (as is the less significant variation in the core radii and shell thicknesses), and this is possibly attributable to the fact that the statistical errors associated with the experimental data were fairly significant for these very low concentrations. (Ideally the data acquisition times for these dispersions should have been considerably longer.)

Also evident from the data in table 6.8 is the fact that the PEO shell chains are strongly stretched relative to their unperturbed radius of gyration. The values of $\frac{r_S}{R_g}$ show that the shell chains are between 4 and 5 times the unperturbed radius of gyration, and it is here that comparisons can be drawn with polymer brush theory. The distance between PEO chains at the PS-PEO boundary, $d_{PEO}$, is considerably less than the unperturbed radius of gyration of the PEO chains. The PEO chains thus effectively form a brush layer grafted over the spherical surface of the polystyrene core (where $d_{PEO}$ represents the distance between grafting sites). Since water is a good solvent for PEO at 298K, excluded volume interactions between the PEO chains cause them to stretch away from the core surface. Dan and Tirrell [10] used self consistent mean field (SCF) theory to investigate interactions between polymer chains tethered to spherical interfaces. They predicted that as the curvature of the grafting surface increased, the monomer density profiles for the tethered chains went from the parabolic decay associated with chains tethered to planar surfaces to the power law decay associated with star polymers.

When fitting the SANS data presented above, linear and exponential forms were also used during the initial fits to describe the decay in PEO monomer density with increasing distance from the PS core. However, it was found that the parabolic shell SLD profile gave significantly better fits to the experimental data as judged by both visual inspection and the value of the least squares minimisation parameter. (The

linear shell profile gave shell thicknesses ~25-30Å greater than those obtained using the parabolic profile while the exponential shell profile gave shell thicknesses ~30-40Å greater than those obtained with the parabolic profile.)

### 6.3.2 High Concentration

For copolymer concentrations of 2% ($2\times10^{-2}$ g $ml^{-1}$) and higher, a peak was seen in the SANS data at low $Q$ due to interference between neutrons scattered from different micelles. When fitting the data for such cases, the inter-particle structure factor $S(Q)$ is no longer equal to unity over the entire $Q$ range, and thus an analytical expression has to be used to describe the effects of inter-particle interference on the differential scattering cross-section.

#### 6.3.2.1 The Structure Factor

The simplest model for describing the inter-micellar interaction is the hard-sphere model proposed in the physics of simple liquids by Percus and Yevick [11-13]. This model is illustrated schematically in figure 6.7. For spherical particles of radius $R$ (where $R = r_C + r_S$ for the core-shell micellar system), the interaction energy rises very steeply to plus infinity at a certain distance of separation ($r$). This distance of separation is defined as $r = 2R_{HS}$ where $R_{HS}$ is defined as the hard-sphere radius ($R_{HS} > R$ in most cases). The hard sphere volume fraction, $\phi_{HS}$ is defined as:

$$\phi_{HS} = \frac{4}{3}\pi R_{HS}^3 N_p \qquad \textbf{Equation 6.4}$$

where $N_p$ is the hard-sphere number density.

Ashcroft and Lekner [14] showed that the Percus-Yevick model led directly to the structure factor, with $S(Q)$ taking the form given in equations 6.5 to 6.7.

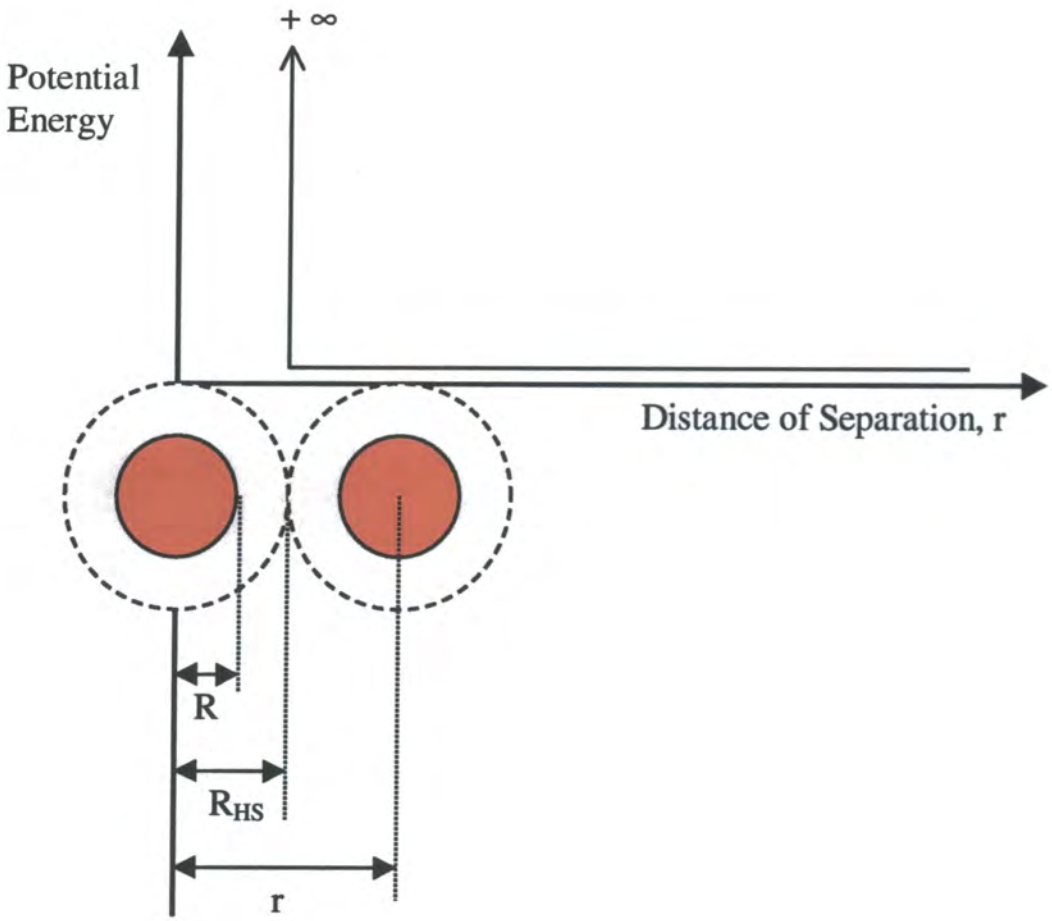


**Figure 6.7** Schematic illustration of the interaction between hard spheres.

$$S(Q) = \frac{1}{1 + 24\phi_{HS}\left(\frac{G(A)}{A}\right)}$$ **Equation 6.5**

where:

$$A = 2QR$$ **Equation 6.6**

and:

$$G(A) = \frac{\alpha}{A^2}(\sin A - A\cos A) + \frac{\beta}{A^3}(2A\sin A + (2 - A^2)\cos A - 2) + \frac{\gamma}{A^5}(-A^4\cos A + 4[(3A^2 - 6)\cos A + (A^3 - 6A)\sin A + 6])$$ **Equation 6.7**

The parameters $\alpha, \beta$ and $\gamma$ in equation 6.7 are expressed in terms of the hard-sphere volume fraction (see refs. 12 and 13 for details).

Hayter and co-workers [15] developed a closed analytic form of $S(Q)$ appropriate for macroion solutions, and their results provide a useful model basis for studying interacting colloidal systems.

For two identical spherical macroions of diameter $\sigma_d$, the repulsive potential is expressed as:

$$U(r) = \pi\varepsilon_0\varepsilon{\sigma_d}^2\psi_0^2 \exp[-\kappa(r-\sigma_d)]/r \qquad r > \sigma_d \qquad \textbf{Equation 6.8}$$

where $\psi_0$ is the surface potential, $\varepsilon$ is the solvent relative permittivity, $\varepsilon_0$ is the permittivity of free space, $\kappa$ is the Debye-Hückel inverse screening length and $r$ is the macroion centre-to-centre distance.

The interaction potential can be expressed in dimensionless from as:

$$\beta U(x) = \gamma \exp(-kx)/x \qquad x > 1 \qquad \textbf{Equation 6.9}$$

where $\beta = \dfrac{1}{k_B T}$ is the reciprocal thermal energy and $k$ is a dimensionless screening constant equal to $\kappa\sigma$. $\gamma$ is a dimensionless coupling constant, and the contact potential for a macroion pair (in units of $k_B T$) is equal to $\gamma \exp(-k)$, where:

$$\gamma\exp(-k) = \beta\pi\varepsilon_0\varepsilon\sigma_d\psi_0^2 \qquad \textbf{Equation 6.10}$$

The particle volume fraction, $\eta$ is expressed as:

$$\eta = \frac{1}{6}\pi n\sigma_d^3 \qquad \textbf{Equation 6.11}$$

where $n$ is the number density.

The structure factor, $S(K)$ (where $K = Q\sigma_d$) is expressed in closed analytic form as:

$$S(K) = \frac{1}{1 - 24\eta a(K)} \qquad \textbf{Equation 6.12}$$

The term $a(K)$ in equation 6.12 is expressed as a function of $K$, $\sigma$, $\eta$, $k$ and $\gamma$ through a series of coefficients and trigonometric terms. The expression for $a(K)$ is too long and complex to be presented here, but is given in Appendix B.

### 6.3.2.2 Results and Discussion

SANS data were obtained for dispersion concentrations of 2, 3, 4, 5, 6 and 6.5%. Attempts were made to fit these data using the FISH program at the Rutherford Appleton Laboratory. In this case, the polydisperse spherical core/parabolic shell model for $P(Q)$ (from fitting the data acquired at low concentration) was used in conjunction with the Percus-Yevick hard-sphere $S(Q)$ (equations 6.5 to 6.7). However, fits to the data obtained using this method were unsatisfactory.

Three fitting programs were written (see Appendix A for the Fortran source codes) in an attempt to achieve satisfactory fits to the experimental data. All of the programs were linked to the Fitfun library of subroutines to allow the actual data fitting procedure to be carried out (using the VA05A minimisation routine).

The program "Ottewill" was written to fit data acquired at low concentration (i.e. $S(Q) = 1$ for all $Q$). This program used a spherical core-shell form factor that is illustrated schematically in figure 6.8. With this form of $P(Q)$, the micelle dimensions are again characterised in terms of the core radius and shell thickness ($r_C$ and $r_S$ respectively). However, unlike the more complex model used in the FISH program, the SLD in this case remains constant throughout the shell region (i.e. the shell SLD profile is uniform and not parabolic).

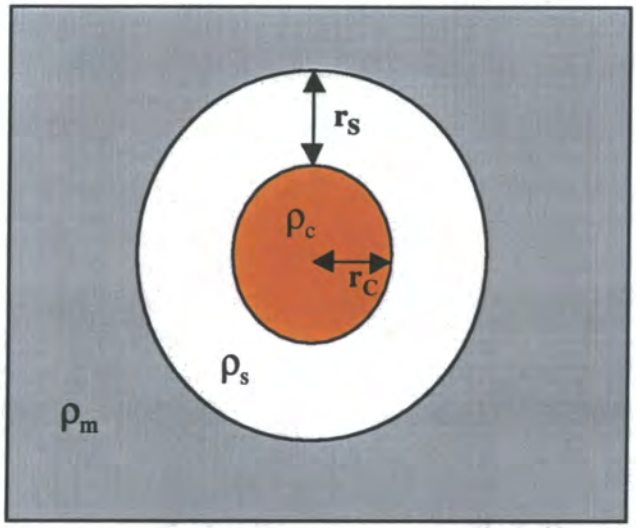


**Figure 6.8** Schematic illustration of a spherical core-shell model appropriate for diblock copolymer micelles. The core region has radius $r_C$ and scattering length density $\rho_C$ while the shell has thickness $r_S$ and scattering length density $\rho_S$. The dispersion medium has scattering length density $\rho_m$.

The differential scattering cross section for this core shell model is expressed as:

$$\frac{d\Sigma}{d\Omega}(Q) = \frac{16\pi^2 n}{9}\left[\begin{array}{l}(\rho_S - \rho_m)\left\{3R^3\left(\frac{\sin QR - QR\cos QR}{(QR)^3}\right) - 3r_C^3\left(\frac{\sin Qr_C - Qr_C\cos Qr_C}{(Qr_C)^3}\right)\right\}^2 \\ +(\rho_C - \rho_m)3r_C^3\left(\frac{\sin Qr_C - Qr_C\cos Qr_C}{(Qr_C)^3}\right)\end{array}\right]$$

**Equation 6.13**

where $n$ is the particle number density and $R = r_C + r_S$.

The program "Percus" was written to fit SANS data acquired at high concentrations. This program uses the form factor given by equation 6.13 coupled with the Percus-Yevick hard-sphere $S(Q)$ given by equations 6.5 to 6.7. However, this program also failed to give satisfactory fits to the SANS data obtained for high concentrations (see figure 6.9 for an example of such a poor fit).

Satisfactory fits to the SANS data were, however, achieved using the program "Hayter". This program used the spherical core-shell form factor given by equation 6.13 coupled with the macroion solution $S(Q)$ developed by Hayter et al (equations 6.8 to 6.12). Although the micellar sytems studied in this work were uncharged, the macroion $S(Q)$ gave good fits to the SANS data. All of the fits to the data acquired at high concentration presented in this chapter were performed using the program "Hayter", and the interpretation of the $S(Q)$ parameters obtained from the fits in terms of sterically based (as opposed to charge based) interactions between micelles is discussed in more detail later in this chapter.

All three of the above programmes use the form factor given by equation 6.13, and when calculating $P(Q)$ a Gaussian distribution was put on the core radius to account for size polydispersity in the micelles. The width of the distribution was controlled by the parameter "$pr$" (the percentage polydispersity of $r_C$), and thus the standard deviation of the Gaussian distribution was defined as:

$$\sigma = \frac{\overline{r_C} \times pr}{2.35 \times 100} \qquad \textbf{Equation 6.14}$$

Figures 6.10 to 6.18 show a selection of the SANS data acquired along with fits to the data obtained using the program "Hayter".

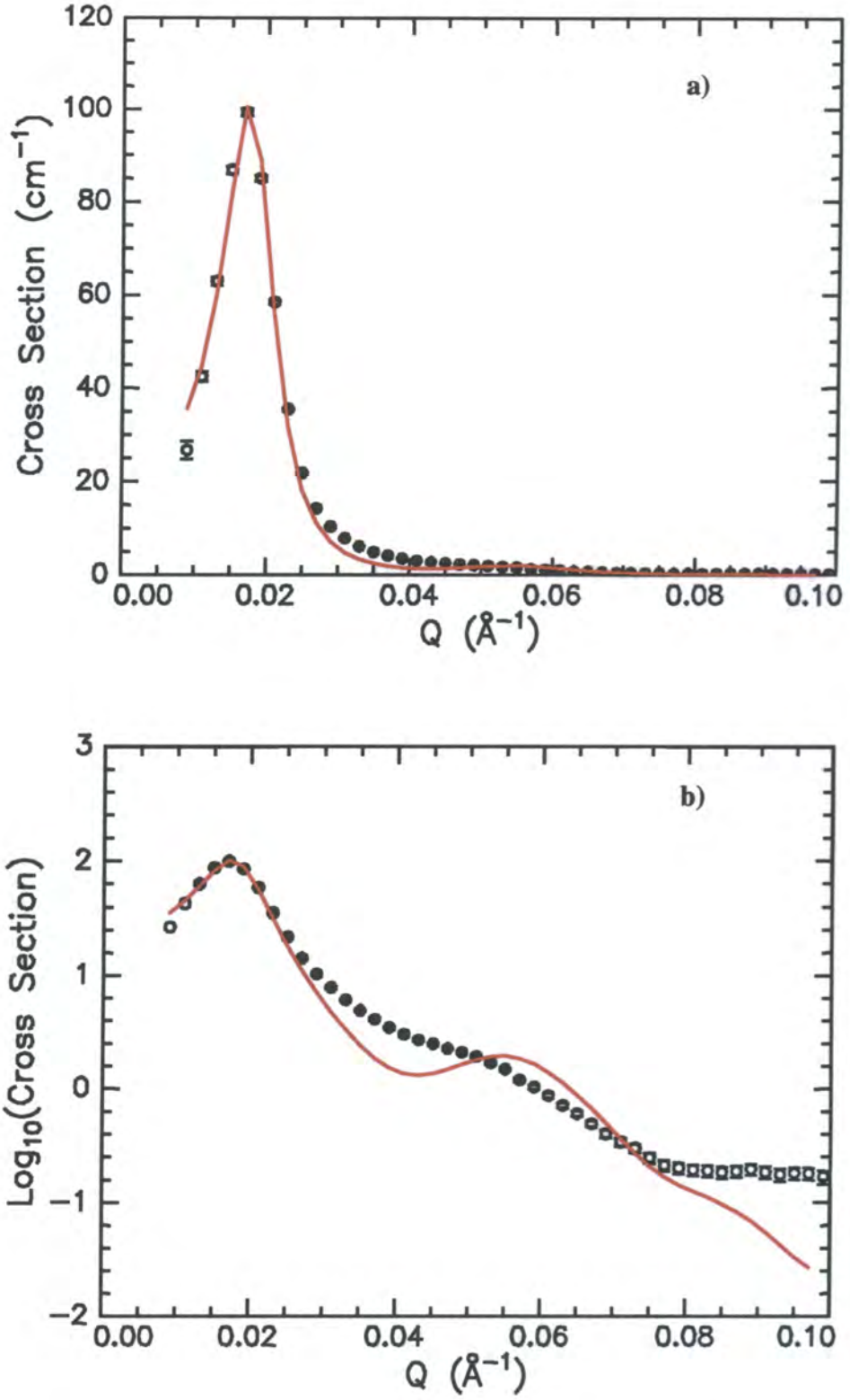


**Figure 6.9** SANS data obtained for 5% hPS-hPEO in $D_2O$. a) Scattering Cross-Section ($cm^{-1}$) versus Q ($Å^{-1}$) b) $Log_{10}$(Scattering Cross-Section ($cm^{-1}$)) versus Q ($Å^{-1}$). Red lines are fits to the data obtained using the program "Percus".

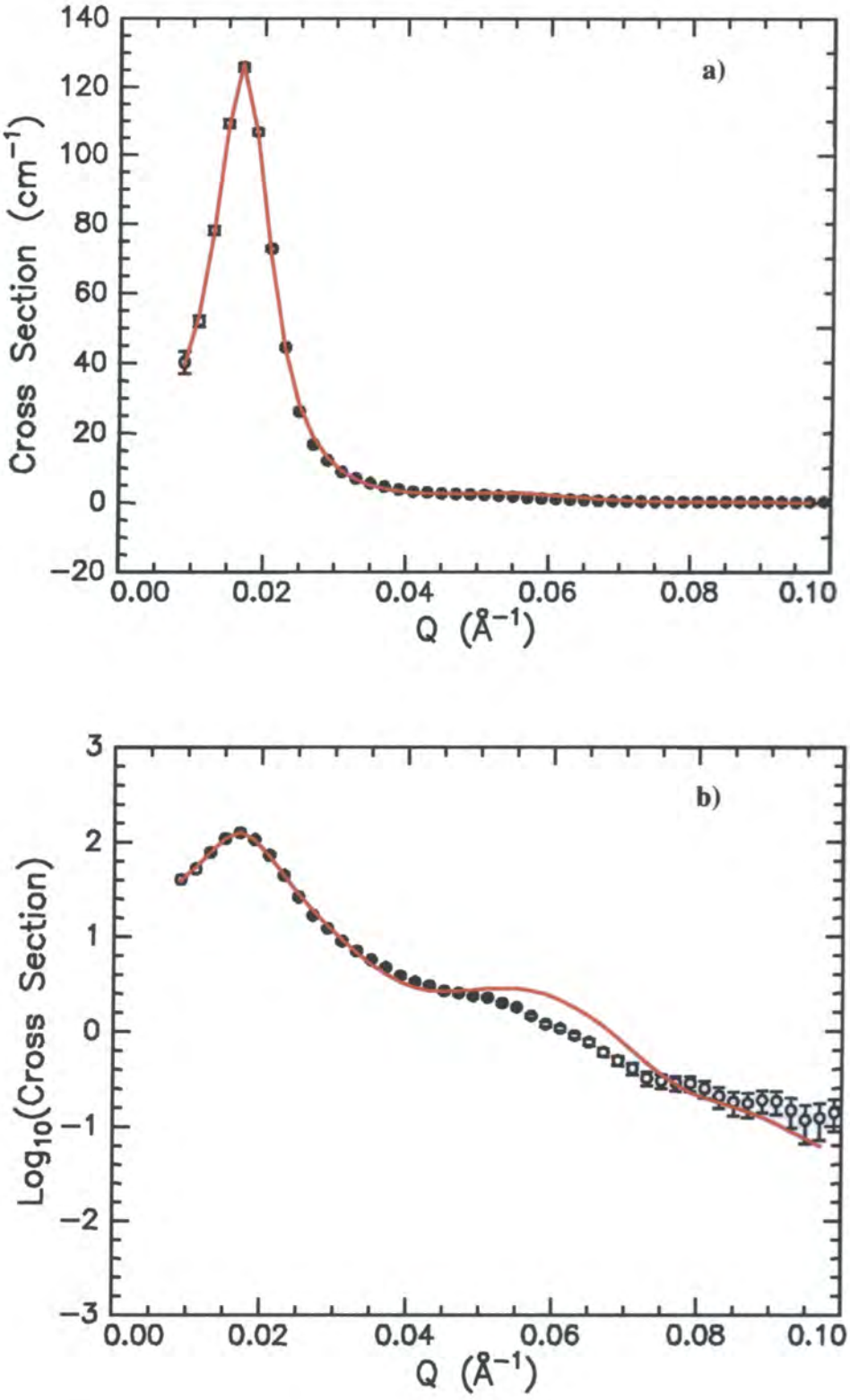


**Figure 6.10** SANS data for 5% dPS-dPEO in zero SLD water. a) Scattering Cross Section ($cm^{-1}$) versus Q ($Å^{-1}$) b) $Log_{10}$ (Scattering Cross Section ($cm^{-1}$)) versus Q ($Å^{-1}$). Red lines are fits to the data.

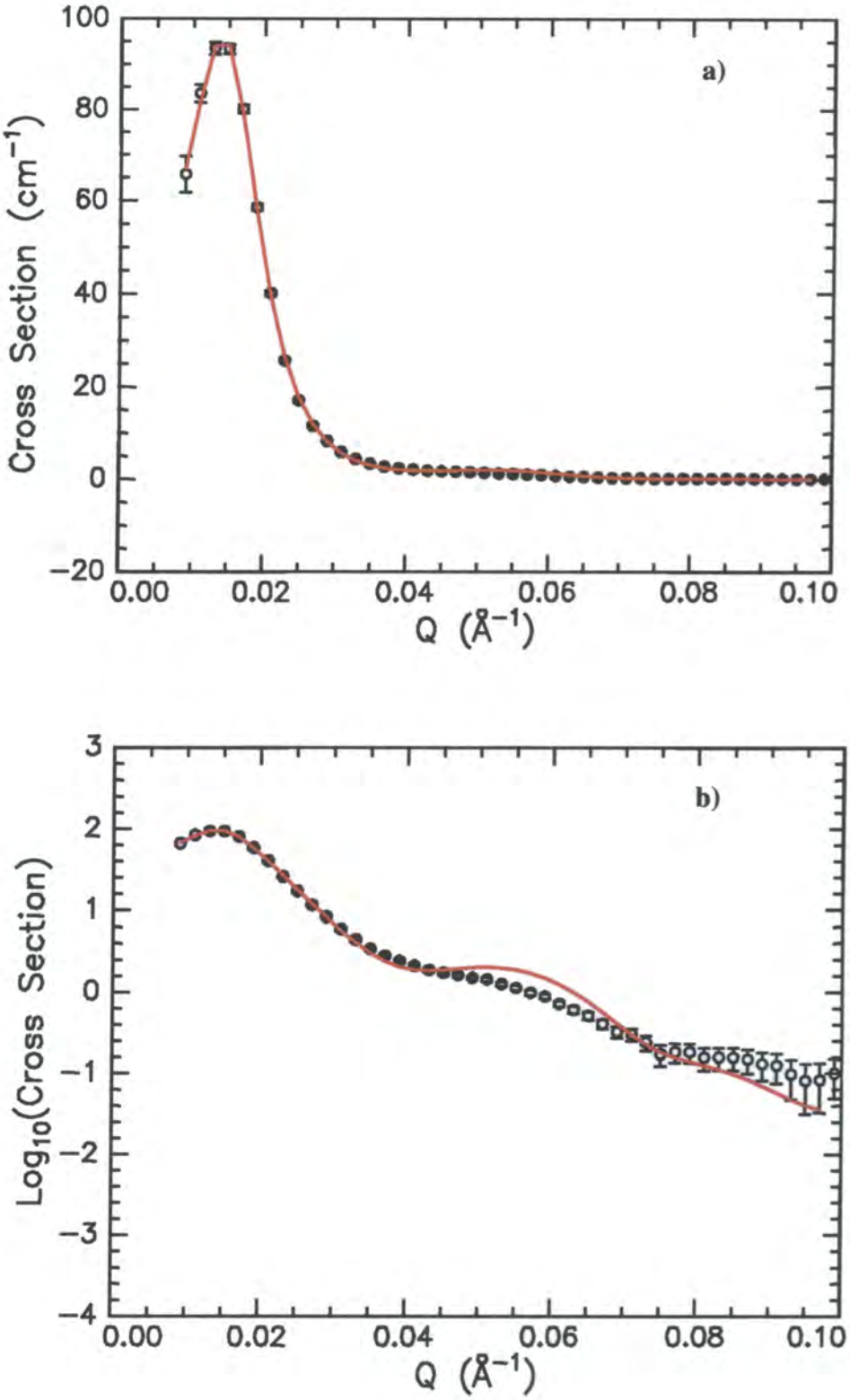


**Figure 6.11** SANS data for 3% dPS-dPEO in zero SLD water. a) Scattering Cross Section ($cm^{-1}$) versus Q ($Å^{-1}$) b) $Log_{10}$ (Scattering Cross Section ($cm^{-1}$)) versus Q ($Å^{-1}$). Red lines are fits to the data.

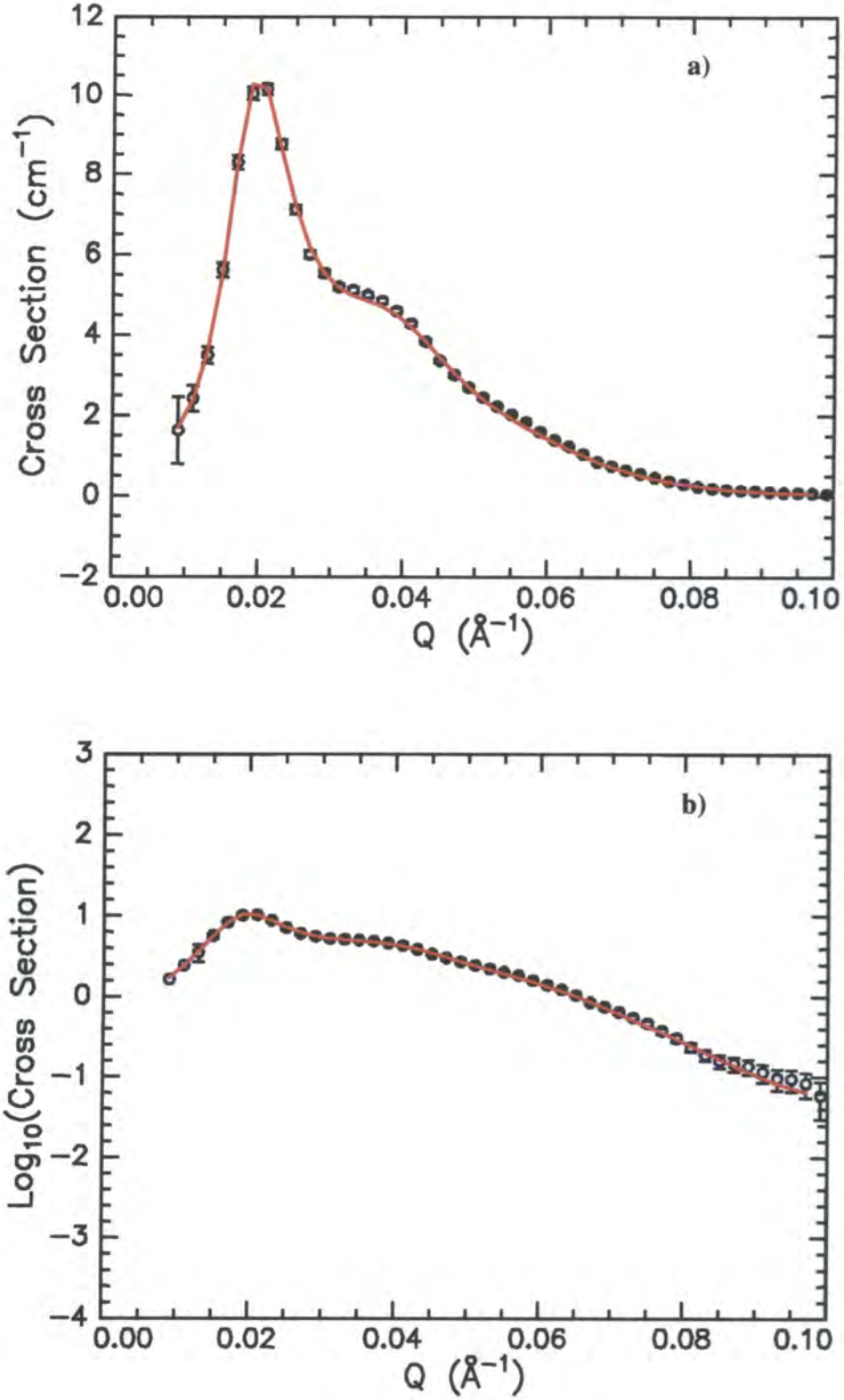


**Figure 6.12** SANS data for 5% dPS-hPEO in water contrast matched to hPEO. a) Scattering Cross Section (cm$^{-1}$) versus Q (Å$^{-1}$) b) Log$_{10}$ (Scattering Cross Section (cm$^{-1}$)) versus Q (Å$^{-1}$). Red lines are fits to the data.

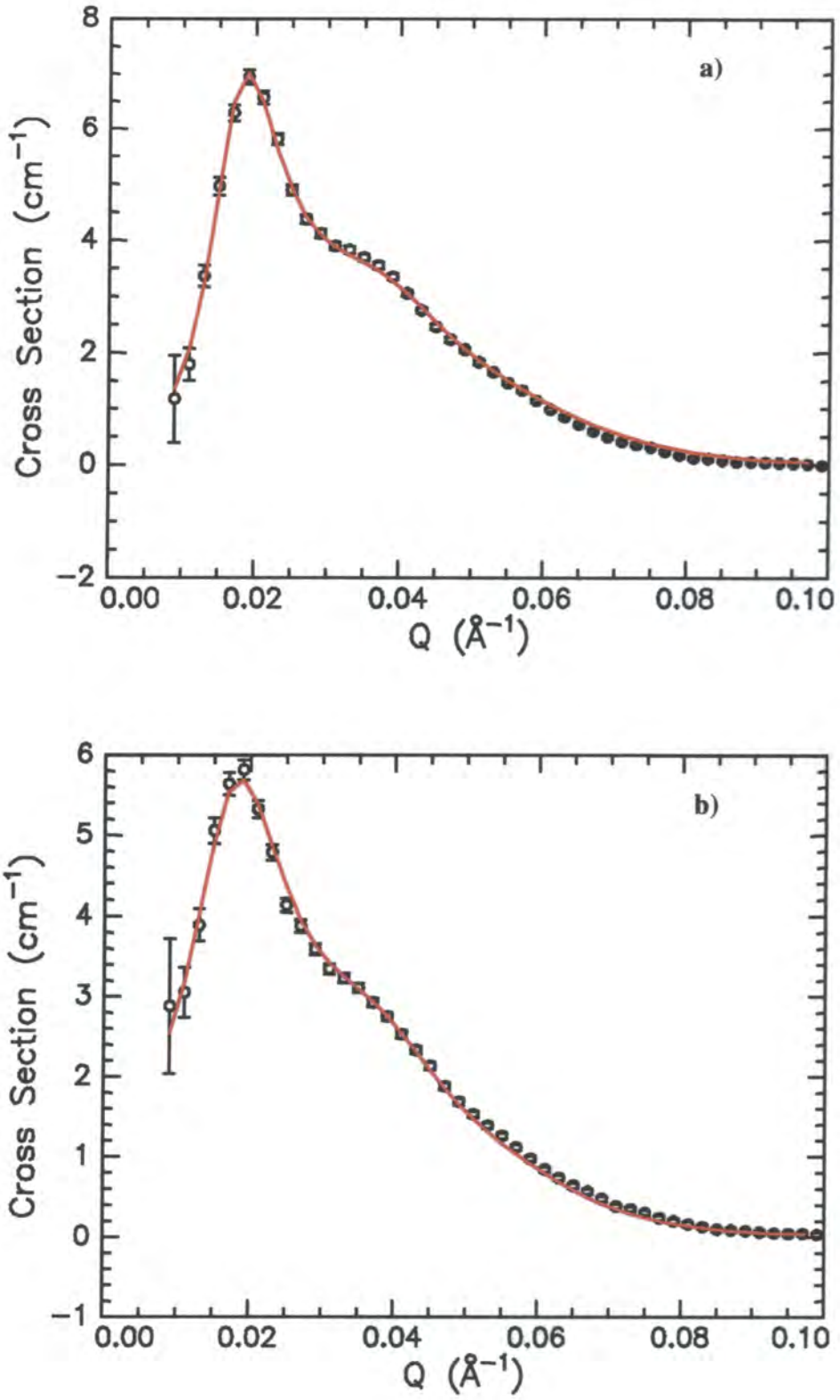


**Figure 6.13** SANS data for dPS-hPEO in water contrast matched to hPEO. a) 4% b) 3%. Red lines are fits to the data.

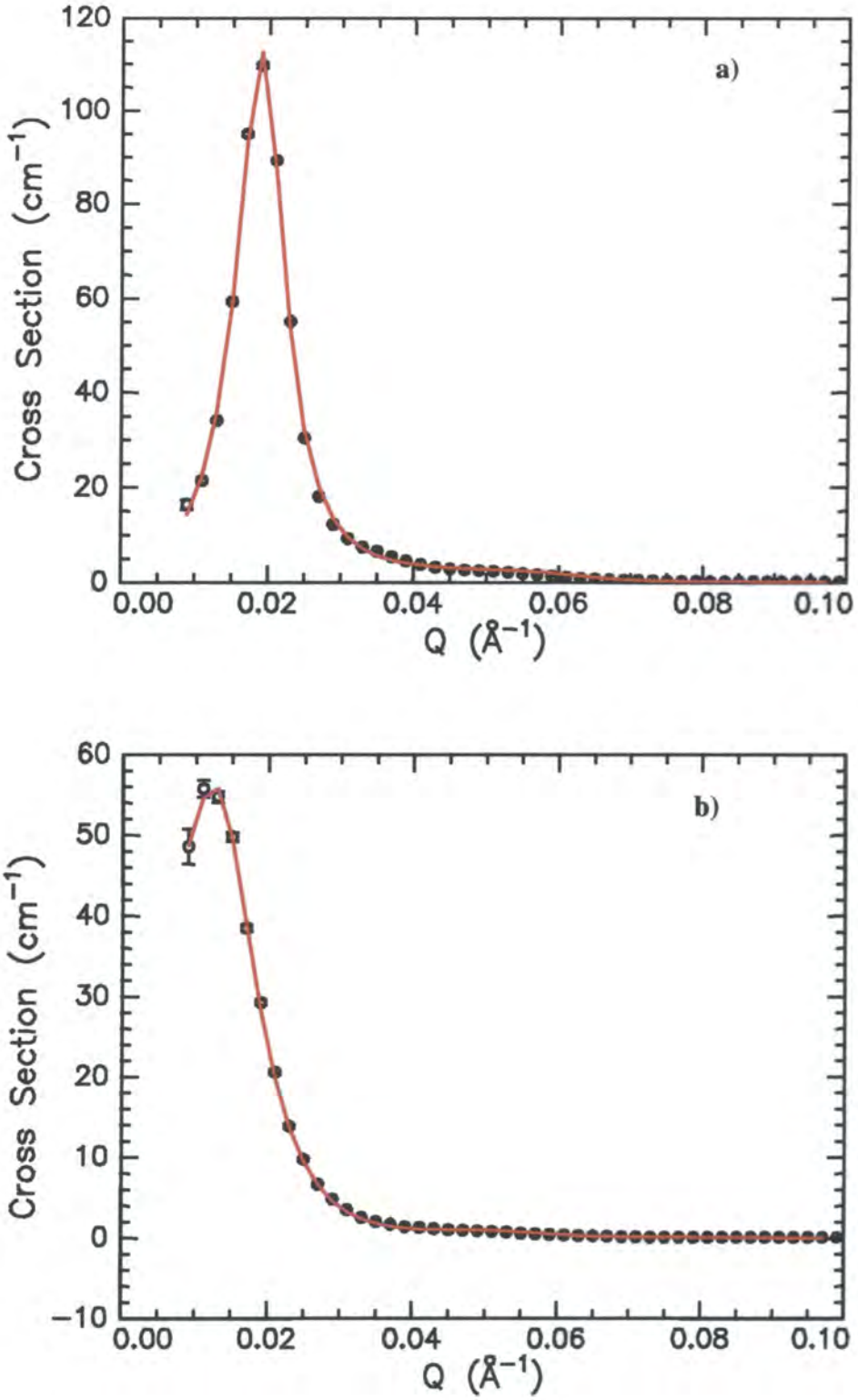


**Figure 6.14** SANS data for hPS-hPEO in $D_2O$. a) 6.5% b) 2%. Red lines are fits to the data.

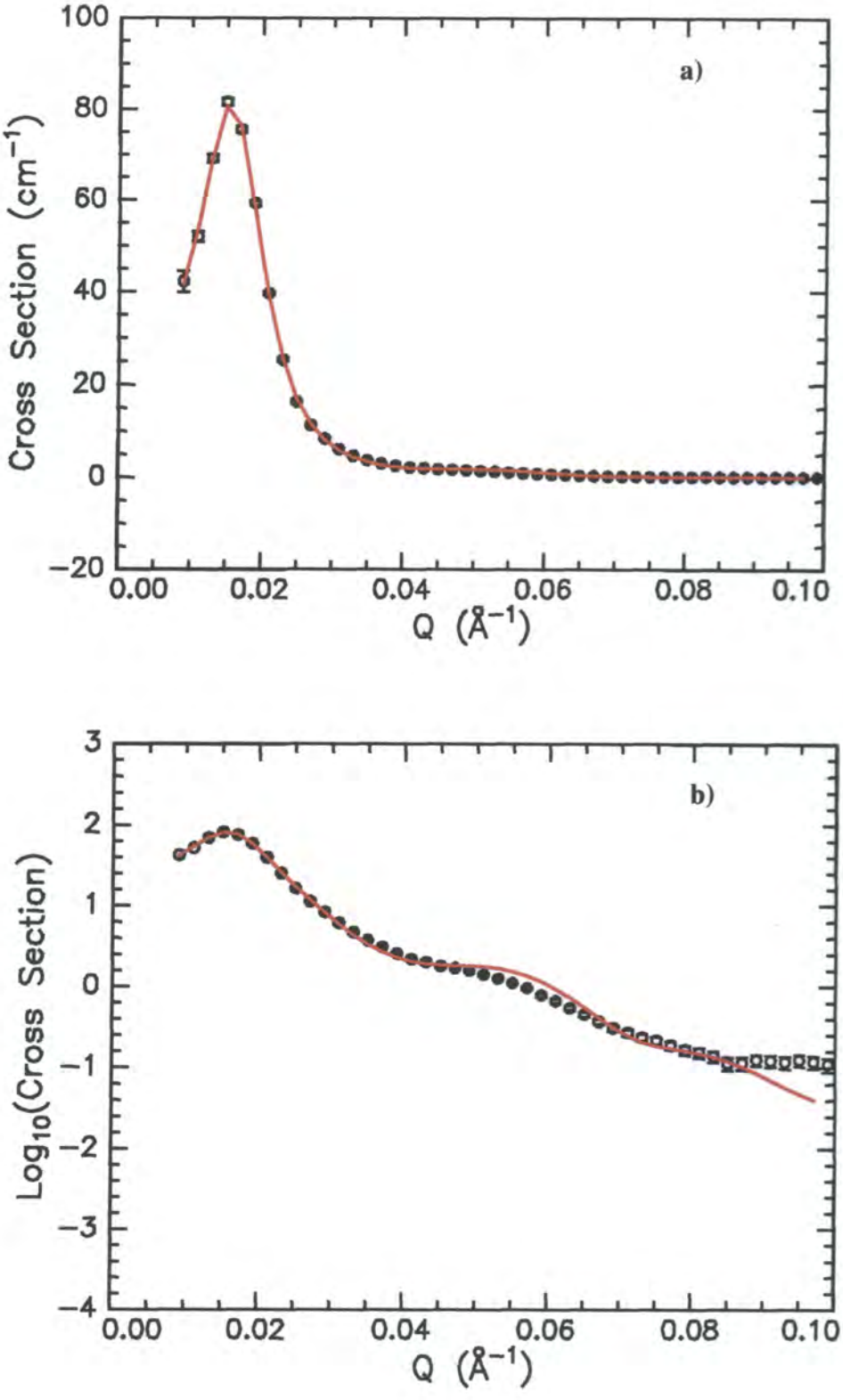


**Figure 6.15** SANS data for 4% hPS-hPEO in $D_2O$. a) Scattering Cross Section ($cm^{-1}$) versus Q ($Å^{-1}$) b) $Log_{10}$ (Scattering Cross Section ($cm^{-1}$)) versus Q ($Å^{-1}$). Red lines are fits to the data.

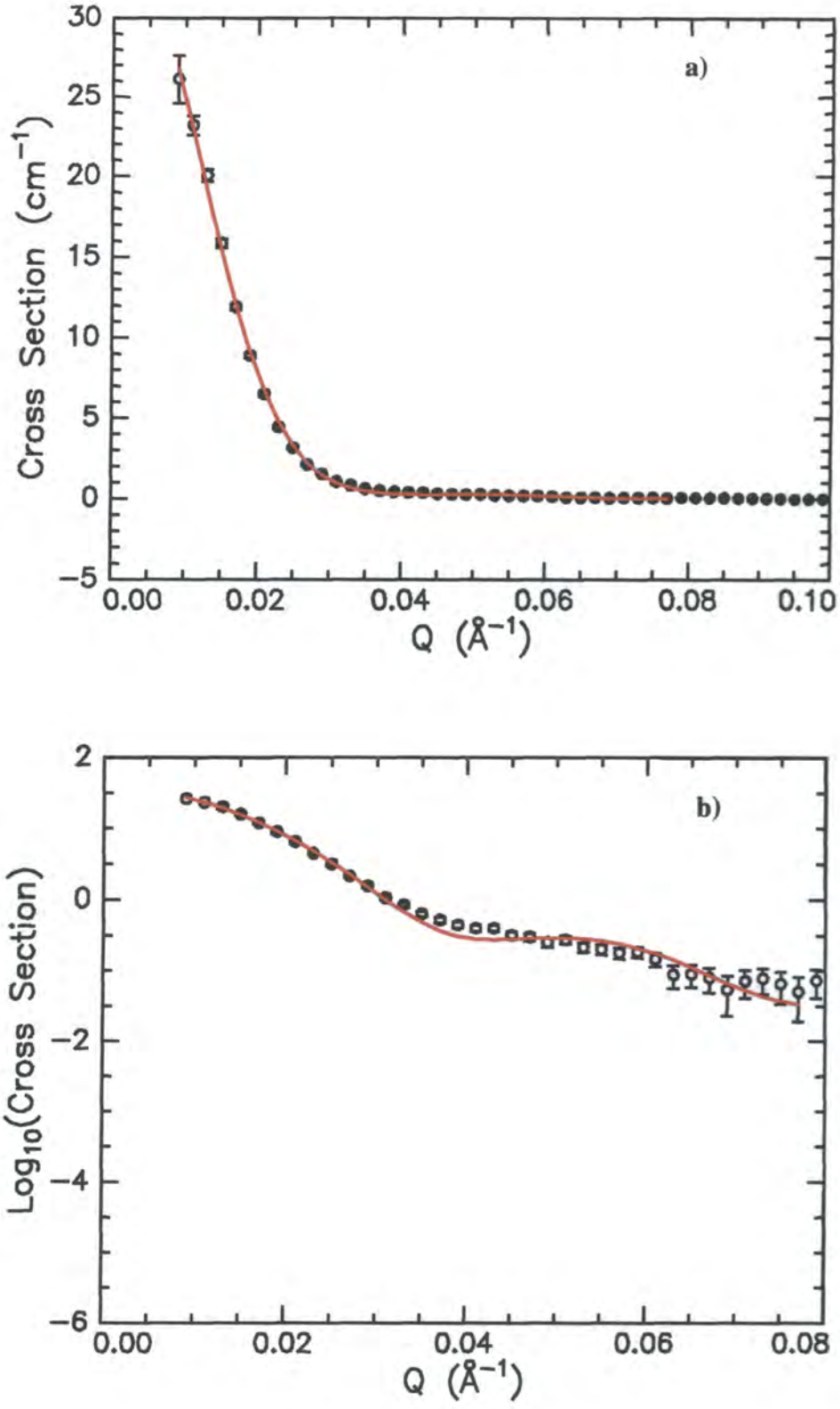


**Figure 6.16** SANS data for 0.5% dPS-dPEO in zero SLD water. a) Scattering Cross Section (cm$^{-1}$) versus Q (Å$^{-1}$) b) $Log_{10}$ (Scattering Cross Section (cm$^{-1}$)) versus Q (Å$^{-1}$). Red lines are fits to the data.

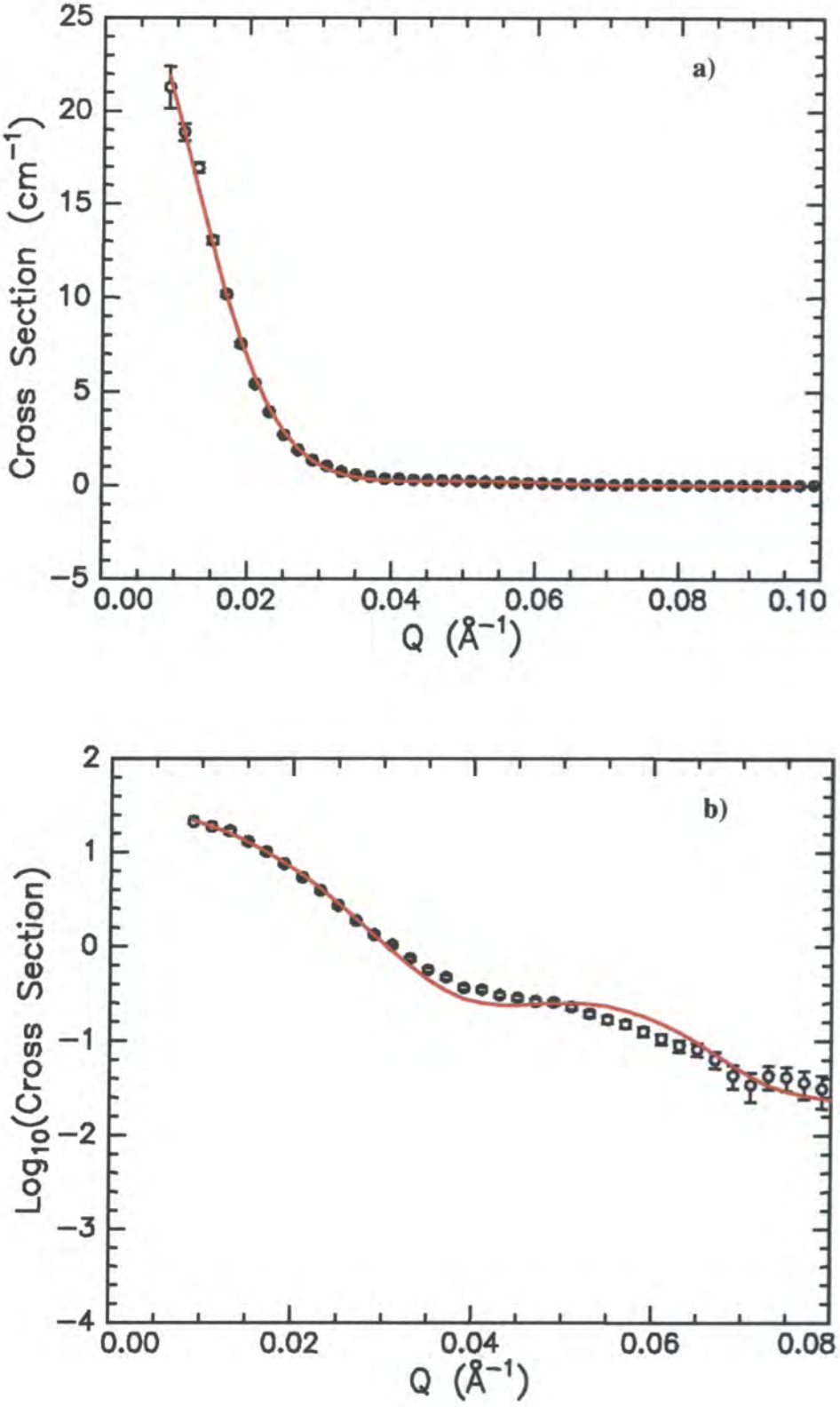


**Figure 6.17** SANS data for 0.5% hPS-hPEO in $D_2O$. a) Scattering Cross Section ($cm^{-1}$) versus Q ($Å^{-1}$) b) $Log_{10}$ (Scattering Cross Section ($cm^{-1}$)) versus Q ($Å^{-1}$). Red lines are fits to the experimental data.

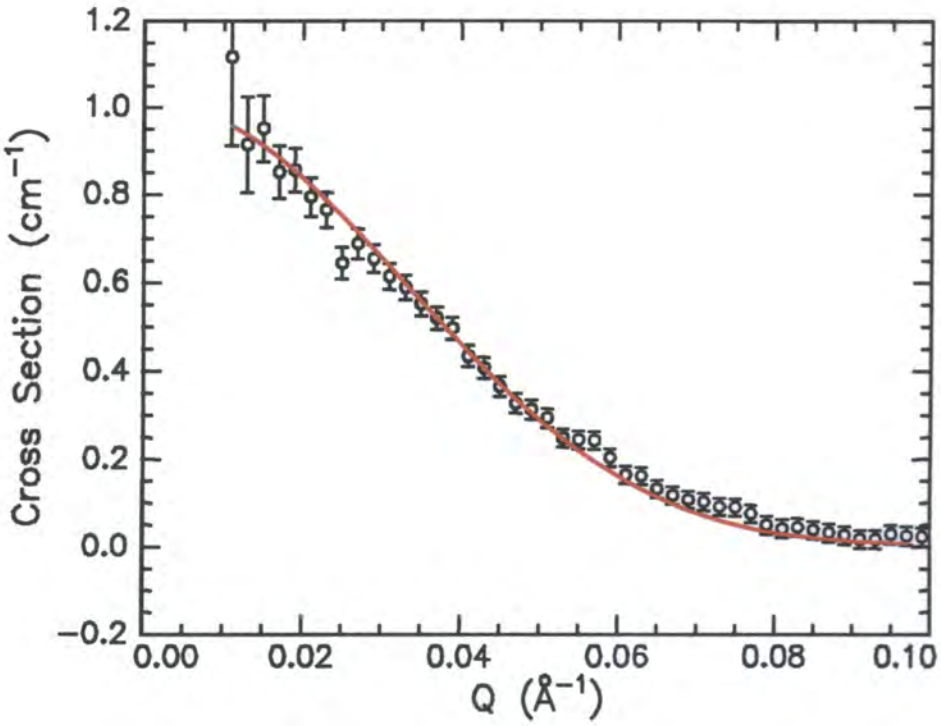


**Figure 6.18** SANS data for 0.5% dPS-hPEO in water contrast matched to hPEO. Red line is a fit to the data.

The program "Hayter" uses a set of Fortran subroutines written by Hansen and Hayter to calculate $S(Q)$. The parameters required for the calculation of $S(Q)$ are: the coupling constant ( $\gamma$ ), the dimensionless screening constant ( $k = \kappa\sigma$ ) and the micelle volume fraction ( $\eta = \frac{\pi\sigma^3 n}{6}$, where $\sigma$ is the micelle diameter ( $= 2(r_C + r_S)$ ) and $n$ is the number density). The total set of parameters that could be allowed to vary during fitting was as follows:

$\rho_C$ - the core SLD

$\rho_S$ - the shell SLD

$\rho_m$ - the dispersion medium SLD

$\overline{r_C}$ - the mean core radius

$pr$ - the % polydispersity of the core radius

$r_S$ - the shell thickness

$n$ - the micelle number density

$\gamma$ - the coupling constant

$k$ - the screening constant

The value of $\rho_C$ was fixed at the SLD of hPS or dPS (depending on the contrast) based on the assumption that the core region consisted purely of PS. The value of $\rho_m$ was also known for each contrast and could thus be fixed. When carrying out initial fits to the data, it was found that the value of $pr$ tended to rise to unrealistically high values if allowed to vary during fitting. The value of $pr$ was thus fixed at 40% for all of the fits (since values less than this reduced the fit quality in most cases). The parameters $r_C$, $r_S$ and $n$ were used in the calculation of both $P(Q)$ and $S(Q)$ and were thus allowed to vary during fitting. The parameters $\rho_S$, $\gamma$ and $k$ were also allowed to vary during fitting.

Tables 6.9 to 6.11 gives values of the parameters obtained from fits to the data (using the program "Hayter") for the various concentrations/contrasts studied by SANS.

| | Concentration (weight % polymer) | | |
|---|---|---|---|
| | 5 | 4 | 3 |
| **Parameter** | | | |
| $\overline{r_C}$ (Å) | 50.2 | 50.4 | 51.3 |
| $r_S$ (Å) | 95.1 | 96.4 | 98.3 |
| $\rho_S$ ($\times 10^6$ Å$^{-2}$) | 0.71 | 0.73 | 0.73 |
| $n$ ($\times 10^8$ Å$^{-3}$) | 1.53 | 1.17 | 0.87 |
| $\gamma$ | 595.8 | 790.6 | 367.4 |
| $k$ | 5.28 | 5.71 | 5.26 |
| $\gamma \exp(-k)$ | 3.04 | 2.62 | 1.90 |

**Table 6.9** Parameters obtained from fits to the SANS data acquired for dPS-dPEO in zero SLD water using the program "Hayter".

| | Concentration (weight % polymer) | | |
|---|---|---|---|
| | 5 | 4 | 3 |
| **Parameter** | | | |
| $\overline{r_C}$ (Å) | 44.4 | 44.2 | 45.0 |
| $r_S$ (Å) | 96.5 | 97.0 | 105 |
| $\rho_S$ ($\times 10^6$ Å$^{-2}$) | - | - | - |
| $n$ ($\times 10^8$ Å$^{-3}$) | 1.88 | 1.66 | 1.09 |
| $\gamma$ | 1270.0 | 50.6 | 6239.0 |
| $k$ | 6.22 | 2.96 | 8.91 |
| $\gamma \exp(-k)$ | 2.53 | 2.61 | 0.84 |

**Table 6.10** Parameters obtained from fits to the SANS data acquired for dPS-hPEO in water contrast matched to hPEO using the program "Hayter".

| | Concentration (weight % polymer) | | | | | |
|---|---|---|---|---|---|---|
| | 6.5 | 6 | 5 | 4 | 3 | 2 |
| **Parameter** | | | | | | |
| $\overline{r_C}$ (Å) | 52.1 | 52.4 | 52.7 | 53.3 | 54.5 | 54.4 |
| $r_S$ (Å) | 93.5 | 93.6 | 96.4 | 96.3 | 99.1 | 97.3 |
| $\rho_S$ ($\times 10^6$ Å$^{-2}$) | 5.86 | 5.87 | 5.85 | 5.83 | 5.84 | 5.82 |
| $n$ ($\times 10^8$ Å$^{-3}$) | 2.23 | 2.10 | 1.63 | 1.18 | 0.86 | 0.57 |
| $\gamma$ | 24.98 | 23.60 | 25.82 | 522.3 | 4774.0 | 388.4 |
| $k$ | 1.60 | 1.87 | 2.29 | 5.62 | 8.14 | 5.38 |
| $\gamma \exp(-k)$ | 5.06 | 3.64 | 2.61 | 1.89 | 1.39 | 1.79 |

**Table 6.11** Parameters obtained from fits to the SANS data acquired for hPS-hPEO in $D_2O$ using the program "Hayter".

In addition to the concentrated dispersions, SANS data were also collected for three different contrasts at dispersion concentrations of 0.5%. These data (for which $S(Q) = 1$ for all $Q$) were fitted using the program "Ottewill" (which uses the same form factor as "Hayter") in order to compare the values of the parameters so obtained with the values obtained for the concentrated dispersions. The data acquired at concentrations of 0.5% are displayed in figures 6.15 to 6.17, and the parameter values obtained from fits to the data using the program "Ottewill" are given in table 6.12.

The values of the parameters obtained from the fits can be used to calculate certain other parameters describing the micelle morphology. Aggregation numbers can be calculated from the mean core volumes (since the block molecular weights and densities for hPS and dPS are known). The volume fraction of PEO present in the shell can be calculated via two different methods: method (i) - using the shell volume and aggregation number (since the block molecular weights and densities for hPEO and dPEO are known) and method (ii) - using the shell SLD (since the PEO and dispersion medium SLD's are known).

| | Polymer | | |
|---|---|---|---|
| | dPS-hPEO | dPS-dPEO | hPS-hPEO |
| **Parameter** | | | |
| $\overline{r_C}$ (Å) | 43.9 | 53.2 | 53.3 |
| $r_S$ (Å) | 100.0 | 95.9 | 94.6 |
| $\rho_S$ ($\times 10^6$ Å$^{-2}$) | - | 0.81 | 5.76 |
| $n$ ($\times 10^8$ Å$^{-3}$) | 0.22 | 0.132 | 0.185 |

**Table 6.12** Parameters obtained from fits to SANS data acquired for dispersion concentrations of 0.5%. The data were fitted using the program "Ottewill".

The veracity of the fits can be checked by calculating the dispersion concentrations (% polymer by weight) based on the aggregation numbers and micelle number densities for each system. These can then be compared with the known solution concentrations.

Table 6.13 gives values for the aggregation number ($N_{agg}$) and the PEO volume fraction within the shell ($\phi_{PEO}$ - calculated using both methods described above) for each concentration/contrast.
Table 6.14 compares the dispersion concentrations calculated using parameters obtained from fits to the experimental data with the known dispersion concentrations.

Core radii for the dPS-dPEO and hPS-hPEO polymer dispersions are all in the range 50-55Å, which is somewhat larger than the 43-47Å obtained from fits to the data acquired at low concentration using FISH. Core radii for the dPS-hPEO dispersions are all approximately 44-45Å, and there is no obvious reason why these radii should be lower than those for the other two polymers.

| Polymer | Concentration (% polymer by weight) | $N_{agg}$ | $\phi_{PEO}$ [a] | $\phi_{PEO}$ [b] |
|---|---|---|---|---|
| dPS-hPEO | 5 | 194 | 0.16 | - |
| dPS-hPEO | 4 | 191 | 0.16 | - |
| dPS-hPEO | 3 | 201 | 0.16 | - |
| dPS-hPEO | 0.5 | 187 | 0.14 | - |
| dPS-dPEO | 5 | 279 | 0.22 | 0.10 |
| dPS-dPEO | 4 | 283 | 0.21 | 0.10 |
| dPS-dPEO | 3 | 299 | 0.21 | 0.10 |
| dPS-dPEO | 0.5 | 332 | 0.24 | 0.11 |
| hPS-hPEO | 6.5 | 262 | 0.23 | 0.09 |
| hPS-hPEO | 6 | 266 | 0.23 | 0.09 |
| hPS-hPEO | 5 | 270 | 0.22 | 0.09 |
| hPS-hPEO | 4 | 281 | 0.22 | 0.10 |
| hPS-hPEO | 3 | 300 | 0.22 | 0.09 |
| hPS-hPEO | 2 | 298 | 0.23 | 0.10 |
| hPS-hPEO | 0.5 | 281 | 0.23 | 0.11 |

**Table 6.13** Aggregation numbers and PEO volume fractions in the shell calculated from fits to the SANS data. ([a] Shell PEO volume fraction calculated from aggregation number ($N_{agg}$), shell volume, PEO molecular weight and PEO density. [b] Shell PEO volume fraction calculated from shell SLD ($\rho_S$).)

Values for the shell thickness are very similar for all of the polymers and at all concentrations, lying mainly in the range 95-100Å. These shell thickness values are considerably lower than those obtained from fits to the data acquired at low concentration using FISH. The most probable reason for this is that the form factor used in the programs "Ottewill" and "Hayter" assumes that the SLD profile through the shell is uniform, whereas in reality there is a decay in EO monomer density with increasing distance from the core. Thus, a SLD profile representing a constant EO monomer density throughout the shell is likely to underestimate the shell thickness.

| Polymer | Concentration [a] (% polymer by weight) | Concentration [b] (% polymer by weight) |
|---|---|---|
| dPS-hPEO | 5 | 4.6 |
| dPS-hPEO | 4 | 4.0 |
| dPS-hPEO | 3 | 2.8 |
| dPS-hPEO | 0.5 | 0.5 |
| dPS-dPEO | 5 | 5.9 |
| dPS-dPEO | 4 | 4.6 |
| dPS-dPEO | 3 | 3.6 |
| dPS-dPEO | 0.5 | 0.6 |
| hPS-hPEO | 6.5 | 8.4 |
| hPS-hPEO | 6 | 8.0 |
| hPS-hPEO | 5 | 6.3 |
| hPS-hPEO | 4 | 4.8 |
| hPS-hPEO | 3 | 3.7 |
| hPS-hPEO | 2 | 2.5 |
| hPS-hPEO | 0.5 | 0.7 |

**Table 6.14** Comparison of [a] known dispersion concentrations with [b] concentrations calculated from the aggregation number ( $N_{agg}$ ) and micelle number density ( $n$ ).

Good agreement is also observed between values for the shell SLD for different concentrations within each contrast, and values for the micelle number densities decrease with decreasing concentration (in all cases) as expected.

Aggregation numbers for the dPS-dPEO and hPS-hPEO copolymers lie in the range 262-332 for all concentrations (slightly higher than those obtained from fits to the data acquired at low concentration using FISH). Aggregation numbers for the dPS-hPEO copolymer dispersions are somewhat lower (table 6.13), reflecting the fact that the core radii obtained for dispersions of this polymer were lower than for the other 2 copolymers. Another interesting feature of the dPS-dPEO and hPS-hPEO systems is that on the whole, the core radius and aggregation number both decrease slightly with increasing concentration. It is difficult, however, to state conclusively whether or not

this represents a genuine feature of the system (i.e. the micelles get slightly smaller as the number density increases) since the changes are very small and might therefore lie within the margin of error inherent in the data fitting process. It is also interesting to compare the calculated values for the volume fraction of PEO present in the shell (table 6.13). Values calculated using method (i) (i.e. using the shell volume and $N_{agg}$ as discussed previously) for the dPS-dPEO and hPS-hPEO copolymers are very similar, while values for the dPS-hPEO copolymer calculated using this method are somewhat lower (again reflecting the fact that the core radii and therefore aggregation numbers were lower for this polymer). Good agreement is also obtained between values for $\phi_{PEO}$ calculated using method (ii) (i.e. using the shell SLD) for the dPS-dPEO and hPS-hPEO copolymers. However, the values for $\phi_{PEO}$ calculated using method (ii) are less than 50% of those calculated using method (i). This discrepancy probably again lies with the fact that the use of a form factor describing uniform EO density throughout the shell is likely to underestimate the PEO volume fraction within the shell (reflected in the value of $\rho_S$ obtained from the fits). Additionally, since the uniform shell model underestimates the shell thickness (and therefore the shell volume), values for $\phi_{PEO}$ calculated using the aggregation number and shell volume (method (i)) are likely to be artificially high. The true value of $\phi_{PEO}$ is thus likely to lie somewhere in between the values calculated using methods (i) and (ii).
It is also observed that values for the dispersion concentrations calculated from fits to the data show reasonable agreement with the known concentrations (table 6.14).

Parameters obtained from fits to the SANS data acquired for dispersion concentrations of 0.5% using the program "Ottewill" (dilute dispersions – table 6.12) show extremely good agreement with those obtained for the concentrated dispersions using the program "Hayter". Since the parameters $r_C$, $r_S$ and $n$ are used in the calculation of both $P(Q)$ and $S(Q)$, this gives an indication of how well the Hayter-Hansen structure factor describes the way in which $\frac{d\Sigma}{d\Omega}(Q)$ is modulated by interference effects between neutrons scattered from different micelles.

The interpretation of the fitted parameters associated with $S(Q)$ is somewhat harder. The Hayter-Hansen $S(Q)$ was developed to describe macroion solutions, but in the micellar system studied here no charge is present and interactions between micelles are therefore sterically based. No trends are observed in the values of $\gamma$ or $k$ with increasing concentration for any of the copolymers studied. However, for macroion solutions, $\gamma \exp(-k)$ represents the contact potential for a macroion pair (expressed in units of $k_B T$), and a definite trend is observed in the values of $\gamma \exp(-k)$ with increasing concentration (tables 6.9 to 6.11) i.e. with only two exceptions, the values of $\gamma \exp(-k)$ obtained from fits to the SANS data increase with increasing concentration. Since the micelle morphology does not change with increasing concentration (as shown by the results of fits to the SANS data discussed above), the value of the contact potential for a micelle pair is expected to be concentration independent. This implies that the values of $\gamma \exp(-k)$ obtained from the fits might be interpreted as a measure of the strength of the interaction between micelles (since this is expected to increase with increasing concentration). Dimensionless interaction potentials as a function of the micelle centre to centre distance ($r$) calculated using equation 6.9 are shown in figure 6.19 for dPS-dPEO concentrations of 3, 4 and 5%. However, the form of these potentials is not strictly valid for the steric interactions between micelles that apply to the experimental system studied here. The micelle shells are diffuse structures containing PEO volume fractions in the semi-dilute regime. Additionally, the PEO volume fraction shows a decay (the form of which is expected to be somewhere between a parabola and a power law) with increasing distance from the core. This means that some degree of overlap can occur between the shell regions of neighbouring micelles as the micelle number density increases (and the mean free path of the micelles decreases). Such overlap is extremely repulsive, but means nonetheless that the interaction potential curve extends a finite distance into the region for which $r < 2(r_C + r_S)$. The potentials calculated from equation 6.9, however, are only valid for $r > 2R$ (where $R$ is the total particle radius). The interaction potential describing steric interactions between spherical core-shell particles is illustrated in figure 6.20. The ability of the micelle shells to overlap means that the interaction potential curve shows a more gradual increase to $+\infty$ as the centre to centre distance decreases. The potential for a hard-sphere interaction, however,

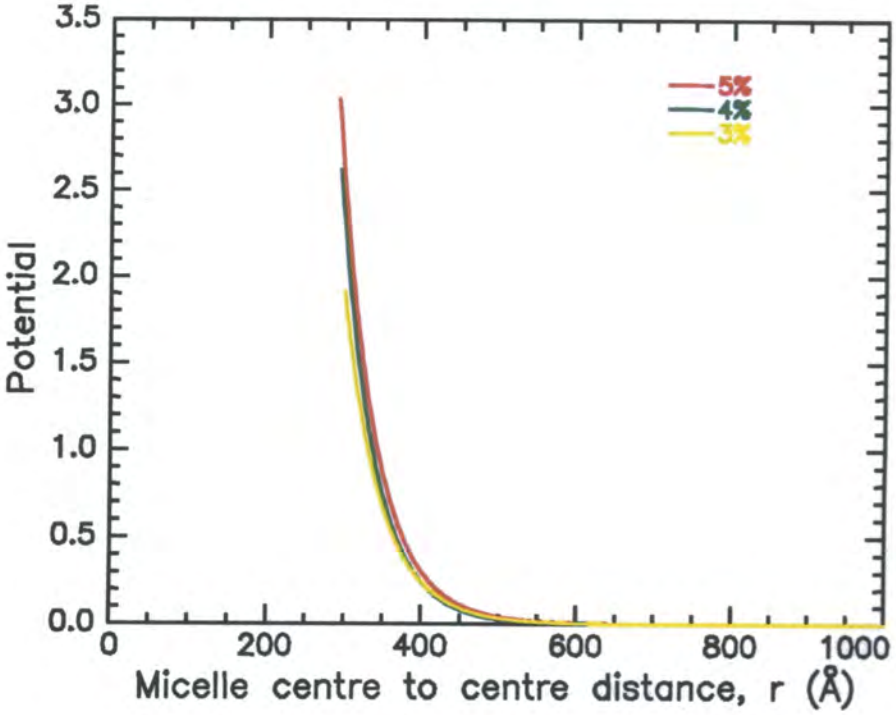


**Figure 6.19** Dimensionless interaction potential curves for dPS-dPEO in $D_2O$ at concentrations of 3, 4 and 5%. The curves were calculated using equation 6.9 using values of $\sigma$, $\gamma$ and $k$ obtained from fits to the SANS data using the program "Hayter".

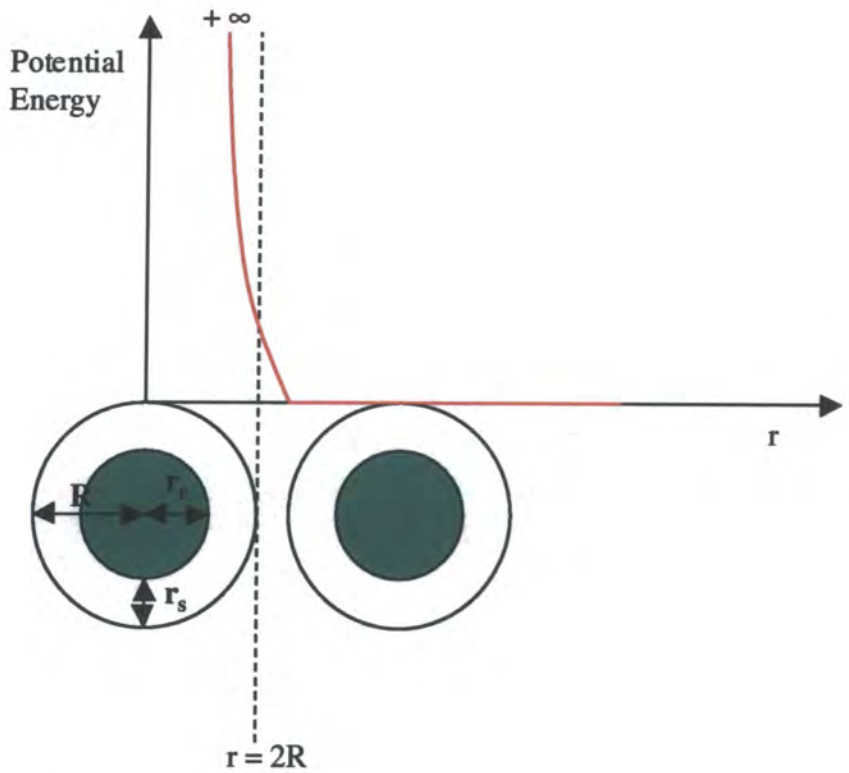


**Figure 6.20** Schematic illustration of a steric interaction between micelles.

rises abruptly to $+\infty$ at $r = 2R_{HS}$ (figure 6.7), and this may well explain why satisfactory fits to the SANS data were not obtained using a hard-sphere model for $S(Q)$. The steep potential barrier associated with the hard-sphere model provides a reasonable approximation for the interaction potential in core-shell systems providing that the shell thickness is small compared to the total particle radius [18]. However, since the shell thickness for the micellar system studied here accounts for the majority of the total particle radius, the interaction potential curve describing the inter-micellar interaction is better represented by figure 6.20.

Various theoretical models have been developed to describe the thermodynamics associated with steric interactions [19-20] (i.e. the overlap of diffuse shell regions for spherical core-shell particles) and the reader is referred to refs. 19 and 20 for examples.

The $Q$ value corresponding to the position of the maximum in the $S(Q)$ peak ($Q_{max}$) can be used to calculate the mean inter-particle spacing, $d$ (i.e. the mean micelle centre to centre distance) according to equation 6.15 [22].

$$Q_{max} d = 2\pi \qquad \textbf{Equation 6.15}$$

Table 6.15 compares $d$ values calculated from the SANS data for each concentration/contrast with the corresponding values of the micelle diameter ($= 2(r_C + r_S)$). This gives an indication of how close together the micelles are in the dispersions which in turn provides a measure of the likelihood of shell overlap occurring.

As the dispersion concentration is increased, the micelles are forced closer together and thus interact more strongly with each other. Eventually, the shell regions of neighbouring micelles start to overlap significantly leading to the formation of a liquid crystalline phase. This corresponds to a transition of the micellar dispersion from a liquid-like state (or sol) to a gel state (where the dispersion will no longer flow under its own weight). For spherical micelles the gel state corresponds to the ordering of the micelles into cubic phases, and for aqueous dispersions of the copolymers used in these studies, gels were formed (at 298K) at concentrations of approximately 8-9%.

Even at the highest dispersion concentration studied in the work presented here (6.5% for hPS-hPEO), the micellar solution was free flowing. This observation can be

| Polymer | Concentration (% polymer by weight) | $d$ (Å) | $2(r_C + r_S)$ (Å) |
|---|---|---|---|
| dPS-hPEO | 5 | 312 | 282 |
| dPS-hPEO | 4 | 326 | 282 |
| dPS-hPEO | 3 | 342 | 300 |
| dPS-dPEO | 5 | 368 | 291 |
| dPS-dPEO | 4 | 407 | 294 |
| dPS-dPEO | 3 | 451 | 299 |
| hPS-hPEO | 6.5 | 332 | 291 |
| hPS-hPEO | 6 | 340 | 292 |
| hPS-hPEO | 5 | 368 | 298 |
| hPS-hPEO | 4 | 410 | 299 |
| hPS-hPEO | 3 | 448 | 307 |

**Table 6.15** Comparison of average inter-micellar distances ($d$) and micelle diameters ($2(r_C + r_S)$).

explained by looking at the data in table 6.15 which show that $d > 2(r_C + r_S)$ for all cases. This means that collisions between micelles involving the highly repulsive overlap of the shell regions will be rare even at the highest concentrations studied in this work (6.5%).

It is also interesting to note from table 6.15 that $d$ values for the dPS-dPEO and hPS-hPEO copolymers at each concentration are very similar in magnitude, while values for the dPS-hPEO copolymer are somewhat smaller. This trend shows agreement with that observed in the core radius values obtained from fits to the SANS data (i.e. core radii for the dPS-hPEO polymer were found to be slightly lower than for the other two polymers). There is no obvious explanation for this phenomenon since the dPS-hPEO and dPS-dPEO copolymers have identical molecular weight PS blocks, and shell thickness values obtained from fits to the SANS data were approximately 100Å in all cases.

Mortensen et al. [23] also investigated a diblock copolymer of styrene and ethylene oxide (dispersed in water) with PS and PEO block molecular weights of 1000 and 3000 g $mol^{-1}$ respectively. Dynamic light scattering and SANS were used to probe the micelle morphology. The SANS data were fitted using a spherical core-shell form factor coupled with a hard-sphere structure factor, and at 293K the micelles were found to have core radii of 56Å (the cores were assumed to be water free and to consist solely of PS). The PEO chains within the shell had $R_g$ = 37Å, and the aggregation number for the micelles was 470. It is interesting to note that the core radius obtained by Mortensen et al is somewhat larger than the average core radius obtained in the work reported here (from fits to the SANS data using the program FISH) in spite of the fact that the copolymer used had a slightly lower molecular weight PS block. (This discrepancy may reflect the different methods used to fit the experimental data.) However, the value for the shell thickness (referred to as the shell chain $R_g$ by Mortensen et al) is considerably lower than the average value obtained in the work reported here. This reflects the fact that the PEO block molecular weight of the copolymer used by Mortensen et al was less than 50% of the average PEO block molecular weight for the copolymers used in the work reported here.

### 6.3.3 Shear Effects

As the concentration of a micellar dispersion is increased, the polymeric micelles undergo a disorder-order transition whereby they organise into arrays of either body-centred cubic (BCC) or face-centred cubic (FCC) symmetry depending on the micellar structure. McConnell et al [24] have shown that the BCC structure is favoured by micelles having large shell thicknesses relative to the core size. The onset of such long-range order in micellar systems can be observed in the 2-dimensional (2D) SANS pattern (i.e. the scattering intensity contour pattern) by the emergence of anisotropy. This anisotropy takes the form of spots in the scattering intensity contour patterns due to Bragg reflections arising from the quasi-crystalline order, and the number of spots and their positions indicate the exact nature of the order.

The 2D SANS plots for the data acquired under quiescent conditions did not display any such spots (i.e. they were isotropic) even at the highest concentration studied (6.5%). This indicated that no long-range order existed on the length scales probed in the SANS experiments.

Dispersions of hPS-hPEO in $D_2O$ were studied under Couette shear flow at concentrations up to 6.5% to see if the presence of shear induced long-range order in this micellar system. All experiments were carried out at 298K.
The LOQ Couette cell [25] is illustrated schematically in figure 6.20. Experiments were carried out with the neutron beam passing through the cell in both radial (beam perpendicular to the plane defined by the flow and vorticity directions)

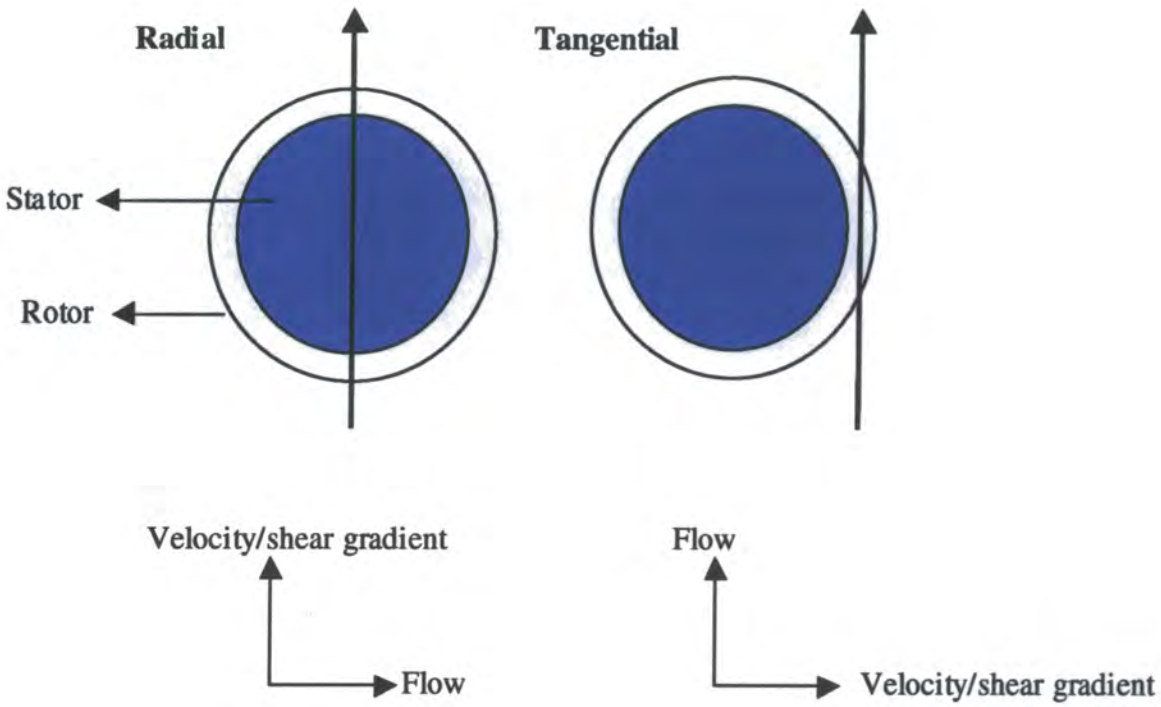


**Figure 6.20** Schematic illustration of the Couette shear cell (viewed from above). The neutron beam paths for radial and tangential beam geometries are illustrated along with the flow directions and velocity/shear gradient directions appropriate for each beam geometry. In both cases, the vorticity (or neutral) direction is perpendicular to the plane of the page.

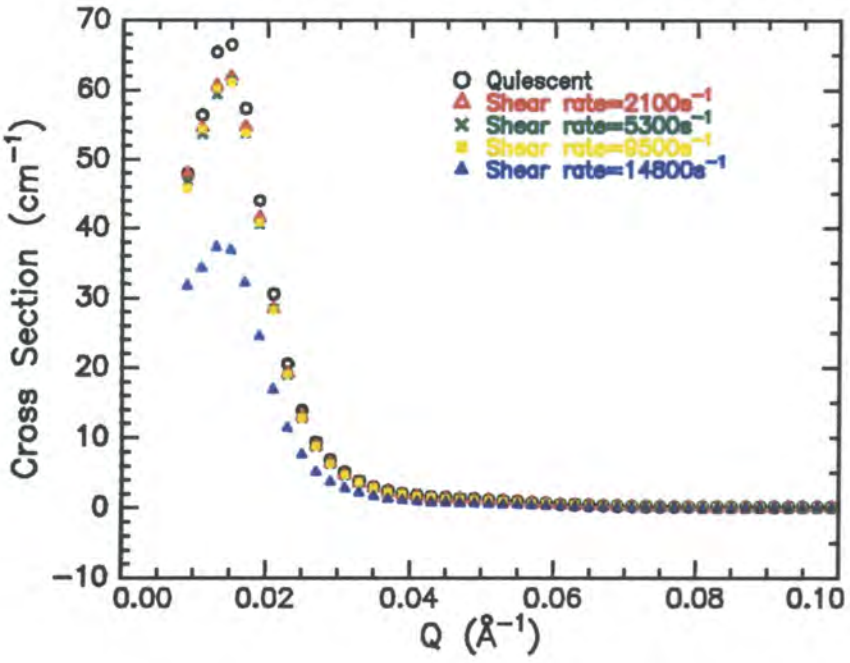


**Figure 6.21** SANS data obtained for 3% hPS-hPEO in $D_2O$ under quiescent and Couette shear conditions. (The pre-shear quiescent data were obtained using a rectangular quartz sample cell.) Radial beam geometry was used.

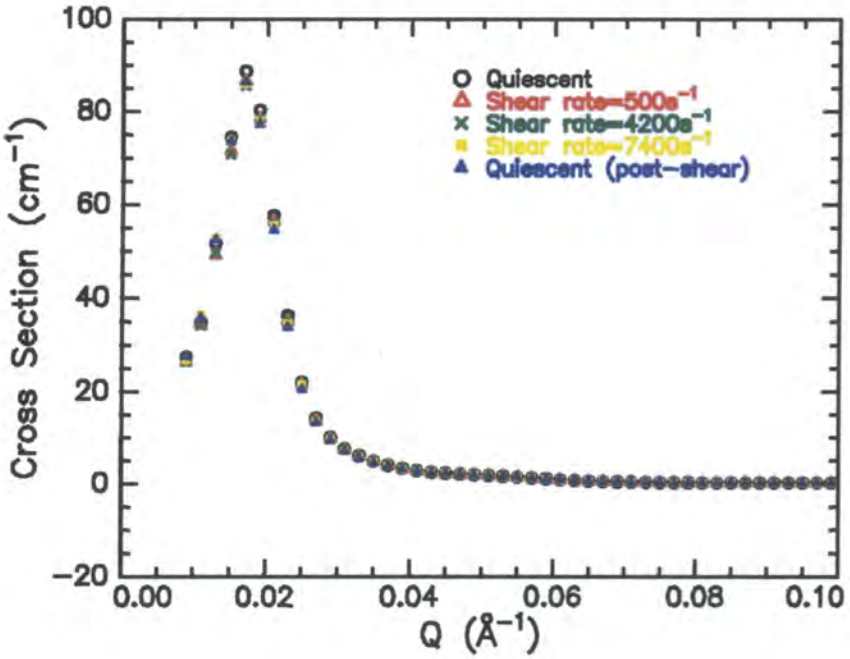


**Figure 6.22** SANS data obtained for 5% hPS-hPEO in $D_2O$ under quiescent and Couette shear conditions. (The pre-shear quiescent data were obtained using a rectangular quartz sample cell. The post-shear quiescent data were obtained using the Couette cell.) Radial beam geometry was used.

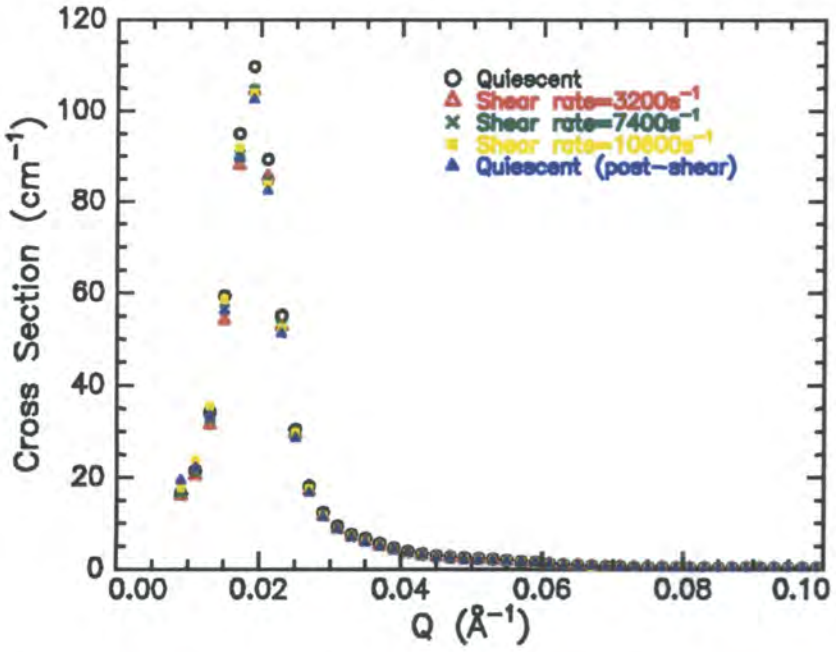


**Figure 6.23** SANS data obtained for 6.5% hPS-hPEO in $D_2O$ under quiescent and Couette shear conditions. (The pre-shear quiescent data were obtained using a rectangular quartz sample cell. The post-shear quiescent data were obtained using the Couette cell.) Radial beam geometry was used.

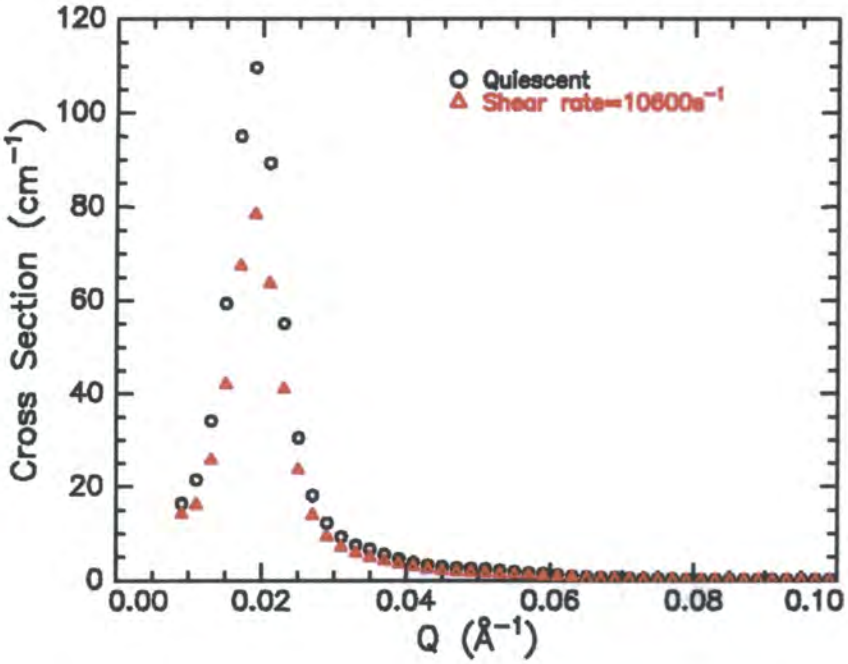


**Figure 6.24** SANS data obtained for 6.5% hPS-hPEO in $D_2O$ under quiescent and Couette shear conditions. (The pre-shear quiescent data were obtained using a rectangular quartz sample cell.) Tangential beam geometry was used.

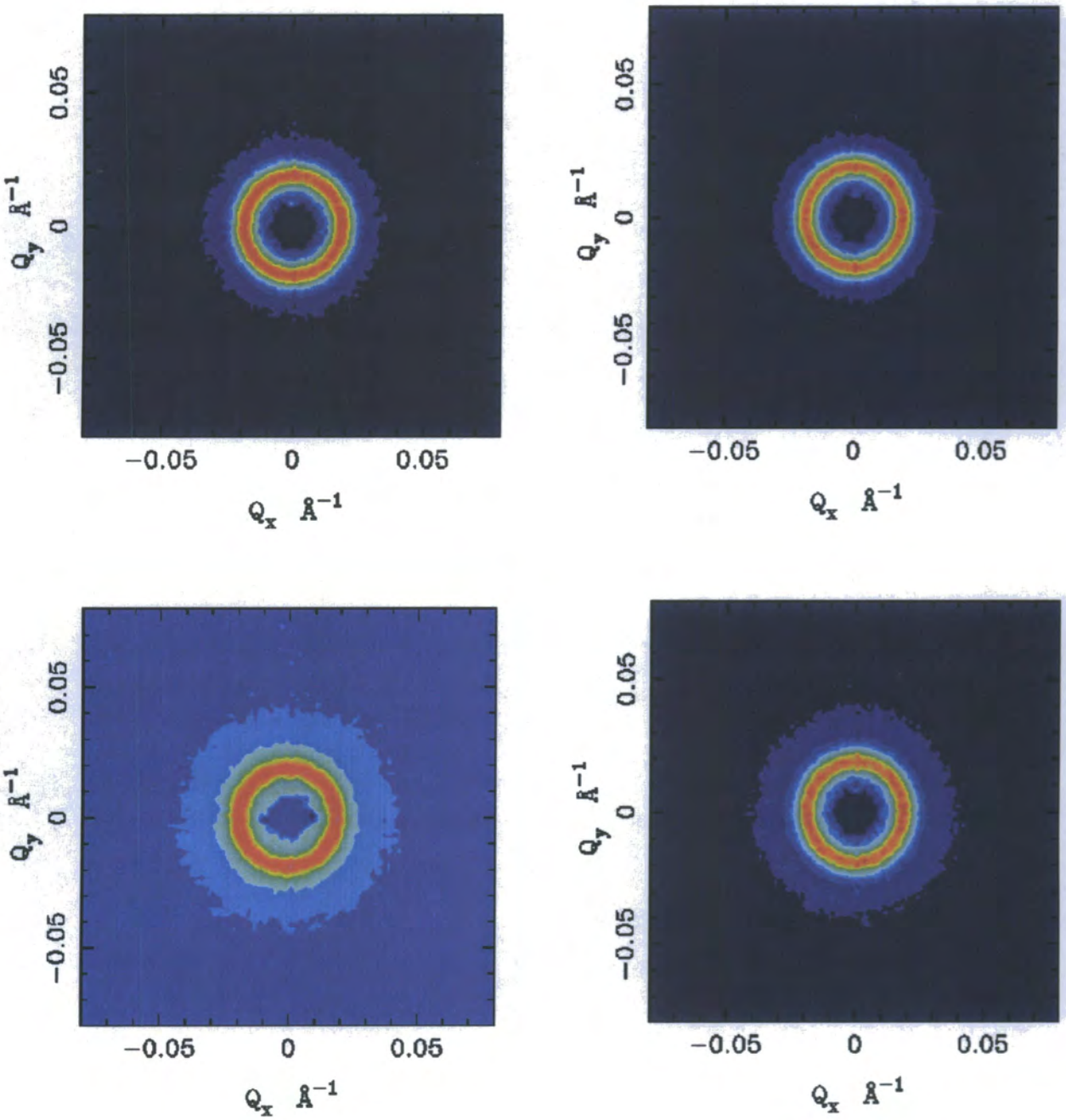


**Figure 6.25** Two-dimensional SANS intensity contour plots of data obtained for 6.5% hPS-hPEO in D2O under quiescent and Couette shear conditions. Clockwise from top left: quiescent (rectangular quartz cell), shear rate=3200$s^{-1}$ (radial), shear rate=10600$s^{-1}$ (radial) and shear rate=10600$s^{-1}$ (tangential).

and tangential (beam parallel to the plane defined by the flow and vorticity directions) geometries.

The results of the shear experiments are shown in figures 6.21 to 6.25. It can be seen from these figures that Couette shear had no effect on the position of the $S(Q)$ peak at any of the concentrations studied. A slight discrepancy is observed in intensity at the maximum between the pre-shear quiescent experiment and the experiments carried out in the Couette cell. This is simply a pathlength effect arising from the fact that the pre-shear quiescent experiments were run using rectangular quartz sample cells while the shear experiments were run in the Couette cell. The more dramatic drop in intensity observed at a shear rate of $14800s^{-1}$ for the 3% dispersion was due to the formation of bubbles in the sample containing region (i.e. between the rotor and the stator in the Couette cell) at this high shear rate.

Figure 6.24 shows data obtained for a 6.5% dispersion under quiescent (rectangular sample cell) and shear flow (Couette cell) conditions with tangential neutron beam geometry. Again, the position of the $S(Q)$ maximum does not change as a result of shear. However, the drop in intensity seen for the data acquired under shear again represents a pathlength effect. In this case, the pathlength through the Couette cell was not known for the tangential beam geometry and thus the data acquired are not on an absolute scale with respect to the differential scattering cross-section.

The position of the $S(Q)$ peaks gives an indication of the short-range order length scales within the micellar systems (equation 6.15), and the observation that shear had no effect on the positions of these peaks indicates that shear had no effect on the mean interparticle spacings.

Figure 6.25 shows a selection of scattering intensity contour plots for data obtained under quiescent and Couette shear conditions using a 6.5% dispersion. No spots are seen in these contour plots (i.e. they are isotropic), and this indicates that no long-range order was induced as a result of shear on the length scales probed in the SANS experiments. The most probable reason for this was that the dispersions were not of sufficiently high concentration. Under quiescent conditions, the organisation of the micelles at concentrations of up to 6.5% (i.e. the highest concentration studied) is liquid-like. For such systems to order in a shear field, the shear field has to stifle and overcome the inherent rotational diffusive motion of the micelles, and for spherical micelles with liquid-like quiescent organisation this is highly unlikely to happen.

Mortensen et al [26] studied the BCC phase of a poly(ethylene oxide-*b*-propylene oxide-*b*-ethylene oxide) triblock copolymer gel in water under Couette shear. It was found that shear caused alignment of the polycrystalline domains into a single crystal.
McConnell et al [27] performed Couette shear experiments on BCC and FCC gel phases of a poly(styrene-*b*-isoprene) copolymer in decane. For the FCC structure it was found that shear caused a transition from polycrystallinity to <111> sliding layers. The BCC crystals were found to orient into a twinned BCC structure with the <110> planes normal to the shear gradient direction. At high shear rates, shear melting of the BCC structure was observed.

## 6.4 Conclusions

Micelle formation by diblock copolymers of styrene and ethylene oxide (PS-PEO) dispersed in water has been investigated using small angle neutron scattering. For dispersion concentrations in the range 0.05 to 1% polymer by weight, no contributions to the scattering arising from inter-micellar interference effects were observed. Satisfactory fits to these data were obtained using a spherical core-shell model for the form factor. The core was assumed to consist solely of PS, while the shell region (consisting of PEO and water) was described in the fitting program as having a parabolic decay in EO monomer density with increasing distance from the core. The shell chains were found to be strongly stretched relative to the radius of gyration of isolated PEO chains in aqueous solution.
For dispersion concentrations in the range 2 to 6.5%, contributions to the scattering arising from inter-micellar interference effects were observed, with the size of the $S(Q)$ peak increasing with increasing concentration. Satisfactory fits to these data were not obtained using a hard-sphere model for the intermicellar interaction. However, good fits to the experimental data were obtained using an analytic structure factor originally developed to describe spherical macroions in solution. The fitted parameters describing this macroion $S(Q)$ have been tentatively interpreted in terms of a sterically based interaction between the PS-PEO micelles.

The effect of Couette shear on dispersions of the hPS-hPEO copolymer in $D_2O$ at concentrations of up to 6.5% was investigated. However, no evidence of shear-induced long-range ordering of the micelles was observed.

## 6.5 Glossary of Symbols

| | |
|---|---|
| $d$ | Mean interparticle spacing |
| $d_{PEO}$ | Distance between PEO chains at the core surface |
| $k$ | Dimensionless screening constant |
| $k_B$ | Boltzmann constant |
| $M_n$ | Number average molecular weight |
| $M_w$ | Weight average molecular weight |
| $n$ | Micelle/macroion number density |
| $N$ | Particle number density |
| $N_p$ | Hard-sphere number density |
| $P(Q)$ | Form factor |
| $Q$ | Momentum transfer |
| $pr$ | Percentage core radius polydispersity |
| $r$ | Inter-particle centre to centre distance |
| $r_C, \overline{r_C}$ | Core radius, mean core radius |
| $r_S$ | Shell thickness |
| $R$ | Total particle radius |
| $R_g$ | Unperturbed radius of gyration |
| $R_{HS}$ | Hard-sphere radius |
| $S(Q)$ | Inter-particle structure factor |
| $T$ | Absolute temperature |
| $V$ | Particle volume |

| | |
|---|---|
| $\beta$ | Inverse temperature in energy units |
| $\varepsilon$ | Dielectric constant of the solvent medium |
| $\varepsilon_0$ | Permittivity of free space |
| $\phi_{H_2O}$ | $H_2O$ volume fraction |
| $\phi_{D_2O}$ | $D_2O$ volume fraction |
| $\phi_{HS}$ | Hard-sphere volume fraction |
| $\phi_{PEO}$ | PEO volume fraction |
| $\gamma$ | Dimensionless coupling constant |
| $\eta$ | Particle (micelle or macroion) volume fraction |
| $\kappa$ | Debye-Hückel inverse screening length |
| $\rho_{D_2O}$ | $D_2O$ scattering length density |
| $\rho_{H_2O}$ | $H_2O$ scattering length density |
| $\rho_N$ | Dispersion medium scattering length density |
| $\Delta\rho$ | Difference in scattering length density |
| $\sigma$ | Standard deviation |
| $\sigma_d$ | Particle diameter |
| $\psi_0$ | Surface potential |
| $\frac{d\Sigma}{d\Omega}(Q)$ | Differential scattering cross-section |

## 6.6 References


1 Pethrick, R A; Dawkins, J V (Eds.). *Modern Techniques for Polymer Characterisation.* John Wiley and Sons Ltd (1999).

2 http://www.isis.rl.ac.uk/largescale/loq/loq.htm

3 King, S M. *Using Colette – A Step-by-Step Guide.* Rutherford Appleton Laboratory (1998).

4 Dewhurst, P F; Lovell, M R; Jones, J L; Richards, R W; Webster, J R P. *Macromolecules*, 1998, **31**, 7851.

5 Heenan, R K. *The "FISH" Manual.* Rutherford Appleton Laboratory Report, 89-129. Revised 1998.

6 Nakano, M; Matsuoka, H; Yamaoka, H; Poppe, A; Richter, D. *Macromolecules*, 1999, **32**, 697.

7 Milner, S T; Witten, T A; Cates, M E. *Macromolecules*, 1988, **21**, 2610.

8 Kotlarchyk, M; Chen, S H. *J. Chem. Phys.* 1983, **79**, 2461

9 Kawaguchi, S; Imai, G; Suzuki, J; Miyahara, A; Kitano, T; Ito, K. *Polymer*, 1997, **38**, 2885.

10 Dan, N; Tirrell, M. *Macromolecules*, 1992, **25**, 2891.

11 Percus, J K; Yevick, G J. *Phys. Rev.* 1958, **110**, 1.

12 Goodwin, J W (Ed.). *Colloidal Dispersions.* Royal Society of Chemistry (1982)

13 Kinning, D J; Thomas, E L. *Macromolecules*, 1984, **17**, 1712.

14 Ashcroft, N W; Lekner, J. *Phys. Rev.* 1966, **45**, 33.

15 Hayter, J B; Penfold, J. *Molecular Physics*, 1981, **42**, 109.

16 http://www.ill.fr/Computing/fitfun.htm

17 Hayter, J B; Hansen, J P. *The Structure Factor of Charged Colloidal Dispersions at Any Density.* Institut Max Von Laue – Paul Langevin, Internal Scientific Report, 1982.

18 Ottewill, R H; Rennie, A R (Eds.). *Modern Aspects of Colloidal Dispersions.* Kluwer Academic Press, Dordrecht (1998).

19 Napper, D H. *Polymeric Stabilization of Colloidal Dispersions.* Academic Press Inc. (London) Ltd (1983).

20 Lin, E K; Gast, A P. *Macromolecules*, 1996, **29**, 390.

21 Hamley, I W. *The Physics of Block Copolymers.* Oxford University Press (1998).

22 Higgins, J S; Blake, S; Tomlins, P E; Ross-Murphy, S B; Staples, E; Penfold, J; Dawkins, J V. *Polymer*, 1988, **29**, 1968.

23 Mortensen, K; Brown, W; Almdal, K; Alami, E; Jada, A. *Langmuir*, 1997, **13**, 3635.

24 McConnell, G A; Gast, A P; Huang, J S; Smith, S D. *Phys. Rev. Lett.* 1993, **71**, 2102

25 King, S M; Heenan, R K. *The LoQ Handbook*, 1996, Rutherford Appleton Laboratory Report, RAL-TR-96-036.

26 Mortensen, K; Brown, W; Norden, B. *Phys. Rev. Lett.* 1992, **68**, 2340

27 McConnell, G A; Lin, M Y; Gast, A P. *Macromolecules*, 1995, **28**, 6754

# CHAPTER 7

# CONCLUSIONS AND FUTURE WORK

# CHAPTER 7

## CONCLUSIONS AND FUTURE WORK

Polymer brush layers have been successfully formed using deuteropolystyrenes end grafted to silicon via short poly-4-vinyl pyridine end-groups. The two polymers used had similar polystyrene chain molecular weights ($M_w = 445\ 000$ and 495 000 g $mol^{-1}$), and the brush layers were studied under quiescent and shear flow conditions using a purpose built flow reflectometry cell, with both cyclohexane and toluene as solvents.

The trends observed in the reflectivity profiles with improving thermodynamic quality of the solvent are consistent with stretching of the brush layers in the direction normal to the grafting plane. This stretching arises from the increasingly repulsive inter-molecular excluded volume interactions between chain segments as the solvent quality is improved. The experimentally obtained reflectivity profiles were well described by parabola-like polymer volume fraction profiles (in accordance with the predictions of self-consistent field (SCF) theory [1]) when fitting the data using the optical matrix method. Comparison of the brush heights ($h$) obtained from the fits with the unperturbed radius of gyration ($R_g$) of the polystyrene chains revealed that the brush chains were strongly stretched. Indeed, the brush height in toluene (a thermodynamically good solvent for polystyrene) was found to be approximately $9R_g$, while even in cyclohexane at near theta temperatures the brush heights were found to be approximately $3-4R_g$. Comparison of the experimentally determined brush heights in cyclohexane at various temperatures with those predicted by SCF theory [1] suggested that the brush height scaled with the normalised grafting density ($\sigma$) as $\sigma^{0.44}$ (compared to $\sigma^{1/3}$ as predicted by SCF theory). However, it is possible

that this discrepancy has its origin in the fact that the grafting densities studied in this work were below the range for which the SCF predictions are valid.

The brush layers were exposed to shear by flowing the solvent past them at area-average shear rates of between 8 000 and 147 000 $s^{-1}$. However, no effect of shear was observed in the reflectivity profiles (apart from a limited degree of shear induced chain desorption when using toluene as the solvent). A possible explanation for this is that the maximum shear rate used was below the threshold for shear-induced brush swelling predicted by recent theory [2]. However, an inherent problem with these studies concerns the determination of the actual shear rate within the brush, since it is this value of the shear rate which will determine the onset and extent of any shear induced changes in the brush structure. A simple model was also proposed to illustrate how shear induced chain tilting and stretching processes could act to cancel one another out (partially or fully) in terms of the overall effect on the brush structure and dimensions.

Future studies should concentrate on exploring higher molecular weight brush polymers, since this provides one way of reaching the shear-induced swelling threshold predicted by theory. However, the fact remains that shear may have no net effect on the overall structure and dimensions of brush layers. Additionally, the lack of sensitivity of neutron reflectometry to subtle changes in the brush structure may limit its usefulness in studying such systems.

Micelles formed by diblock copolymers of styrene and ethylene oxide (PS-PEO) dispersed in water have been investigated using small angle neutron scattering. Four different copolymers were used in order to explore the full range of contrasts in the SANS experiments, and the polymers were synthesised to be as near identical as possible in terms of the block lengths. The average PS and PEO block lengths were 1355 and 7330 g $mol^{-1}$ respectively.

At concentrations of 0.05 to 1%, no contributions to the scattering arising from inter-micellar interference effects were observed, and these data were successfully fitted using a spherical core-shell model. The core was assumed to consist solely of PS, while a parabolic decay in monomer density (with increasing distance from the core) was used to describe the shell region. The average core radius obtained from the fits

was 45Å, and the average shell thickness was 132Å indicating that the PEO chains are strongly stretched relative to the $R_g$ of isolated PEO chains in aqueous solution. (The average $R_g$ of the PEO block is 27Å). The origin of this strong PEO chain stretching in the micelle shells is analogous to the stretching observed in planar polymer brush layers. The PEO chains are effectively grafted over the spherical surface of the core, with a mean distance between grafting sites of 10.7Å. This is considerably less than the $R_g$ of the PEO chains, and they thus stretch away from the core due to repulsive excluded volume interactions. In so doing, the EO segments maximise their enthalpically favourable interaction with the water molecules.

For dispersion concentrations in the range 2 to 6.5%, contributions to the scattering arising from inter-micellar interference effects were observed, with the size of the $S(Q)$ peak increasing with increasing concentration. Satisfactory fits to these data were not obtained using a hard-sphere model for the intermicellar interaction. However, good fits to the experimental data were obtained using an analytic structure factor originally developed to describe spherical macroions in solution. The fitted parameters describing this macroion $S(Q)$ have been tentatively interpreted in terms of a sterically based interaction between the PS-PEO micelles.

The effect of Couette shear on dispersions of the hPS-hPEO copolymer in $D_2O$ at concentrations of up to 6.5% was investigated. However, no evidence of shear-induced long-range ordering of the micelles was observed.

With regard to future work in this area, it would be interesting to investigate the following:

- The effect of different relative block sizes on the micelle morphology. This would enable theoretical predictions for the scaling of the core and total micelle radii with the degree of polymerisation of the core and shell chains [3-6] (discussed in chapter 2) to be tested. It would also be interesting to investigate whether or not a sphere-to-rod transition occurred for copolymers containing very long hydrophobic PS blocks [7].

- The effect of increasing temperature on the micellisation behaviour. Studying fixed dispersion concentrations over a range of temperatures using a combination of light scattering and small angle neutron scattering would enable critical micelle temperatures to be determined. The effect of increasing temperature on the micelle morphology could also be investigated (e.g. Mortensen et al [8] found that increasing the temperature of PS-PEO micellar dispersions lead to a slight reduction in the core radius and an increased degree of swelling of the PEO shell chains).

- The effect of Couette shear on gel phases of aqueous PS-PEO diblock copolymer dispersions. Since the shell thickness of the micelles studied is large relative to the core radius, they are expected to form a body-centred cubic (BCC) structure in the gel phase. Subjecting the gel phase to Couette shear would enable the nature of any shear-induced long-range ordering of the polycrystalline domains to be ascertained (from the position and arrangement of any Bragg reflection "spots" in the 2-dimensional diffraction pattern).

## References


1 Milner, S T; Witten, T A; Cates, M E. *Macromolecules*, 1988, **21**, 2610.

2 Aubouy, M; Harden, J L; Cates, M E. *J. Phys. II France*. 1996, **6**, 969.

3 Liebert, L (Ed). '*Solid State Physics*.' Volume **14**. Academic, New York (1978).

4 Daoud, M; Cotton, J P. *Journal de Physique*, 1982, **43**, 531.

5 Halperin, A. *Macromolecules*, 1987, **20**, 2943.

6 Nagarajan, R; Ganesh, K. *Journal of Chemical Physics*, 1989, **90**, 5843.

7 Nakano, M; Matsuoka, H; Yamaoka, H; Poppe, A; Richter, D. *Macromolecules*, 1999, **32**, 697.

8 Mortensen, K; Brown, W; Almdal, K; Alami, E; Jada, A. *Langmuir*, 1997, **13**, 3635.

# CHAPTER 8

# APPENDICES

# APPENDIX A

## FORTRAN PROGRAMS

The Fortran source codes for three programs written to fit small angle neutron scattering data are presented below. All three programs were written to fit data obtained for spherical core-shell micelles in solution.

### A1 Common Parameters

The following parameters are common to all three of the programs presented below:

*rhoc* = core scattering length density ($Å^{-2}$)
*rhos* = shell scattering length density ($Å^{-2}$)
*rhom* = dispersion medium scattering length density ($Å^{-2}$)
*r1* = core radius (Å)
*r2* = shell thickness (Å)
*nd* = micelle number density (micelles $Å^{-3}$)
*pr* = % polydispersity on the core radius

### A2 Program "Ottewill"

This program was written to fit small angle neutron scattering data for micellar dispersions in the absence of interparticle interference effects (i.e. $S(Q) = 1$ for all $Q$). The program uses a spherical core-shell model for the form factor (the monomer density is assumed to be uniform throughout the shell – see chapter 6, ref. 12 for

details of $P(Q)$ ). A Gaussian distribution can be placed on the core radius (expressed as the parameter " *pr* ", the % polydispersity of the core radius).

```
$DEBUG
c
c   WRITTEN BY GAVIN J BOWN    MAY 1999
c
c
c   A programme to fit SANS data for diblock copolymer micellar
c   dispersions.
c
          program Ottewill
          external readin,model
          common/titles/names(20),tx,ty
          common/titlep/nparas
          common/work/w(3066)
          common/version/verp
          common/modl/contrast
          character*8 names
          character*4 pnam
          character*20 tx,ty
c
          data names/'rhos','rhoc','rhom','r1',
         &'pr','r2','nd',13*' '/
          data pnam/'otte'/
          data tx/'Q /A^-1'/
          data ty/'Cross Section (cm-1)'/
          data nparas/7/
c
c         Write(6,'(a)')' Enter dPS molecular weight'
c         read(5,*)mwt
c
c   Call the fitting library
c
          call fitfun(pnam,readin,model)
c
c
c
c
          write(6,'(a)')' Finished'
          stop
c
          end
c
c   Set up the functional forms within a Gaussian routine
c   to account for polydispersity in the micelle sizes
c
          subroutine model(npar,parm,npts,xuse,yuse,yruse,
         &ycalc,F)
          real pr,rhos,rhoc,rhom,r1,r2,nd,xuse(npts),yuse(npts)
          real ycalc(200),SQ(200),F(200)
          common/modl/contrast
          dimension parm(7)
c
c
          rhos=parm(1)
          rhoc=parm(2)
```

```
      rhom=parm(3)
      r1=parm(4)
      pr=parm(5)
      r2=parm(6)
      nd=parm(7)
c
c
      pie=3.141592654
      nit=12
      dr=(r1*pr)/(2.35*100)
      rmax=r1+(dr*3)
      rmin=r1-(dr*3)
      div=(rmax-rmin)/nit
      do i=1,npts
      ycalc(i)=0
      do 50 j=1,(nit+1)
      rval=rmin+div*(j-1)
      f1=(16.0*(pie**2))/9.0
      f2=(rhos-rhom)
      f3=(rhoc-rhom)
      f4=xuse(i)*rval
      f5=xuse(i)*(rval+r2)
      f6=(sin(f5)-(f5*cos(f5)))/(f5**3)
      f7=(sin(f4)-(f4*cos(f4)))/(f4**3)
      f8=3*(rval+r2)**3
      f9=3*(rval**3)
      SQ(i)=f1*(f2*((f8*f6)-(f9*f7))+(f3*f9*f7))**2
      gauss=(1/(dr*2.51))*exp(-0.5*((r1-rval)/dr)**2)
      SOQ=SQ(i)*gauss
      ycalc(i)=ycalc(i)+SOQ*div
50    continue
      ycalc(i)=nd*ycalc(i)*1e8
      open(10,file='out.dat',status='unknown')
      write(10,*)xuse(i),ycalc(i)
      F(i)=ycalc(i)-yuse(i)
      enddo
      close(10)
      return
      end
c
c  Readin routine for LoQ .asc files
c
c
      subroutine readin(npts,xuse,yuse,yruse,text)
      dimension xuse(1000),yuse(1000),yruse(1000),temp(1000)
      character*50 text,garb
      character*20 fname
      logical exists
 10   write(6,15)
 15   format(/,' Give filename: ',$)
      read(5,20)fname
      inquire(file=fname,exist=exists)
      if(.not.exists)then
      write(6,25)
      goto 10
      endif
      open(7,file=fname,status='old')
      read(7,20)text
      read(7,20)garb
      read(7,20)garb
```

```
      read(7,20)garb
      read(7,20)garb
      npts=1
 30   read(7,*,end=99)xuse(npts),yuse(npts)
      npts=npts+1
      goto 30
 99   npts=npts-1
      close(7)
c     kount=0
c     j=0
      do i=1,npts
      yruse(i)=0.0
c     if(yuse(i).gt.0)then
c     j=j+1
c     temp(j)=log10(yuse(i))
c     else
c     kount=1
c     endif
c 50  enddo
c     npts=npts-kount
c     do i=1,npts
c     yuse(i)=temp(i)
      enddo
 20   format(a)
 25   format('No file of that name present!!')
      return
      end
```

## A3 Program "Hayter"

This program uses the same form factor as the program "Ottewill". Contributions to the scattering arising from inter-micellar interference effects are accounted for by the use of a structure factor originally developed by Hayter et al (see chapter 6, ref. 15 for details) to describe spherical macroions in solution. The parameters *r1, r2* and *nd* are used in the calculation of both $P(Q)$ and $S(Q)$. The subroutine "model" calls the $P(Q)$ and $S(Q)$ subroutines ("form" and "stru" respectively), and uses the values returned by these two subroutines to calculate the differential scattering cross-section. The subroutine "stru" calls a set of four subroutines ("SQHPA", "SQCOEF", "SQFUN" and "SQHCAL" – written by Hayter et al, see chapter 6 ref.17 for details) which carry out the actual calculation of $S(Q)$. In addition to *r1, r2* and *nd*, the parameters *gam* ($\gamma$, the dimensionless coupling constant) and *AK* ($k$, the dimensionless screening constant) can be allowed to vary during the calculation of $S(Q)$.

```
$DEBUG
c
c   WRITTEN BY GAVIN J BOWN   MAY 1999
c
c
          program hayter
c         use msflib
          external readin,model
          common/titles/names(20),tx,ty
          common/titlep/nparas
          common/work/w(3066)
          common/version/verp
          common/modl/contrast
          character*8 names
          character*4 pnam
          character*20 tx,ty
c
c
c
          data names/'rhos','rhoc','rhom','r1',
         &'pr','r2','nd','gam','AK',11*' '/
          data pnam/'hayt'/
          data tx/'Q /A^-1'/
          data ty/'Cross Section (cm-1)'/
          data nparas/9/
c
c
c
c
c   Call the fitting library
c
          call fitfun(pnam,readin,model)
c
c
c
c
          write(6,'(a)')' Finished'
          stop
c
c
c
          end
c
c
c
c   Set up the functional forms with a Gaussian loop
c   to account for polydispersity in the micelle size
c
          subroutine model(npar,parm,npts,xuse,yuse,yruse,
          &ycalc,F)
          external form,stru
          REAL*4 ycalc(200),SQ(200),F(200),SP(200),forf(200),
         &yuse(200),yruse(200),xuse(200),qq(200)
          DIMENSION PARM(NPAR)
c
c
          open(10,file='out.dat',status='unknown')
c
```

```
      call form(npar,parm,npts,xuse,forf,SP)
      call stru(npar,parm,QQ,SQ,xuse,npts)
c
      do i=1,npts
      ycalc(i)=0
      ycalc(i)=ycalc(i)+(forf(i)*SQ(i))
      write(10,*)xuse(i),ycalc(i)
      F(i)=ycalc(i)-yuse(i)
      enddo
      close(10)
      return
      end
c
c
c
c
      subroutine form(npar,parm,npts,xuse,forf,SP)
      real*4 pr,rhos,rhoc,rhom,r1,r2,xuse(npts),nd
      dimension parm(npar)
      real*4 SP(200),forf(200)
      common/moose/r1,r2,nd,pr
c
c
      rhos=parm(1)
      rhoc=parm(2)
      rhom=parm(3)
      r1=parm(4)
      pr=parm(5)
      r2=parm(6)
      nd=parm(7)
c
c
      nit=12
      dr=(r1*pr)/(2.35*100)
      rmax=r1+(dr*3)
      rmin=r1-(dr*3)
      div=(rmax-rmin)/nit
      do i=1,npts
      forf(i)=0
      do 50 j=1,(nit+1)
      rval=rmin+div*(j-1)
      f1=(16*(3.14159265**2))/9.0
      f2=(rhos-rhom)
      f3=(3*((rval+r2)**3))*(sin(xuse(i)*(rval+r2))-((xuse(i)*(rval+r2))
     &*cos(xuse(i)*(rval+r2))))/((xuse(i)**3)*((rval+r2)**3))
      f4=(3*(rval**3))*(sin(xuse(i)*rval)-((xuse(i)*rval)*cos(xuse(i)*
     &rval)))/((xuse(i)**3)*(rval**3))
      f5=(rhoc-rhom)
      SP(i)=f1*(f2*(f3-f4)+(f5*f4))**2
      gauss=(1/(dr*2.51))*exp(-0.5*((r1-rval)/dr)**2)
      SOQ=SP(i)*gauss
      forf(i)=forf(i)+SOQ*div
50    continue
      forf(i)=nd*forf(i)*1e8
      open(30,file='oit.dat',status='unknown')
      write(30,*)xuse(i),forf(i),nd,r1,r2
      enddo
      close(30)
      return
      end
```

```
c
c
c
      subroutine stru(npar,parm,QQ,SQ,xuse,npts)
      real*4 QQ(200),SQ(200),xuse(200)
      dimension parm(npar)
      REAL*8 A,B,C,FF
      COMMON /SQHPB/ A,B,C,FF,ETA,GEK,AK,U,V,GAMK,SETA,SGEK,SAK,SCAL,G1
      real*4 r1,r2,nd,gam,AK
      common/moose/r1,r2,nd,pr
C
      r1=parm(4)
      pr=parm(5)
      r2=parm(6)
      nd=parm(7)
      gam=parm(8)
      AK=parm(9)
c
c  Calculate the array K=Qσ (Q=xuse(i), sigma=particle diameter=2(r1+r2))
      do i=1,npts
      QQ(i)=xuse(i)*(2*(r1+r2))
      enddo

c
c  Define the macroion/micelle volume fraction
      ETA=(3.141592654)*nd*((2*(r1+r2))**3)*(0.166666667)
c  Define the contact potential
      GEK=gam*exp(-AK)
      open(20,file='oot.dat',status='unknown')
      write(20,*)nd,eta,r1,r2,GEK
      call sqhpa(qq,sq,npts,ierr)
      close(20)
      RETURN
      end
c
c
c
C     ROUTINE TO CALCULATE S(Q*SIG) FOR A SCREENED COULOMB
C     POTENTIAL BETWEEN FINITE PARTICLES OF DIAMETER 'SIG'
C     AT ANY VOLUME FRACTION.  THIS ROUTINE IS MUCH MORE POWER-
C     FUL THAN "SQHP" AND SHOULD BE USED TO REPLACE THE LATTER
C     IN EXISTING PROGRAMS.  NOTE THAT THE COMMON AREA IS
C     CHANGED; IN PARTICULAR, THE POTENTIAL IS PASSED
C     DIRECTLY AS 'GEK' = GAMMA*EXP(-K) IN THE PRESENT ROUTINE.
C
C     JOHN B.HAYTER     (I.L.L.)     19-AUG-81
C
C     CALLING SEQUENCE:
C
C          CALL SQHPA(QQ,SQ,NPT,IERR)
C
C     QQ:  ARRAY OF DIMENSION NPT CONTAINING THE VALUES
C        OF Q*SIG AT WHICH S(Q*SIG) WILL BE CALCULATED.
C     SQ:  ARRAY OF DIMENSION NPT INTO WHICH VALUES OF
C        S(Q*SIG) WILL BE RETURNED.
C     NPT:  NUMBER OF VALUES OF Q*SIG.
C
C     IERR > 0:  NORMAL EXIT;  IERR=NUMBER OF ITERATIONS.
C        -1:  NEWTON ITERATION NON-CONVERGENT IN "SQCOEF"
C        -2:  NEWTON ITERATION NON-CONVERGENT IN "SQFUN".
```

```
C       -3:  CANNOT RESCALE TO G(1+) > 0.
C
C    ALL OTHER PARAMETERS ARE TRANSMITTED THROUGH A SINGLE
C    NAMED COMMON AREA:
C
C    REAL*8 A,B,C,F
C    COMMON /SQHPB/ A,B,C,F,ETA,GEK,AK,U,V,GAMK,SETA,SGEK,SAK,SCAL,G1
C
C    ON ENTRY:'
C
C    ETA:  VOLUME FRACTION
C    GEK:  THE CONTACT POTENTIAL GAMMA*EXP(-K)
C    AK:   THE DIMENSIONLESS SCREENING CONSTANT
C        K = KAPPA*SIG WHERE KAPPA IS THE INVERSE SCREENING
C        LENGTH AND SIG IS THE PARTICLE DIAMETER.
C
C    ON EXIT:
C
C    GAMK IS THE COUPLING:  2*GAMMA*S*EXP(-K/S), S=ETA**(1/3).
C    SETA, SGEK AND SAK ARE THE RESCALED INPUT PARAMETERS.
C    SCAL IS THE RESCALING FACTOR:  (ETA/SETA)**(1/3).
C    G1=G(1+), THE CONTACT VALUE OF G(R/SIG).
C    A,B,C,F,U,V ARE THE CONSTANTS APPEARING IN THE ANALYTIC
C    SOLUTION OF THE MSA [HAYTER-PENFOLD; MOL.PHYS. 42: 109 (1981)]
C
C    NOTES:
C
C    (A)  AFTER THE FIRST CALL TO SQHPA, S(Q*SIG) MAY BE EVALUATED
C    AT OTHER Q*SIG VALUES BY REDEFINING THE ARRAY QQ AND CALLING
C    "SQHCAL" DIRECTLY FROM THE MAIN PROGRAM.
C
C    (B)  THE RESULTING S(Q*SIG) MAY BE TRANSFORMED TO G(R/SIG)
C    USING THE ROUTINE "TROGS".
C
C    (C)  NO ERROR CHECKING OF INPUT PARAMETERS IS PERFORMED;
C    IT IS THE RESPONSIBILITY OF THE CALLING PROGRAM TO VERIFY
C    VALIDITY.
C    SUBROUTINES REQUIRED BY SQHPA:
C
C    (1) SQCOEF     RESCALES THE PROBLEM AND CALCULATES THE
C             APPROPRIATE COEFFICIENTS FOR "SQHCAL".
C
C    (2) SQFUN      CALCULATES VARIOUS VALUES FOR "SQCOEF".
C
C    (3) SQHCAL     CALCULATES H-P S(Q*SIG) GIVEN A,B,C,F.
C
C
     SUBROUTINE SQHPA(QQ,SQ,NPTS,IERR)
C
     REAL*4 QQ(200),SQ(200)
     REAL*8 A,B,C,FF
     COMMON /SQHPB/ A,B,C,FF,ETA,GEK,AK,U,V,GAMK,SETA,SGEK,SAK,SCAL,G1
     common/moose/r1,r2,nd,pr
c
     IERR=0
C
C     FIRST CALCULATE COUPLING.
C
     S=ETA**(0.333333333)
c         print*,s
```

```
      GAMK=2.0*S*GEK*EXP(AK-AK/S)
c
C
C     CALCULATE COEFFICIENTS, CHECK ALL IS WELL
C
  100 IERR=0
      CALL SQCOEF(IERR)
      IF(IERR.GE.0)GOTO 200
      RETURN
C
C     CALCULATE S(Q*SIG)
C
  200 CALL SQHCAL(QQ,SQ,NPTS)
C
      RETURN
      END
c
c
C     CALCULATES S(Q) FOR "SQHPA"
C
C     ** THIS ROUTINE WORKS LOCALLY IN DOUBLE PRECISION **
C
C     JOHN B.HAYTER     (I.L.L.)     19-AUG-81
C
      SUBROUTINE SQHCAL(QQ,SQ,NPTS)
C
      IMPLICIT REAL*8 (A-H,O-Z)
      REAL*4 QQ(200),SQ(200),ETAZ,GEKZ,AKZ,U,V,GAMK,SETA,SGEK,SAK,SCAL,
     &G1
      COMMON /SQHPB/ A,B,C,FF,ETAZ,GEKZ,AKZ,U,V,GAMK,SETA,SGEK,SAK,SCAL,
     1G1
C
      ETA=SETA
      AK=SAK
      GEK=SGEK
      E24=24.0D0*ETA
      X1=DEXP(AK)
      X2=0.0D0
      IF(SAK.LT.20.0)X2=DEXP(-AK)
      CK=0.5D0*(X1+X2)
      SK=0.5D0*(X1-X2)
      AK2=AK*AK
C
      DO 200 I=1,NPTS
      IF(QQ(I).LE.0.0)GOTO 100
      QK=QQ(I)/SCAL
      Q2K=QK*QK
      QK2=1.0D0/Q2K
      QK3=QK2/QK
      QQK=1.0D0/(QK*(Q2K+AK2))
      SINK=DSIN(QK)
      COSK=DCOS(QK)
      ASINK=AK*SINK
      QCOSK=QK*COSK
      AQK=(A*(SINK-QCOSK)
     1+B*((2.0D0*QK2-1.0D0)*QCOSK+2.0D0*SINK-2.0D0/QK)
     2+0.5D0*ETA*A*(24.0D0*QK3+4.0D0*(1.0D0-6.0D0*QK2)*SINK
     3-(1.0D0-12.0D0*QK2+24.0D0*QK2*QK2)*QCOSK))*QK3
     4+C*(CK*ASINK-SK*QCOSK)*QQK
     5+FF*(SK*ASINK-QK*(CK*COSK-1.0D0))*QQK
```

```
     6+FF*(COSK-1.0D0)*QK2
     7-GEK*(ASINK+QCOSK)*QQK
      SQ(I)=1.0D0/(1.0D0-E24*AQK)
      GOTO 200
  100 SQ(I)=-1.0D0/A
  200 CONTINUE
      open(40,file='oat.dat',status='unknown')
            do i=1,npts
            write(40,*)qq(i),sq(i),eta
            enddo
      close(40)
      RETURN
      END
c
c
C     CALCULATES VARIOUS COEFFICIENTS AND FUNCTION
C     VALUES FOR "SQCOEF" (USED BY "SQHPA").
C
C     ** THIS ROUTINE WORKS LOCALLY IN DOUBLE PRECISION **
C
C     JOHN B.HAYTER     (I.L.L.)     21-AUG-81
C
C     IX=1: SOLVE FOR LARGE K, RETURN G(1+).
C       2: RETURN FUNCTION TO SOLVE FOR ETA(GILLAN).
C       3: ASSUME NEAR GILLAN, SOLVE, RETURN G(1+).
C       4: RETURN G(1+) FOR ETA=ETA(GILLAN).
C
      SUBROUTINE SQFUN1(FVAL,EVAR,IX,IR)
C
      IMPLICIT REAL*8 (A-H,O-Z)
      REAL*4 RETA,RGEK,RAK,U,V,EVAR,FVAL,GAMK,
     1SETA,SGEK,SAK,SCAL,G1
C
      COMMON /SQHPB/ A,B,C,FF,RETA,RGEK,RAK,U,V,GAMK,SETA,SGEK,SAK,SCAL,
     1G1
C
C     CALCULATE CONSTANTS; NOTATION IS HAYTER-PENFOLD (1981).
C
      DATA ACC/1.0D-6/,ITM/40/
      ETA=EVAR
      ETA2=ETA*ETA
      ETA3=ETA2*ETA
      E12=12.0D0*ETA
      E24=E12+E12
      SCAL=(RETA/EVAR)**0.33333333
      SAK=RAK/SCAL-2.0*ALOG(1.0-EVAR)*EVAR**0.3333333
      SGEK=RGEK*SCAL*EXP(RAK-SAK)/(1.0-EVAR)**2
      GEK=SGEK
      AK=SAK
      AK2=AK*AK
      AK1=1.0D0+AK
      DAK2=1.0D0/AK2
      DAK4=DAK2*DAK2
      D=1.0D0-ETA
      D2=D*D
      DAK=D/AK
      DD2=1.0D0/D2
      DD4=DD2*DD2
      ETA3D=3.0D0*ETA
      ETA6D=ETA3D+ETA3D
```

```
      ETA32=ETA3+ETA3
      ETA2D=ETA+2.0D0
      ETA2D2=ETA2D*ETA2D
      ETA21=2.0D0*ETA+1.0D0
      ETA22=ETA21*ETA21
C
C     ALPHA(I)
C
      AL1=-ETA21*DAK
      AL2=(14.0D0*ETA2-4.0D0*ETA-1.0D0)*DAK2
      AL3=36.0D0*ETA2*DAK4
C
C     BETA(I)
C
      BE1=-(ETA2+7.0D0*ETA+1.0D0)*DAK
      BE2=9.0D0*ETA*(ETA2+4.0D0*ETA-2.0D0)*DAK2
      BE3=12.0D0*ETA*(2.0D0*ETA2+8.0D0*ETA-1.0D0)*DAK4
C
C     NU(I)
C
      VU1=-(ETA3+3.0D0*ETA2+45.0D0*ETA+5.0D0)*DAK
      VU2=(ETA32+3.0D0*ETA2+42.0D0*ETA-2.0D1)*DAK2
      VU3=(ETA32+3.0D1*ETA-5.0D0)*DAK4
      VU4=VU1+E24*AK*VU3
      VU5=ETA6D*(VU2+4.0D0*VU3)
C
C     PHI(I)
C
      PH1=ETA6D/AK
      PH2=D-E12*DAK2
C
C     TAU(I)
C
      TA1=(ETA+5.0D0)/(5.0D0*AK)
      TA2=ETA2D*DAK2
      TA3=-E12*GEK*(TA1+TA2)
      TA4=ETA3D*AK2*(TA1*TA1-TA2*TA2)
      TA5=ETA3D*(ETA+8.0D0)*1.0D-1-2.0D0*ETA22*DAK2
C
C     DOUBLE PRECISION SINH(K), COSH(K)
C
      EX1=DEXP(AK)
      EX2=0.0D0
      IF(SAK.LT.20.0)EX2=DEXP(-AK)
      SK=0.5D0*(EX1-EX2)
      CK=0.5D0*(EX1+EX2)
      CKMA=CK-1.0D0-AK*SK
      SKMA=SK-AK*CK
C
C     A(I)
C
      A1=(E24*GEK*(AL1+AL2+AK1*AL3)-ETA22)*DD4
      A2=E24*(AL3*SKMA+AL2*SK-AL1*CK)*DD4
      A3=E24*(ETA22*DAK2-0.5D0*D2+AL3*CKMA-AL1*SK+AL2*CK)*DD4
C
C     B(I)
C
      B1=(1.5D0*ETA*ETA2D2-E12*GEK*(BE1+BE2+AK1*BE3))*DD4
      B2=E12*(-BE3*SKMA-BE2*SK+BE1*CK)*DD4
      B3=E12*(0.5D0*D2*ETA2D-ETA3D*ETA2D2*DAK2
```

```
     1-BE3*CKMA+BE1*SK-BE2*CK)*DD4
C
C      V(I)
C
       V1=(ETA21*(ETA2-2.0D0*ETA+1.0D1)*2.5D-1
     1-GEK*(VU4+VU5))*DD45
       V2=(VU4*CK-VU5*SK)*DD45
       V3=((ETA3-6.0D0*ETA2+5.0D0)*D
     1-ETA6D*(2.0D0*ETA3-3.0D0*ETA2+18.0D0*ETA+1.0D1)*DAK2
     2+E24*VU3+VU4*SK-VU5*CK)*DD45
C
       PP1=PH1*PH1
       PP2=PH2*PH2
       PP=PP1+PP2
       P1P2=PH1*PH2*2.0D0
C
C      P(I)
C
       P1=(GEK*(PP1+PP2-P1P2)-0.5D0*ETA2D)*DD2
       P2=(PP*SK+P1P2*CK)*DD2
       P3=(PP*CK+P1P2*SK+PP1-PP2)*DD2
C
C      T(I)
C
       T1=TA3+TA4*A1+TA5*B1
       T2=TA4*A2+TA5*B2+E12*(TA1*CK-TA2*SK)
       T3=TA4*A3+TA5*B3+E12*(TA1*SK-TA2*(CK-1.0D0))
     1-4.0D-1*ETA*(ETA+1.0D1)-1.0D0
C
C      MU(I)
C
       UM1=T2*A2-E12*V2*V2
       UM2=T1*A2+T2*A1-E24*V1*V2
       UM3=T2*A3+T3*A2-E24*V2*V3
       UM4=T1*A1-E12*V1*V1
       UM5=T1*A3+T3*A1-E24*V1*V3
       UM6=T3*A3-E12*V3*V3
C
C      GILLAN CONDITION?
C
C      YES - G(X=1+)=0
C
C      COEFFICIENTS AND FUNCTION VALUE.
C
       IF(IX.EQ.1)GOTO 100
       IF(IX.EQ.3)GOTO 100
       CA=AK2*P1+2.0D0*(B3*P1-B1*P3)
       CA=-CA/(AK2*P2+2.0D0*(B3*P2-B2*P3))
       FA=-(P1+P2*CA)/P3
       IF(IX.EQ.2)FVAL=UM1*CA*CA+(UM2+UM3*FA)*CA+UM4+UM5*FA+UM6*FA*FA
       IF(IX.EQ.4)FVAL=-(P1+P2*CA+P3*FA)
    50 FF=FA
       C=CA
       B=B1+B2*CA+B3*FA
       A=A1+A2*CA+A3*FA
       V=(V1+V2*CA+V3*FA)/A
       G24=E24*GEK*EX1
       U=(AK*AK2*CA-G24)/(AK2*G24)
       RETURN
C
```

```
C     NO - CALCULATE REMAINING COEFFICIENTS.
C
C     LAMBDA(I)
C
  100 AL1=E12*P2*P2
      AL2=E24*P1*P2-B2-B2
      AL3=E24*P2*P3
      AL4=E12*P1*P1-B1-B1
      AL5=E24*P1*P3-B3-B3-AK2
      AL6=E12*P3*P3
C
C     OMEGA(I,J)
C
      W16=UM1*AL6-AL1*UM6
      W15=UM1*AL5-AL1*UM5
      W14=UM1*AL4-AL1*UM4
      W13=UM1*AL3-AL1*UM3
      W12=UM1*AL2-AL1*UM2
      W26=UM2*AL6-AL2*UM6
      W25=UM2*AL5-AL2*UM5
      W24=UM2*AL4-AL2*UM4
      W36=UM3*AL6-AL3*UM6
      W35=UM3*AL5-AL3*UM5
      W34=UM3*AL4-AL3*UM4
      W32=UM3*AL2-AL3*UM2
      W46=UM4*AL6-AL4*UM6
      W56=UM5*AL6-AL5*UM6
      W3526=W35+W26
      W3425=W34+W25
C
C     QUARTIC COEFFICIENTS W(I)
C
      W4=W16*W16-W13*W36
      W3=2.0D0*W16*W15-W13*W3526-W12*W36
      W2=W15*W15+2.0D0*W16*W14-W13*W3425-W12*W3526
      W1=2.0D0*W15*W14-W13*W24-W12*W3425
      W0=W14*W14-W12*W24
C
C     ESTIMATE THE STARTING VALUE OF F
C
      IF(IX.EQ.1)GOTO 200
C
C     ASSUME NOT TOO FAR FROM GILLAN CONDITION.
C     IF BOTH GEK AND AK ARE SMALL, USE P-W ESTIMATE.
C
      G1=0.5D0*ETA2D*DD2*DEXP(-GEK)
      IF(SGEK.GT.2.0.OR.SAK.GT.1.0)GOTO 150
      E24G=E24*GEK*DEXP(AK)
      PWK=DSQRT(E24G)
      QPW=(1.0D0-DSQRT(1.0D0+2.0D0*D2*D*PWK/ETA22))*ETA21/D
      G1=-QPW*QPW/E24+0.5D0*ETA2D*DD2
  150 PG=P1+G1
      CA=AK2*PG+2.0D0*(B3*PG-B1*P3)+E12*G1*G1*P3
      CA=-CA/(AK2*P2+2.0D0*(B3*P2-B2*P3))
      FAP=-(PG+P2*CA)/P3
      GOTO 250
C
C     LARGE K.
C
  200 FAP=(W14-W34-W46)/(W12-W15+W35-W26+W56-W32)
```

```
C
C     AND REFINE IT ACCORDING TO NEWTON
C
  250 I=0
  300 I=I+1
      IF(I.GT.ITM)GOTO 400
      FA=FAP
      FUN=W0+(W1+(W2+(W3+W4*FA)*FA)*FA)*FA
      FUND=W1+(2.0D0*W2+(3.0D0*W3+4.0D0*W4*FA)*FA)*FA
      FAP=FA-FUN/FUND
      IF(DABS((FAP-FA)/FA).GT.ACC)GOTO 300
      IR=IR+I
      GOTO 500
C
C     FAILED TO CONVERGE IN ITM ITERATIONS
C
  400 IR=-2
      RETURN
C
  500 FA=FAP
      CA=-(W16*FA*FA+W15*FA+W14)/(W13*FA+W12)
      G1=-(P1+P2*CA+P3*FA)
      FVAL=G1
      IF(ABS(FVAL).LT.1.0E-3)FVAL=0.0
      SETA=EVAR
      GOTO 50
C
      END
c
c
C     CALCULATES RESCALED VOLUME FRACTION AND CORRESPONDING
C     COEFFICIENTS FOR "SQHPA".
C
C     JOHN B.HAYTER     (I.L.L.)     21-AUG-81
C
C     ON EXIT:
C
C     SETA IS THE RESCALED VOLUME FRACTION.
C     SGEK IS THE RESCALED CONTACT POTENTIAL.
C     SAK IS THE RESCALED SCREENING CONSTANT.
C     A,B,C,F,U,V ARE THE MSA COEFFICIENTS.
C     G1=G(1+) IS THE CONTACT VALUE OF G(R/SIG);
C     FOR THE GILLAN CONDITION, THE DIFFERENCE FROM
C     ZERO INDICATES THE COMPUTATIONAL ACCURACY.
C
C     IR > 0:  NORMAL EXIT, IR IS THE NUMBER OF ITERATIONS.
C       < 0:  FAILED TO CONVERGE.
C
      SUBROUTINE SQCOEF(IR)
      REAL*8 A,B,C,FF
      COMMON /SQHPB/ A,B,C,FF,ETA,GEK,AK,U,V,GAMK,SETA,SGEK,SAK,SCAL,G1
C
      DATA ITM/40/,ACC/5.0E-6/
      IG=1
      IF(AK.LT.(1.0+8.0*ETA))GOTO 50
      IG=0
      CALL SQFUN1(G1,ETA,1,IR)
      IF(IR.LT.0.OR.G1.GE.0.0)RETURN
   50 SETA=AMIN1(ETA,0.20)
      IF(IG.EQ.1.AND.GAMK.LT.0.1)GOTO 400
```

```
      J=0
  100 J=J+1
      IF(J.GT.ITM)GOTO 200
      IF(SETA.LE.0.0)SETA=ETA/J
      IF(SETA.GT.0.6)SETA=0.35/J
      E1=SETA
      CALL SQFUN1(FF1,E1,2,IR)
      E2=SETA*1.01
      CALL SQFUN1(FF2,E2,2,IR)
      E2=E1-(E2-E1)*FF1/(FF2-FF1)
      SETA=E2
      DEL=ABS((E2-E1)/E1)
      IF(DEL.GT.ACC)GOTO 100
      CALL SQFUN1(G1,E2,4,IR)
      IR=J
      IF(IG.EQ.1)GOTO 300
      RETURN
  200 IR=-1
      RETURN
  300 IF(SETA.GE.ETA)RETURN
  400 CALL SQFUN1(G1,ETA,3,IR)
      IF(IR.LT.0.OR.G1.GE.0.0)RETURN
      IR=-3
      RETURN
C
      END
C
c
c
c
c
c
c
c
c
c  Readin routine for LoQ .asc files
c
c
          subroutine readin(npts,xuse,yuse,yruse,text)
          dimension xuse(1000),yuse(1000),yruse(1000),temp(1000)
          character*50 text,garb
          character*20 fname
          logical exists
   10     write(6,15)
   15     format(/,' Give filename: ',$)
          read(5,20)fname
          inquire(file=fname,exist=exists)
          if(.not.exists)then
          write(6,25)
          goto 10
          endif
          open(7,file=fname,status='old')
          read(7,20)text
          read(7,20)garb
          read(7,20)garb
          read(7,20)garb
          read(7,20)garb
          npts=1
   30     read(7,*,end=99)xuse(npts),yuse(npts)
          npts=npts+1
```

```
        goto 30
 99     npts=npts-1
        close(7)
c       kount=0
c       j=0
        do i=1,npts
        yruse(i)=0.0
c       if(yuse(i).gt.0)then
c       j=j+1
c       temp(j)=log10(yuse(i))
c       else
c       kount=1
c       endif
c 50    enddo
c       npts=npts-kount
c       do i=1,npts
c       yuse(i)=temp(i)
        enddo
 20     format(a)
 25     format('No file of that name present!!')
        return
        end
```

## A4 Program "Percus"

This program uses the same spherical core-shell form factor as the program "Ottewill". However, contributions to the scattering arising from intermicellar interference effects are calculated using the Percus-Yevick hard-sphere model for $S(Q)$ (see chapter 6, refs.12 and 13 for further details). The subroutine "model" calls the subroutines "form" and "stru" which calculate $P(Q)$ and $S(Q)$ respectively. These values are then returned to the "model" subroutine where the differential scattering cross-section is calculated. The subroutine "stru" uses the parameters *nd* and *hsr* (the hard-sphere radius) in the calculation of $S(Q)$.

```
$DEBUG
c
c   WRITTEN BY GAVIN J BOWN   MAY 1999
c
c
        program Percus
c       use msflib
        external readin,model
        common/titles/names(20),tx,ty
        common/titlep/nparas
        common/work/w(3066)
        common/version/verp
        common/modl/contrast
```

```
      character*8 names
      character*4 pnam
      character*20 tx,ty
c
c
c
      data names/'rhos','rhoc','rhom','r1',
     &'pr','r2','nd','hsr',12*' '/
      data pnam/'perc'/
      data tx/'Q /A^-1'/
      data ty/'Cross Section (cm-1)'/
      data nparas/8/
c
c
c
c
c  Call the fitting library
c
      call fitfun(pnam,readin,model)
c
c
c
c
      write(6,'(a)')' Finished'
      stop
c
c
c
      end
c
c
c
c  Set up the functional forms with a Gaussian routine
c  to account for polydispersity in the micelle size
c
      subroutine model(npar,parm,npts,xuse,yuse,yruse,
      &ycalc,F)
      external form,stru
      REAL*4 ycalc(200),SQ(200),F(200),SP(200),forf(200),
     &yuse(200),yruse(200),xuse(200)
      DIMENSION PARM(NPAR)
c
c
      open(10,file='out.dat',status='unknown')
c
      call form(npar,parm,npts,xuse,forf,SP)
      call stru(npar,parm,SQ,xuse,npts)
c
      do i=1,npts
      ycalc(i)=0
      ycalc(i)=ycalc(i)+(forf(i)*SQ(i))
      write(10,*)xuse(i),ycalc(i)
      F(i)=ycalc(i)-yuse(i)
      enddo
      close(10)
      return
      end
c
c
c
```

```
c
      subroutine form(npar,parm,npts,xuse,forf,SP)
      real*4 pr,rhos,rhoc,rhom,r1,r2,xuse(npts),nd
      dimension parm(npar)
      common/moose/nd
      real*4 SP(200),forf(200)
c     common/moose/r1,r2,nd,pr
c
c
      rhos=parm(1)
      rhoc=parm(2)
      rhom=parm(3)
      r1=parm(4)
      pr=parm(5)
      r2=parm(6)
      nd=parm(7)
c
c
      nit=12
      dr=(r1*pr)/(2.35*100)
      rmax=r1+(dr*3)
      rmin=r1-(dr*3)
      div=(rmax-rmin)/nit
      do i=1,npts
      forf(i)=0
      do 50 j=1,(nit+1)
      rval=rmin+div*(j-1)
      f1=(16*(3.14159265**2))/9.0
      f2=(rhos-rhom)
      f3=(3*((rval+r2)**3))*(sin(xuse(i)*(rval+r2))-((xuse(i)*(rval+r2))
     &*cos(xuse(i)*(rval+r2))))/((xuse(i)**3)*((rval+r2)**3))
      f4=(3*(rval**3))*(sin(xuse(i)*rval)-((xuse(i)*rval)*cos(xuse(i)*
     &rval)))/((xuse(i)**3)*(rval**3))
      f5=(rhoc-rhom)
      SP(i)=f1*(f2*(f3-f4)+(f5*f4))**2
      gauss=(1/(dr*2.51))*exp(-0.5*((r1-rval)/dr)**2)
      SOQ=SP(i)*gauss
      forf(i)=forf(i)+SOQ*div
50    continue
      forf(i)=nd*forf(i)*1e8
      open(30,file='oit.dat',status='unknown')
      write(30,*)xuse(i),forf(i),nd,r1,r2
      enddo
      close(30)
      return
      end
c
c
c
      subroutine stru(npar,parm,SQ,xuse,npts)
      real*4 SQ(200),xuse(200)
      dimension parm(npar)
      common/moose/nd
      real*4 hsr,nd
c
      nd=parm(7)
      hsr=parm(8)
c
c
      do i=1,npts
```

```
      pi=3.141592654
      f1=(4.0/3.0)*pi*(hsr**3)*nd
      f2=((1-f1)**4)
      f3=((1+(2*f1))**2)/f2
      f4=((-6.0*f1)*(1+(f1/2.0))**2)/f2
      f5=((0.5*f1)*(1+(2*f1))**2)/f2
      f6=2.0*xuse(i)*hsr
      f7=sin(f6)
      f8=cos(f6)
      f9=(f3/(f6**2))*(f7-(f6*f8))
      f10=(f4/(f6**3))*((2.0*f6*f7)+((2.0-(f6**2))*f8)-2.0)
      f11=(f5/(f6**5))
      f12=-(f6**4)*f8
      f13=((3.0*(f6**2))-6.0)*f8
      f14=((f6**3)-(6.0*f6))*f7
      f15=f11*(f12+4.0*(f13+f14+6.0))
      f16=f9+f10+f15
      SQ(i)=1.0/(1.0+(24.0*f1)*(f16/f6))
      enddo
      return
      end
c
c
c
c
c
c
c
c
c  Readin routine for LoQ .asc files
c
c
      subroutine readin(npts,xuse,yuse,yruse,text)
      dimension xuse(1000),yuse(1000),yruse(1000),temp(1000)
      character*50 text,garb
      character*20 fname
      logical exists
 10   write(6,15)
 15   format(/,' Give filename: ',$)
      read(5,20)fname
      inquire(file=fname,exist=exists)
      if(.not.exists)then
      write(6,25)
      goto 10
      endif
      open(7,file=fname,status='old')
      read(7,20)text
      read(7,20)garb
      read(7,20)garb
      read(7,20)garb
      read(7,20)garb
      npts=1
 30   read(7,*,end=99)xuse(npts),yuse(npts)
      npts=npts+1
      goto 30
 99   npts=npts-1
      close(7)
c     kount=0
c     j=0
      do i=1,npts
```

```
      yruse(i)=0.0
c     if(yuse(i).gt.0)then
c     j=j+1
c     temp(j)=log10(yuse(i))
c     else
c     kount=1
c     endif
c 50  enddo
c     npts=npts-kount
c     do i=1,npts
c     yuse(i)=temp(i)
      enddo
 20   format(a)
 25   format(' No file of that name present!!')
      return
      end
```

# APPENDIX B

## AN ANALYTIC STRUCTURE FACTOR FOR MACROION SOLUTIONS

$$S(K) = \frac{1}{1 - 24\eta a(K)} \qquad \text{where: } K = Q\sigma$$

The macroion volume fraction, $\eta$, is expressed in terms of the number density ($n$) and the macroion diameter ($\sigma$) as:

$$\eta = \frac{\pi n \sigma^3}{6}$$

$$\begin{aligned} a(K) &= A(\sin K - K\cos K)/K^3 + B\left[(2/K^2 - 1)K\cos K + 2\sin K - 2/K\right]/K^3 \\ &+ \eta A\left[24/K^3 + 4(1 - 6/K^2)\sin K - (1 - 12/K^2 + 24/K^4)K\cos K\right]/2K^3 \\ &+ C(k\cosh k\sin K - K\sinh k\cos K)/K(K^2 + k^2) \\ &+ F\left[k\sinh k\sin K - K(\cosh k\cos K - 1)\right]/K(K^2 + k^2) \\ &+ F(\cos K - 1)/K^2 \\ &- \gamma\exp(-k)(k\sin K + K\cos K)/K(K^2 + k^2) \end{aligned}$$

where: $k$ is the dimensionless screening constant and $\gamma$ is the dimensionless coupling constant. $\gamma\exp(-k)$ is the contact potential for a macroion pair (expressed in units of $k_B T$).

The coefficients $A, B, C$ and $F$ are expressed in terms of several further sets of coefficients. For further details, the reader is referred to: Hayter, J B; Penfold, J. *Molecular Physics*, 1981, **42**, 109.

# APPENDIX C

## LECTURES AND CONFERENCES ATTENDED

### C.1 Lectures Attended

#### C.1.1 Academic Year 1996/97

| | |
|---|---|
| 23 October | Prof. H. Ringsdorf<br>Johannes Gutenberg Universitat, Mainz, Germany<br>"Function Based on Organisation" |
| 20 November | Prof. J. Earnshaw<br>The Queen's University, Belfast<br>"Surface Light Scattering: Ripples and Relaxation" |
| 27 November | Dr R. Templer<br>Imperial College, London<br>"Molecular Tubes and Sponges" |
| 6 December | Dr A. C. Barnes<br>University of Bristol<br>"Application of Neutron Spectroscopy and Diffraction to Studies of Disordered Systems" |

| | |
|---|---|
| 22 January | Dr N. Cooley<br>BP Chemicals, Sunbury<br>"Synthesis and Properties of Alternating Polyketones" |
| 29 January | Prof. Julian Clarke<br>UMIST<br>"Molecular dynamics simulations of polymers and biopolymers: Computer generated nanosecond movie clips." |
| 26 February | Dr A. Ryan<br>UMIST<br>"Making Hairpins from Rings and Chains" |
| 11 March | Dr A D Taylor<br>ISIS, Rutherford Appleton Laboratory<br>"Expanding the Frontiers of Neutron Scattering" |
| 19 March | Dr K. Reid<br>University of Nottingham<br>"Probing Dynamical Processes with Photoelectrons" |
| 17 April | Prof. D. Geschke<br>University of Leipzig, Germany<br>"NMR of Liquid Crystalline Polymers" |
| 7 May | Prof. M. Harrington<br>Caltech, Pasadena, USA<br>"Polymers which both Enable and Limit the Recovery of Protein Alterations in Studies Ranging from Gene Regulation to Mad Cow Disease" |
| 13 June | Prof. H. Yu |

University of Wisconsin, USA

"Dynamics of Macromolecular Monolayers"

## C.1.2 Academic Year 1997/98

21 October — Prof. A. F. Johnson
University of, Leeds
"Reactive Processing of Polymers: Science and Technology"

28 October — Prof. A. P. de Silva
The Queen's University, Belfast
"Luminescent Signalling Systems"

12 November — Dr J. Frey
University of Southampton
"Spectroscopy of Liquid Interfaces: from Bio-organic Chemistry to Atmospheric Chemistry"

26 November — Professor R. W. Richards
University of Durham
"Inaugural Lecture: A Random Walk in Polymer Science"

2 December — Dr C. J. Ludman
University of Durham
"Explosions"

28 January — Dr S. Rannard
Courtaulds Coatings, Coventry
"The Synthesis of Dendrimers using Highly Selective Chemical Reactions"

| | |
|---|---|
| 18 February | Professor G. Hancock<br>University of Oxford<br>"Surprises in the Photochemistry of Tropospheric Ozone" |
| 4 March | Professor T. C. B. McLeish<br>University of Leeds<br>"The Polymer Physics of Pyjama Bottoms" |

### C.1.3 Academic Year 1998/99

| | |
|---|---|
| 7 October | Dr S. Rimmer<br>University of Lancaster<br>"New Polymer Colloids" |
| 27 October | Professor A. Unsworth<br>University of Durham<br>"What's a Joint Like this Doing in a Nice Girl Like You?" |
| 28 October | Professor J. P. S. Badyal<br>University of Durham<br>"Inaugural Lecture: Tailoring Solid Surfaces" |
| 18 November | Dr R. Cameron<br>University of Cambridge<br>"Biodegradable Polymers" |
| 1 December | Professor N. Billingham<br>University of Sussex<br>"Plastics in the Environment - Boon or Bane?" |

| | |
|---|---|
| 10 February | Dr C. Bain<br>University of Oxford<br>"Surfactant Adsorption and Marangoni Flow at Expanding Liquid Surfaces" |
| 9 March | Dr M. Warhurst<br>Friends of the Earth<br>"Is the Chemical Industry Sustainable?" |
| 11 May | Dr J. Sodeau<br>University of East Anglia<br>"Ozone Holes and Ozone Hills" |

## C.2 Conferences Attended

| | |
|---|---|
| October 1996 | First European Conference on Neutron Scattering<br>Interlaken, Switzerland |
| April 1997 | Macro Group UK Spring Meeting for Younger Researchers<br>Queens's Hotel, Leeds |
| July 1997 | Polymer Surfaces and Interfaces III<br>University of Durham |
| April 1998 | RSC National Congress and Young Researchers' Meeting<br>University of Durham |
| September 1998 | New Perspectives in Neutron and Muon Science: A Meeting for Young Researchers<br>Cosener's House, Abingdon |
| September 1998 | Neutron and Muon Beam Users' Meeting<br>Rutherford Appleton Laboratory, Oxfordshire |
| September 1998 | IRC Industrial Club Meeting<br>University of Durham |

September 1999 Neutron and Muon Beam Users' Meeting

University of Durham